Optomechanical Damping of a Microcantilever Force Sensor in Liquid

Khalid Eidah Al Zahrani

Submitted in accordance with the requirements for the degree of Doctor of philosophy

The University of Leeds, School of Physics and Astronomy

October, 2010

Acknowledgements

First and foremost, I am eternally grateful to a number of people without whom this work would not have been possible. I would like to express to everyone who contributed to this thesis my sincere gratitude.

I am indebted to my supervisor, Dr. Simon Connell, for his constant guidance, patience and support through my studies. Thank you for giving me the opportunity to study for PhD and giving me the freedom to pursue what I found interesting in this project. Your support and inspiration have allowed my research skills to develop. Despite of your limited time, you have generously leant your time to discuss my results and sometimes to answer my silly questions.

I am indebted to Dr. David Brockwell for his support and many fruitful discussions on the work presented here. Thank you for providing supplies of protein. I am grateful to Dr. Neal Crampton for his advice and useful discussions. I also thank Mr. Richard Oliver, a member of electronics workshop, for his help and useful advice. I also acknowledge the generous funding from Saudi government.

I am forever grateful to my family for their unconditional love, understanding and support. Thank you for everything you have done for me.

Abstract

A new instrument, constant deflection atomic force microscopy (CD-AFM) constructed to perform force spectroscopy measurements without mechanical instabilities associated with the use of soft AFM cantilevers has been developed, tested and calibrated.

One of the major limitations associated with the use of soft AFM cantilevers in force spectroscopy measurements is cantilever mechanical instabilities. This includes thermodynamic noise and the cantilever non-equilibrium deflection close to the surface. This limitation can obscure ultrahigh force resolution and short range force measurements, and limits the accessible dynamic range. More stable stiff cantilevers have poor force resolution.

The force resolution of the softest standard cantilever limited by thermodynamic noise has been improved from approximately 30 pN to ~2 pN using the CD-AFM system. It was proved that the discontinuity in the force distance curve close to the surface, approximately 7 nm, was prevented using CD-AFM. The cantilever deflection is kept constant even after the cantilever jumps to the surface. Using CD-AFM, inaccessible regions near the surface can be explored and valuable information about very short tip-surface interactions can be studied.

The need to lock cantilever deflection prevents the use of the deflection signal to record tip-surface interactions. Alternatively, the laser signal used to keep the cantilever deflection constant is employed to record the interactions. The curves obtained using CD-AFM were scaled in force using a new method introduced for this purpose. The new calibration

method was tested, and validated through electrostatic force measurements, with curves obtained using conventional AFM or CD-AFM showing the same behavior.

Application of CD-AFM to unfold a five concatamer of the protein immunoglobulin 27 showed that CD-AFM has a wider dynamic range than conventional AFM. For example, loading rate in conventional AFM is limited by the cantilever stiffness and the pulling speed. Using CD-AFM the loading rate increases but without degenerating the force resolution. Moreover, protein L shows no refolding event using conventional AFM due to the tension loaded on the refolded protein by cantilever recoil. Using CD-AFM the cantilever recoil was removed and the refolding events become observable.

Contents

List of Figures

List of Tables

Acronyms and Abbreviations

AFM	Atomic force microscopy
CD-AFM	Constant deflection AFM
SEM	Scanning electron microscopy
SPM	Scanning probe microscopy
DNA	Deoxyribonucleic acid
IFM	Intermolecular force spectroscope
RMS	Root mean square
DLVO	Derjaguin, Landau, Verwey and Overbeek theory
DMT	Derjaguin-Mulller-Toporov model
JKR	Johnson-Kendall –Roberts model
PSD	Power spectral density
FP	Fabry-Perot resonator
PSPD	Position-sensitive photodetector
SNR	Signal to noise ratio
LVZ	Low voltage Z
OBD	Optical beam deflection method
NMR	Nuclear magnetic resonance
WLC	Worm-like chain model
MD	Molecular dynamic method
IR	Infra-red
PEVK	Proline ,Glutamic acid(E), Valine(V) and Lysine residues(K) segment
FNIII	Fibronectin
Ig	Immunoglobulin
PI	Proportional-Integral gains
I27	Immunoglobulin 27
Si_3N_4	Silicon nitride
Au	Gold
LD1	Diode laser with power of 5mW and wavelength of 670nm
LD2	Diode laser with power of 50mW and wavelength of 780nm
e(t)	Error signal
A_H	Hamaker's constant
ε	Medium dielectric constant
ε_0	Vacuum permittivity constant
K_B	Boltzmann constant
c	Speed of light
F	Force
F_{ad}	Adhesion force
F_{rd}	Radiation force

F_{van}	Van der Waals force
F_L	Langevin force
ω	Angular frequency
δF	Minimum detectable force
n	Reflective index
R	Radius of sphere
υ_s	Poisson ratio
E	Young's modulus
P	Laser power
W	Energy
W_A	Energy per unit area
W_{Av}	Van der Waals interaction energy per unit area
W_{Ad}	Double layer interaction energy per unit area
ρ	Density
ρ_f	Density of fluid
m	mass
m_c	Mass of cantilever
m_t	Mass of cantilever tip
m_{eff}	Effective mass
T	Temperature
T_{eff}	Effective temperature
ΔT	Change of temperature
ΔZ	Vertical displacement of the free end of the cantilever
ΔV	Change of the voltage output of the PSPD
Δx	Laser spot shift on PSPD
$\Delta z_{heating}$	Cantilever deflection due to bimetallic effect
ΔG_u	Height of energy barrier
$\Delta\omega$	Bandwidth
k	Cantilever stiffness (spring constant)
Φ	Opening angle of cone
v	Cantilever velocity
s	Cantilever deflection sensitivity
υ_0	Resonance frequency of cantilever
l	Cantilever length
j	Width of cantilever
h	Thickness of cantilever
Q	Mechanical quality factor of cantilever
ω_0	Angular resonance frequency of cantilever
$\Im_T$	Cantilever tip potential

$\Im_S$	Surface potential
C_d	Output of PI controller
ψ	Laser wavelength
ψ_z	Spatial period
φ	Incidence angle of laser beam
D	Sample-tip separation
U	Piezoscanner displacement
r	Distance between molecules
L_D	Debye length
δi	Indentation
a	Contact area
Γ_i	Imaginary component of the hydrodynamic function
A_p	Area below the peak of the power spectrum density
δz	Root mean square of the cantilever thermal deflection
PH	A measure of the acidity or basicity
H	Hamiltonian
S_Z	Power spectral density of thermodynamic noise of the cantilever displacement
S_F	Power spectrum of Langevin force
G	Transfer function
X(w)	Fourier transformer of Z(t)
γ	Damping factor
RF	Radio frequency
Ω	Frequency of the resonant circuit
L_0	Inductance
C_0	Capacity
V_{rf}	Applied voltage to maintain setpoint in a resonance frequency circuit
$\delta\phi$	Phase shift
δx	Displacement of the Fabry-Perot cavity length
χ	Fabry-Perot cavity Finesse
ξ	A constant related to the optics and electrical components used in the AFM experiment
x	Diameter of the laser spot on the PSPD
d	Distance between the cantilever and the PSPD
d_f	Focusing length
a	Diameter of the collimated laser beam

n_{sh}	Shot noise
e	Electron charge
η	Conversion efficiency of photodetectors from light to current
P	Laser power
Π	Attenuation of laser power in its optical path
Λ	Resultant of forces
M	Momentum
A	Oscillation amplitude
F_s	Force sensitivity
α	Thermal expansion coefficient
$\alpha(0)$	Unfolding rate in the absence of the mechanical force
C	Specific heat
r_f	Loading rate
x_u	Width of the potential for unfolding protein
x_f	Width of the potential for folding protein
λ	Thermal conductivity
t	Time
R_H	Changing rate of laser signal to driving frequency
p	Persistence length
L	Contour length
x_t	Extension of protein
ς	Decay length
T	Temperature
τ	Relaxation time
β	Absorbed fraction of the radiant power
H_C	Heat capacity

Chapter 1
Introduction

Unlike optical or electronic microscopes, which produce an image by focusing scattered radiation through lenses, scanning probe microscopes measure a local property, such as force, electronic tunnelling current or magnetic field, with a small probe. The probe is scanned over the surface to build-up a 3D image. In 1986, Binnig *et al (1)* invented the atomic force microscope (AFM), which is a member of the scanning probe microscope (SPM) family, to overcome the limitations of the scanning tunnelling microscope (STM)(*1*). The most significant limitation of STM is that the specimen surface must be conducting or semiconducting because the imaging is based on the detection of electrons tunnelling between a sharp tip and a conducting or semiconducting surface. AFM is a mechanical microscope in which the mechanical displacement of a sharp probe is converted into an image of the scanned surfaces via an optical detection system.

AFM is a powerful tool for visualizing the structures of a sample surface with up to atomic resolution, and is capable of detecting very small forces of the order of hundreds to tens of piconewtons. Despite the existence of

alternative techniques for measuring forces in this low range, for example optical or magnetic tweezers(*2-4*), AFM has been widely adopted by researchers worldwide as the method of choice due to its availability, wide dynamic range and ease of use.

Measuring very small forces has many applications in both biological and physical fields(*5*). For instance, AFMs have been used for more than a decade for investigating the mechanical properties of single proteins(*6*) and single strands of DNA(*7*) by a procedure in which the deflection of the AFM cantilever and hence force is monitored while the sample is extended between a cantilever tip and surface. The operating principle of AFM in such applications is based on a force sensor that is composed of a nano-scale tip mounted on a soft cantilever. The interaction forces between the tip and sample results in a bending of the cantilever. Usually, the force is plotted as a function of the tip-surface separation and that plot is known as a force-distance curve.

In order to achieve high force resolution, very soft microcantilevers are employed, namely, the spring constant of the AFM cantilever must be sufficiently small to deflect with very minute forces. The use of very soft cantilevers to increase the force resolution is limited by a serious technical problem, mechanical instability. The first source of this instability originates from thermodynamic noise. A soft cantilever experiences large Brownian motion due to collisions of the surrounding's molecules with the cantilever. The amplitude of the fluctuations of AFM cantilevers induced by thermodynamic noise could be comparable to the magnitude of the sample-cantilever interactions. Thus, the signal generated from a true force signal could be indistinguishable from the thermal response of the cantilever. Consequently, forces below this thermal noise limit will be undetectable and crucial data could be lost. For instance, a protein

domain, which cannot withstand the forces transmitted to it from the thermodynamic noise of the cantilever, may unfold stochastically.

The second source of instability that causes a loss in information about the forces near the sample surface, is due to the jump-to contact process. When the force gradient in the vicinity of surface exceeds the stiffness of the cantilever, the tip jumps to the surface causing a discontinuity in the force distance curves.

Various force feedback techniques have been proposed to prevent mechanical instability of AFM cantilevers. The major aim of such techniques is to maintain zero deflection of the cantilever via an external feedback circuit. The output of the feedback circuit is used to extract the interaction force. Magnetic force feedback(*8*) is a widely adopted technique that is based on attaching a magnet to an AFM cantilever and flowing a current through a coil placed perpendicularly near the cantilever. The force applied to the cantilever is controlled by the magnetic field. The magnetic force feedback was used to overcome both the cantilever instability associated with jumping(*9*) and thermodynamic noise(*10*). However, such a method is technically demanding and not user-friendly because attaching magnets to the cantilever and placing the coils near the tip are time consuming and tedious processes. In addition, to our best knowledge, such a method has not been applied to detect a very small force for biological and non-biological samples. Moreover, by investigating many force curves obtained by this technique, we noticed the force resolution may be limited to ~100 pN(*9, 11*)

Force feedback techniques based on optical means have been entirely limited to experiments directed to cooling cantilevers via reducing the thermodynamic noise(*12-14*). The common setup of such experiments is to place a mirror mounted on an AFM cantilever inside a Fabry-Perot cavity

in vacuum. Thus, such experiments were not aimed at acquiring force-distance curves.

We have overcome the disadvantages related to the above techniques by means of an optical-based force feedback system called constant deflection AFM (CD- AFM). The cantilever deflection control proceeds with the use of two diode lasers, the first one with low power is used to read out the position of the cantilever, and the secondary high powered laser provides the force feedback. The error signal, which is the difference between the predefined set point and the cantilever deflection, processed by a PI controller is sent to the laser diode driver by which the high powered laser is modulated in order to produce an adequate feedback force that counteracts the motion of the cantilever. CD-AFM can be operated in liquid that enables force measurements on biological samples as well as non-biological samples.

In addition, a calibration method to quantify the force associated with using laser power as a feedback force and the tip-sample separation have been developed that allows us to record the force distance curve.

CD-AFM and the calibration methods were tested via some applications. Force curves using the softest cantilever commercially available in different ionic strength were obtained and compared to the conventional measurements. Moreover, a construct of five I27 protein and Im9 protein were unfolded by means of CD-AFM.

The force resolution of our system for microcantilever C with spring constant of 0.01 N/m limited by the thermodynamic noise is reduced from~30 pN to ~3 pN, peak to peak, and from ~7 pN to<1 pN in RMS. However, we showed that more reduction is possible if the noise related to the deflection system is minimized further so the system would be

operated in the sub-piconewton regime. However, the performance of this new instrument is still limited by electronic noise associated with the laser signal, thus, we hope in the future the level of electronic noise will allow further reduction enabling sub-piconewton measurements.

To our best knowledge, CD-AFM is the first successful attempt to cool the softest cantilevers available commercially in an ambient liquid by using just the optical beam deflection system, and the first time force curves of proteins can be acquired using optical force feedback. We succeeded in introducing a calibration method by which the laser power is converted into force and this method gave results close to those obtained by the deflection system. The resolution of the system is currently limited to ~30 pN purely due to electronic noise in the feedback loop at a level of ~ 15 mV. An electronic noise level of 1 mV should be possible to achieve, which would results in a force resolution approaching level of thermal noise remaining on the cantilever, approximately 3 pN.

1.1 Working principle of AFM

The design of an AFM is based on three parts; the sensor, the detection system and the positioning system. These are controlled by a feedback control system whose role is to make the AFM work by keeping the cantilever deflection or amplitude constant during the scan.

1.1.1 Sensor

The sensor (probe), shown in Figure 1.1, comprises a sharp tip mounted on the free end of a soft, flexible and microscale cantilever. The cantilever and the tip are usually made of silicon or silicon nitride and coated with a layer of, for example, gold to enhance its reflectivity to the laser beam. The cantilever with the integrated tip is the heart of an AFM that interacts with the scanned sample.

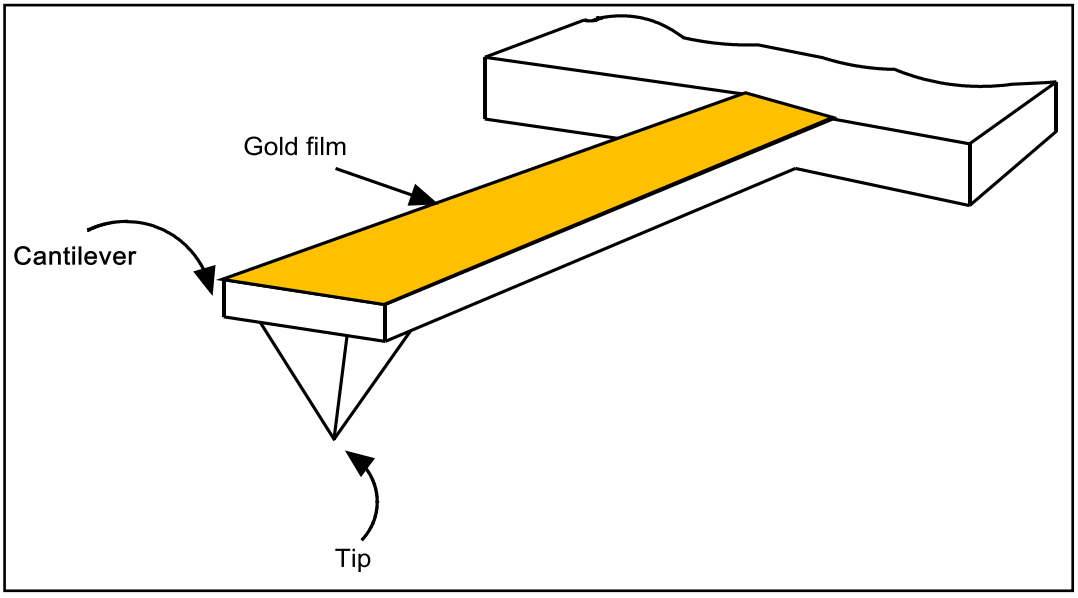

FIG.1.1 Schematic of the AFM probe; a sharp tip is attached at the free end of a soft cantilever

Typically, there are two main types of cantilevers, depending on their shapes: rectangular and V- shaped, as illustrated in Figure 1.2. The V-shaped was developed because it was thought that this geometry can better resist the twisting forces. Therefore, it has become a popular design(*15*) . However, it has recently been shown in a theoretical study by Sader et al.(*16*) that this assumption may not be valid, and that V-shaped cantilevers are actually more prone to twisting. This has yet to be verified experimentally.

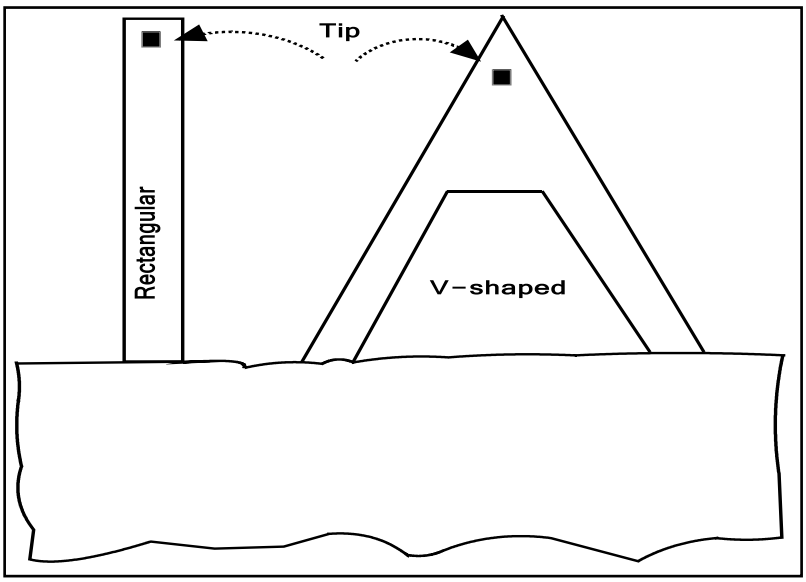

FIG.1.2 Cantilevers shapes used in AFM.

1.1.2 Detection system

In order to detect the sensor's response, a precise detection system is a central part of AFMs. Today, most AFMs use a laser deflection technique (*17, 18*) to measure the movement of the cantilever deflection, where a laser beam reflects off the cantilever onto a position sensitive photodetector (PSPD), Figure 1.3. This is called the Optical Lever Deflection method. The photodetector can be made out of two or four segments of photodiode, so enabling both normal and lateral displacement

of the cantilever to be recorded. Using the optical lever detection system, it is possible to achieve a vertical detection of the order of 1Å (*19*).

In response to the cantilever deflection, the PSPD measures the difference in light intensities between the upper and lower photodetectors, after which it is converted into a voltage signal.

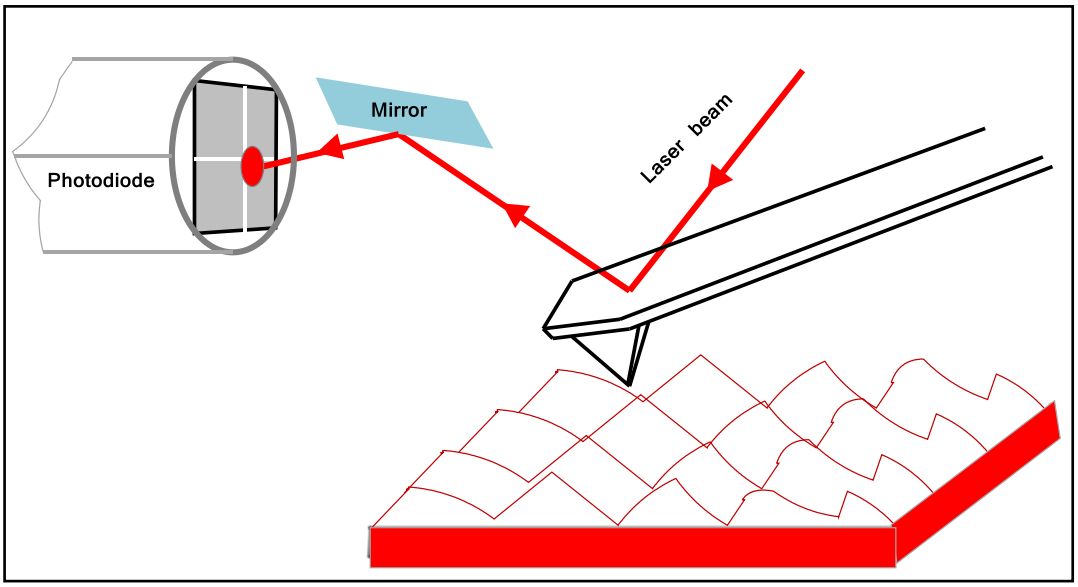

FIG.1.3 Schematic of the optical lever detection system used in an AFM head.

1.1.3 Positioning system

The precise scanning of the sample is essential to construct an accurate image of the sample surface or to measure forces. An AFM system uses a positioning system made of a tube-shaped piezoelectric actuator (referred to as piezoscanner or piezo).

Today, two designs of the piezoscanner are commercially available. A common design is that the sample is positioned on the piezoscanner and scanned beneath a fixed cantilever. Whereas in the second design, the

piezoscanner is attached to the cantilever and the sample is held constant that allows the tip to scan the sample surface.

The piezoscanner which is made of piezoelectric crystal expands or contracts in response to applied voltage and is controlled by a feedback control system which works to keep the cantilever interaction at a fixed level. The piezoscanner design allows three dimensional motion, XYZ, of the order of sub- angstroms up to 180 µm (*20*).

When the tip is scanned across the sample in an XY raster, the PSPD measures the difference in light intensities between the upper and the lower segment resulting from the cantilever interacting with the surface topography. The changes in light intensity are converted into voltage signals. The difference between the acquired signal and a reference signal, (setpoint), chosen by the user, is called the error signal (e(t)). It is this error signal which is held to a minimum by a feedback circuit which is used to drive the z- piezoscanner (Z component of the scanner). It is the voltage on the z- piezoscanner which is used to construct the image.

The feedback system used in AFMs, Figure 1.4, plays a crucial rule in acquiring images and controlling the performance of AFMs by regulating the force applied to the sample. An important feature of a feedback loop is to maintain the system stable at the setpoint. Uncontrolled movement of the piezoscanner can cause damage to either the probe or the sample.

AFMs use a negative feedback system based on a PI controller designed to minimize the error signal. PI is an acronym for proportional and integral gains. The performance of the PI controller and hence the stability of the system can be controlled by varying two mathematical values related to the PI elements, that is, proportional gain (P) and integral gain (I). The output

of the PI controller (C_d), used to drive the scanner, is given by ($C_d = Pe(t) + I\int e(t)dt$)(*21, 22*).

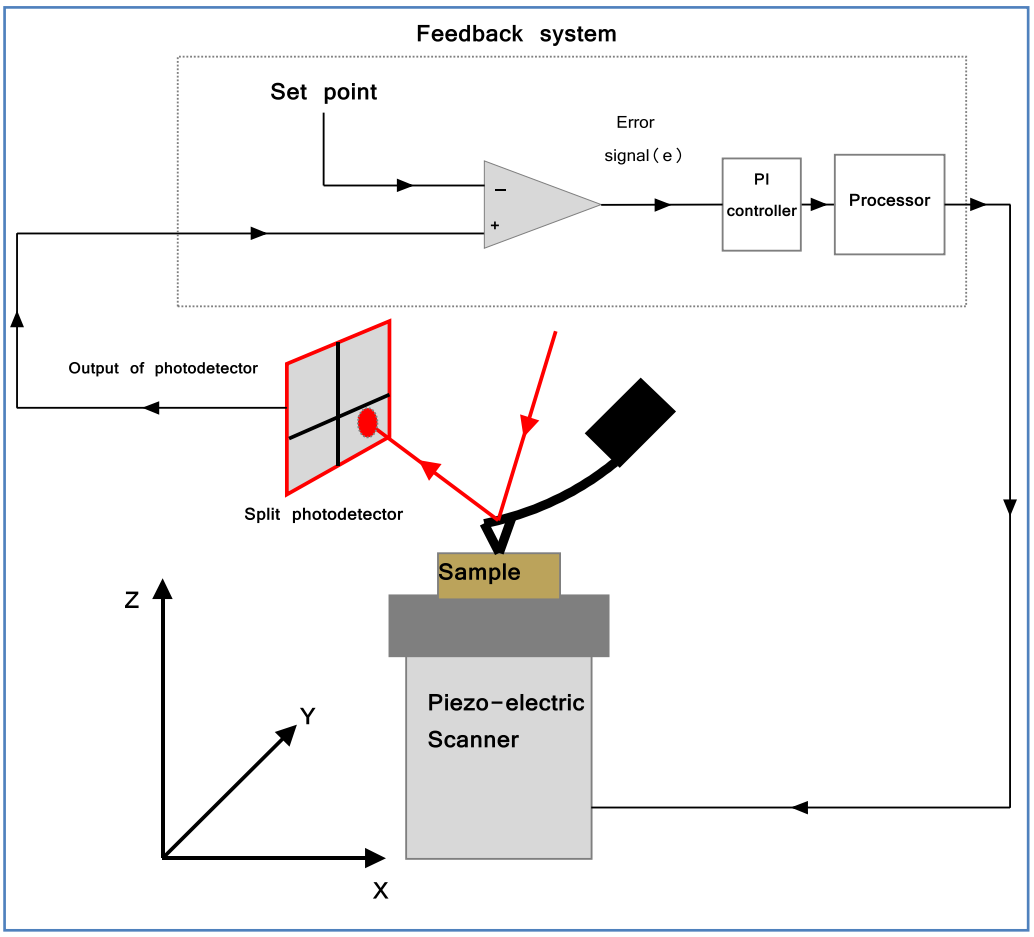

FIG.1.4 Schematic representation of the atomic force microscope

As mentioned above, movement of the sample is induced by applying a voltage to the piezoscanner. This effect is called "inverse piezoelectric effect" where the piezoscanner material expands and contract in response to applied voltage. Ideally, the displacement of the piezoscanner in response to the applying voltage is linear (*20*). The piezoscanner shows the same response to a given applied voltage. However, positional precision of the piezoscanner can be deteriorated by hysteresis and creep effects. Hysteresis and creep may cause a deviation from linearity(*20*).

The hysteresis of a piezoscanner is defined as a divergence between the expansion and contraction displacement of the piezoscanner as illustrated in Figure 1.5. Plotting the piezoscanner displacement as function of the applied voltage shows that the contraction path (decreasing voltage) of the piezoscanner does not follow its expansion path (increasing voltage). The scanner shows different displacement to the same applied voltage when reversing the direction of the applied voltage.

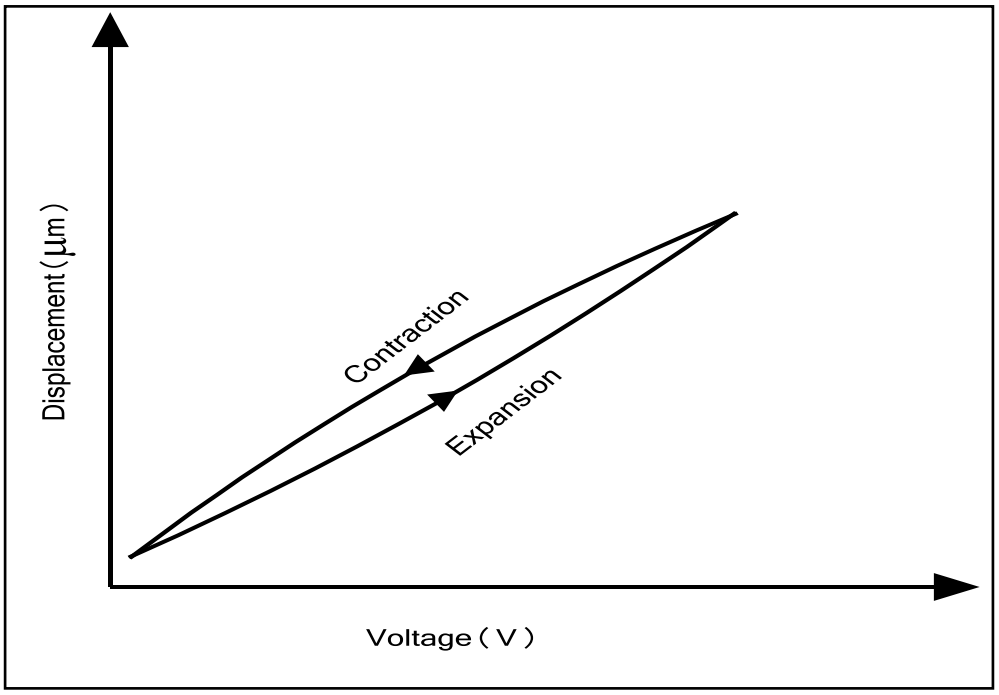

FIG.1.5 Hysteresis of the piezoscanner between its contraction and expansion displacement

When a sudden change in the voltage is applied to the piezoscanner two responses occur. An instantaneous response which is followed by a slower and longer one, Figure 1.6. The slow response is known as creep and manifests as a shift in the piezoscanner position (*23*) that can cause a distortion to an AFM image or causes inconvenience when trying to zoom in on a smaller feature of a sample due to the targeted area being missed(*23*). In force-distance curves obtained by AFM, hysteresis and creep effects manifest as a difference in path between the approach and

retract curve that would impact the measurements of force and mechanical properties(*20, 23*).

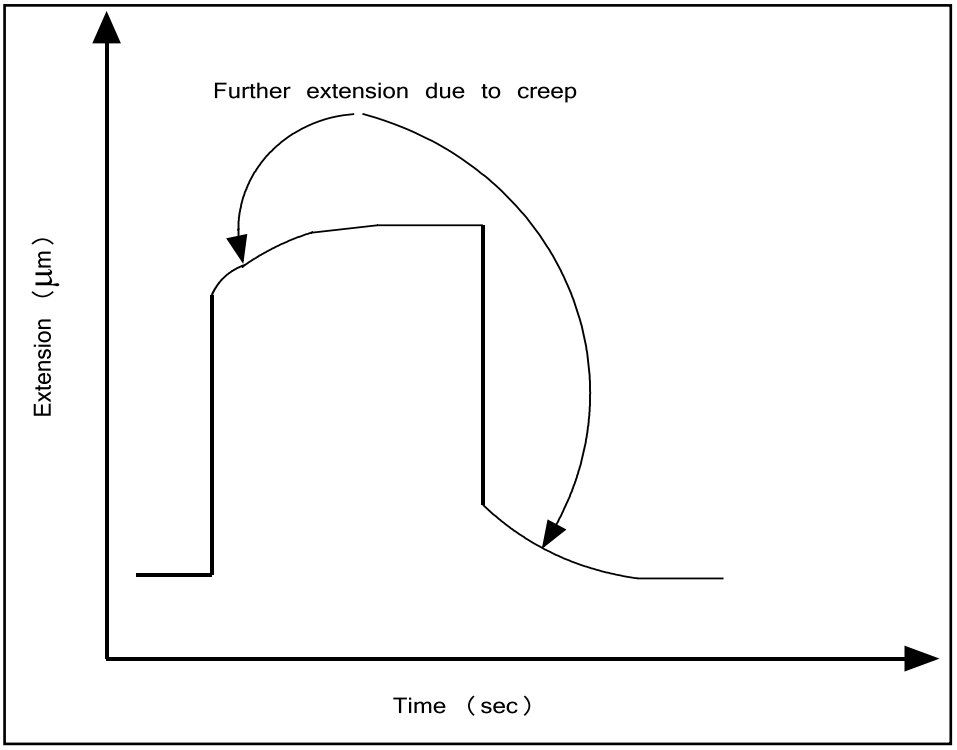

FIG.1.6 Schematic diagram shows non-linearity response in the piezo movement due to creep.

The effect of hysteresis and creep can be eliminated or minimized by applying some compensation techniques. The most common techniques used are a capacitor inserted in series with the piezoscanner(*23*), a charge control (*24*) and a feedback-based control(*25*).

1.2 AFM imaging operation modes

In order to image surfaces, there are two main types of operation mode in AFM; contact mode and dynamic mode.

1.2.1 Contact mode

In contact mode, Figure 1.7, the tip is brought into hard contact with the sample and is then dragged over it. The image can be created in two ways; constant force and constant height. In the constant force mode, the deflection of the cantilever is kept at a constant value (setpoint) by moving the scanner in the Z direction. Thus, the image is created by plotting the scanner movement in the Z direction as a function of its motion in X-Y. In the constant height mode, the image is constructed directly from the deflection signal as the feedback loop is switched off. We cannot use constant height mode to image a rough surface because this may lead to a damage to the tip, due to high forces generated on high features, or to image biological samples because the biological samples are soft and the force applied is uncontrolled and therefore, the lateral motion of the tip, resulting in the creation of shear forces, may deform the sample and distort the images (*26*).

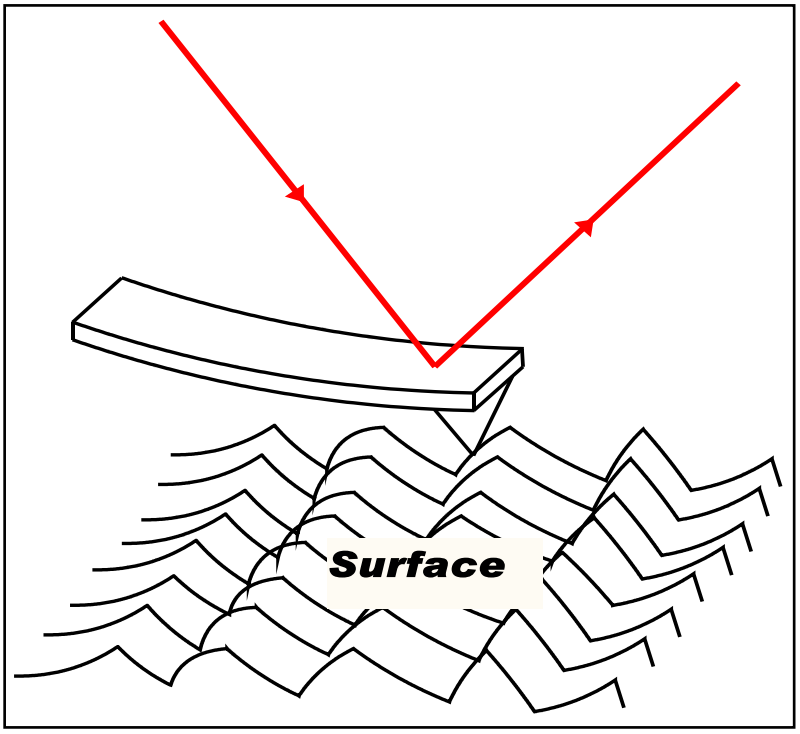

FIG.1.7 Schematic of contact mode operation. .

1.2.2 Dynamic mode

The other operation mode is called dynamic mode, Figure 1.8. It is based on the principle that the cantilever is oscillated at, or near, its resonant frequency and brought close enough that the tip is in intermittent contact with the surface. The amplitude or frequency of oscillation is changed due to the interactions between the tip and forces presented on the surface. For example, when the amplitude of tip oscillation reaches a certain value (the “setpoint” amplitude), the scanner starts moving the sample beneath the tip in the X-Y direction. When scanning over a lump or depression, the amplitude will momentarily decrease or increase due to the change in interaction between the tip and the surface as the distance changes; therefore, the feedback loop moves the sample upwards or downwards to maintain the setpoint amplitude. An image can also be recorded of the changes in amplitude. The dynamic mode can be operated in two main operation modes; tapping mode (repulsive regime tapping), or non-contact mode (also known as attractive regime tapping mode) (*27*).

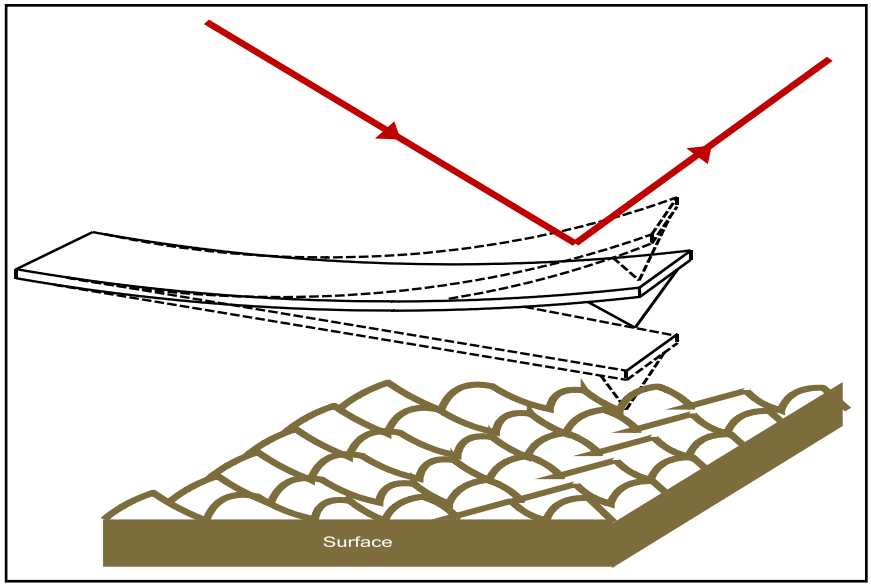

FIG1.8 Schematic of tapping mode AFM operation.

1.3 Force spectroscopy

AFM was initially developed as a useful tool for imaging samples surfaces. Later a non-imaging mode has been introduced(*28-30*). This mode is commonly known as a force spectroscopy mode in which the AFM cantilever is used as a force sensor. In the force mode tip-sample interaction forces are plotted as a function of the tip-sample distance. Such a curve is known as a force-distance curve.

The force-distance curve is obtained by moving the sample, mounted on a piezoelectric scanner, up and down along the z-direction (the vertical direction) while monitoring the AFM cantilever deflection (Δz). When the sample is moved towards the tip the curve is called an approach curve whereas the retract curve is obtained by moving the sample away from the tip (or cantilever).

As the sample is moved along the z-direction, surface forces cause the cantilever to bend towards or away from the surface. Such deflection is transferred into force by multiplying the cantilever deflection by its stiffness, Hooke's law ($F = \kappa \ \Delta Z$) where κ is the cantilever stiffness.

Figure 1.9 shows a typical force-distance curve acquired by AFM. The curve can be divided into three regions depending on the type of interaction forces with the cantilever tip; zero force line, non-contact regions and the contact line. Furthermore, the figure shows two distinct area; attractive force (negative or below the x-axis) and repulsive force (positive or above the x-axis)(17).

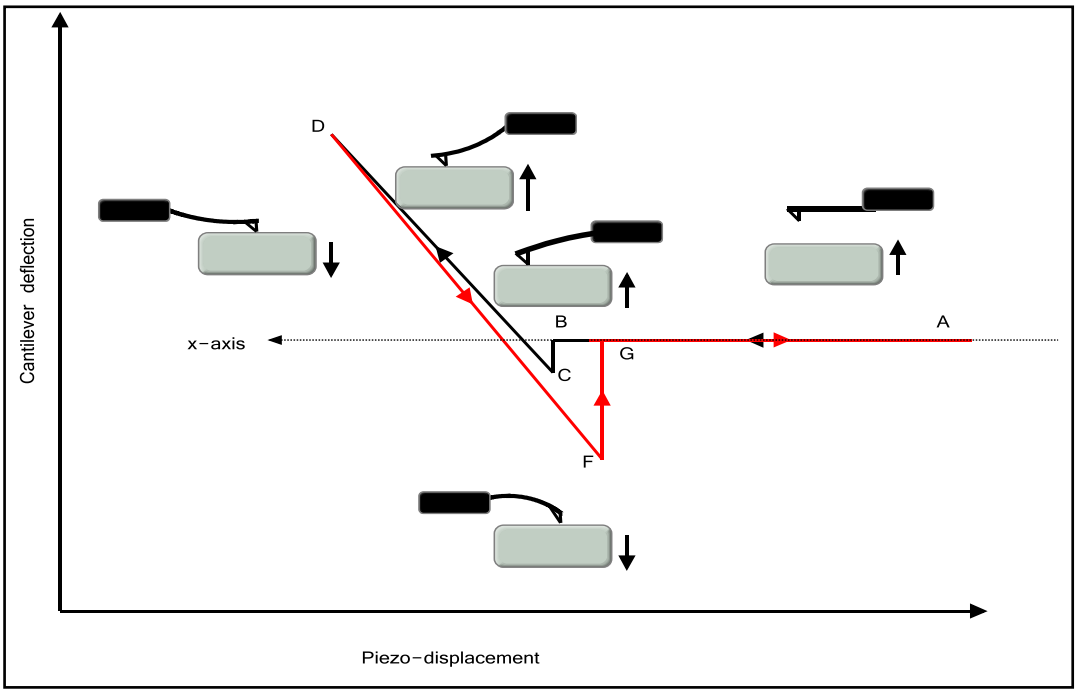

FIG.1.9 Schematic diagram showing a typical force- distance curve using AFM cantilever, explained in the text.

1.3.1 Zero force line

The first region is $|AB|$ or $|GA|$, where the effect of surface forces on the deflection of the cantilever is zero because the separation distance between the tip (or the cantilever) and the sample is large, therefore, there is no force on the cantilever. The cantilever usually does not bend and its deflection remains constant.

However, in the zero force portion of the curve the cantilever is not perfectly stable. In this part of the curve, the cantilever is susceptible to continuous bombardment from its surrounding molecules that cause a mechanical oscillation in its rest position (called Brownian motion). For example, a cantilever with stiffness of 0.01 N/m shows a peak to peak oscillation of 2-3 nm at its resonance frequency (more details are given in chapter 3).

On the other hand, the output of a PSPD may show an oscillation in the zero line force. This oscillation is artificial and caused by optical interference. When the laser spot exceeds the width of the cantilever a portion of the laser beam may be reflected by the sample surface and interfere at the PSPD with the beam scattered by the backside of the cantilever. The interference results in a constant spatial oscillation in the zero line with a spatial period given by(*31*)

$$\Psi_z = \frac{\Psi \cos\varphi}{n(1+\cos 2\varphi)} \qquad [1.1]$$

Where ψ is the wavelength of the laser beam, n is the reflective index of the medium and φ is the incidence angle of the laser beam.

1.3.2 Non-contact region

The second region is the non-contact region in which the tip is not in real contact with surface and the deflection of the cantilever is prone to surface forces. This region can be divided in two parts; non-contact-on-approach and non-contact-on-retract.

As the piezoscanner moves the sample towards the cantilever surface forces become more apparent causing the cantilever to bend. When the gradient of the attractive forces, $\mathrm{dF/dD}$, becomes dominant and exceeds the stiffness of the cantilever, $\frac{dF}{dD} \geq \kappa$, a sudden jump to the surface occurs. The non-contact-on-approach part can be defined as the area that precedes the jump-to contact $|BC|$.

The non-contact-on-retract, called the adhesion region, starts when the retract curve passes the contact point, and the dominant force becomes

attractive and the tip is drawn to the surface. This part ends when the tip jumps off the surface $|FG|$ and the forces affecting the cantilever become zero again (*32, 33*).

Prior to the jump-to-contact or the jump-off the surface point, the cantilever is influenced by the tip-sample interactions. The interactions affecting the cantilever may be attractive or repulsive forces. A brief overview of the common forces acting between the cantilever tip and the surface follows.

1.3.2.1 Van der Waals forces

The Van der Waal forces are intermolecular forces acting between molecules. Despite the weakness of Van der Waals forces, they are responsible for many physical and chemical phenomena. For instance, both polar and non-polar cooled gas molecules would not condense if attractive forces between them did not exist(*34*). Van der Waals forces are the sum of contributions from three distinct forces, London, Keesom and Debye forces(*34*). All forces are proportional to the inverse-sixth power of the distance between molecules($1/r6$) (*35*). These forces can be divided in two categories(*36*)

1. **Forces between polar molecules**

In some molecules the distribution of electrons cloud is not even. There is some shift of charge, so that one end of the molecule is more electronegative than the other, that is, one end is slight negative and the other is slight positive, Figure 1.10. Such molecules have an electric dipole and therefore called polar. Otherwise they are called non-polar.

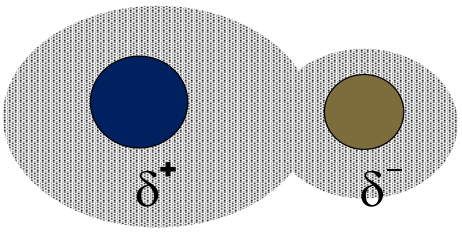

FIG.1.10 Polar molecule. One end is more electronegative than the other

When a permanent dipole molecule such as a water molecule interacts with an induced dipole molecule such as a carbon molecule, the interaction is called the Debye force or a dipole-induced dipole interaction. If the interaction happens between two permanent dipoles such as two water molecules, the interaction is known as Keesom forces or a dipole-dipole interaction, and sometimes is referred to as the hydrogen bond. Both Debye and Keesom forces contribute to the total Van der Waals forces.

2. Forces between non-polar molecules

The distribution of the electron cloud around non-polar molecules is symmetric. However, there will be an instant when that distribution is distorted to be asymmetric, a random fluctuation in electron density. This distortion lasts for a short time but enough to create a temporary dipole which in return induces a temporary dipole in its neighboring molecule. The attractive force between transient, fluctuating dipoles, is called the London force or dispersion force(*34*). The presence of this force accounts for attractions between neutral molecules or atoms.

Although Van der Waals forces are modeled as short-range force, effective distances can be greater than 10 nm (*34, 37*), acting between atoms or molecules, in AFM experiments one should consider macroscopic bodies(*35*). Hamaker(*38*) realized the existence of the Van der Waals

forces between two macro-scale objects. Adhesive forces can exist, for example, between two spherical bodies or a sphere and a flat surface. In 1937 Hamaker derived the Van der Waals interactions between two spheres.

$$F_{van} = -\frac{A_H}{6D^2}\frac{R_1 R_2}{R_1 + R_2} \qquad [1.2]$$

Where A_H is the Hamaker constant, D is the separation between two bodies, R_1 and R_2 are radii of the two spheres.

Besides the interactions between two spheres, the Hamaker formula can be extended to include different geometries such as a sphere on a flat surface ($F_{van} = -\frac{A_H R}{6D^2}$ where R is the radius of the sphere) and a cone on flat surface ($F_{van} = -\frac{A_H \tan^2 \phi}{6D}$ where Φ is the opening angle of the cone)(*31*).

1.3.2.2 Electrostatic double layer force

In the previous section, it has been shown that the Van der Waals forces are usually attractive, so that all particles should stick to each other. As a result, dissolved particles should coagulate, forming a mass. Fortunately, that does not happen, for example, milk does not coagulate in normal conditions(*39*). The existence of a repulsive force, called the electrostatic double layer force, prevents such a process.

An electrostatic double layer arises when a charged surface is placed into an electrolyte solution, containing ions. Even pure water at pH 7 can be considered as an electrolyte solution(*34*). Surfaces become charged when placed into water(*40*). The surface charge is balanced by an equal but

oppositely charged layer of counter-ions close to the surface. Counter-ions cluster at liquid-surface interface forming a charged layer. Thus, the charged layer may be called an ionic atmosphere(*41*). The charged layer can be divided into two layers; tightly bound layer, known as Stern layer, and a diffusive layer extending above. The diffusive double layer has a high concentration of co-ions (the same sign of the surface charge). When two surfaces covered by electric double layers approach each other an exponential repulsive force, with a decay length called the Debye length, arises due to the overlap of two diffusive layers (*34, 40, 42*).

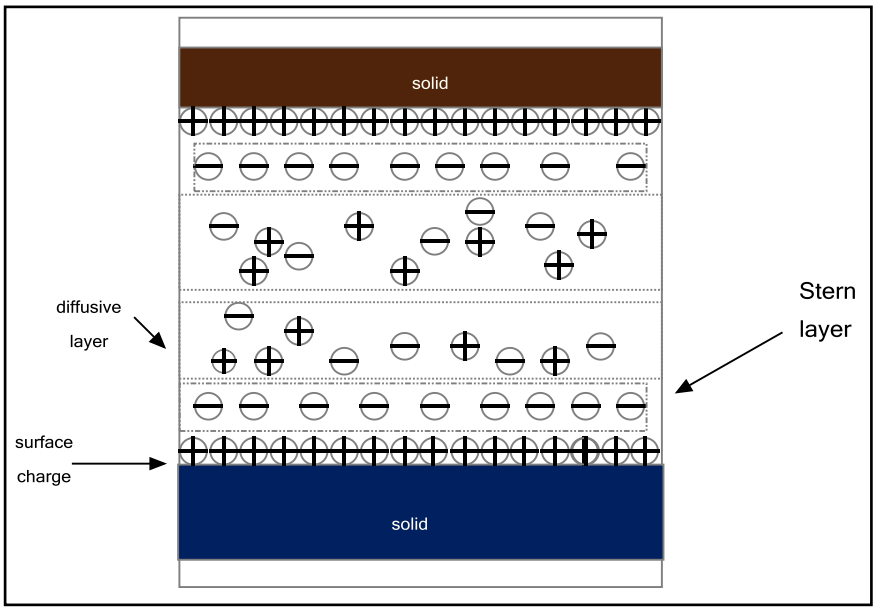

FIG.1.11 Electrostatic double layer confined between two charged surfaces.

DLVO (Derjaguin, Landau, Verwey and Overbeek) theory suggests the stability of a colloid system is a result of two competing interactions; the Van der Waals and double layer forces (*43, 44*). In AFM measurements, the DLVO theory is used to fit the force-distance curves resulting from the interactions between colloidal systems(*45-48*). In most studies, the force between the colloidal systems is normalized by the radius of colloidal sphere attached to the cantilever tip. According to Derjaguin's

approximation (*49*) the energy per unit area (W_A) between two planar surfaces can be related to the force (F) between colloidal bodies

$$\frac{F}{R} = 2\pi W_A \qquad [1.3]$$

According to the DLVO theory and the Derjaguin approximation, the normalized force can be given by(*45, 50*)

$$\frac{F}{R} = 2\pi(W_{AV} + W_{Ad}) \qquad [1.4]$$

Where W_{Av} is the Van der Waals interaction energy per unit area [$W_{Av} = \frac{A_H}{6D^2}$] and W_{Ad} is the double layer interaction energy per unit area [for $D \gg L_D$ and $R \gg D$, $W_{Ad} = \frac{2\varepsilon\varepsilon_0 \Im_T \Im_S}{L_D} e^{\frac{-D}{L_D}}$ (*35, 50*) where ε is the medium dielectric constant, ε_0 is the vacuum permittivity, $\Im_T$ is the tip potential, $\Im_S$ is the surface potential and L_D is the Debye length.

1.3.2.3 Non-DLVO forces

The DLVO model fails to describe the behavior of the AFM tip at a distance less than ~5 nm from the surface(*51*). The divergence of the DLVO theory from experimental results at a small separation from the surface may be attributed to the presence of additional forces(*52-54*), called non-DLVO forces. The prominent examples of non-DLVO forces are hydrophobic, solvation and hydration forces(*34*). However, the origin of these forces are not fully understood(*55*).

1. Hydrophobic force

The hydrophobic effect denotes the tendency of non-polar molecules (hydrophobes), such as oil, to cluster when placed in water (*31*). Hydrophobic interactions are of importance in most biological processes(*34, 35, 56*). For instance, protein folding is dominantly governed by hydrophobic interactions.

Although the origin of hydrophobic interactions is not entirely understood, it has been suggested that hydrophobic interactions are an entropy driven process. When apolar molecules are placed in water, the hydrogen bonded network is disrupted as apolar molecules cannot form hydrogen bonds with water molecules. As a result, a void is created due to exclusion of water molecules from the volume occupied by the apolar molecule. Water molecules order around the apolar molecule building a water cage. The price of such an ordered structure is a remarkable reduction in the water molecules' entropy. Consequently, the overall solvation free energy increases. In order to reduce the free energy, the apolar molecules stick together, minimizing the area exposed to water (*57*).

2. Solvation force

The origin of the solvation force is thought to be solvent molecules adsorbed and confined between two surfaces. When the two surfaces approach each other the molecules reorder themselves into quasi-discrete layers(*34*). Further approach causes the layers to be squeezed out layer after layer(*35*). Reordering the molecules to allow accommodation in the gap and density fluctuations of the molecules according to the separation between the two surfaces result in the solvation force(*35*). AFM measurements show that the solvation force has an oscillatory profile(*58, 59*). The periodicity of the oscillation approximates the depth of each molecular layer.

3. Hydration force

When two hydrophilic surfaces, such as mica or silica, are placed in water and approach each other a repulsive force with an effective range of 1-3 nm is observed (*56, 60*). This is twice the range of the solvation force(*34*). This force is called the hydration force. Due to its short-range, the hydration force can be discriminated from the double layer force. At a salt concentration higher than 0.1M the double layer force diminishes and the effect of the hydration force can be identified easily(*56*).

The hydration force is a repulsive interaction and decays monotonically with the separation between two surfaces. However, at separations less than 1.5 nm the force profile exhibits oscillation with a periodicity equals to the diameter of a water molecule(*61*).

The roots of such forces are not quite clear. However, the hydration force may be a special case of the solvation force when the solution used is water.

1.3.3 Contact region

The third region is the contact part of the force distance curve that starts when the cantilever jumps to the sample surface $|BC|$. As the tip is in physical contact with surface a further movement of the piezoscanner pushes the sample surface up and the cantilever back until the maximum load is achieved $|CD|$, known as loading curve. When the tip is retracted, the loading decrease along $|DC|$ leads to a decline in the repulsive force. As a result, the cantilever deflection reverses its direction. This part of the contact region is called the unloading curve.

1.3.3.1 Theoretical models for contact region

Valuable information about mechanical properties of the sample, such as elasticity and plasticity of the surface, can be drawn from the contact region (contact line) of force-distance curves (*62*). However, knowledge of the real contact region requires the use of a suitable model to describe it. For example, Young's modulus (E) used to describe the elastic deformation of the sample surface cannot be extracted without using an adequate model. The deformation of the objects shape can be considered elastic if the object recovers its original unloaded shape.

When the piezoscanner pushes the sample against the cantilever tip while they are in contact, their shape will be distorted (always assuming the tip is infinitely hard). The sample surface deformation is referred to as an indentation (δi), Figure 1.12.

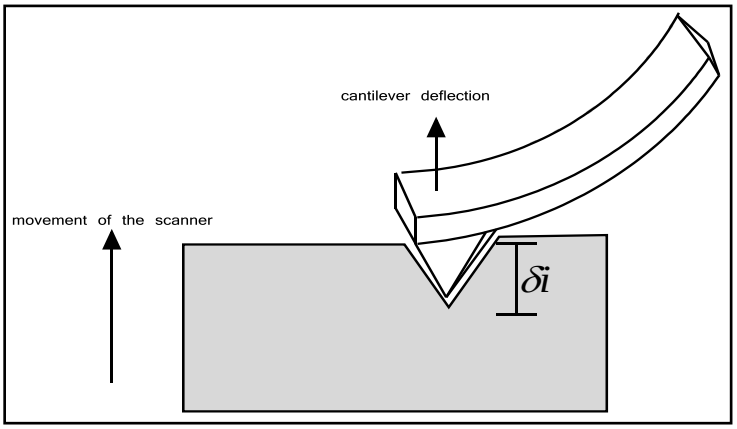

FIG.1.12 Indentation of the AFM tip on a surface

The indentation increases with increasing loading force. Figure 1.13 shows an indentation approach trace. The loading force is plotted versus the surface-tip distance (separation) calculated by subtracting the cantilever

deflection from the piezoscanner displacement (discussed further in chapter 2). The loading force is calculated by multiplying the cantilever deflection (Δz) by its spring constant (k).

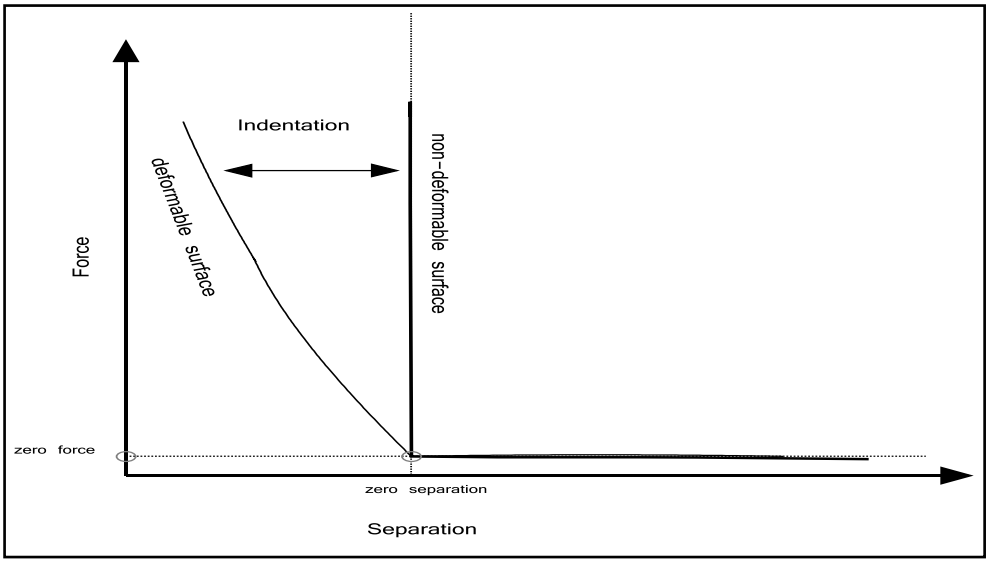

FIG.1.13 Schematic diagram showing the comparison between force-distance curve taken on an infinity hard surface and on a soft surface. At contact point, there is no indentation in the case of a very hard surface.

In the case of a non-deformable surface (infinitely hard) the sample surface undergoes no indentation leading to a zero separation. In the case of a deformable (softer) surface, an increase in load results in further indentation. Usually the indentation depends on the geometry of the cantilever tip and the elastic modulus of the surface. Theoretical models employed to calculate the elastic modulus of a surface relate the loading force to the indentation of the surface.

Hertz's model(*63*) is a common and simple model used to describe the indenting process. This model predicts the indentation of a sample surface (δi) under loading force (F), Eq.1.5. By fitting the Hertz model to the contact region of the force-distance curve, Young's modulus of the sample surface can be extracted(*64*).

$$F = \frac{4}{3}\frac{E}{(1-\nu_s{}^2)}(\delta i)^{\frac{3}{2}}\sqrt{R} \qquad [1.5]$$

Where ν_s is the Poisson ratio, ranging between 0 and 0.5 depends on the surface(*65*) and R is the sphere radius.

However, some assumptions must be considered when applying the Hertz model:

1- Plastic deformation of the surfaces is neglected (the surface is ideally elastic) hence the loading and unloading parts of the contact curve overlap each other, Figure 1.14.

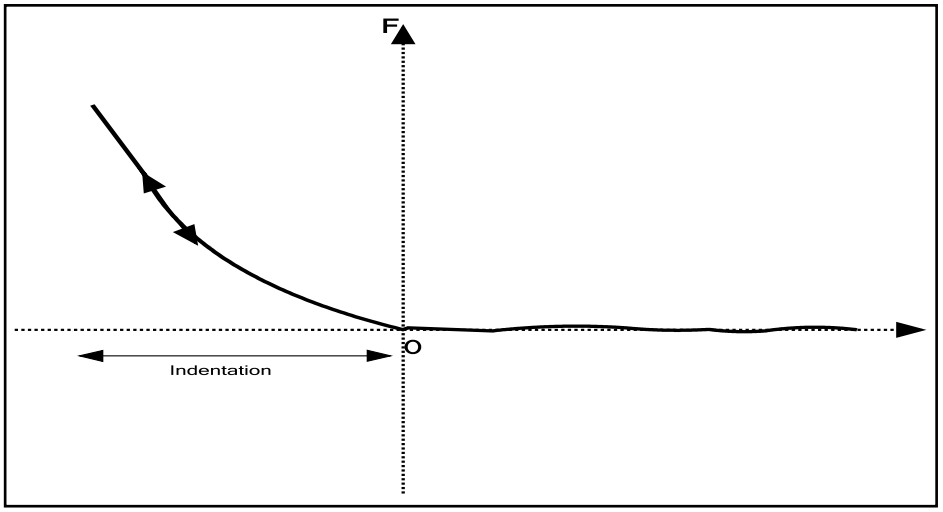

FIG.1.14 Force-distance curve obtained by the AFM tip on a fully elastic surface. The approach and retract curves show no hysteresis.

2- The tip is modeled as a rigid sphere and the sample surface as a flat surface, Figure 1.15.
3- The tip is stiffer than the surface; the elastic modulus of the surface <<the elastic modulus of the tip materials.

When the cantilever tip is modeled as a cone, the Sneddon model is employed(*66*). In Sneddon's model the relationship between the loading force and the indentation is given by

$$F = 2\frac{E}{(1-\nu_s)}\tan(\phi)\delta i^2 \qquad [1.6]$$

Where Φ is the opening angle of the cone, Figure 1.15.

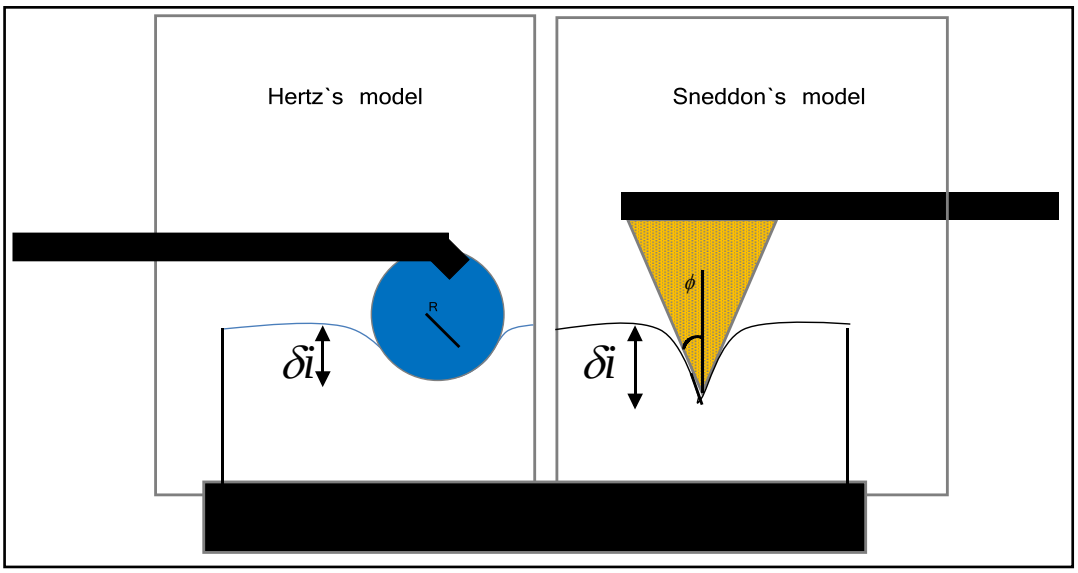

FIG.1.15 Schematic representation of the Hertz and Sneddon models.

When the adhesion of the tip with a sample surface is very low, either the Hertz or Sneddon models is employed, depending on the tip shape used. However, in the presence of surface forces neither the Hertz nor Sneddon models fit the contact line accurately. This shows the need for a model that takes into account the effect of surface forces. The DMT (Derjaguin-Mullller-Toporov)(*67*), Maugis(*68*) and JKR (Johnson-Kendall –Roberts)(*69*) models are common applied. For instance, in the JKR model the adhesion force is considered where the cantilever tip and the surface are modeled

as a rigid sphere on a flat surface. Thus, the elastic modulus can be given by

$$E = \frac{3}{4}(1-\nu_s{}^2)F_{ad}\,\frac{a^{\frac{3}{2}}}{\delta i^{\frac{3}{2}}\sqrt{3R}} \qquad [1.7]$$

Where a is the contact area and F_{ad} is the adhesion force.

Although the limitations of the Hertz and Sneddon models, researchers continue to use them to measure the elastic modulus (Young`s modulus) for either a soft or hard surface. Those models were employed fruitfully to model the contact region of force-distance curves on polymeric films, due to their low adhesion with the cantilever tip(*35*). Radmacher et al(*70*) have measured the Young modulus for a thin gelatin film in water and propanol. Moreover, Matzelle et al(*71*) employed the models to calculate Young's modulus of Poly (*N*-isopropylacrylamide) and poly (acrylamide) hydrogels at different temperatures. In addition, the Hertz model was used to fit the elastic area on a harder surface such as Au(*72*).

1.4 Calibration of AFM Cantilever spring constant

Accurate determination of the spring constant is important to properly measure the forces involved, as the AFM system only measures the cantilever deflection. AFM cantilevers act as a Hookean spring, so from knowledge of the deflection and the spring constant, a force may be calculated. We must also be aware of the uncertainty in the calibration, and hence in the final force measurement.

Manufacturers usually provide nominal values of the spring constant of the cantilever, κ , which can vary substantially from its real value(*15*) .Due to

its crucial importance, many methods have been developed to calibrate the spring constant of the atomic force microscope cantilever. These approaches can be divided into three categories; dimensional, static and dynamic.

1.4.1 Dimensional model

In dimensional methods, the determination of the normal spring constant (κ) depends upon the size, shape and material properties of the cantilever, and hence the equation is

$$\kappa = \frac{Ejh^3}{4\ell^3} \qquad [1.8]$$

Where E is Young's modulus, j is width, h is the thickness and ℓ is length of a rectangular cantilever (Figure 1.16).

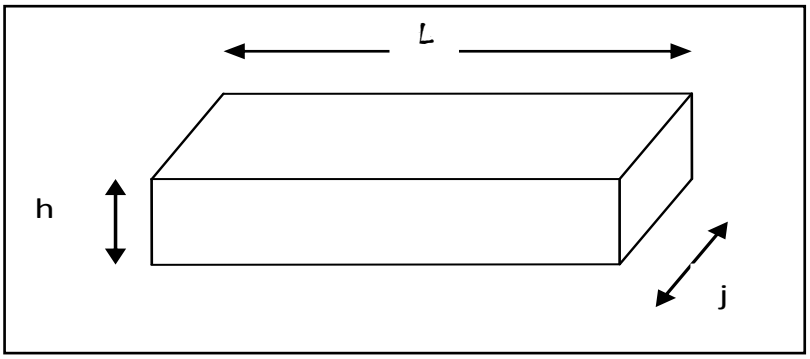

FIG.1.16 Dimensions of a rectangular cantilever

Eq.1.8 is not suitable for V-shape cantilevers. Therefore, it has been replaced(*73*)

$$k = \frac{Eh^3 j_w}{2\ell^3}\cos\Theta\left\{1+\frac{4 j_w{}^3}{j^3}(3\cos\Theta-2)\right\}^{-1} \qquad [1.9]$$

Where j_w is the width of the leg parallel to the base line, j is the width at the base, ℓ is the length from apex to the base of the cantilever perpendicularly and Θ is half the angle between the two legs, Figure 1.17.

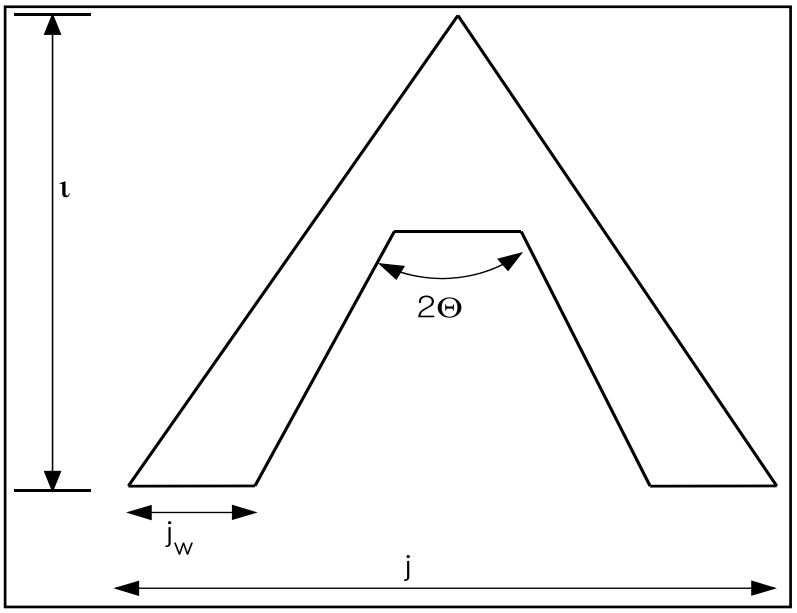

FIG.1.17 Dimensions of a V-shaped cantilever.

Therefore, the dimensions and material properties of the cantilever are essential for calculation of its normal stiffness. Although this appears to be straightforward, there are some challenges that place limitations on its use. For instance, the thickness of a cantilever, <1 μm, is hard to measure directly(*74*) . Furthermore, a given value by manufacturers is not necessarily accurate(*35*). Therefore, uncertainty in measuring the thickness (h) would lead to a significant error in κ, since $\kappa \propto h^3$. To overcome this difficulty, several approaches have been described. One of them is the use of scanning electron microscopy (SEM) to measure the thickness(*75*).

1.4.2 Static models

The principle of this model is straightforward and is based on applying a normal known force to the free end of the cantilever and then measuring its normal defection (Δz), then via Hooke's law($F = -\kappa\Delta z$) the spring constant can be calculated. However, the application is complicated. In general, the difficulty arises from measuring the force. Many techniques have been proposed to cope with this difficulty; which include, for example, use of a hydrodynamic force(*76*) , acoustic pressure(*77*) , a reference cantilever or even gravitational force(*74*) .

The deflection can be achieved via the gravitational force by attaching a tiny added mass, such as tungsten spheres (10-60 μm in diameter) onto a cantilever. Accuracy of this technique is approximately 15%(*78*). Moreover, a well calibrated cantilever (as a reference cantilever) is used to determine the spring constant for other cantilevers by pressing them against a calibrated reference cantilever, Figure 1.18.

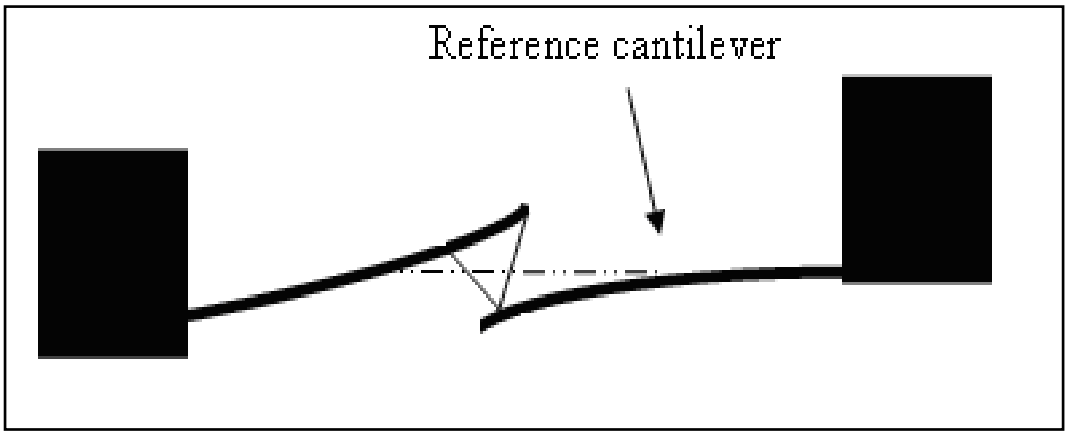

FIG.1.18 Calibration of an unknown cantilever by pressing it against a reference cantilever.

The deflection sensitivity of the unknown cantilever (s) is measured on hard surface (s_{hard}) and on a reference cantilever (s_{refer}). If the spring

constant of the reference cantilever (κ_{refer}) is known, the following equation can be applied to obtain the spring constant for the unknown cantilever (κ)

$$\kappa = \kappa_{refer}\left\{\frac{s_{refer}}{s_{hard}} - 1\right\} \qquad [1.10]$$

However, the use of this method is not easy. There are some complications, for example, the unknown cantilever must contact the reference cantilever at its free end as closely as possible because the reference cantilever will read as stiffer near its base (*79*), $\kappa_{refer} \alpha \frac{1}{l^3}$. This method requires a high degree of accuracy, with an uncertainty of this approach ranging from 10% to 30% (*80*).

1.4.3 Dynamic models

In this model, the deflection is time-dependent. Three widely used calibration techniques will be discussed here. The first is based on using added masses, which change the resonance frequency of the cantilever. The second, published by Sader, is based on a combination of the resonance frequency of the cantilever in air with its mechanical properties. The third approach is known as the thermal method.

The added masses method, also known as Cleveland's method (*81*), is based on reducing the resonance frequency of the cantilever by adding to it a known mass. If the added mass is m and the effective mass is m_{eff}, the resonance frequency before adding the mass is υ_0 and the resonance frequency after attaching the mass is υ , then

$$m = \left(\frac{1}{2\pi\upsilon}\right)^2 \kappa_z - m_{eff} \qquad [1.11]$$

$$m_{eff} = 0.2427 m_c + m_t \qquad [1.12]$$

Where m_c is the cantilever mass and m_t is the tip mass.

By plotting m versus $\left(\frac{1}{2\pi\upsilon}\right)^2$ the κ can be measured.

However, κ can be calculated by using one mass as the following

$$\kappa = \frac{m(2\pi\upsilon\upsilon_0)^2}{(\upsilon_0{}^2 - \upsilon^2)} \qquad [1.13]$$

One serious problem which limits the accuracy of this method is the position of the added mass on the cantilever. When the mass is placed closer to the base of the cantilever, it will have less effect on the resonance frequency of the cantilever. Moreover, this technique is experimentally difficult and the accuracy is approximately 15-25% (*15, 78*).

The second method is that created by Sader (*82*), who has performed much work in this field. It involves measuring κ by the measurements of the resonance frequency, quality factor Q of the cantilever in fluid and air, and a knowledge of plan view dimensions of the cantilever. The formula is only applicable in the case of a rectangular cantilever and given by

$$\kappa = 01906\ell j^2 \rho_f Q_f \Gamma_i (2\pi\upsilon_0)^2 \qquad [1.14]$$

Where ℓ is the length, j is the width of the cantilever, ρ_f is the density of the fluid, Q_f is the quality factor of the cantilever oscillation in air, υ_0 is the resonance frequency in air and Γ_i is the imaginary component of the hydrodynamic function. The accuracy of this technique is 10%-15% (*78, 83*).

The last technique to calibrate a cantilever is the thermal method. It takes advantage of the equipartition theorem, where the cantilever is considered as a harmonic oscillator. This method is attractive due to its simplicity. It requires only knowledge of the absolute temperature (T) and the area under the main peak of the power spectrum density curve of the cantilever thermal fluctuation (A_p) (*75, 80*)

$$\kappa = \frac{k_B T}{A_p} \qquad [1.15]$$

This technique is limited because it is reliable only for soft cantilevers ($\kappa < 0.5 \, {}^{N}\!/_{m}$) due to sensitivity limits of optical lever deflection system measuring the very small fluctuations of stiffer cantilevers, the accuracy of this method is 10%-25% (*78*).

Finally, Table 1 summarizes some aspects of these methods. However, there is no one accurate method that can be utilized to calibrate the spring constant of the cantilever, thus, the use of more than one method seems to be the best way to achieve accurate measurements of the stiffness, as each technique has own advantages and disadvantages.

Table 1.1 A comparison between calibrations methods discussed in this section.

	Dimensional	(Static)		(Dynamic)		
		Mass attachment	Reference cantilever	Mass attachment	Sader's method (resonant frequency in air)	Thermal method
Uncertainty	10-25%	15%	10-30%	15-25%	10-15%	10-25%
Potential damage to tip	low	high	medium	high	low	low
User friendliness	high	poor	medium	poor	medium	high

1.5 Biological applications of AFM

Contributions of AFM in biological fields have encompassed a broad range of subjects. Due to its ability to be operated under physiological conditions without specific preparations of the samples, and its ability to obtain three-dimensional images of the sample surface with high resolution in different environments (*84*), it is widely employed to measure the topography of various biological samples, such as DNA(*85*), proteins(*86*) and viruses(*87*). In addition to imaging, AFMs can be used as a sensitive force sensor and to measure mechanical properties of biological samples, such as elasticity (*26, 27, 88*).

This section focuses on selected biological applications in which the AFM is used as a force sensor.

1.5.1 Estimation of bond strength

AFM can be used to estimate the strength of molecular bond formed between biomolecules(*89*). The principle of such an experiment is to attach one molecule to the apex of the AFM tip and tether another one to the substrate, Figure 1.19. Mica, silicon and gold are common substrates (*90*). For example, biomolecules can be linked to a gold surface through forming a covalent bond with sulphur atoms(*91*). In order to measure the bond strength, the tip is approached to the surface, until the molecule type one bind to the molecule type two. When the tip is retracted, the cantilever bends due to the strength of the bond. The maximum strength of the bond is measured at the rupturing point of the molecules.

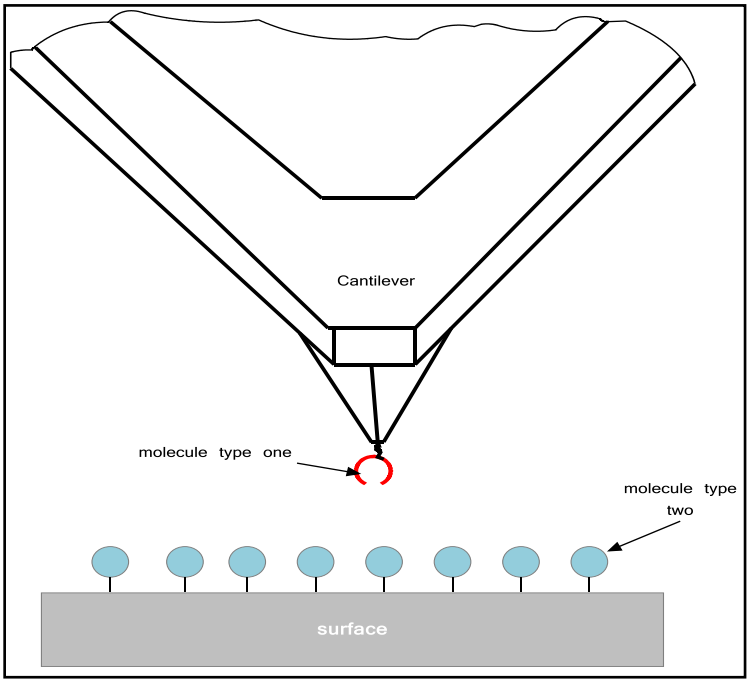

FIG.1.19 Schematic representation of bond strength measurements. One molecule is linked to the surface and another is cross-linked to the tip.

This concept has been used successfully to measure bond strength for different systems. Prominent examples include protein-protein interactions of the ligand-receptor type such as avidin-biotin(*92*), streptavidin-biotin(*93, 94*).

1.5.2 Mechanical Unfolding of proteins by AFM

Proteins are organic compounds made of a linear chain of amino acids, linked to each other via peptide bonds, and folded into specific shapes, Figure 1.20. The two ends of an amino acid chain are called the N-terminal (amino-terminus) and C-terminal (carboxyl-terminus), and the physical and chemical properties of an amino acid result from its side group (R)(*95*).

Each protein has its own unique sequence of amino acids, which determine its shape and function(*96*). For example, if two proteins have the same number but a different sequence of amino acids, the proteins will be different. The sequence is determined by the gene that encodes it(*95*).

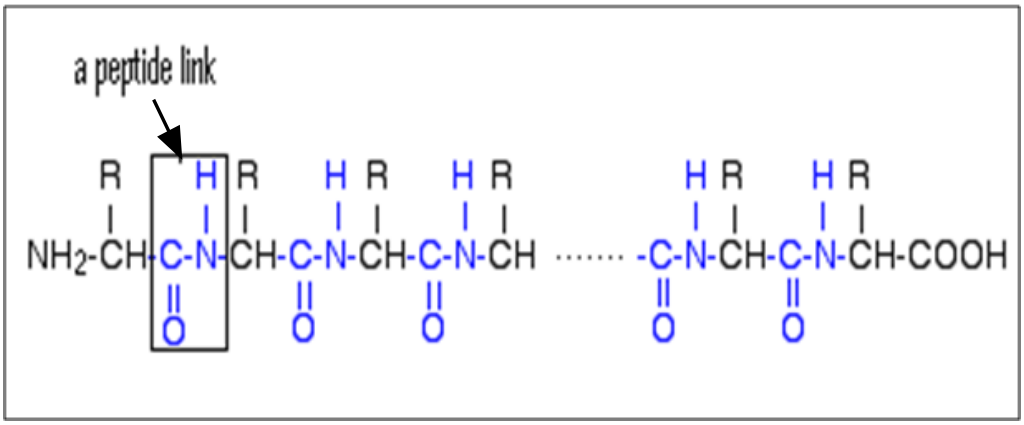

FIG.1.20 An amino acid chain.

Proteins play an important role in most physiological processes. For example, many chemical reactions that supply the body with energy could not occur fast enough without the presence of enzymes, most of which are

proteins(*96*). Also, proteins help to defend against diseases, as antibodies(*95, 96*). In muscles, proteins are crucial for the conversion of chemical energy into mechanical energy (*95, 96*).

To be biologically active, a protein must fold into its native state; the final and natural shape(*95, 97*). Therefore, a protein is assembled into three structural levels; primary, secondary and tertiary structure. The sequence of amino acids along a chain is known as the primary level of protein structure, Figure 1.21. This linear sequence, a polypeptide, is held together by covalent peptide bonds.

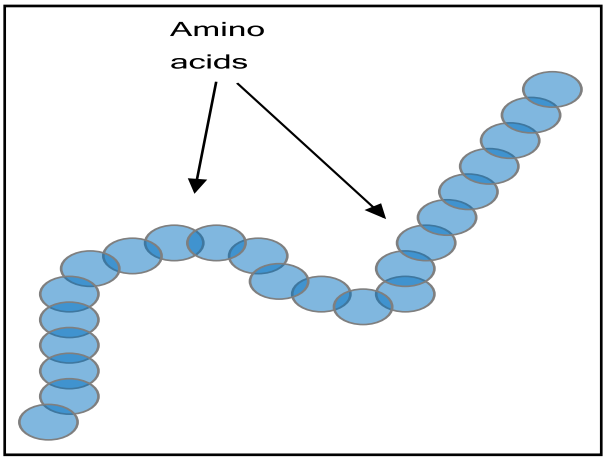

FIG.1.21 Schematic of primary level structure of protein

The secondary level of protein structure refers to the way in which the primary structure of protein either twists or folds back upon itself. This structure is stabilized due to hydrogen bonds generated between a hydrogen atom attached to a nitrogen atom on one amino acid and an oxygen atom of another (*98*). The bonds cause the primary structure to twist to form an alpha (α) helix or to fold back and forth to create a beta (β) sheet, Figure 1.22. α helix and β sheet are very common forms of secondary structure observed in proteins. α helix repeats itself every 5.4 Å along the axis of helix and has 3.6 amino acid residues per turn(*96*). The

beta sheet is an arrangement of two or more strands of amino acids chains joined together regularly by hydrogen bonds. If the strands lie in the same direction, it is called a parallel sheet, but if they are in the opposite direction, they are called an antiparallel sheet.

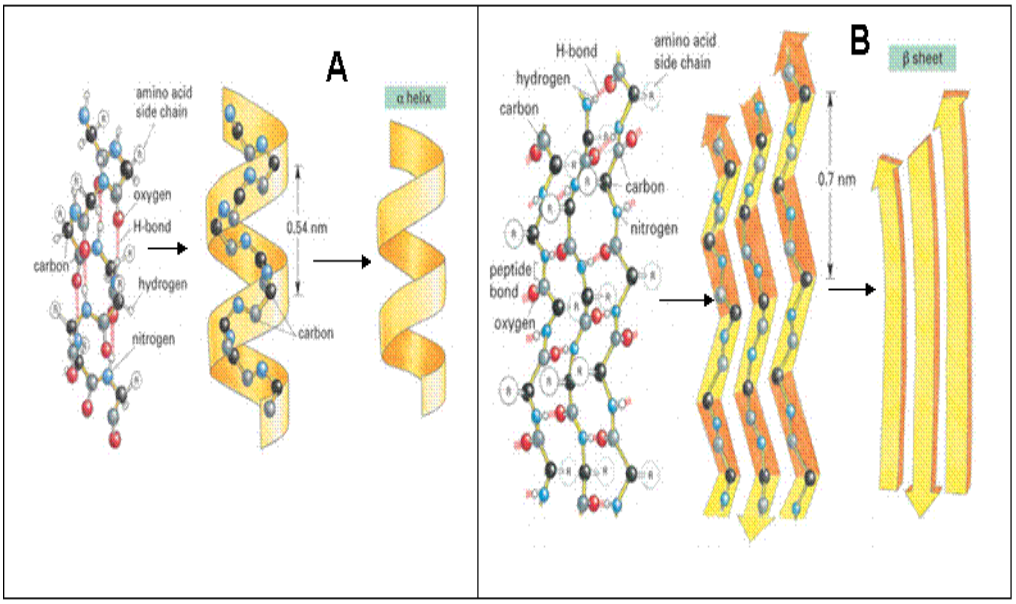

FIG.1.22 Schematic of secondary structure of a protein, alpha helix (A) and beta sheet (B), taken from (*99*)

The tertiary structure is the complete three-dimensional structure of proteins, Figure 1.23. The tertiary structure is the native state, or final folded form, of a single protein chain. Also, it is called the functional form. This structure is constructed from several domains. Several proteins are constructed out of repeated copies of one or more domains(*96*).

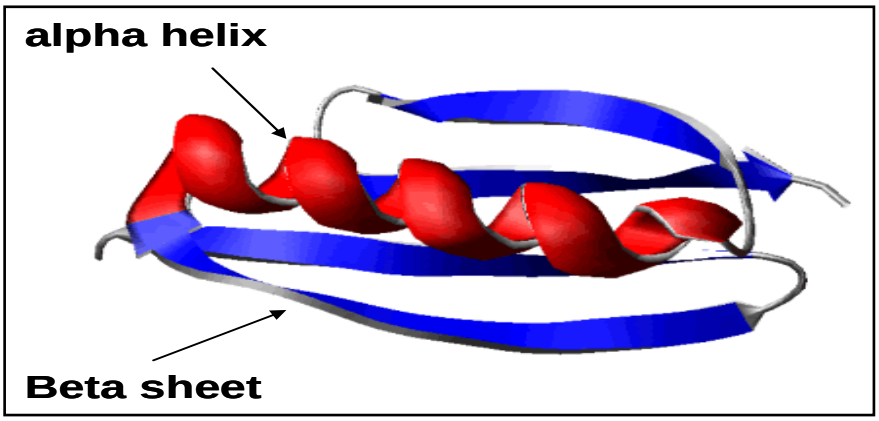

FIG.1.23 Tertiary structure of a protein.

The process by which a protein folds rapidly and reliably into a unique three-dimensional structure is poorly understood, known as the protein folding problem. However, it is well known that the sequence of amino acids, the primary structure of protein, contains the all information necessary to determine the tertiary structure of the protein (*100*,*101*).

Many proteins, but not all, are able to fold spontaneously without any assistance(*102*). Single domain proteins fold spontaneously, whereas multi-domain proteins require chaperonins (protein complexes) for folding (*102, 103*). Typically, they take seconds, or even milliseconds for small proteins, to attain their tertiary structure (*98, 103, 104*).

If only the unfolded state (U) and the native state (N) are populated on the folding path, the system is called two-state, whereas if the folding process involves the population of one or more partially folded intermediates (I) prior to the native state, i.e., a protein may fold to a native structure via one or more partially folded intermediates, the system will be called three-state. Most proteins greater than 100 residues in length fold by a three state (*105*). The role of intermediates in folding cannot be generalized, because they vary from one protein to another (*106*).

If we imagine a protein made of 100 amino acids and each amino acid has two possible conformations, this means 2^{100} possible conformations. If the protein attempts all of the conformations randomly, it would take an unrealistically long time to reach its final state. This argument is the so called Levinthal's paradox (*107*). To limit the conformational search, different scenarios have been proposed to model the folding problem. These includes the hydrophobic collapse model, diffusion-collision model, nucleation-condensation model, viscosity-collision model and energy-landscape theory, which describes folding kinetics through a statistical characterizations of the energies of different conformations dominated by a funnel shape where the native state is at the bottom (*97, 105, 108*),Figure 1.24.

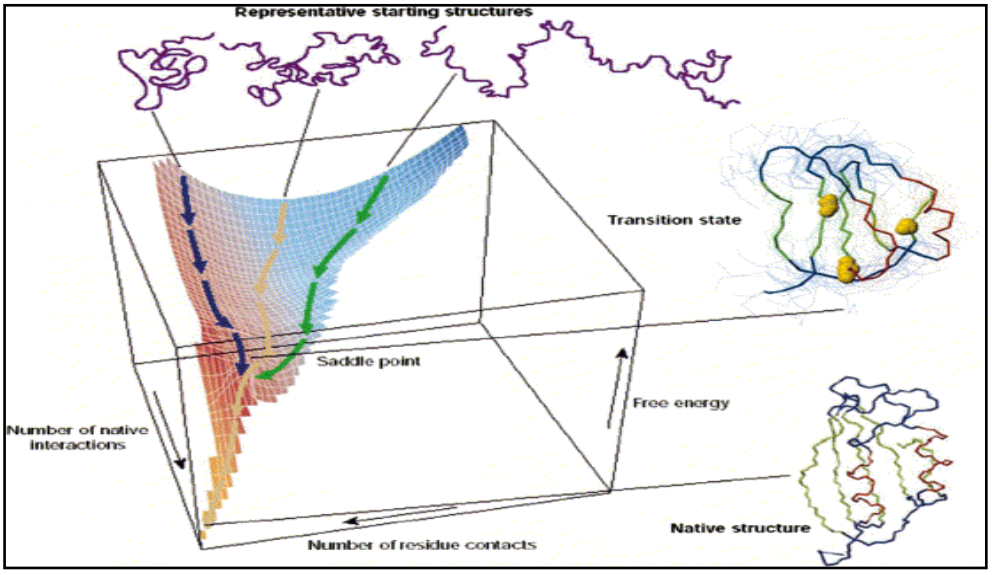

FIG.1.24 A schematic energy landscape for protein folding , taken from(*105*).

The mechanisms by which proteins fold have been intensively studied, using both experimental and theoretical approaches (*105*), however, because of the complexity, just one technique is insufficient to describe this process (*109*). For example, nuclear magnetic resonance (NMR) spectroscopy has been used to follow protein folding reactions (*110*), but for some proteins that fold very fast NMR is not suitable and other

techniques such as fluorescence quenching or infrared (IR) spectroscopy may be better used (*111*).

In order to describe the protein folding mechanism with an accurate model, it is essential to understand the structural properties of protein. Mechanical unfolding of proteins is one of the abundant approaches to accomplish that understanding (*112*). Developments in single molecule spectroscopy techniques have paved the way for the study of the mechanical properties of proteins at a single molecule level. The use of dynamic force spectroscopy techniques has advantages over conventional bulk experiments in terms of unfolding proteins. For example, the conventional chemical denaturants may explore one part of the energy landscape whereas use of, for example, AFM can explore different parts of this landscape (*113*). Moreover, in contrast with the bulk methods, it allows monitoring of the unfolding process of individual domains (*114*).

Many techniques of dynamic force spectroscopy, such as optical tweezers, magnetic tweezers and AFM, have emerged to manipulate single molecules, such as proteins. AFM is the most well known among the single molecule techniques, where the force mode of AFM is used to unfold a protein (*115*). Mechanical unfolding of proteins by use of AFM is based on a protein of interest being attached between the tip of flexible cantilever and a flat substrate, for instance a gold or glass substrate (*116*), mounted on highly accurate piezoelectric actuator, Figure 1.25 . The protein is attached to the tip via non-specific interaction and to the substrate, for example, by the strong adsorption of the sulphur atoms of the C-terminal cysteine to the substrate (*91, 117*).

In order to pick up the protein (which could be at anywhere along its contour) the cantilever is pressed against the flat substrate for a time in order to allow adhesion of the protein. The AFM stage, on which the

protein is attached, is moved apart, at constant velocity, causing an extension of the protein length. Consequently, the cantilever bends. This results in deflection of the laser beam which is monitored with Angstrom - scale resolution(*118*) . The deflection is directly proportional to the force that causes the cantilever to bend, thus, the stronger the force becomes, the larger the deflection of the cantilever, as shown in Figure 1.25. The applied force versus elongation is plotted to obtain the force-distance curve. An AFM force sensor can detect forces ranging from several piconewtons to nanonewton (*119*). The unfolding of individual domains appears as successive force peaks along the curve, a saw-tooth pattern.

When a protein is stretched under mechanical stress, the force applied to a protein domain to unfolding increases. At a certain value of force, the domain unravels and the length of the protein increases allowing the force on the cantilever to decrease. This process is repeated again until all domains are unfolded (*120, 121*).

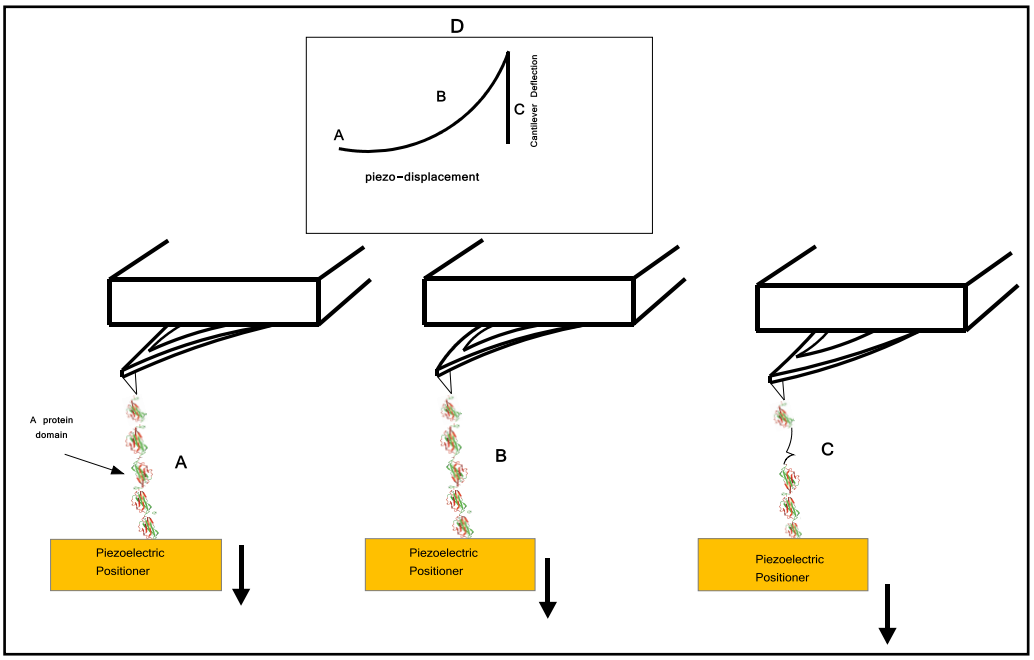

FIG.1.25 Schematic diagram of unfolding of a multi-domain protein experiment. (A) The protein is sandwiched between the AFM tip and substrate mounted on a piezoscanner and then the scanner is retracted allowing the application of unfolding force onto the protein. (B) Due to the mechanical resistance of the protein to the unfolding force the cantilever deflects downwards. (C) The cantilever recoils back when one domain of the protein is unfolded. (D)The deflection of the cantilever as function of the piezoscanner motion (inset).

AFM has been applied with great success to unfold a number of proteins. The earliest attempt to unfold a protein AFM has been performed in 1996 by Mitsui et al. (*122*). A single protein, called α-macroglobulin, was sandwiched between the AFM tip and surface, both of them covered with gold. Because of the surface-tip interaction, the interpretation of results was difficult.

Non-specific interactions of tip-surface were averted via using titin(*123*) , a giant muscle protein which plays a critical mechanical role in muscle contraction.(*124,125*). Titin is a multi-domain protein that enables the detection of unfolding domains and overcomes the drawback associated with the use of a single domain(*123*). However, it is not easy to ascertain which domain may be unraveled and whether the unfolding event

represents the true domain or not, because the heterogeneous proteins differ in their size, stability and structure (*126*).

To overcome this drawback, Carrion-Vazquez adopted a new approach based on protein engineering to construct a homopolymer from a single domain (*118*). A construct of repeated domains of Ig module 27 of I band of titin (I27) has been used. Later this technique was widened to include more proteins such as protein L(*127*), FnIII(*128*) and barnase (*129*).

Since the seminal work of Mitsui , many proteins have been investigated in order to understand their mechanical properties as well as the importance of their topology to resistance to an applied force and their stability (*118, 130, 131*). It was found that the most mechanically stable proteins investigated so far have the same topology, in which the terminal β-strands lie in parallel and are directly tied to each other via non-covalent interactions(*132*), therefore, in general, all α-helical proteins are mechanically weaker than β-sheet proteins (*131*).

1.6 Laser cooling

1.6.1 Atoms and ions cooling

The concept of laser cooling dates back to 1975 when Hansch and Schawlow (133) proposed the use of laser light to cool low density gas. However, the first cooling experiment using laser was reported three years later in independent papers by Wineland et al(*134*) and Neuhasuser et al (*135*).

Laser cooling is based upon the reduction in the thermally induced random velocities of atoms or ions via the scattering the light photons(*136*). The

velocity of ions or atoms in a gas varies with the temperature of the gas. The more familiar expression of mean kinetic energy of ions or atoms in a gas can be given by $\langle E_{ke} \rangle = \frac{1}{2} m \langle v^2 \rangle = \frac{3}{2} K_B T$, where K_B is the Boltzmann constant, T is temperature, v is the ions or molecules velocity and m is the mass.

The principle behind laser cooling is the Doppler effect, illustrated in Figure 1.26. Cooling is achieved by tuning the laser frequency below an electronic transition in the atom resonance and making the applied force onto the atom velocity dependent using the Doppler effect(*133*). The atom moving toward the laser beam absorbs more photons (as it is detuned). As a consequence, the atom moving in the opposite direction of the laser scatters more photons than it moves in the same direction, and it retards. The atom will lose the same amount of momentum to the scattered photon, applying an opposing force to the atom motion. So if the recoil velocity of the atom due to scattering photon is smaller than its initial velocity, the atom slows down. By adding more laser beams along other coordinates axes, cooling can be observed in three dimension (*136*). However, this technique is only possible with gaseous atoms that have particular electronic transitions, such as Rubidium.

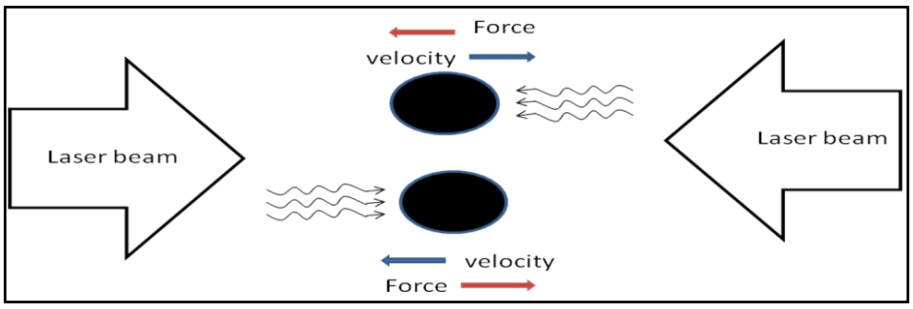

FIG. 1.26 Laser cooling of atoms or ions in one dimension.

A variant of this technique uses absorption and emission during anti-stockes fluorescence to achieve the same effect.

1.6.2 Mechanical resonator cooling

A mechanical oscillator can be cooled using the same laser cooling principle but with a different mechanism. This is required for the detection of gravitational waves, and the quantum ground state of the resonator. In such experiments, Fabry-Perot cavity is used. The cavity is built with two mirrors; static and flexible. The flexible or moveable mirror moves under the influence of its Brownian motion. In such experiments, the velocity of the moveable mirror is detected and an optical feedback force is applied via an active feedback system. When the velocity of the moveable mirror increases the feedback loop pumps more laser leading to an increase in scattering photons and vice versa . The change of the photon momentum applies optical force to the mirror that minimizes its velocity and hence its mean energy.

In chapter 3 we will present in detail three techniques used to cool vibrational mode of mechanical oscillators. The techniques based on optical, magnetic or electrostatic force will be illustrated.

1.7 References

(1) Binnig, G., Quate, C. F., and Gerber, C. (1986) Atomic Force Microscope. *Physical Review Letters 56*, 930-933.

(2) Nambiar, R. N., Gajraj, A. G., and Meiners, J.-C. (2004) All-Optical Constant-Force Laser Tweezers. *Biophysical Journal 87*, 1972-1980.

(3) Gosse, C., and Croquette, V. (2002) Magnetic Tweezers: Micromanipulation and Force Measurement at the Molecular Level. *Biophysical Journal 82*, 3314-3329.

(4) Kollmannsberger, P., and Fabry, B. (2007) High-force magnetic tweezers with force feedback for biological applications. *Review of Scientific Instruments 78*, 114301.

(5) Brockwell, D. J. (2007) Probing the mechanical stability of proteins using the atomic force microscope. *Biochemical Society Transactions 35*, 1564-1568.

(6) Li, H., Oberhauser, A. F., Fowler, S. B., Clarke, J., and Fernandez, J. M. (2000) Atomic force microscopy reveals the mechanical design of a modular protein. *Proceedings of the National Academy of Sciences of the United States of America 97*, 6527-6531.

(7) Rief, M., Clausen-Schaumann, H., and Gaub, H. E. (1999) Sequence-dependent mechanics of single DNA molecules. *Nature Structural Biology 6*, 346 - 349.

(8) Yamamoto, S., Yamada, H., and Tokumoto, H. (1997) Precise force curve detection system with a cantilever controlled by magnetic force feedback. *Review of Scientific Instruments 68*, 4132.

(9) Jarvis, S. P., Yamada, H., Yamamoto, S. I., Tokumoto, H., and Pethica, J. B. (1996) Direct mechanical measurement of interatomic potentials.

(10) Liang, S., Medich, D., Czajkowsky, D. M., Sheng, S., Yuan, J. Y., and Shao, Z. (2000) Thermal noise reduction of mechanical oscillators by actively controlled external dissipative forces. *Ultramicroscopy 84*, 119-125.

(11) Ashby, P. D., Chen, L., and Lieber, C. M. (2000) Probing Intermolecular Forces and Potentials with Magnetic Feedback

Chemical Force Microscopy. *Journal of the American Chemical Society 122*, 9467-9472.

(12) Favero, I., Metzger, C., Camerer, S., König, D., Lorenz, H., Kotthaus, J. P., and Karrai, K. (2007) Optical cooling of a micromirror of wavelength size. *Applied Physics Letters 90*, 104101.

(13) Favero, I., and Karrai, K. (2009) Optomechanics of deformable optical cavities. *Nature Photonics 3*, 201-205.

(14) Poggio, M., Degen, C. L., Mamin, H. J., and Rugar, D. (2007) Feedback Cooling of a Cantilever's Fundamental Mode below 5 mK. *Physical Review Letters 99*, 017201.

(15) Clifford, C. A., and Seah, M. P. (2005) The determination of atomic force microscope cantilever spring constants via dimensional methods for nanomechanical analysis. *Nanotechnology 16*, 1666-1680.

(16) Sader, J. E., and Sader, R. C. (2003) Susceptibility of atomic force microscope cantilevers to lateral forces: Experimental verification. *Applied Physics Letters 83*, 3195-3197.

(17) Meyer, G., and Amer, N. M. (1988) Novel optical approach to atomic force microscopy. *Applied Physics Letters 53*, 1045-1047.

(18) Alexander, S., Hellemans, L., Marti, O., Schneir, J., Elings, V., Hansma, P. K., Longmiro, M., and Gurley, J. (1989) An atomic-resolution atomic-force microscope implemented using an optical lever. *Journal of Applied Physics 65*, 164-167.

(19) Yaralioglu, G. G., Atalar, A., Manalis, S. R., and Quate, C. F. (1998) Analysis and design of an interdigital cantilever as a displacement sensor. *Journal of Applied Physics 83*, 7405-7415.

(20) Hues, S. M., Draper, C. F., Lee, K. P., and Colton, R. J. (1994) Effect of PZT and PMN actuator hysteresis and creep on nanoindentation measurements using force microscopy. *Review of Scientific Instruments 65*, 1561-1565.

(21) Zhang, P. (2008) *Industrial Control Technology: A Handbook for Engineers and Researchers*, 1st ed., William Andrew Inc, Norwich.

(22) Tan, K. K., Wang, Q.-G., Hang, C. C., and Hägglund, T. (1999) *Advances in Pid Control*, Springer, Berlin.

(23) Kaizuka, H., and Siu, B. (1988) A Simple Way to Reduce Hysteresis and Creep When Using Piezoelectric Actuators. *Japanese Journal of Applied Physics 27*, L773-L776.

(24) Goldfarb, M., and Celanovic, N. (1997) A Lumped Parameter Electromechanical Model for Describing the Nonlinear Behavior of Piezoelectric Actuators. *Journal of Dynamic Systems, Measurement, and Control 119*, 478-485.

(25) Croft, D., Shed, G., and Devasia, S. (2001) Creep, Hysteresis, and Vibration Compensation for Piezoactuators: Atomic Force Microscopy Application. *Journal of Dynamic Systems, Measurement, and Control 123*, 35-43.

(26) Jalili, N., and Laxminarayana, K. (2004) A review of atomic force microscopy imaging systems: application to molecular metrology and biological sciences. *Mechatronics 14*, 907-945.

(27) Shao, Z., Mou, J., Czajkowsky, D. M., Yang, J., and Yuan, J.-Y. (1996) Biological atomic force microscopy: what is achieved and what is needed. *Advances in Physics 45*, 1-86.

(28) Weisenhorn, A. L., Hansma, P. K., Albrecht, T. R., and Quate, C. F. (1989) Forces in atomic force microscopy in air and water. *Applied Physics Letters 54*, 2651-2654.

(29) Ducker, W. A., and Cook, R. F. (1990) Rapid measurement of static and dynamic surface forces. *Applied Physics Letters 56*, 2408-2411.

(30) Martin, Y., Williams, C. C., and Wickramasinghe, H. K. (1987) Atomic force microscope–force mapping and profiling on a sub 100-Å scale. *Journal of Applied Physics 61*, 4723-4730.

(31) Cappella, B., and Dietler, G. (1999) Force-distance curves by atomic force microscopy. *Surface Science Reports 34*, 1-104.

(32) Cappella, B., and Dietler, G. (1999) Force-distance curves by atomic force microscopy. *Surf. Sci. Rep 34*, 1-104.

(33) Cappella, B., Baschieri, P., Frediani, C., Miccoli, P., and Ascoli, C. (1997) Force-distance curves by AFM. *IEEE Engng.Med. Bio. 16*, 56-65.

(34) Israelchvili, J. N. (1997) *Iintermolecular and surface forces*, 6th ed., Academic Press, London.

(35) Butt, H.-J., Cappella, B., and Kappl, M. (2005) Force measurements with the atomic force microscope: Technique, interpretation and applications. *Surface Science Reports 59*, 1-152.

(36) Margenau, H. (1939) Van der waals forces. *Reviews of Modern Physics 11*, 1.

(37) Askeland, D. R., and Fulay, P. P. (2008) *Essentials of Materials Science and Engineering* 2nd ed., CL-Engineering, Toronto.

(38) Hamaker, H. C. (1937) The London--van der Waals attraction between spherical particles. *Physica 4*, 1058-1072.

(39) Visser, H. (1998) The role of surface forces in fouling of stainless steel in the dairy industry. *Journal of Dispersion Science and Technology 19*, 1127 - 1150.

(40) Butt, H.-J. (1991) Measuring electrostatic, van der Waals, and hydration forces in electrolyte solutions with an atomic force microscope. *Biophysical Journal 60*, 1438-1444.

(41) Morris, V. J., Kirby, A. R., and Gunning, A. P. (2001) *Atomic force microscopy for biologists*, Imperial College Press, London.

(42) Ennis, J., Sjostrom, L., Akesson, T., and Jonsson, B. (1998) Attractive Osmotic Pressure in an Electric Double Layer with Grafted Polyelectrolytes. *The Journal of Physical Chemistry B 102*, 2149-2164.

(43) Das, P. K., Bhattacharjee, S., and Moussa, W. (2003) Electrostatic Double Layer Force between Two Spherical Particles in a Straight Cylindrical Capillary: Finite Element Analysis. *Langmuir 19*, 4162-4172.

(44) Ducker, W. A., Senden, T. J., and Pashley, R. M. (1991) Direct measurement of colloidal forces using an atomic force microscope. *Nature 353*, 239 - 241.

(45) Larson, I., Chan, D. Y. C., Drummond, C. J., and Grieser, F. (1997) Use of Atomic Force Microscopy Force Measurements To Monitor Citrate Displacement by Amines on Gold in Aqueous Solution. *Langmuir 13*, 2429-2431.

(46) Dorobantu, L. S., Bhattacharjee, S., Foght, J. M., and Gray, M. R. (2009) Analysis of Force Interactions between AFM Tips and

Hydrophobic Bacteria Using DLVO Theory. *Langmuir 25*, 6968-6976.

(47) Giesbers, M., Kleijn, J. M., and Cohen Stuart, M. A. (2002) The Electrical Double Layer on Gold Probed by Electrokinetic and Surface Force Measurements. *Journal of Colloid and Interface Science 248*, 88-95.

(48) Rutland, M. W., and Senden, T. J. (1993) Adsorption of the poly(oxyethylene) nonionic surfactant C12E5 to silica: a study using atomic force microscopy. *Langmuir 9*, 412-418.

(49) Derjaguin, B. V. (1934) Untersuchungen fiber die Reibung und Adhaision, IV. *Kolloid Zeitschrift 69*, 155-164.

(50) Hogg, R., Healy, T. W., and Fuerstenau, D. W. (1965) Mutual coagulation of colloidal dispersions. *Transactions of the Faraday Society 62*, 1638 - 1651.

(51) Hillier, A. C., Kim, S., and Bard, A. J. (1996) Measurement of Double-Layer Forces at the Electrode/Electrolyte Interface Using the Atomic Force Microscope: Potential and Anion Dependent Interactions. *The Journal of Physical Chemistry 100*, 18808-18817.

(52) Israelachvili, J. N., and Adams, G. E. (1978) Measurement of forces between two mica surfaces in aqueous electrolyte solutions in the range 0–100 nm. *Journal of the Chemical Society, Faraday Transactions 1 74* 975 - 1001.

(53) Shubin, V. E., and Kékicheff, P. (1993) Electrical Double Layer Structure Revisited via a Surface Force Apparatus: Mica Interfaces in Lithium Nitrate Solutions. *Journal of Colloid and Interface Science 155*, 108-123.

(54) O'Shea, S. J., Welland, M. E., and Pethica, J. B. (1994) Atomic force microscopy of local compliance at solid--liquid interfaces. *Chemical Physics Letters 223*, 336-340.

(55) Grasso, D., Subramaniam, K., Butkus, M., Strevett, K., and Bergendahl, K. (2002) A review of non-DLVO interactions in environmental colloidal systems *Reviews in Environmental Science and Biotechnology 1*, 17-38.

(56) Cappella, B., Baschieri, P., Frediani, C., Miccoli, P., and Ascoli, C. (1997) Force-distance curves by AFM. *IEEE Engineering in Medicine and Biology 16*, 58-65.

(57) Forsman, J., Jonsson, B., and Woodward, C. E. (1996) Computer Simulations of Water between Hydrophobic Surfaces: The Hydrophobic Force. *The Journal of Physical Chemistry 100*, 15005-15010.

(58) O'Shea, S. J., Welland, M. E., and Rayment, T. (1992) Solvation forces near a graphite surface measured with an atomic force microscope. *Applied Physics Letters 60*, 2356-2359.

(59) Patil, S., Matei, G., Dong, H., and Hoffmanna, P. M. (2005) A highly sensitive atomic force microscope for linear measurements of molecular forces in liquids. *Review of Scientific Instruments 76*, 103705-1.

(60) Israelachvili, J., and Wennerstrom, H. (1996) Role of hydration and water structure in biological and colloidal interactions. *Nature 379*, 219-225.

(61) Israelachvili, J. N., and Pashley, R. M. (1983) Molecular layering of water at surfaces and origin of repulsive hydration forces. *Nature 306*, 249-250.

(62) Nancy, A. B., and Richard, J. C. (1989) Measuring the nanomechanical properties and surface forces of materials using an atomic force microscope. *Journal of Vacuum Science & Technology A: Vacuum, Surfaces, and Films 7*, 2906-2913.

(63) Hertz, H. (1882) Über die berührung fester elastischer körper (on the contact of elastic solids). *Journal of Reine Angewandte Math 94*, 156–71.

(64) Plassard, C., Lesniewska, E., Pochard, I., and Nonat, A. (2004) Investigation of the surface structure and elastic properties of calcium silicate hydrates at the nanoscale. *Ultramicroscopy 100*, 331-338.

(65) Perl, M., and Ore, E. (1986) Effect of geometry and poisson ratio on stress-intensity factors in a sen specimen under fixed-grip conditions. *Engineering Fracture Mechanics 23*, 843-849.

(66) Sneddon, I. N. (1965) The relation between load and penetration in the axisymmetric boussinesq problem for a punch of arbitrary profile. *International Journal of Engineering Science 3*, 47-57.

(67) Derjaguin, B. V., Muller, V. M., and Toporov, Y. P. (1975) Effect of contact deformations on the adhesion of particles. *Journal of Colloid and Interface Science 53*, 314-326.

(68) Maugis, D. (1992) Adhesion of spheres: The JKR-DMT transition using a dugdale model. *Journal of Colloid and Interface Science 150*, 243-269.

(69) Johnson, K. L., Kendall, K., and Roberts, A. D. (1971) Surface Energy and the Contact of Elastic Solids. *Proceedings of the Royal Society A 324*, 301-313.

(70) Radmacher, M., Fritz, M., and Hansma, P. K. (1995) Imaging soft samples with the atomic force microscope: gelatin in water and propanol. *69*, 264-270.

(71) Matzelle, T. R., Geuskens, G., and Kruse, N. (2003) Elastic Properties of Poly(N-isopropylacrylamide) and Poly(acrylamide) Hydrogels Studied by Scanning Force Microscopy. *Macromolecules 36*, 2926-2931.

(72) Kiely, J. D., and Houston, J. E. (1998) Nanomechanical properties of Au (111), (001), and (110) surfaces. *Physical Review B 57*, 12588.

(73) Sader, J. E., Larson, I., Mulvaney, P., and White, L. R. (1995) Method for the calibration of atomic force microscope cantilevers. *Review of Scientific Instruments 66*, 3789-3798.

(74) Senden, T., and Ducker, W. (1994) Experimental Determination of Spring Constants in Atomic Force Microscopy. *Langmuir 10*, 1003-1004.

(75) Jing, G. Y., Ma, J., and Yu, D. P. (2007) Calibration of the spring constant of AFM cantilever. *J Electron Microsc (Tokyo) 56*, 21-25.

(76) Maeda, N., and Senden, T. J. (2000) A Method for the Calibration of Force Microscopy Cantilevers via Hydrodynamic Drag. *Langmuir 16*, 9282-9286.

(77) Degertekin, F. L., Hadimioglu, B., Sulchek, T., and Quate, C. F. (2001) Actuation and characterization of atomic force microscope cantilevers in fluids by acoustic radiation pressure. *Applied Physics Letters 78*, 1628-1630.

(78) Holbery, J. D., Eden, V. L., Sarikaya, M., and Fisher, R. M. (2000) Experimental determination of scanning probe microscope cantilever spring constants utilizing a nanoindentation apparatus. *Review of Scientific Instruments 71*, 3769-3776.

(79) Walters, D. J., Cleveland, J. P., Thomson, N. H., and Hansma, P. K. (1996) Short cantilevers for atomic force microscopy. *Review of Scientific Instruments 67*, 3583-3590.

(80) Burnham, N. A., Chen, X., Hodges, C. S., Matei, G. A., Thoreson, E. J., Roberts, C. J., Davies, M. C., and Tendler, S. J. B. (2003) Comparison of calibration methods for atomic-force microscopy cantilevers. *Nanotechnology 14*, 1-6.

(81) Cleveland, J. P., and Manne, S. (1993) A nondestructive method for determining the spring constant of cantilevers for scanning force microscopy. *Review of Scientific Instruments 64*, 403-405.

(82) Sader, J. E., Chon, J. W. M., and Mulvaney, P. (1999) Calibration of rectangular atomic force microscope cantilevers. *Review of Scientific Instruments 70*, 3967-3969.

(83) Gibson, C. T., Smith, D. A., and Roberts, C. J. (2005) Calibration of silicon atomic force microscope cantilevers. *Nanotechnology 16*, 234-238.

(84) Fotiadis, D., Scheuring, S., Müller, S. A., Engel, A., and Müller, D. J. (2002) Imaging and manipulation of biological structures with the AFM. *Micron 33*, 385-397.

(85) Pang, D., Vidic, B., Rodgers, J., Berman, B. L., and Dritschilo, A. (1997) Atomic force microscope imaging of DNA and DNA repair proteins: Applications in radiobiological research. *Radiation Oncology Investigations 5*, 163-169.

(86) Karrasch, S., Hegerl, R., Hoh, J. H., Baumeister, W., and Engel, A. (1994) Atomic force microscopy produces faithful high-resolution images of protein surfaces in an aqueous environment. *Proceedings of the National Academy of Sciences of the United States of America 91*, 836-838.

(87) Kuznetsov, Y. G., Malkin, A. J., Lucas, R. W., Plomp, M., and McPherson, A. (2001) Imaging of viruses by atomic force microscopy. *Journal of General Virology 82*, 2025-2034.

(88) Santos, N. C., and Castanho, M. A. R. B. (2004) An overview of the biophysical applications of atomic force microscopy. *Biophysical Chemistry 107*, 133-149.

(89) Kasas, S., Thomson, N. H., Smith, B. L., Hansma, P. K., Miklossy, J., and Hansma, H. G. (1997) Biological applications of the AFM: From single molecules to organs. *International Journal of Imaging Systems and Technology 8*, 151-161.

(90) Bizzarri, A. R., and Cannistraro, S. (2009) Atomic Force Spectroscopy in Biological Complex Formation: Strategies and Perspectives. *The Journal of Physical Chemistry B 113*, 16449-16464.

(91) Bizzarri, A. R., and Cannistraro, S. (2010) The application of atomic force spectroscopy to the study of biological complexes undergoing a biorecognition process. *Chemical Society Reviews 39*, 734 - 749.

(92) Roberto De, P., Torsten, S., Krisztina, O., Hans-Joachim, G., and Martin, H. (2000) Force Spectroscopy and Dynamics of the Biotin-Avidin Bond Studied by Scanning Force Microscopy. *Single Molecules 1*, 285-290.

(93) Yuan, C., Chen, A., Kolb, P., and Moy, V. T. (2000) Energy Landscape of Streptavidin-Biotin Complexes Measured by Atomic Force Microscopy. *Biochemistry 39*, 10219-10223.

(94) Félix, R., and Vincent, T. M. (2007) Energy landscape roughness of the streptavidin-biotin interaction. *Journal of Molecular Recognition 20*, 495-501.

(95) Lesk, A. M. (2001) *Introduction to Protein Architecture: The Structural Biology of Proteins*, 1st ed., Oxford University Press, Oxford.

(96) Tramontano, A., and Lesk, A. M. (2006) *Protein Structure Prediction: Concepts and Applications*, 1st ed., Wiley-VCH, Weinheim.

(97) Dill, K. A., and Chan, H. S. (1997) From Levinthal to pathways to funnels. *Nature Structural Biology 4*, 10-19.

(98) Nölting, B. (2006) *Protein folding kinetics : biophysical methods*, 2nd ed., Springer, Berlin.

(99) http://fig.cox.miami.edu.

(100) Gething, M.-J., and Sambrook, J. (1992) Protein folding in the cell. *Nature 355*, 33-45.

(101) Rumbley, J., Hoang, L., Mayne, L., and Englander, S. W. (2001) An amino acid code for protein folding. *Proceedings of the National Academy of Sciences of the United States of America 98*, 105-112.

(102) Pande, V. S., Grosberg, A. Y., and Tanaka, T. (2000) Heteropolymer freezing and design: Towards physical models of protein folding. *Reviews of Modern Physics 72*, 259.

(103) Herwig, S., Uno, L., Clarence, E. S., and Roger, K. (2000) Thermal unfolding of G-actin monitored with the DNase I-inhibition assay. *European Journal of Biochemistry 267*, 476-486.

(104) Eaton, W. A., Munoz, V., Thompson, P. A., Henry, E. R., and Hofrichter, J. (1998) Kinetics and Dynamics of Loops, alpha-Helices, beta-Hairpins, and Fast-Folding Proteins. *Accounts of Chemical Research 31*, 745-753.

(105) Christopher, M. D., Andrej, S., and Martin, K. (1998) Protein Folding: A Perspective from Theory and Experiment. *Angewandte Chemie International Edition 37*, 868-893.

(106) Brockwell, D. J., Smith, D. A., and Radford, S. E. (2000) Protein folding mechanisms: new methods and emerging ideas. *Current Opinion in Structural Biology 10*, 16-25.

(107) Zwanzig, R., Szabo, A., and Bagchi, B. (1992) Levinthal's paradox. *Proceedings of the National Academy of Sciences of the United States of America 89*, 20-22.

(108) Joseph, D. B., José Nelson, O., Nicholas, D. S., and Peter, G. W. (1995) Funnels, pathways, and the energy landscape of protein folding: A synthesis. *Proteins: Structure, Function, and Genetics 21*, 167-195.

(109) Deniz, A. A., Laurence, T. A., Beligere, G. S., Dahan, M., Martin, A. B., Chemla, D. S., Dawson, P. E., Schultz, P. G., and Weiss, S. (2000) Single-molecule protein folding: Diffusion fluorescence resonance energy transfer studies of the denaturation of chymotrypsin inhibitor 2. *Proceedings of the National Academy of Sciences of the United States of America 97*, 5179-5184.

(110) Zeeb, M., and Balbach, J. (2004) Protein folding studied by real-time NMR spectroscopy. *Methods 34*, 65-74.

(111) Roder, H., and Shastry, M. C. R. (1999) Methods for exploring early events in protein folding. *Current Opinion in Structural Biology 9*, 620-626.

(112) Povarova, O. I., Kuznetsova, I. M., and Turoverov, K. K. (2007) Different disturbances - one pathway of protein unfolding. Actin folding-unfolding and misfolding. *Cell Biology International 31*, 405-412.

(113) Best, R. B., Brockwell, D. J., Toca-Herrera, J. L., Blake, A. W., Smith, D. A., Radford, S. E., and Clarke, J. (2003) Force mode atomic force microscopy as a tool for protein folding studies. *Analytica Chimica Acta 479*, 87-105.

(114) Best, R. B., and Clarke, J. (2002) What can atomic force microscopy tell us about protein folding? *Chemical Communications 3*, 183 - 192.

(115) Ikai, A., Mitsui, K., Tokuoka, H., and Xu, X. M. (1997) Mechanical measurements of a single protein molecule and human chromosomes by atomic force microscopy. *Materials Science and Engineering: C 4*, 233-240.

(116) Rounsevell, R., Forman, J. R., and Clarke, J. (2004) Atomic force microscopy: mechanical unfolding of proteins. *Methods 34*, 100-111.

(117) Dakkouri, A. S., Kolb, D. M., Edelstein-Shima, R., and Mandler, D. (1996) Scanning Tunneling Microscopy Study of l-Cysteine on Au(111). *Langmuir 12*, 2849-2852.

(118) Carrion-Vazquez, M., Oberhauser, A. F., Fowler, S. B., Marszalek, P. E., Broedel, S. E., Clarke, J., and Fernandez, J. M. (1999) Mechanical and chemical unfolding of a single protein: A comparison. *Proceedings of the National Academy of Sciences of the United States of America 96*, 3694-3699.

(119) Rukman, H., and Atsushi, I. (2002) Unfolding mechanics of holo- and apocalmodulin studied by the atomic force microscope. *Protein Science 11*, 1532-1538.

(120) Smith, D. A., and Radford, S. E. (2000) Protein folding: Pulling back the frontiers. *10*, R662-R664.

(121) Fisher, T. E., Oberhauser, A. F., Carrion-Vazquez, M., Marszalek, P. E., and Fernandez, J. M. (1999) The study of protein mechanics

with the atomic force microscope. *Trends in Biochemical Sciences 24*, 379-384.

(122) Mitsui, K., Hara, M., and Ikai, A. (1996) Mechanical unfolding of alpha2-macroglobulin molecules with atomic force microscope. *FEBS Letters 385*, 29-33.

(123) Rief, M., Gautel, M., Oesterhelt, F., Fernandez, J. M., and Gaub, H. E. (1997) Reversible Unfolding of Individual Titin Immunoglobulin Domains by AFM. *Science 276*, 1109-1112.

(124) Li, H. B., Oberhauser, A. F., Fowler, S. B., Clarke, J., and Fernandez, J. M. (2000) Atomic force microscopy reveals the mechanical design of a modular protein. *PNAS 97*, 6527–6531.

(125) Linke, W. A., Ivemeyer, M., Olivieri, N., Kolmerer, B., Rüegg, C. J., and Labeit, S. (1996) Towards a Molecular Understanding of the Elasticity of Titin. *Journal of Molecular Biology 261*, 62-71.

(126) Scott, K. A., Steward, A., Fowler, S. B., and Clarke, J. (2002) Titin; a multidomain protein that behaves as the sum of its parts. *Journal of Molecular Biology 315*, 819-829.

(127) Brockwell, D. J., Beddard, G. S., Paci, E., West, D. K., Olmsted, P. D., Smith, D. A., and Radford, S. E. (2005) Mechanically Unfolding the Small, Topologically Simple Protein L. *Biophysical Journal 89*, 506-519.

(128) Oberdorfer, Y., Fuchs, H., and Janshoff, A. (2000) Conformational Analysis of Native Fibronectin by Means of Force Spectroscopy. *Langmuir 16*, 9955-9958.

(129) Best, R. B., Li, B., Steward, A., Daggett, V., and Clarke, J. (2001) Can Non-Mechanical Proteins Withstand Force? Stretching Barnase by Atomic Force Microscopy and Molecular Dynamics Simulation. *Biophysical Journal 81*, 2344-2356.

(130) Brockwell, D., Beddard, G., Paci, E., West, D., Olmsted, P., Smith, D., and Radford, S. (2005) Mechanically Unfolding the Small, Topologically Simple Protein L. *Biophys.J. 89*, 506–519.

(131) Sharma, D., Perisic, O., Peng, Q., Cao, Y., Lam, C., Lu, H., and Li, H. (2007) Single-molecule force spectroscopy reveals a mechanically stable protein fold and the rational tuning of its mechanical stability. *Proceedings of the National Academy of Sciences 104*, 9278-9283.

(132) Carrion-Vazquez, M., Oberhauser, A. F., Fisher, T. E., Marszalek, P. E., Li, H., and Fernandez, J. M. (2000) Mechanical design of proteins studied by single-molecule force spectroscopy and protein engineering. *Progress in Biophysics and Molecular Biology 74*, 63-91.

(133) Hänsch, T. W., and Schawlow, A. L. (1975) Cooling of gases by laser radiation. *Optics Communications 13*, 68-69.

(134) Wineland, D. J., Drullinger, R. E., and Walls, F. L. (1978) Radiation-Pressure Cooling of Bound Resonant Absorbers. *Physical Review Letters 40*, 1639.

(135) Neuhauser, W., Hohenstatt, M., Toschek, P., and Dehmelt, H. (1978) Optical-Sideband Cooling of Visible Atom Cloud Confined in Parabolic Well. *Physical Review Letters 41*, 233.

(136) Phillips, W. D. (1998) Nobel Lecture: Laser cooling and trapping of neutral atoms. *Reviews of Modern Physics 70*, 721.

Chapter 2
Experimental methods

In this chapter, we illustrate the most common experimental methods used through the thesis. However, each chapter contains more details of their application.

2.1 Surface-tip distance correction

The output of the force spectroscopy mode in AFM is more correctly described as a deflection versus piezoscanner displacement curve. However, we are interested in measuring the force on an AFM probe as a function of tip sample separation. In order to convert the piezoscanner displacement into tip-sample separation, Figure 2.1, the z-piezoelectric displacement is subtracted from the cantilever deflection(*1*)

[2.1]

$$D = U - \Delta z$$

Where U is the piezoscanner displacement and Δz is the cantilever deflection.

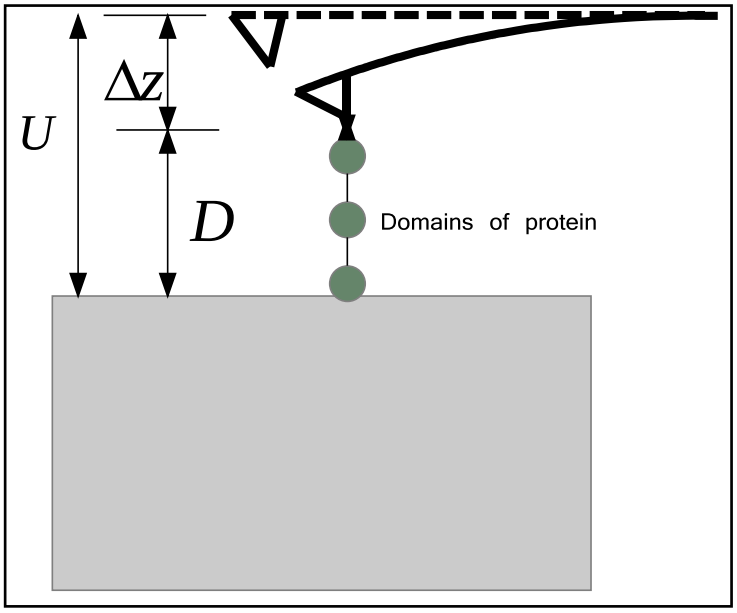

FIG.2.1 The tip-sample separation (D) is the difference between the z-piezo displacement(U) and the deflection of the cantilever(Δz).

When the cantilever tip contacts a hard flat surface mounted on the piezoscanner, the cantilever deflects the same amount as the piezoscanner displacement, and the tip-surface separation is zero.

Figure 2.2 illustrates the output voltage of the position sensitive photodetector (PSPD) representing the cantilever deflection and the piezoscanner displacement recorded simultaneously versus time during force measurements. The raw photodiode voltage and the piezoscanner displacement were collected through a National Instruments PC capture card controlled via Labview 6 software (custom written by Masaru Kawakami, University of Leeds). The bit resolution of the capture card was 2.44 mV/bit hence the digitized curves were converted to volts by multiplying the data points by 2.44 mV/bit prior to further analysis.

Eq.2.1 shows that the tip-surface separation is the result of subtracting the piezo-displacement from the cantilever deflection. Consequently, in order to get zero separation, the piezoscanner displacement and the cantilever deflection curves in the contact line should overlap perfectly. However, in Figure 2.2 it can be seen the two curves have different slopes in the contact line.

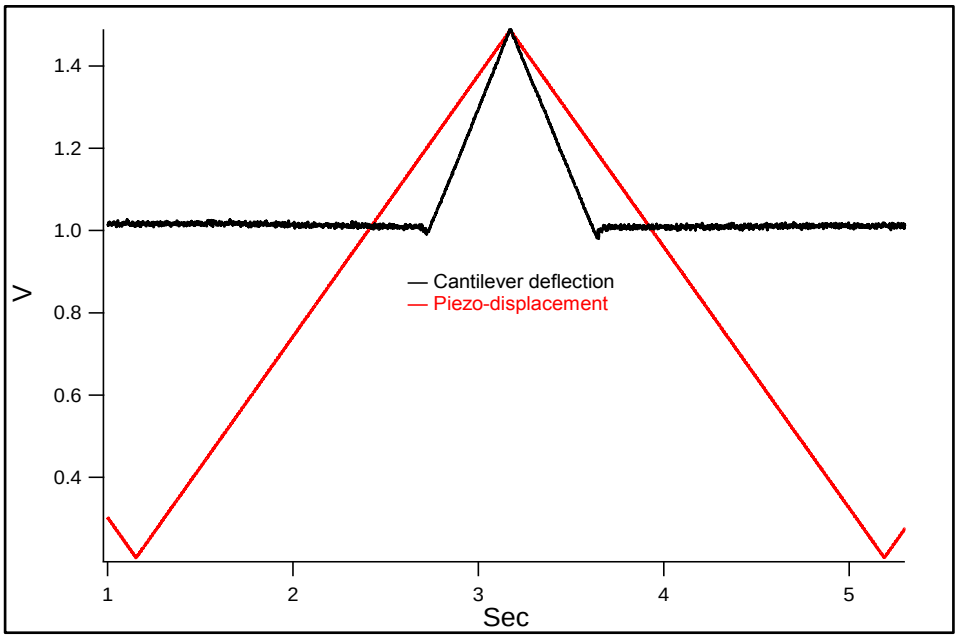

FIG.2.2 Uncorrected cantilever deflection (black) and the piezoscanner displacement (red) versus time.

By plotting the raw data of the output of PSPD, in volts, versus the raw data of the piezo displacement, in volts, we can get the correction factor which is the slope of the contact line, Figure 2.3.

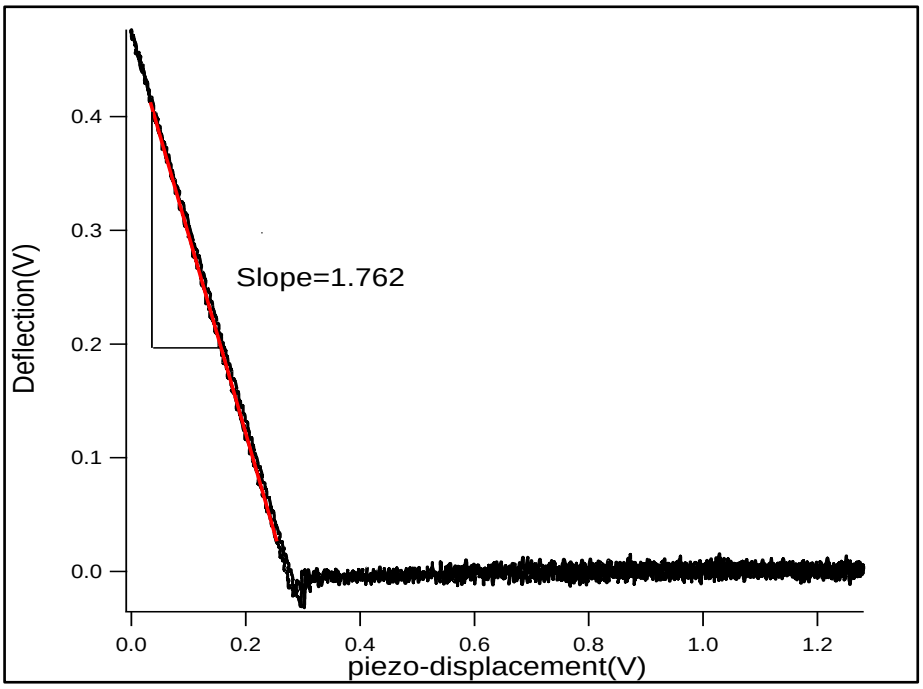

FIG.2.3 The cantilever deflection versus the piezoscanner displacement. The red line is the fit of the contact line where its slope is used to correct the cantilever deflection.

By dividing all the raw data of the output of PSPD by the correction factor, the two curves overlap perfectly in the contact line, Figure 2.4.

In order to convert the piezo-displacement to separation, the data points of output voltage of PSPD is subtracted from the data points of the piezo-displacement using Eq.2.1 and then the separation is converted into meters by multiplying each point of the separation by the position sensitivity of the piezoscanner used in the experiment, calibrated against known Z-standard silicon gratings (step-height 26 nm and 100 nm, NT-MDT, TGZ01 and TGZ02.

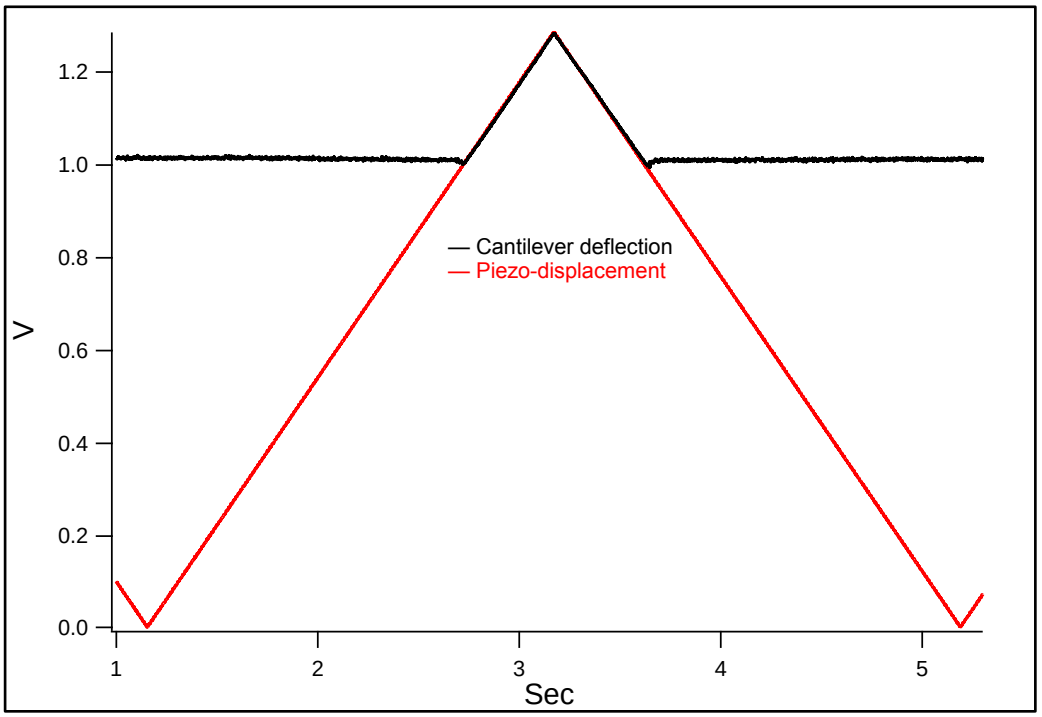

FIG.2.4 The corrected cantilever deflection (black) and the piezoscanner displacement (red) versus time.

Now the piezo-displacement is converted to tip-sample separation by plotting the cantilever deflection, in volts, versus separation, Figure 2.5.

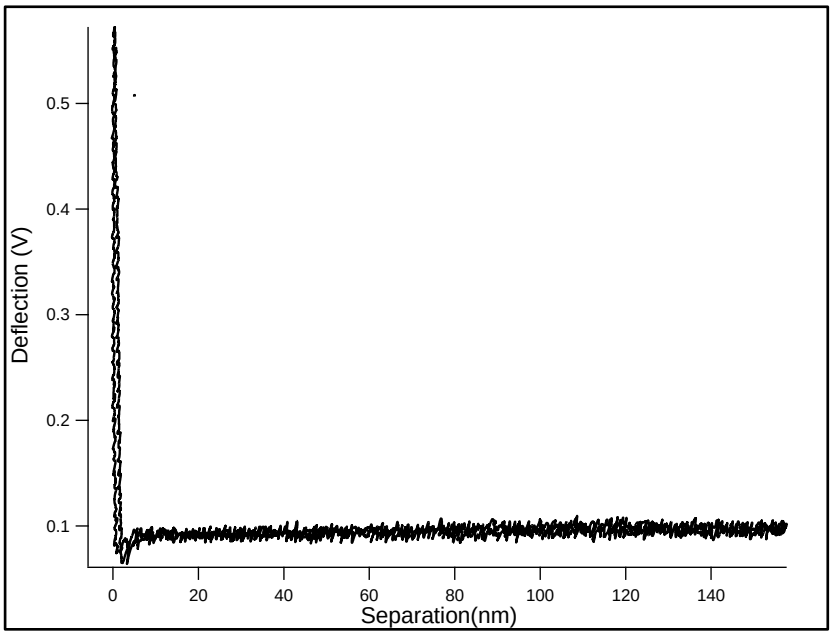

FIG.2.5 Deflection-separation curve obtained by AFM.

2.2 Cantilever stiffness calibration

A number of methods used to calibrate cantilever stiffness were described in chapter 1. A method based on employing the cantilever thermal noise associated with the cantilever Brownian motion has become acceptable standard method. In this thesis, we adopt the thermal noise method, taking advantage of the equipartition theorem. As a result, the cantilever stiffness can be given by

$$\kappa = \frac{k_B T}{\delta z^2} \qquad [2.2]$$

Where K_B is Boltzmann constant, T is temperature and δz^2 is the mean square of the cantilever thermal fluctuation.

Hutter et al(*2*) demonstrated that δz^2 can be measured by means of the power spectral density curve (PSD). Consequently, the mean square of the cantilever thermal oscillation δz^2 is equivalent to the area (A_p) under the peak corresponding to the cantilever resonance frequency. Thus, Eq.2.2 becomes $\kappa = \frac{k_B T}{A_p}$.

The area (A_p) can be determined by fitting the PSD curve to a Lorentzian curve(*3*), Figure 2.6.

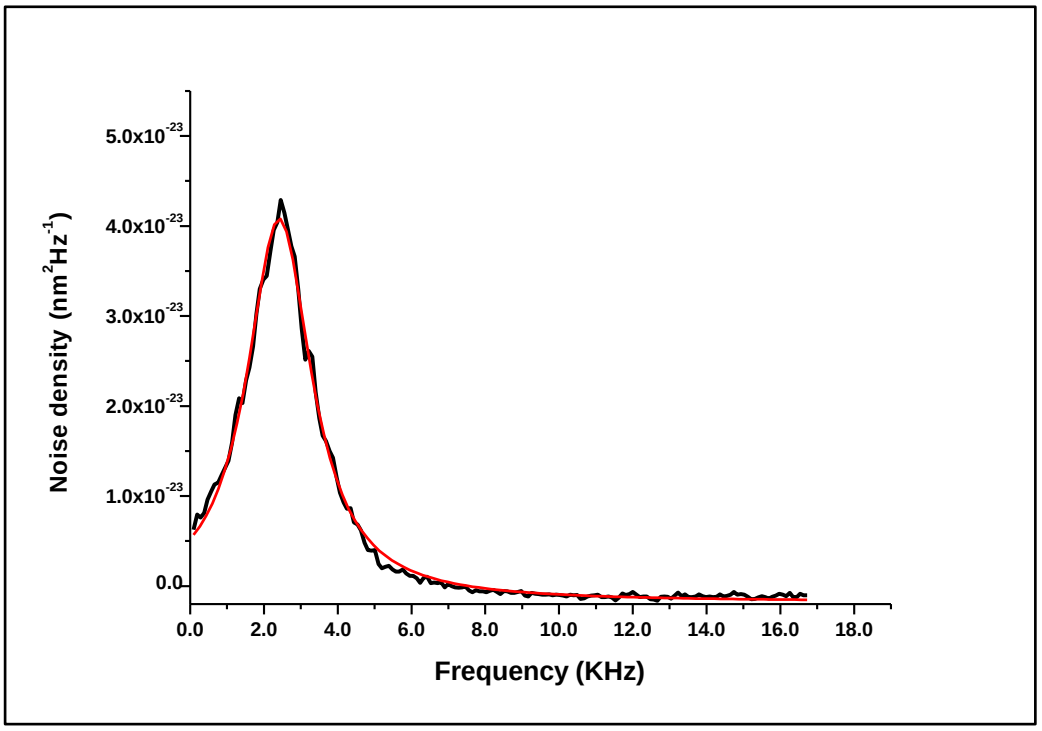

FIG.2.6 PSD of the thermal noise of an AFM cantilever fitted to Lorentzian line shape (red).

In practical terms, the above steps to estimate the cantilever spring constant are automated via the thermal tune feature available with the Veeco MultiMode PicoForce and several Veeco instrument Nanoscope controllers. Note that the deflection sensitivity must be accurately obtained first by measuring a force curve against a hard non-identable surface. The aim of determining the deflection sensitivity is to convert the output of the PSPD in volts to a calibrated distance.

2.3 Proteins

Two protein concatamers were used in this work $(I27)_5$ and $(I27)_4(Im9)_3$. These proteins were kindly provided by Dr. David Brockwell (Astbury Centre for Structural Molecular Biology) as freeze dried 0.05 mg aliquots. $(I27)_5$ concatamer consists of five copies of (C47S, C63S I27) domain(*4*),

Figure 2.7, and $(I27)_4(Im9)_3$ is composed of three Im9 domains alternating with four I27 domains, Figure 2.8.

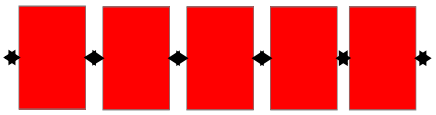

FIG.2.7 Cartoon representation of an I27 construct, consisting of five identical I27 domains.

FIG.2.8 Cartoon representation of $(I27)_4$ $(Im9)_3$ construct.

Both protein concatamers were reconstructed to100 μg/ml in PBS buffer at pH 7.2 and centrifuged at 13,000 rpm for 5 minutes. 40 μl of the protein solution was pipette into 100 μl of PBS and the two solutions left to mix. The protein solution and PBS buffer was dropped onto a freshly cleaved template stripped gold substrate and left for an incubation time of 15-20 minutes. The protein covalently binds to the gold via a cysteine residue(*5*). At this concentration the probability of picking up a construct is low (typically 2%) but ensured a single construct was measured, leading to clean unfolding curves.

All force spectroscopy experiments have been performed using the CD-AFM system configuration based on a Veeco Picoforce microscope controlled by a Nanoscope IIIA controller (Digital Instruments, Santa Barbara, California) to permit the standard force spectroscopy to be done when the feedback circuit of CD-AFM is off. A Veeco microcantilever C, with a stiffness of 10 pN/nm, and fluid cell were employed. Prior to an experiment the fluid cell was thoroughly cleaned with ethanol and rinsed by Milli-Q water (18 MΩ).

The sample is mounted on the piezoscanner and approached the cantilever tip at a constant speed. Afterwards, the cantilever tip is pressed on the surface for a while (<1 second) and then retracted. During retraction, the position sensitive photodetector records the cantilever deflection in response to tip-protein interactions, more details in chapter 6.

2.4 Lipid bilayer sample preparation

The lipid bilayer used in this work is formed from 30% sphingomyelin (purchased from Sigma), 30% DOPC (di-oleogl-phosphatidyl-choline) (purchased from Avanti) and 40% cholesterol (purchased from Sigma), hence in the so called liquid-ordered phase. Each lipid was dissolved in chloroform to form stock solutions at 5 µg/ml. The stocks were combined together in the proportion above to a total lipid mass of 250 µg. To form a dry thin lipid film, the solvent was evaporated off under a gentle steam of N_2 gas. To remove excess solvent, the lipid was placed in a vacuum dessicator overnight. The lipid film was rehydrated by adding 0.5 ml of PBS buffer, and the solution vortexed until forming hydrated multilamellar vesicles, indicating the solution turning cloudy white. The multilamellar vesicles were broken down with a pulsed ultrasonic probe for 20 minutes at 4°C, when complete the lipid solution should be clear, indicating formation of small unilamellar vesicles (SUVs) which are more likely to unroll, or burst open when contacting the surface, thereby forming a surface supported bilayer.

A drop of 50 µl of the SUVs solution was placed on a freshly cleaved mica substrate, and left to incubate for 30 minutes. Excess lipids in the vesicle solution is then removed by carefully exchanging the solution with clean (filtered to 0.2 µm) PBS buffer, with at least 7 exchanges, leaving a single defect free lipid bilayer on the surface.

2.5 References

(1) Cappella, B., Baschieri, P., Frediani, C., Miccoli, P., and Ascoli, C. (1997) Force-distance curves by AFM. *IEEE Engineering in Medicine and Biology Magazine 16*, 58-65.

(2) Hutter, J. L., and Bechhoefer, J. (1993) Calibration of atomic force microscope tips. *Review of Scientific Instruments 64*, 1868.

(3) Heer, C. V. (1972) *Statistical mechanics, kinetic theory, and stochastic processes* Academic Press, New york.

(4) Brockwell, D. J., Beddard, G. S., Clarkson, J., Zinober, R. C., Blake, A. W., Trinick, J., Olmsted, P. D., Smith, D. A., and Radford, S. E. (2002) The effect of core destabilization on the mechanical resistance of I27. *Biophysical Journal 83*, 458-472.

(5) Grandbois, M., Beyer, M., Rief, M., Clausen-Schaumann, H., and Gaub, H. E. (1999) How Strong Is a Covalent Bond? *Science 283*, 1727-1730.

Chapter 3
Thermodynamic noise cancellation system

3.1 Introduction

In order to achieve high force resolution, very soft cantilevers are employed, namely, the spring constant of the AFM cantilever must be sufficiently small to detect small forces. Unfortunately, such a soft cantilever may be susceptible to stochastic (random) driving forces leading to large spatial oscillations around its equilibrium position. This random motion of the cantilever, due to impacts with surrounding molecules, is more commonly known as Brownian motion or thermodynamic noise.

The amplitude of the fluctuations of AFM cantilevers induced by thermodynamic noise could be comparable to the magnitude of the sample-cantilever interactions. Thus, the signal generated from a true force signal could be indistinguishable from the thermal response of the

cantilever. Consequently, the forces below this thermal noise limit will be undetectable and crucial data could be lost(*1, 2*).

Use of a stiffer cantilever, on the one hand, can greatly reduce the spatial fluctuations of the cantilever. On the other hand, it is disadvantageous for the force sensitivity. According to the equipartition theorem, the root mean square (RMS) in force measurement (δF), the minimum detectable force, is

$$\delta F = \sqrt{k_B T \cdot \kappa} \qquad [3.1]$$

Where k_B is the Boltzmann constant, T is the ambient temperature and k is the cantilever stiffness (spring constant).

According to Eq.3.1, the magnitude of a minimum detectable force can be given by δF because the minimum detectable force is limited by thermodynamic noise in force measurement. Therefore, δF is proportional to the cantilever stiffness value and the ambient temperature. Thus, if we use a cantilever with a spring constant around 10 pN/nm, the RMS force noise, δF , at room temperature should be approximately 7 pN, while the force noise (peak to peak) will be larger.

This force noise places a limitation upon a number of ultrahigh sensitive force and position measurements, such as single molecule force spectroscopy. One example of these experiments is measurements of the interaction forces that govern the structure of proteins. A protein domain, which cannot withstand the forces transmitted to it from thermodynamic noise of the cantilever, may unfold stochastically. For example Im9 which unfolds at loading force of < 20 pN(*3*).The sudden unfolding of the protein

domain due to the thermodynamic oscillations of the cantilever would be neither monitored nor recorded.

To circumvent the problems illustrated above we introduce a novel method based on eliminating AFM cantilever thermodynamic noise by using laser radiation pressure (or photon force). Radiation pressure is a force per unit area applied onto the back side of a cantilever due to the change in momentum of laser light. In principle, the total force exerted on the cantilever due to the change in momentum of photons reflecting off the back side of a cantilever coated with a thin layer of gold can be calculated by (the derivation of Eq.3.2 is given in chapter 4)

$$F = \frac{2P}{c} \qquad [3.2]$$

Where P is laser power at the cantilever and c is the speed of light

In this setup, a secondary high-powered feedback- controlled laser is used to suppress the thermodynamic oscillation of standard commercially available AFM cantilevers. No major modifications, aside from the addition of a secondary laser, have been necessary keeping the AFM compact and user-friendly. It is worth noting that the output of the secondary high-powered laser can be exploited to record force-distance curves via the change of the secondary high-powered laser intensity required to maintain the predefined setpoint constant (more details in chapter 5).

The deflection of the cantilever has been reduced to be equivalent to cooling to ~3 K. This opens up possibilities for experimental applications impossible before due to thermodynamic limitations, for instance motor proteins interaction(*4*).

Our system (CD-AFM) was a result of collaboration between the Molecular and Nanoscale Physics group in Leeds and Yanagida's group in Osaka. However, our system differs from Yanagida's system, called Intermolecular Force Microscopy (IFM). In the CD-AFM system, we use the commercially available cantilevers whereas the Osaka group uses specially constructed cantilevers with a stiffness of 0.1 pN/nm, 100 times softer than those commercially available. This cantilever is composed of a thin glass coverslip drawn to 0.2 μm in thickness and a tip made of a sharp whisker of ZnO, 10 μm in length. The opposite side of the tip is covered with 30 nm of a gold film in order to enhance the reflectivity of the cantilever. Such a cantilever with a stiffness of 0.1 pN/nm undergoes huge thermal fluctuation in its position due to Brownian motion (thermodynamic noise). The positional uncertainty of this glass cantilever, due to thermodynamic noise, is ~40 nm peak to peak, inducing an uncertainty in force measurement of 4 pN(*4*).

Figure 3.1 shows a schematic diagram of IFM. The feedback system used to control the thermal noise associated with the cantilever motion is based on radiation force. In IFM two lasers were used; L1 (3 mW diode laser) for position sensing and L2 (20 mW diode laser) for position controlling.

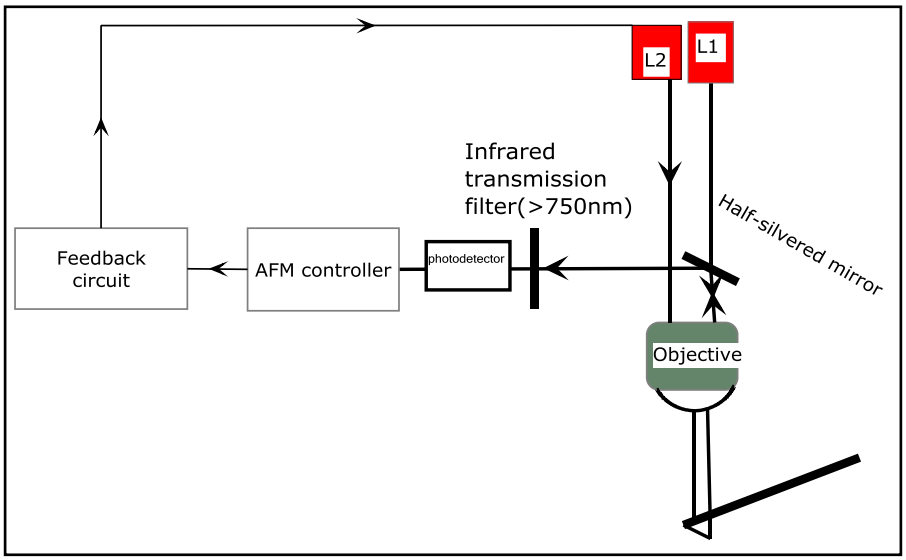

FIG.3.1 The setup of IFM system used to control the AFM cantilever oscillation.

Most improvements in force resolution acquired by using IFM were due to the cantilever used. When Yanagida's group used IFM to improve the force resolution for the standard cantilevers they failed. This failure limits the use of their system. In addition, massive modifications were needed that make it difficult to use.

In CD-AFM, we overcome those problems related to IFM. In the following sections we will show how we managed to make CD-AFM effective and accessible.

3.2 Methods for calculating RMS of cantilever thermal deflection

The Brownian motion of a microscopic particle suspended in fluid was first described in 1827 by Robert Brown(*5*) and describes the random positional fluctuations of the particle. The random motion is a direct result of stochastic impacts of the medium molecules.

Every oscillator (such as a cantilever) oscillates naturally when it is excited at or near its natural resonance frequency. Each cantilever has numerous harmonic modes but the lowest mode, the fundamental mode, has the most energy of the oscillation(*6, 7*).

A submerged cantilever in a fluid at thermal equilibrium is constantly subject to stochastic motion attributed to the bombardments of the fluid molecules with the cantilever. Therefore, the random motion of the molecules at the fundamental mode triggered by their thermal energy is given by the equipartition theorem, according to which each quadratic term of a system in thermal equilibrium has the same average of energy. As a result, the RMS amplitude of the cantilever thermal deflection, δz , in the vertical direction, is

$$\delta z = \sqrt{\frac{K_B T}{\kappa}} \qquad [3.3]$$

Where k_B, k and T are Boltzmann's constant, stiffness of the cantilever and ambient temperature respectively.

In order to relate the temperature of a system with its energy, a one-dimensional harmonic oscillator in thermal equilibrium with its surroundings will be considered. The energy of such a system is given by its Hamiltonian (H)

$$\mathrm{H} = \frac{\mathrm{M}^2}{2\mathrm{m}} + \frac{1}{2}\kappa\delta\mathrm{z}^2 \qquad [3.4]$$

Where $\frac{\mathrm{M}^2}{2\mathrm{m}}$ is the kinetic energy of the oscillator and $\frac{\kappa\delta z^2}{2}$ its potential energy. Each term is quadratic in terms of its variable. Hence, in accordance with the equipartition theorem, $\frac{\mathrm{M}^2}{2\mathrm{m}} = \frac{K_B T}{2}$ and $\frac{\kappa\delta z^2}{2} = \frac{K_B T}{2}$.

Using the theorem, the effective temperature of the cantilever is given by $T_{eff} = \frac{\kappa(\delta z)^2}{K_B}$.

In the equipartition theorem, the value of spring constant and the mean square of the oscillator displacement are used to estimate the temperature of the oscillator. The approximated value of RMS of random oscillations of an oscillator can be deduced directly from the raw signal of thermal noise deflection of the cantilever.

A second method of measuring the RMS displacement of the cantilever is the power spectral density function by which the integrated area under the positional power spectral density (PSD) is equivalent to the mean square amplitude of the oscillations. The values of RMS and the mechanical quality factor of the cantilever (Q) can be obtained by fitting the experimental data to the power spectral density of a damped harmonic oscillator(*8*)

$$m\frac{d^2Z(t)}{dt^2} + \frac{m\omega_0}{Q}\frac{dZ(t)}{dt} + kZ(t) = F_L \qquad [3.5]$$

Where m is the oscillating mass, ω_0 is the angular resonance frequency, Q is the mechanical quality factor, k is the spring constant, Z is the displacement of the oscillator and $F_L(t)$ is Langevin force representing the thermal noise force.

In general, Langevin force is frequency independent, thus, the power spectrum of the force has a white spectrum distribution(*9*). Eq.3.5 can be solved by using Fourier transform, $X(\omega) = \int_{-\infty}^{\infty} Z(t)e^{-i\omega t}dt$, by which Eq.3.5 can be reformulated in the frequency domain as follows

$$-m\omega^2 X(\omega) + i\frac{m\omega\omega_0}{Q}X(\omega) + kX(\omega) = F_L \qquad [3.6]$$

Hence, the displacement of the cantilever in the frequency domain is given by

$$X(\omega) = \frac{F_L}{m\left(\omega_0^2 - \omega^2 + i\frac{\omega\omega_0}{Q}\right)} \qquad [3.7]$$

In principle, the power spectral density of a signal can be defined by the squared magnitude of the Fourier transform of the signal(*10*), $|X(\omega)|^2$ in which $|X(\omega)|^2 = X(\omega)\times X^*(\omega)$ where $X^*(\omega)$ is the Fourier transform complex conjugate. Thus, the power spectral density of thermodynamic noise of the cantilever displacement, S_Z, is

$$S_z = \left\langle |X(\omega)|^2 \right\rangle = \frac{\left\langle |F_L|^2 \right\rangle}{m^2\left[\left(\omega_0^2 - w^2\right)^2 + \frac{\omega_0^2\omega^2}{Q^2}\right]} \qquad [3.8]$$

Using the fluctuation dissipation theorem, the power spectrum of Langevin force (*9*), S_F, is

$$S_F = \left\langle |F_L|^2 \right\rangle = 4\gamma K_B T \qquad [3.9]$$

Where $\gamma = \frac{m\omega_0}{Q}$.

Combining Eq.3.8 and 3.9 yields

$$S_z = G_w^2 S_F \qquad [3.10]$$

Where G is the transfer function.

Eq.3.8 can be expressed by taking Eq.3.9 into consideration, giving

$$S_z = \frac{4\omega_0^3 K_B T}{Q\kappa\left[\left(\omega_0^2 - w^2\right)^2 + \frac{\omega_0^2\omega^2}{Q^2}\right]} \qquad [3.11]$$

Using Eq.3.11, the peak value of thermal noise spectrum at the resonance frequency is $\frac{4K_BTQ}{\kappa\omega_0}$. This equation can be used to find the effective temperature as illustrated in Figure 3.2

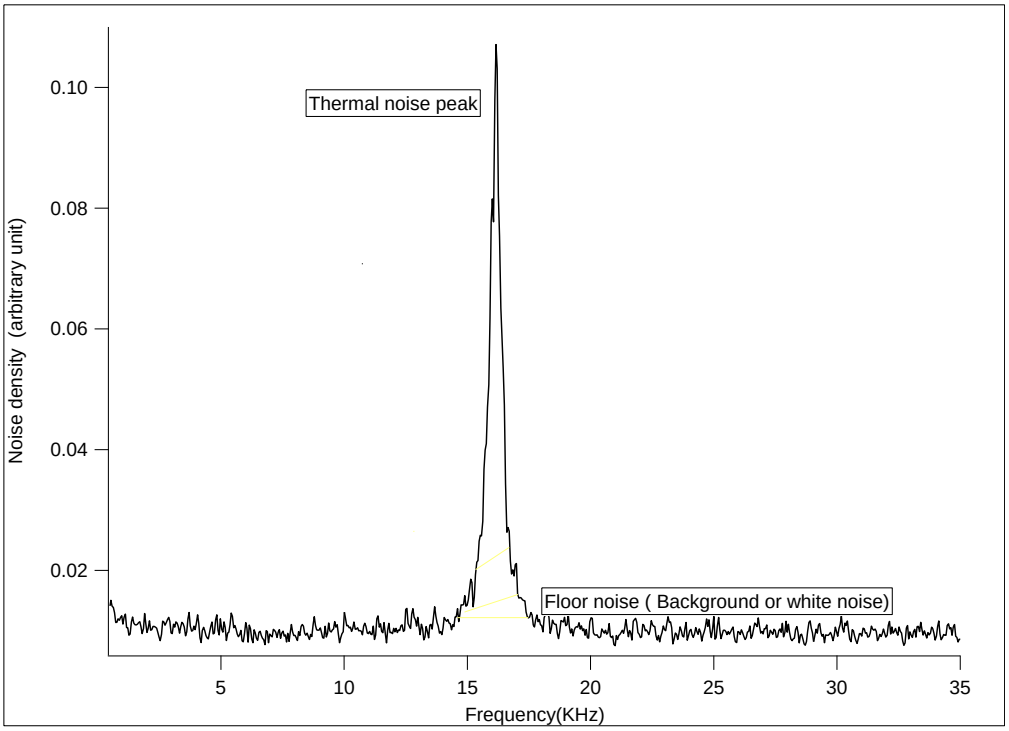

FIG.3.2 Power spectral density of a cantilever. The peak represents the thermodynamic noise and the flat line is white noise.

In order to calculate the RMS fluctuation (δZ) of a cantilever, one can use Parseval's relation, $\int_{-\infty}^{\infty}\langle \delta z^2 \rangle dt = \int_{-\infty}^{\infty}\langle |X(\omega)|^2 \rangle d\omega$, which states that the time domain and frequency domain of a signal have the same energy. Thus, the average mean square of a cantilever random thermal oscillation can be defined as

$$\delta z^2 = \frac{1}{2\pi}\int_{-\infty}^{\infty} S_z d\omega \qquad [3.12]$$

Substituting Eq.3.11 into Eq.3.12 yields

$$\delta z^2 = \int_{(\omega_0-\frac{\Delta\omega}{2})}^{(\omega_0+\frac{\Delta\omega}{2})} \frac{4\omega_0^3 K_B T(d\omega)}{Q\kappa 2\pi\left[\left(\omega_0^2 - w^2\right)^2 + \frac{\omega_0^2\omega^2}{Q^2}\right]} \qquad [3.13]$$

Most oscillation power of the cantilever is concentrated at its fundamental mode (the first peak in the power spectral density of the cantilever oscillation) (*6, 7*), see Figure 3.2. Integrating over all frequencies of bandwidth ($\Delta\omega$), Eq.3.13, of the first peak gives δz^2 by which the RMS can be calculated.

3.3 Review of thermal noise cancellation methods

Many researchers have realized the effect of thermodynamic fluctuation of AFM cantilevers and its role in limiting force sensitivity. Many approaches and techniques have been proposed in order to minimize the impact of thermodynamic fluctuations of AFM cantilevers. This review is structured mainly around two respects relevant to AFM cantilevers.

3.3.1 Modification of the cantilever properties or its surroundings

1. **Operating at cryogenic temperature**

   One method of reducing the thermal fluctuations of the cantilever would be to operate the AFM at low temperature. According to the equipartition theorem, the RMS of the cantilever response to

thermal oscillation is proportional to the temperature of the medium in which the cantilever is placed, Eq.3.3.

However, in the case of biological samples, significant reduction of the experimental temperature is not always possible, due to the fact that the cryogenic temperature alters some biological properties of the specimen, moving away from physiological conditions(*1*). Moreover, physiological experiments are usually carried out at a defined range of temperature. For instance, if the experiment is performed in water below $0^0 C$ the water will freeze. Therefore reducing the temperature to cryogenic temperatures is not practical.

2. Reducing the cantilever dimensions

Hansma's group (*11*) showed that, by using a small cantilever, but with a spring constant as low as that of longer cantilevers, it is possible to lower the measured force limit. The minimum detectable force limited by the thermal impact can be rewritten in terms of the coefficient of viscous damping factor γ (*12*).

$$\delta F = \sqrt{4 k_B T \gamma \Delta w} \qquad [3.14]$$

Where, Δw is the detection bandwidth.

In order to lower the minimum detectable force, either γ or the temperature of experiments must be lowered. γ can be reduced by decreasing the size of the cantilever.

However, small-sized cantilevers suffer from several practical drawbacks. One of them is that use of these cantilevers on normal AFM heads is difficult because they require high aperture lenses to focus the light onto the back of the cantilever and there is not

enough space(*13*). Additionally, these cantilevers are not yet commercially available, and require expensive facilities to produce.

3.3.2 Coupling the cantilever to an external dissipative force

The coupling between external forces and a moving AFM cantilever via a feedback system in order to control its Brownian motion has been of a major interest of researchers in the field of ultra-sensitive force measurement. The approaches used to suppress the thermal motion of the cantilever fall into three categories.

1. Magnetic force

Magnetic force feedback has been exploited to control the motion of the cantilever and so reduce instability in cantilever position(*14*). A small magnet was glued onto the cantilever so as to magnetize the cantilever and provide an external magnetic field, induced by a coil(*15*), used to damp the undesired fluctuations of the cantilever, Figure 3.3.

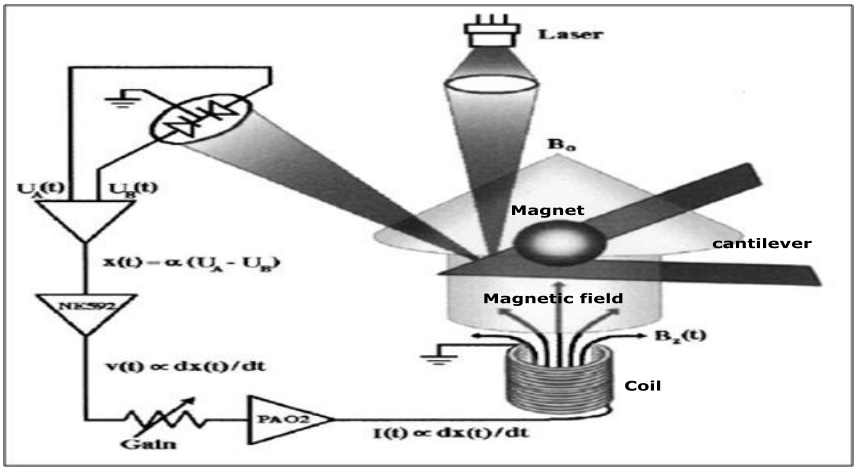

FIG. 3.3 Illustration of the feedback system used to control the thermal oscillation of cantilever using magnetic force(*15*).

Obviously, this approach is difficult to use because it requires a special setup, and the cantilever is prone to damage while mounting magnets. It is also limited by the strength of the magnetic field that may be applied, and by the speed with which the magnetic field can be adjusted (due to hysteresis and inductance in the magnetic coils)(*16*). The best cooling of a cantilever with a spring constant of 0.12 N/m achieved via using magnetic feedback force was to 25 K with an environment temperature at 295 K in air(*15*) and to 1.6 K starting from 10 K in high vacuum for a cantilever with a stiffness of 0.028 N/m(*17*).

2. Electromechanical force

Cooling of a cantilever could be achieved via a force created by the electrical field energy stored in a capacitor. The experimental setup of this approach is composed of a conducting cantilever placed a distance (y) from a rigid conducting plate connected to a resonant electric circuit, Figure 3.4. The cantilever and the plate act as parallel plates of a capacitor with a capacitance of C_c.

The resonant circuit is a radio frequency (RF) circuit consisting of an inductor with an inductance of L_0 and a capacitor with capacity of C_0. The frequency of the resonant circuit is given by (*18*)

$$\Omega = \frac{1}{\sqrt{L_0(C_0 + C_c)}} \qquad [3.15]$$

The fluctuations of the cantilever modulate the overall capacitance of RF circuit leading to changes of resonant frequency of the circuit

thereby changing the voltage applied to the capacitor C_c. If the applied voltage across C_c to maintain the setpoint is V_{rf}, the force experienced by the cantilever and the rigid plate (C_c plates) can be described by(*18-20*)

$$F = \frac{C_c V_{rf}^{\ 2}}{4y} \qquad [3.16]$$

Where V_{rf} depends on Ω.

If the circuit resonance frequency and the applied force are set so the resulting force opposes the cantilever motion, the cantilever fluctuation can be reduced(*20*).

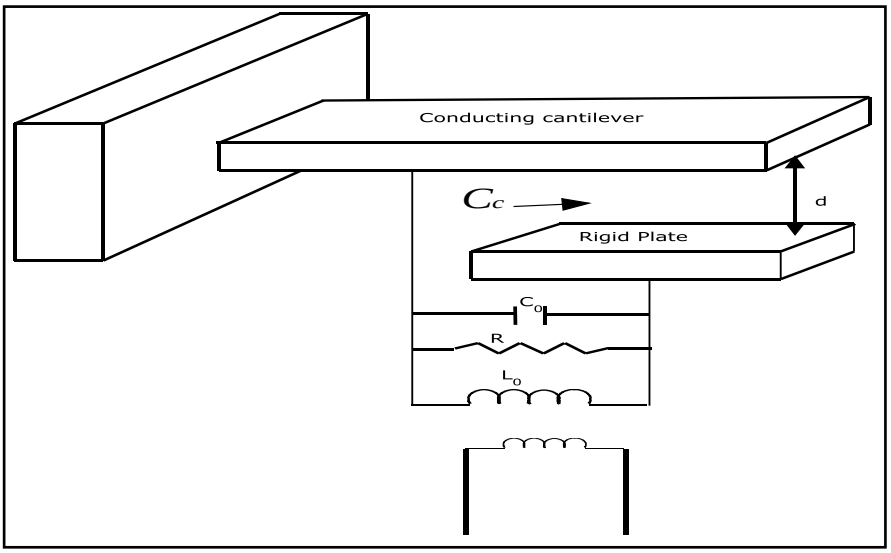

FIG.3.4 Schematic of the layout used to reduce the thermal noise of the cantilever using RF circuit.

There are some drawbacks associated with using such a technique to cool an oscillator. First, the use of a miniature cantilever requires an ultra-sensitive excitation and detection system for the cantilever vibration creating a design challenge (*21*). Second, the maximum cooling achieved was only 45 K(*18*). Third, the use of such a setup

is still limited for performing force spectroscopy experiments because the presence of an object in the gap will change the capacitance.

3. Optomechanical force

The concept of light-induced force and its effect on the dynamics of a compliant oscillator is well established (*8, 22-24*). When a beam of coherent light (laser) is incident on a mechanical oscillator such as an AFM cantilever, the amplitude of the mechanical oscillation of the oscillator is affected. Changes in the oscillator amplitude are due to coupling the spring to photons of light by means of optomechanical forces generated from radiation force or photothermal force or both. The radiation force (photon force) is due to the momentum change of photons reflected off the cantilever backside whereas the photothermal force is a result of absorbed photons by which optical energy is transformed into mechanical energy via the bimetallic effect. This process will be described in detail in chapter 4.

The optomechanical impact of light, either directly as radiation force or indirectly as photothermal effect were used to cool a cantilever actively controlled through a feedback circuit. The setup used in such an experiment (depicted in Figure 3.5) comprises a miniature optical cavity similar to that in a Fabry-Perot resonator (FP) where a resonant cavity is formed by two highly parallel and reflecting mirrors. In Figure 3.5 a miniaturized resonator is made of a movable mirror constructed by gluing a high reflecting mirror on a flexible spring(*25*) or coating a cantilever with a high reflecting film(*26*) and a rigid semitransparent mirror. The rigid mirror is aligned to be perfectly parallel to the movable one (cantilever). The purpose of

using Fabry-Perot resonator is to measure a cantilever displacement(*27*).To date the best displacement sensitivity achieved by FP is 10^{-18} m for a bandwidth of 100 Hz(*28*).

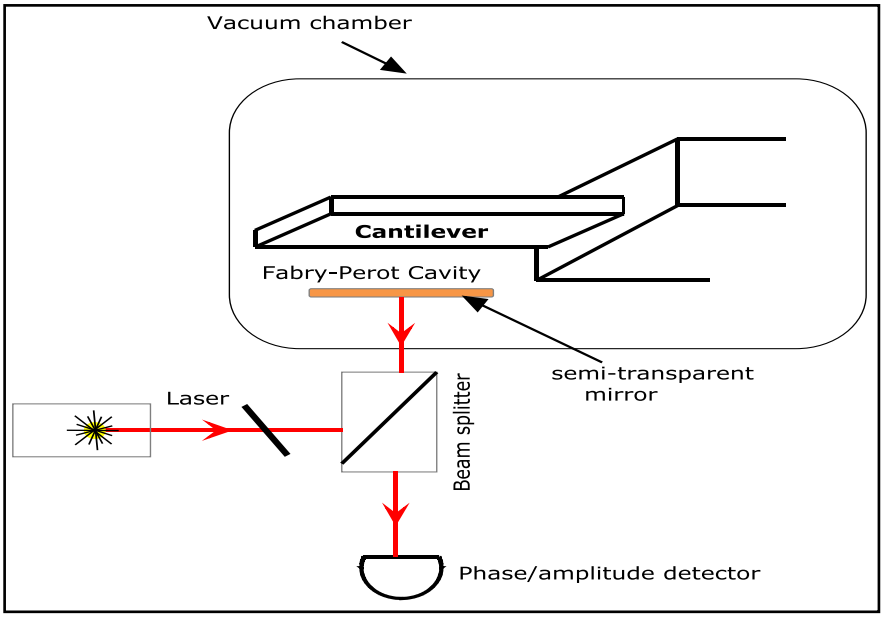

FIG.3.5 Schematic figure of the experimental setup for cooling the cantilever by radiation pressure.

Changes in the cavity length induced by the thermomechanical noise of the cantilever (the movable mirror) lead to a phase shift in cavity resonance frequency (*27*). The shift in phase is(*29*)

$$\delta\phi = \frac{8\chi\delta x}{\Psi} \qquad [3.17]$$

Where δx is the displacement of the cavity length, ψ is laser wavelength and χ is the cavity Finesse, which is a measure of the roundtrips made by a photon before escaping the cavity and by which the resolution power of FP can be determined. Therefore, thermodynamic noise would be measured via variations of the light phase. Optical cooling strategies may fall into two categories: active (cold) cooling and passive (self cooling or backaction).

In active cooling, the forces induced by light and applied onto the cantilever are controlled by an active external electronic feedback circuit. The variations of light phase are fed back to the feedback system by which the intensity of a second laser is adjusted or modulated to provide the cantilever with a sufficient force to control its thermal oscillation(*29-32*). Observations of optical cooling of a micro-oscillator placed in a high finesse cavity were reported. Using the active cooling strategy, the oscillation of oscillators has been frozen to 135 mK from 295 K(*33*) and to 5 mK starting from 4 K(*34*).

On the contrary, passive cooling does not require an external feedback loop. It depends only on the forces generated inside an optical cavity (FP) by the light. The change of the mirror position due to the thermal noise of the microcantilever results in changing the forces induced by the laser radiation. Cooling occurs as a result of the time lag between the response of the oscillator to the force and the thermomechanical motion of the oscillator(*35-37*). In pioneering work, Hohbereg et al (*26*) demonstrated that the passive cooling by photothermal force can provide cooling to 18 K starting from room temperature. In recent experiments, self cooling of a micromirror by radiation pressure forces, in a high finesse optical cavity within FP, has made it possible to lower the micromirror temperature to 2.9 mK from a starting temperature of 2 K (*35*) or to 10 K from room temperature(*38*). Most of these experiments have been directed at detecting gravitational waves and achieving the quantum ground state of the oscillator(*39*).

In terms of measuring forces at or near a surface, this setup is inadequate as the presence of a sample in the optical cavity prevents the use of the static mirror thereby destroying the working principle of the system.

Contrary to the previous attempts that rely on doing the experiment in vacuum and by forces that are stored inside an optical cavity, Yanagida(*4*) used an external feedback circuit based on the radiation pressure of laser to control position of an ultra-soft cantilever (0.1 pN/nm) in aqueous solutions. Although fabrication of such a cantilever and mounting it on an AFM require more attention and effort, the thermal fluctuations of the cantilever was improved to approximately 1 nm in RMS. However, such a cantilever is not available commercially at present.

3.4 Apparatus and experimental design

In the following section, the experimental setup designed to actively damp the cantilever thermodynamic fluctuations, and hence cooling it, is described. This setup is referred to as CD-AFM and this term will be used throughout the thesis.

All measurements have been taken using a modified AFM head based upon a commercial AFM system (Veeco Multimode with Nanoscope IV controller) and performed in Milli-Q water (18 MΩ). The modified head has a standard optical beam deflection system, but the original laser diode has been replaced with a focusing lens into which an optical fiber feeds two separate lasers, Figure 3.6. The system was designed at University of Leeds, School of Physics and Astronomy by Simon Connell.

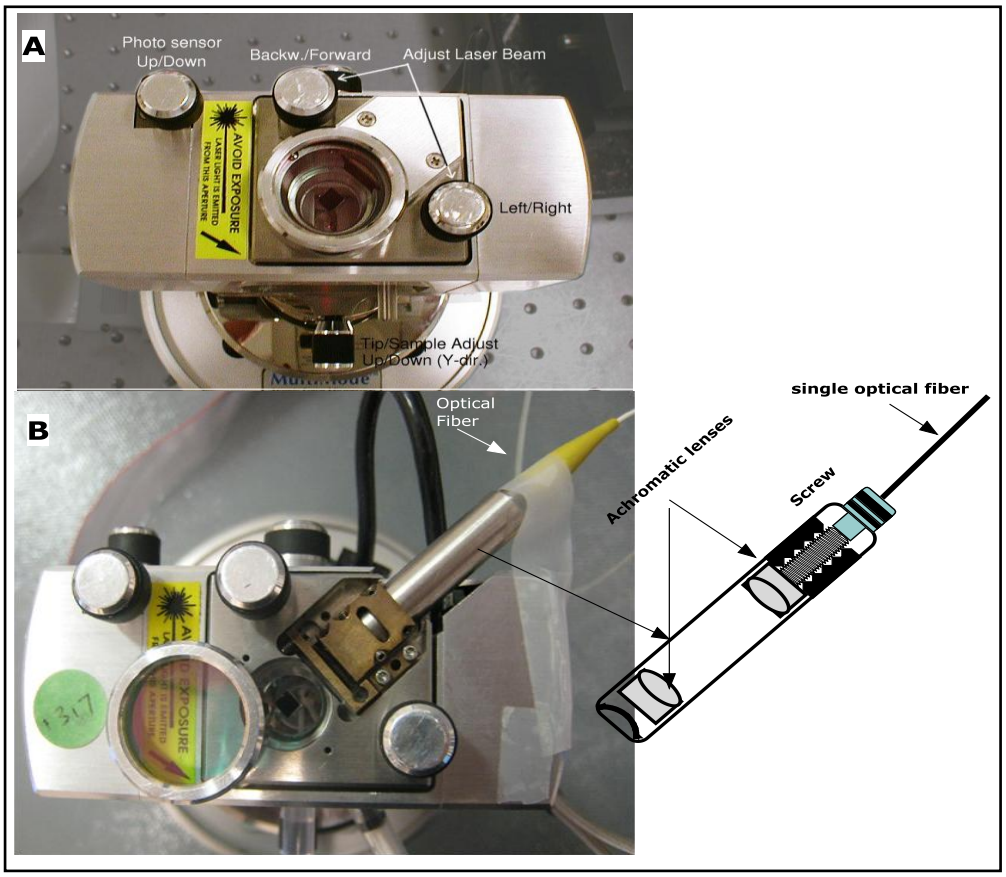

FIG.3.6 Illustration of a standard AFM head (A) and AFM head used in the CD-AFM system (B).

Two laser diodes, 780 nm and 670 nm, were required. The 670 nm laser (LD1) (HL6722G-Hitachi 5 mW, Edwards Optics, 670 nm), is used to provide the position of the cantilever with a high degree of accuracy and the 780 nm laser (LD2) (HL7851G, 50 mW, 780 nm, Hitachi), provides the radiation force which is required to dampen the thermal oscillation of the lever. These are combined using a Power Combiner (Oz Optics) and sent down a single mode optical fiber to the AFM head. This arrangement was necessary due to the need for keeping the AFM head compact and useable as a normal AFM. The output of the fiber, the laser beam, is collimated and then focused on the back of the cantilever using achromatic lenses, diameter 6 mm, placed in an adjustable tube to control their separation distance. The use of achromatic lenses is essential to correct

the focal lengths of the two wavelengths fed into the AFM head, as normal lenses have differing focal length for different wavelengths and hence focusing the two laser radiations on the cantilever. A dichroic mirror was employed in place of the normal mirror to reflect the 670 nm laser into the split photodiode detector but transmit the 780 nm beam, diverting the high power laser from the photodiode and dumping it in the body of the AFM head, Figure 3.7.

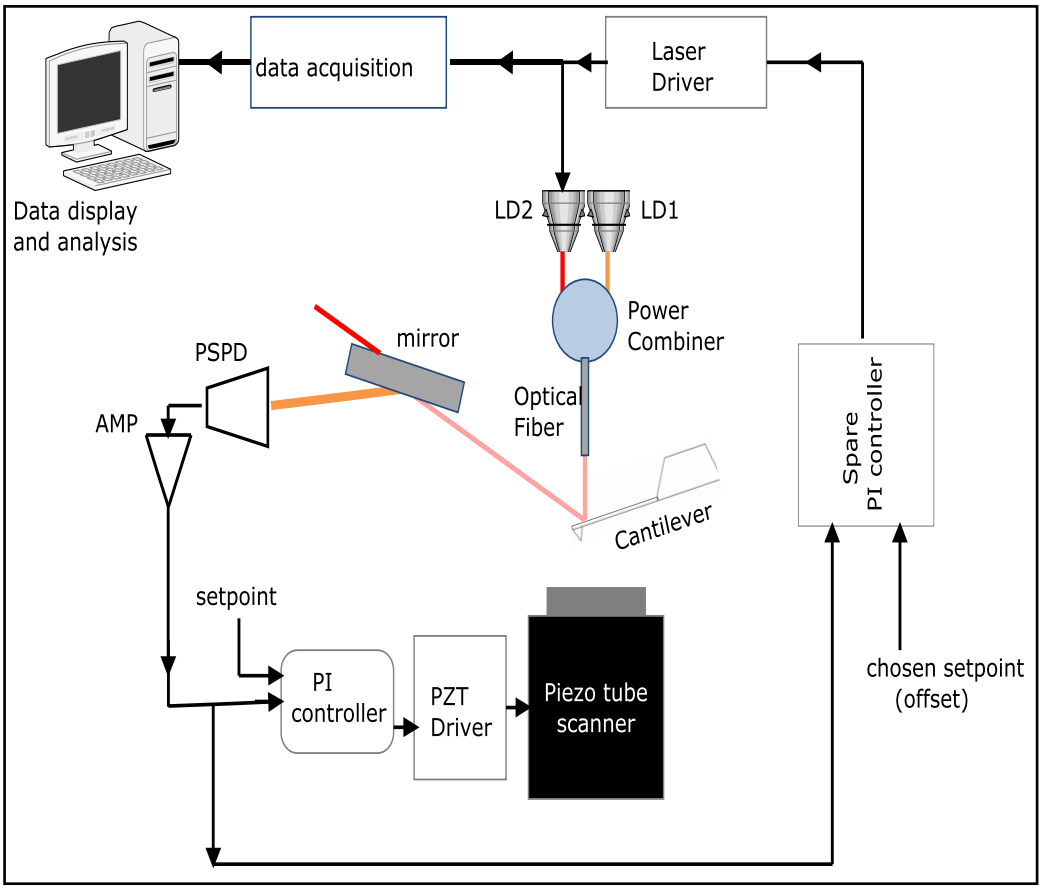

FIG.3.7 Schematic diagram of the thermal cancellation unit used in CD-AFM.

The raw photodiode voltage was collected through a National Instruments PC capture card controlled via Labview 6 software (custom written by Masaru Kawakami, University of Leeds). The deflection voltage was captured at 200 kHz for as long as the capture card buffer memory

allowed, usually 2 seconds. Igor Pro software (Wavemetrics, Lake Oswego, Oregon,USA)) was used to post-process the deflection measurements and to determine a noise spectrum using the standard power spectral density (PSD) function.

The deflection signal is amplified by a low noise, high bandwidth 10x gain stage before being sent to a digitally controlled hardware feedback circuit in the Nanoscope IV controller (Veeco). This circuit compares the incoming deflection signal with a setpoint (reference level) and outputs a voltage according to the feedback parameters. The output from this is sent through a further variable gain stage to a laser driver circuit designed for DVD writers (DBDL 200 T/S, Microlaser Systems). This can modulate the power up to 50 mW within 2 nanoseconds (measured but not shown).

To operate the device, the average power of the ψ=780nm modulation laser (LD2) must be set to approximately 50% full power. This allows for either an increase or decrease in the laser power, to counteract fluctuations up and down. This is achieved by switching the CD-AFM electronics on when the deflection is below, or negative of, the reference level. In this position the feedback circuit is outputting a zero signal. The deflection is then slowly increased by adjusting the photodetector's vertical position so that the deflection voltage approaches the reference level. When it reaches and passes the reference level the feedback circuit attempts to keep the cantilever deflection at the reference level by increasing the laser power, driving the lever back down. The photodetector adjustment then continues until the laser is at 50% full power. The current sent to the laser diode is monitored and displayed on the front panel of CD-AFM to aid this procedure, Figure 3.8.

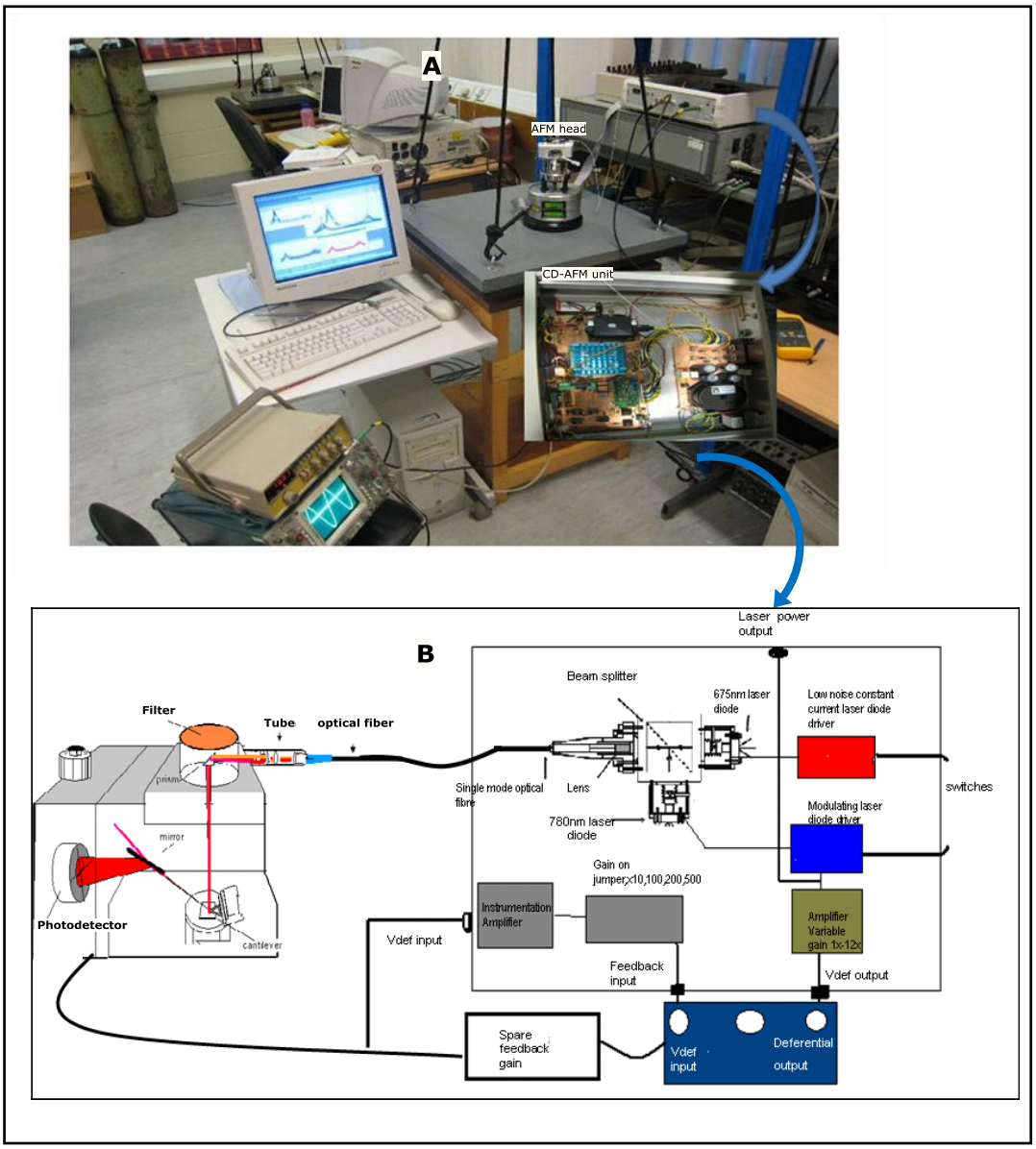

FIG.3.8 (A) The CD-AFM system. The main component is the CD-AFM unit connected with a modified AFM head via an optical fiber. (B) A block diagram of the CD-AFM unit.

The feedback and electronic stage gains for each cantilever must then be adjusted to achieve optimum damping. The initial analogue gain stage can be set to x1, x10, x100 and x500. The digital proportional and integral feedback gain have a range of 0 to 120, and the final gain stage is variable from x1 to x12. This wide range of feedback gains reflects the different laser powers needed in different environments to drive the huge variety of

cantilevers that are commercially available. For example, much higher gains are required in water than air.

Three low spring constant cantilevers have been tested. Two of them are Veeco microcantilever-V shaped; microlever C (320μm in length, spring constant of 10 pN/nm and natural frequency of 8 kHz in air) and microlever D (220μm in length, spring constant of 30 pN/nm and natural frequency of 18 kHz in air). The third is Olympus Biolever-B (100μm in length, spring constant of 6 pN/nm and natural frequency 13 kHz in air). All of them are coated with a layer of gold, Figure 3.9. The spring constant was obtained using the thermal noise method(*40*).

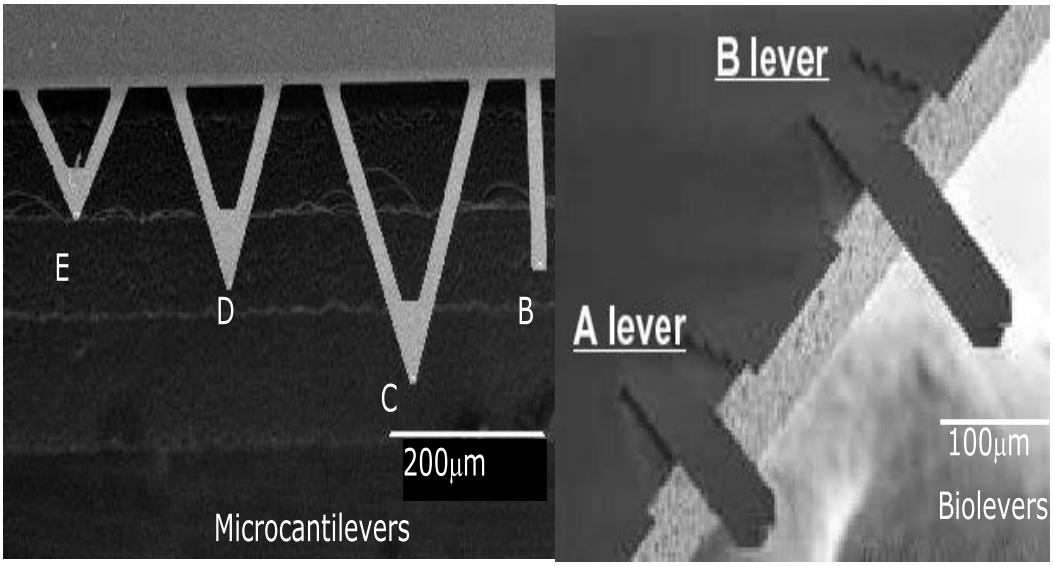

FIG.3.9 An image of the cantilevers used in this experiment.

3.5 Upper frequency limit of the system

The CD-AFM system is employed to control the deflection of AFM cantilever using a feedback circuit. The output of the feedback acts to oppose the motion of the cantilever leading to attenuating its spatial

oscillation. Operating the cantilever in a particular frequency regime can create a time delay between the cantilever response and the feedback signal that leads to instabilities in the cantilever oscillation amplitude that affects the force spectroscopy measurements. Moreover, introducing a phase lag in the feedback system used to maintain the setpoint can induce instability in the whole system. For this reason, the system was designed to minimize phase lags. This included the removal of electronic noise and filters. As a result, when the lag is in the vicinity of 180 degrees the system will no longer suppress the cantilever oscillation, instead it will be actively enhancing the oscillation (positive feedback). In order to characterize the system performance related to its stability, we will determine the upper frequency limit at which the system can be driven.

The block diagram in Figure 3.10 shows the experimental setup used to measure lag in the system as a whole. The experiment was performed with microlevers C and D. To estimate the frequency limit, the cantilever was driven by the second high-powered laser (LD2) at different drive amplitudes with frequencies ranging from 1 Hz to 50 kHz. A sinusoidal-wave voltage (with amplitude 60,120 and 240 mV) generated from Function Generator (Thurlby Thandar Instruments, TG1304) is fed into the feedback offset (setpoint). The feedback system tries to match the variation in the setpoint by applying appropriate force to the cantilever. In this way the response of the electronics and feedback circuit are tested rather than just the mechanical response of the lever to a modulated laser. Both the driving signal and the response of the cantilever are sent to a Lock-in amplifier (Signal-Recovery 726SDSP) to measure the phase shift and the resultant amplitude.

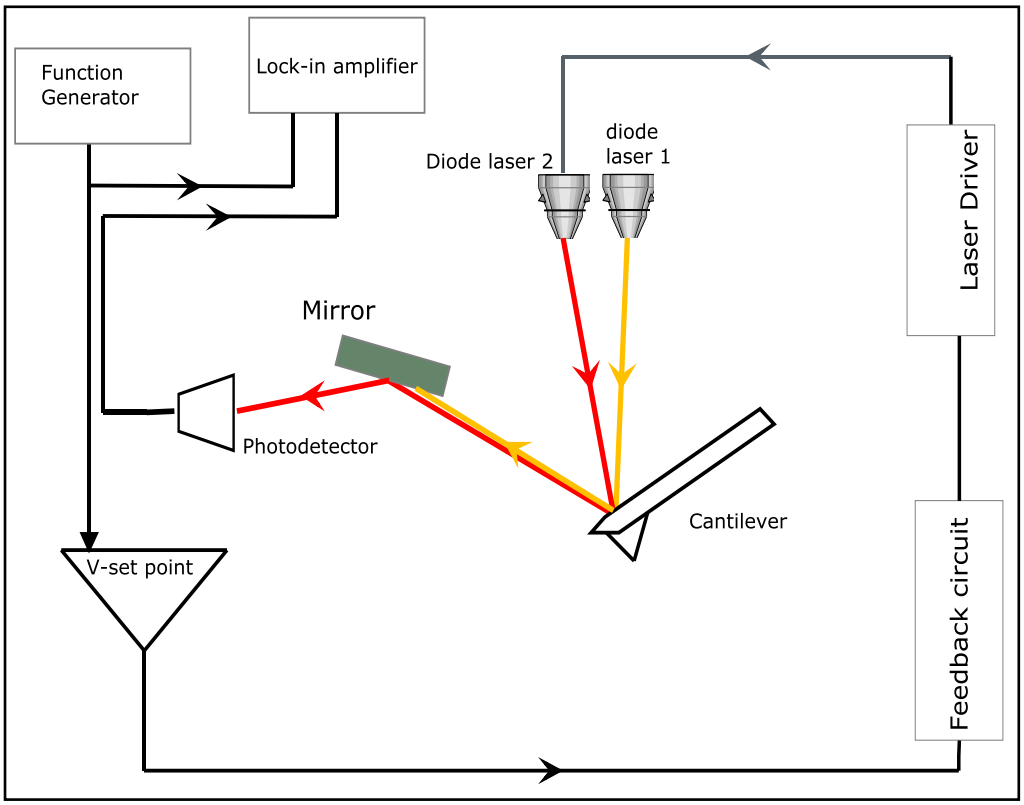

FIG.3.10 Schematic drawing of the experimeta1 setup used to determine the frequency limit in our system.

Figure 3.11 illustrates the amplitude response of the free end of the cantilever normalized to the driving amplitude of 60,120 and 240 mV at frequencies ranging from 1 to 50 kHz in water as well as the phase lag between them. The aim of the feedback loop is to maintain the setpoint value which is oscillating with the driving signal. However, the amplitude of the cantilever vibration decreases with increasing driving frequency due to dissipative tip-fluid interactions. When increasing the driving frequency the speed of the cantilever escalates. The hydrodynamic drag force, acting on the cantilever during its oscillation, is velocity-dependent. At low frequencies the impact of hydrodynamic force would be neglected and appears most significant at higher driving frequencies. The hydrodynamic force is given by

$$F = -bv \qquad [3.18]$$

Where v is the cantilever velocity and b is a constant that relies on the dimensions of the cantilever and fluid properties.

The amplitude of the oscillated cantilever starts to increase when the drive amplitude reaches a certain frequency. Figure 3.11-A exhibits the response of microlever C (10 pN/nm) to the drive amplitude and shows a rise in the cantilever response occurs at ~33 kHz when the phase lag drops rapidly to the critical 180 degree level.

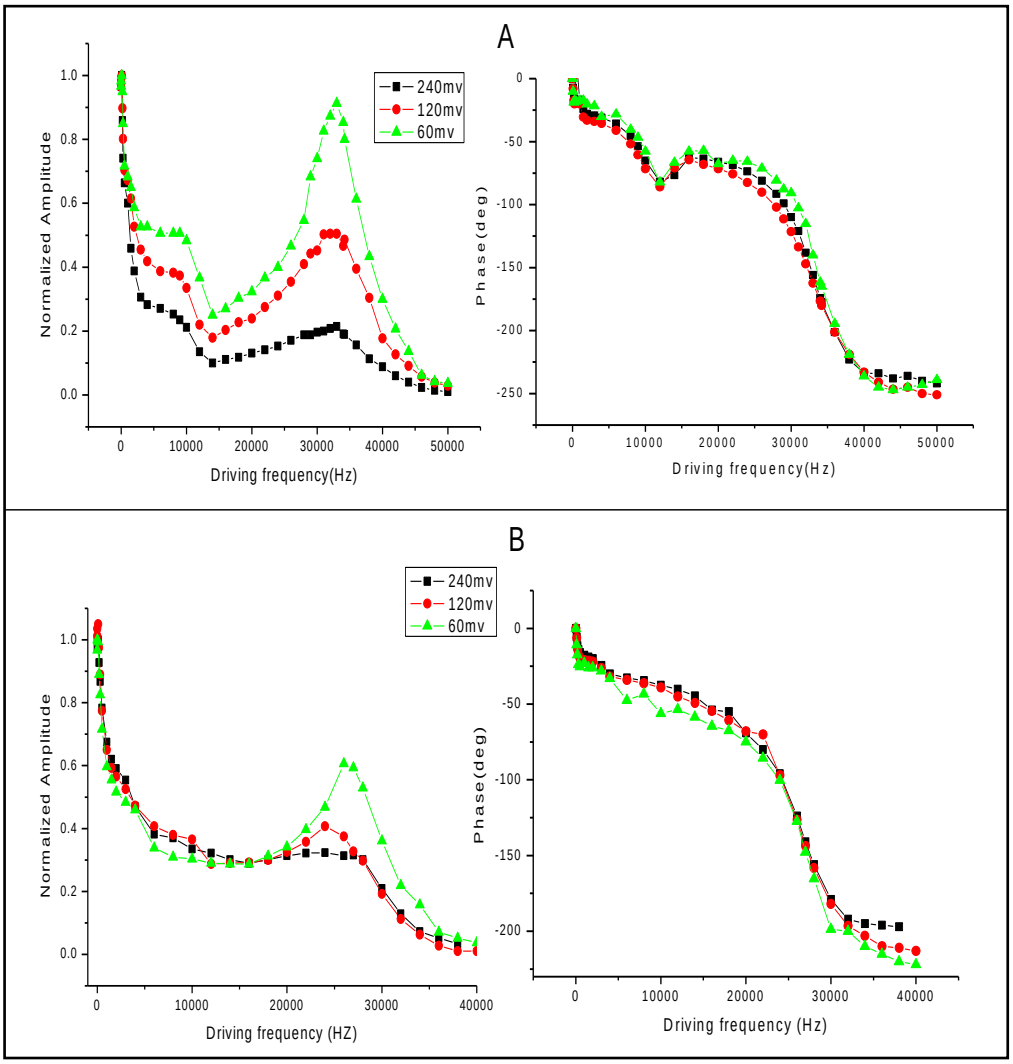

FIG.3.11 Frequency dependence of the amplitude and phase of two microlevers driven by three drive amplitudes at different frequencies. (A) Microlever C. (B) Microlever D.

The graphs indicate that the damping performance extends to approximately 30 KHz with two soft cantilevers C and D in water. Although this experiment provides a good estimate of the upper frequency limit and the system phase lag versus frequency, the scenario is artificial. In a real damping experiment the amplitude of the cantilever will be zero, and hence hydrodynamic force will be zero as well. A range of amplitudes were tested (60,120 and 240 mV) in order to characterize the hydrodynamic components but the lowest amplitude of 60 mv was required to provide a strong enough signal for the lock in amplifier to measure. However, at each amplitude the phase lag response was identical.

Microlever C (10 pN/nm) and Biolever B (6 pN/nm) are the softest cantilevers available commercially. Both cantilevers have a resonance frequency in water, 1 kHz and 2 kHz respectively, far less than the upper frequency limit of our system, hence suitable for use. Cantilevers of higher stiffness were not tested as they do not have the required force-sensitivity for high-resolution force experiments.

3.6 Optimization of optical sensitivity of the cantilevers

Most AFMs used today rely on the optical lever detection system to sense vertical deflection of the cantilever. Therefore, optimization and accurately measuring the optical lever sensitivity and spring constant of cantilevers are essential for force and position measurements.

In order to convert the photodiode output into cantilever deflection, the ratio between photodiode output voltages to the cantilever bending must be accurately known. Increase of the deflection sensitivity results in an

increased single to noise ratio (SNR) via a magnification of the output voltage of split-photodetectors. Figure 3.12 shows how the background noise level from a PSD depends upon the deflection sensitivity. Therefore, this part of the chapter has been devoted to measurement and optimization of the value of optical lever sensitivity.

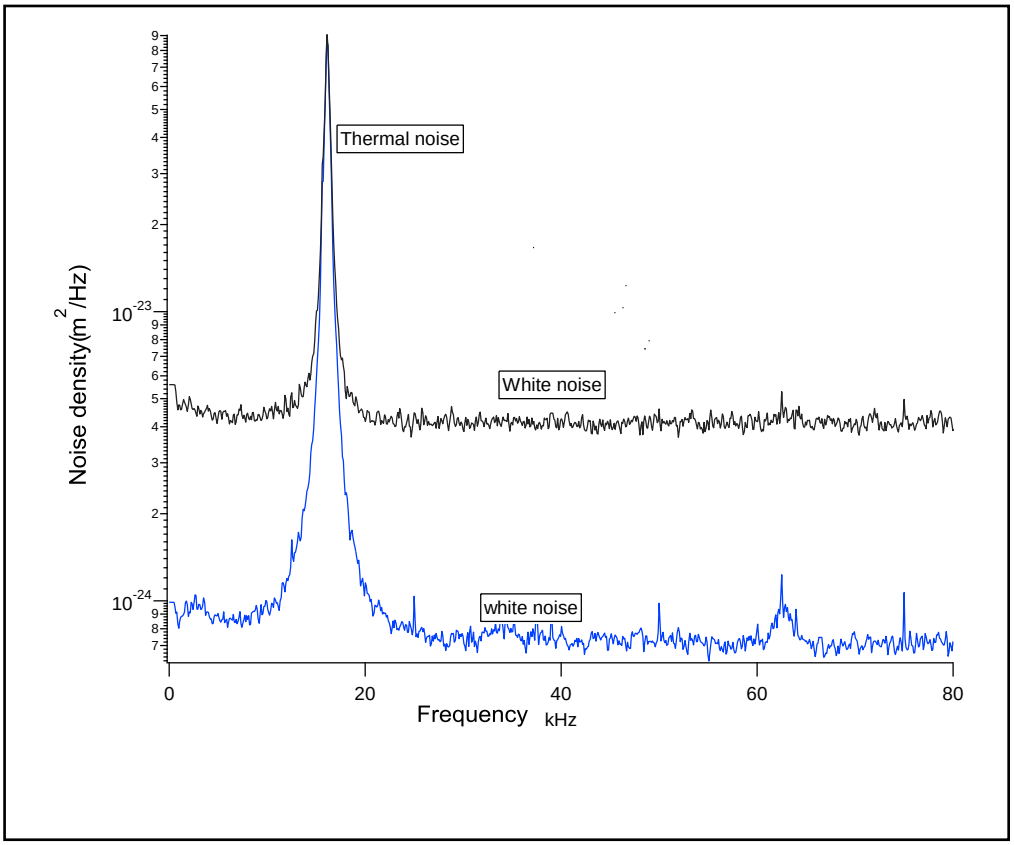

FIG.3.12 The measured noise density of cantilever D using the CD-AFM head at a deflection sensitivity of 70nm/V (or 14mV/nm) (Blue) and 160nm/V (or 6mV/nm) (Black) in air. The flat background corresponds to white noise of the system and the peak is due to thermal noise associated with the cantilever's Brownian motion. Note the thermal noise peak overlap exactly in both measurements. Also the lower noise level at 70 nm/V allows detection of the second harmonic thermal peak at 62 kHz.

In order to determine the deflection sensitivity of the cantilever the tip is pressed against a hard flat surface and undergoes an approach-retraction cycle of known distance. Use of a hard surface will result in the piezo movement being equal to the deflection of the cantilever. When the tip is in

contact with the surface, the piezo moves a known distance causing the cantilever to deflect a similar distance. During that operation, the output voltage of PSPD, as a response to the cantilever deflection, is recorded. The resulting voltage versus piezo movement is observed as a line, the slope is the optical lever sensitivity of the cantilever. Typically the optical lever sensitivity of the cantilever in a vertical direction is easily acquired by the force-distance curve in the force mode of AFM.

The deflection sensitivity (s) is defined as the change of the voltage output of the PSPD (ΔV) with respect to the vertical displacement of the free end of the cantilever (ΔZ), in the Z-direction.

$$s = \frac{\Delta V}{\Delta Z} \qquad [3.19]$$

It is worth noting that the change of the voltage output of the PSPD (ΔV) is a result of the laser spot shift (Δx) on PSPD, Figure 3.13.

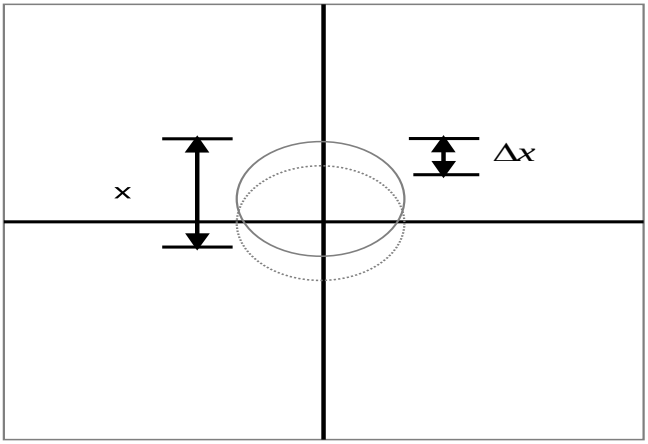

FIG.3.13 Laser spot on the PSPD, the Δx corresponds to the shift of the laser spot on the PSPD

As mentioned above, the higher the deflection sensitivity the higher the SNR. To increase the cantilever optical deflection sensitivity, we must first understand the parameters that affect it. Eq.3.19 is not adequate to

describe the parameters employed to increase the optical lever sensitivity. To satisfy these requirements, we will rewrite E.q.3.19 by assuming that the laser spot on the PSPD has a Gaussian distribution. As a result, the deflection sensitivity (*41*) can be given by

$$s = \xi \frac{d}{xl} P \qquad [3.20]$$

Where ξ is a constant related to the optics and electrical components used in this experiment, *x* is the diameter of the laser spot on the PSPD, *P* is laser power measured on PSPD, ℓ is the cantilever length and *d* is the distance between the cantilever and the PSPD.

The relationship shown above suggests that the laser power *P* and the distance between the cantilever and photodetector *d* should be maximized and *x* and ℓ should be minimized in order to maximize s.

The change of the laser spot diameter on the photodetector depends on the focusing length d_f as described in the following equation(*41*)

$$x = \frac{d}{d_f} a \qquad [3.21]$$

Where a is the diameter of the collimated laser beam. In our system the focusing length d_f of the laser beam can be changed by using an adjustable tube to control the separation distance between lenses (see section 3.4).

Eq.3.21 shows that *x* can be reduced by increasing the focusing length. The distance between the cantilever and PSPD is constant and cannot be changed. The laser spot diameter on the backside of the cantilever

depends on the focusing length. Maximization of the laser spot diameter on the cantilever will lead to a decrease in the divergence angle of the reflected beam onto the PSPD resulting in decreasing the diameter of the laser spot on the PSPD, as shown in Figure 3.14.

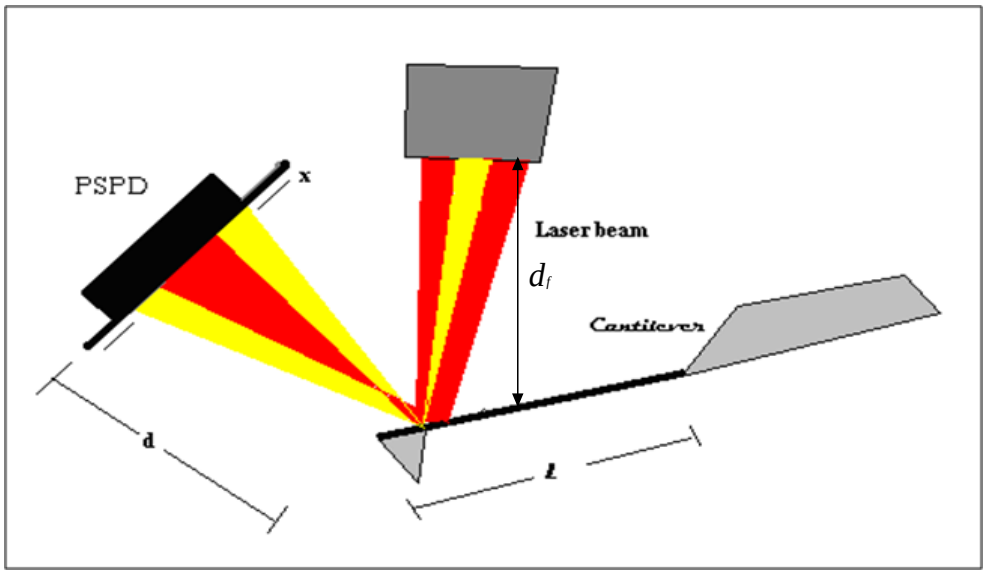

FIG.3.14 Change of a diode laser beam diameter focused on a cantilever results in different divergence of the reflected beam onto the PSPD.

However, the laser spot diameter on the cantilever should not exceed the cantilever width because some of the power of the laser beam may be lost, which will attenuate the laser power incident onto the PSPD and then s, as illustrated by Figure 3.15.

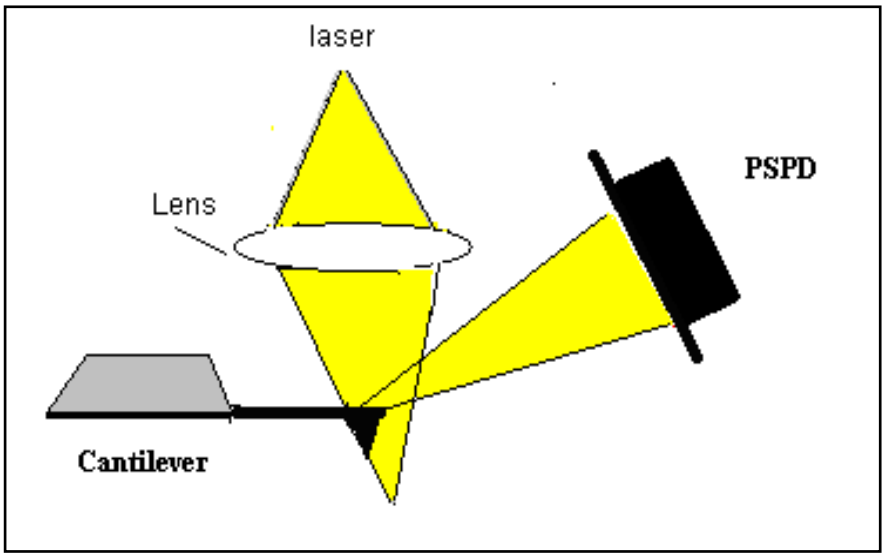

FIG.3.15 The laser beam diameter exceeds the width of the cantilever, resulting in loss of power.

The design of the system enables us to adjust the laser spot size to fit the width of the reverse side of the cantilever. Consequently, the smallest divergence of angle of the reflected beam was acquired. As a result of the above optimizations, the optical lever sensitivity has been improved more than threefold from 145 nm/V to 53 nm/V for microlever C, twofold for microlever D, from 77 nm/V to 44 nm/V, and from 27 nm/V to 14 nm/V for the Bio-lever. Using standard multimode AFM heads it is 153 nm/V, 69 nm/V and 38 nm/V for Levers C and D and the Bio-lever respectively.

3.7 Correcting Power Spectral Density scale

Power spectral density (PSD) can be used to describe the amplitude of the random oscillation of the cantilever, due to its Brownian motion, as a function of frequency. The flat part of PSD represents the white noise or background noise of the system related to the system electronic noise whereas the peaks corresponds to thermal noise of the cantilever

associated with its Brownian motion, Figure 3.2. In principle, as mentioned above, we can calculate the amplitude of the thermal oscillation of a cantilever by integrating the area under the peak but if PSD is scaled incorrectly, the measured amplitude will be incorrect.

Up until this point in the study (and during the development of the CD-AFM system since 2003) the power spectral density of the noise had only been analyzed in an internally consistent manner for a particular set-up, where the raw deflection signal is analyzed directly by IgorPro in order to obtain PSD curves. It was found that this approach resulted in inconsistent readings when it was used to compare the PSD produced by different cantilevers in air and water, and between four different Multimode AFM heads, 1819EX, 1477EX, 1423EX and the modified CD-AFM.

In Figure 3.16-A., the PSD of the cantilever thermal oscillation has been acquired at different deflection sensitivities (139 nm/v (red), 155 nm/v (green) and 170 nm/V (black) in air by changing the size of the laser spot on the reverse side of the microlever because the shape of the laser spot on the PSPD plays a significant role in increasing or decreasing the deflection sensitivity (*42*), see preceding section.

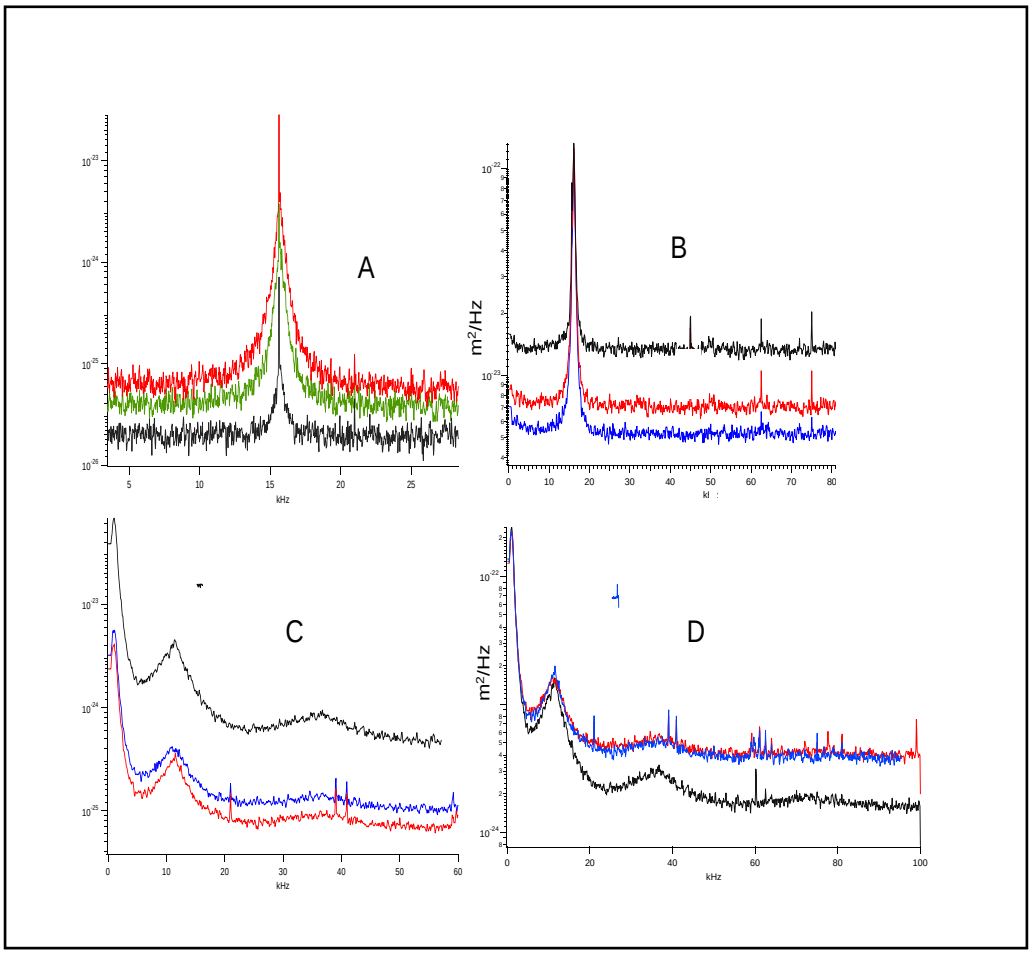

FIG.3.16 PSD of thermal fluctuation of the microcantilevers at different deflection sensitivities. (A) and (B) microlever-D in air, before and after correction of PSD measurements, respectively. (C) and (D) microlever-C in water, before and after correction of PSD measurements respectively.

It is clear that what has been acquired in Figure 3.16-A. is not correct for two reasons. First, the size of the laser spot affects SNR due to the change of deflection sensitivity, but not the area under the resonant peak of a free cantilever oscillation induced by thermal noise as the Brownian motion of the cantilever is associated with the cantilever motion not the floor noise of the system. Thermal noise is widely used to calibrate the spring constant of cantilevers; hence the absolute area under the thermal noise peak should vary only on spring constant and temperature. Therefore the size of the laser spot should not be effective. Secondly, the same curves have been acquired by the Nanoscope software and we observed no difference

between the three curves in terms of area below the curve. A similar observation had been noted for microlever-C in water, Figure 3.16-C. The thermal noise peaks should all overlay perfectly as the thermal fluctuations for a particular lever will always be the same given the same conditions of air pressure and temperature.

It was found that a discrepancy existed between PSD curves analyzed on IgorPro and captured externally via LabView and those measured by the NanoScope software. To overcome this problem, two steps were taken. First, we used the deflection sensitivity value measured independently by LabView and rejected the value measured via the Nanoscope software. The deflection sensitivity is the standard for the Nanoscope software. Since we aim to determine the optical lever sensitivity accurately and Labview records the signal via an external capture card, the optical lever sensitivity should be read by the same circuit and software. We proposed that the optical lever sensitivity must be measured outside of the Nanoscope software due to consistent errors in the measurements found when using the sensitivity determined within the AFM software.

Using Labview via the external circuit, the deflection signal and low voltage Z (LVZ) signal (the drive signal for the vertical motion z-piezo) were recorded, the deflection signal was converted into volts and the LVZ into meter (using the piezo calibration) to obtain the force-distance curve independently of the Nanoscope software, Figure 3.17. Using the new values the real deflection sensitivity is obtained, in nm/V, and was found to be consistently different to the value measured by the Nanoscope software.

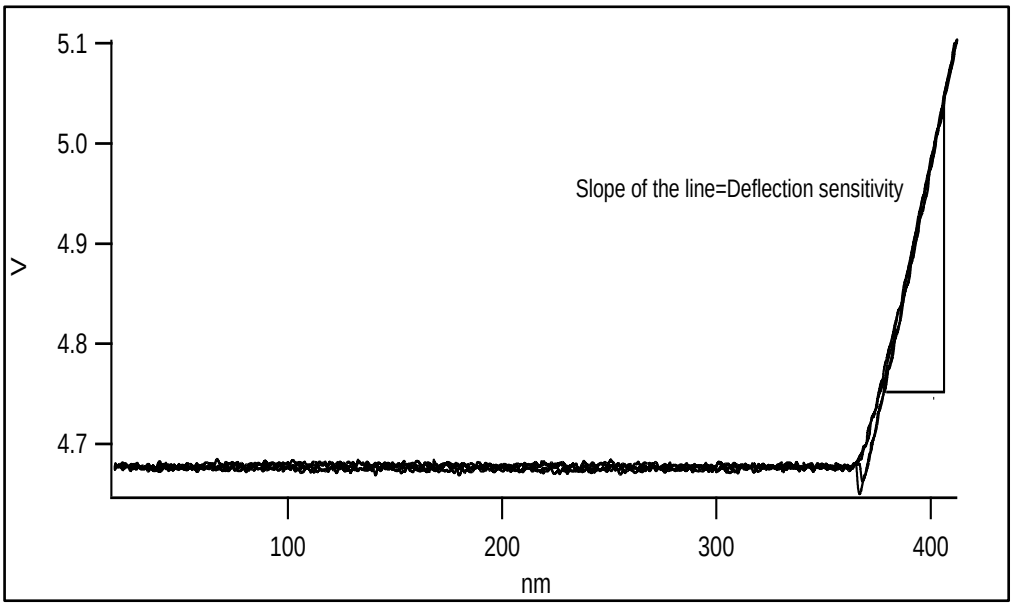

FIG.3.17 Deflection sensitivity acquired by LabView. The output voltage of the photodetector is plotted against the movement of the piezoscanner. The slope of the contact line represents the deflection sensitivity.

Second, IgorPro software can plot a PSD curve by acquiring raw data directly from LabView software. The compatibility between IgorPro and LabView software is in doubt due to errors in PSD curves obtained for the cantilever. In order to avoid that, we proposed the use of PSD function independent of LabView.

The new data obtained by the proposed acquisition method was sent to IgorPro for PSD analysis, and the noise curve now shows a good agreement with that expected (Figure 3.16-B and D). The thermal noise peaks all overlay precisely, despite measurements being taken on different heads and the deliberate placing of the laser beam in different positions on the free end of the cantilever to achieve different deflection sensitivities. Moreover, the white noise can now be measured absolutely, with m^2/Hz or $m/\sqrt{Hz}$.

3.8 Further Improvements in the single to noise ratio

In this section, my experimental efforts are aimed at further reduction of the noise floor of the CD-AFM system. As described above, the flat part of PSD curves represents what is called white noise or floor noise of the system. The CD-AFM head employs the optical beam deflection method (OBD) to sense the bending of the tip. The use of OBD involves contributions of non-thermal noise sources to optical noise measurements.

3.8.1 Shot and hop noise

A major noise source in OBD is shot noise generated in the photodiode and caused by the random fluctuations of the number of photons that arrive at the detector. Shot noise is considered white noise. For the OBD method, the power spectrum of shot noise can be given by (*41*)

$$n_{sh} = \frac{\ell x}{3d}\sqrt{\frac{2e}{\eta \Pi P_0}} \qquad [3.22]$$

Where, ℓ , d , e, η,Π , x and P_0 are the cantilever length, the distance between the cantilever and the position sensitive photodetector (PSPD), an electron charge, the conversion efficiency of photodetectors from light to current, the attenuation of laser power in its optical path, the diameter of the laser spot on PSPD and the laser power output, respectively.

Eq.3.22 predicts that n_{sh} reduces with decreasing the length of the cantilever and increasing laser power. Since the photodiode shot noise is a major source of white noise in the OBD system, we will assume that the flat line of the deflection power spectrum is a measure of shot noise.

The experimental setup enables us to control both the laser power of the diode laser (HL6722G-Hitachi 5mW, 670 nm) and the diameter of the laser beam. Figure 3.18 demonstrates the dependence of the shot noise spectrum density on laser power. The laser power increase implies a decrease in the white noise spectrum. Thus, SNR will increase. The cantilever with a longer length, 320 μm, illustrates higher noise level than that with a shorter length, 220 μm, Figure 3.18-A and B. However, when laser power exceeds 6 mW white noise level shows an increase.

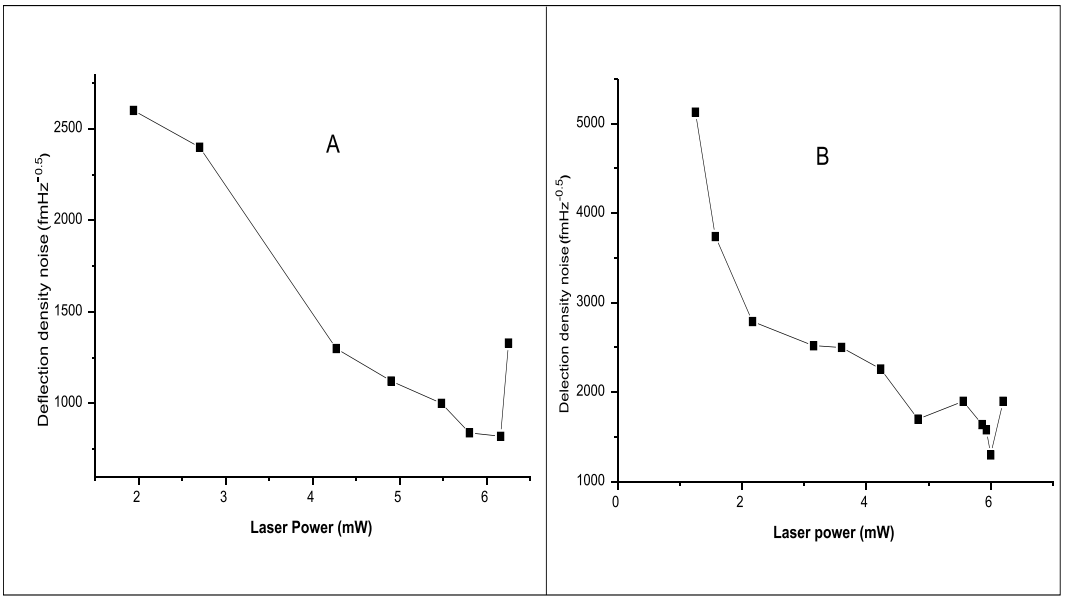

FIG.3.18 The output of laser power dependence of the microlevers deflection noise density measured in water by the CD-AFM head. (A) microlever-D, (B) microlever-C

The deflection noise increase that occurs beyond 6 mW introduces a new contribution to the overall noise level associated to the particular laser. This is due to a contribution from the mode hop noise of a diode laser, arising from fluctuations of the laser diode intensity. Under some circumstances, such as operation of a diode laser at high power, an instability of diode laser wavelength results in the optical intensity of the laser diode output fluctuating, causing oscillation of the laser spot on the PSPD, which is termed mode-hop noise (*43*). From Figure 3.18 it can be

seen that the laser can be driven too hard. The laser power was therefore reduced to the point just before mode-hop noise becomes apparent. So although this improved the random noise levels, it was not possible to further increase the laser power because of an increase of mod- hop noise. As a result, the laser power was set to 6 mW. In contrast, at low laser power quantum noise (intensity fluctuation of laser beam induced by spontaneous emission inside the laser cavity) becomes the dominate source of noise(*44*).

As mentioned in section 3.6, improvement of deflection sensitivity will help to increase the SNR. Thus, the deflection sensitivity (s) has been optimized prior to amending the laser power. In Figure 3.18-A., the noise level was optimized to be around 800 fm/√HZ in water, whereas in a normal AFM head it is more than 3000 fm/√HZ. Although we used a 5 mW diode laser with the CD-AFM head and the multimode head uses 1 mW, the maximum SUM (the sum of outputs voltage of the PSPD segments measured by PSPD of the CD-AFM head) is less than that measured by a normal head. There are several reasons for the poor SUM. One is that the attenuation of laser power is due to transmission through the optical fiber, power combiner and optical lenses used to bring the beam to the tip. A second reason is a large gap between the photodiode segments that is not smaller than the diameter of the laser spot on the PSPD. In addition, some of the 670 nm laser power is being lost through the dichroic mirror. Finally, the laser spot size may be too large, so that a proportion of the laser power spills over the edge of the cantilever.

3.8.2 Effect of optical fibre on the noise level

The optical fibre used in this experiment is a potential source of noise. It is a single mode fiber which may lead to an increase in white noise which

then deteriorates the SNR. The reflection of the beam at the end of the fiber results in fluctuations of laser intensity and so generates optical feedback noise(*41, 44*). Moreover, the use of single mode fiber diminishes and attenuates the laser power, Figure 3.19. However, this is partially compensated by the advantages of using the single mode optical fiber which is the best way to get a high quality laser beam with small divergence, aberration and a circular cross section. (*44*)

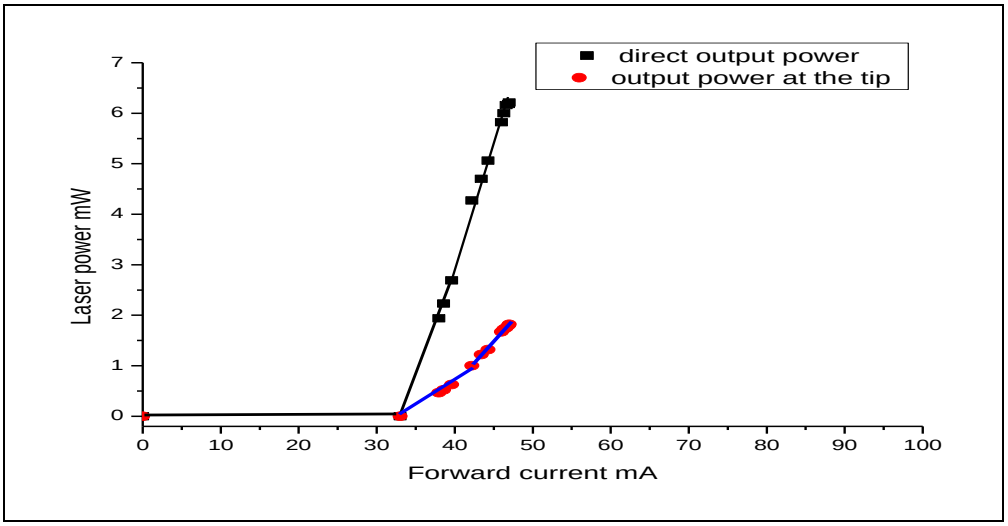

FIG.3.19 The current dependences of output power of HL6722G diode laser (LD1). The laser power measured before (direct) and after (at the tip) attenuation of the single mode fiber.

3.8.3 Noise generated by interference of the laser radiation

Although the noise source related to vibrations of the building is excluded by mounting the system on a vibration-free solid base, optical interference of the laser beam reflected from the surface and laser beam reflected from the back side of the cantilever can also have an effect on the level of the system floor noise, Figure 3.20.

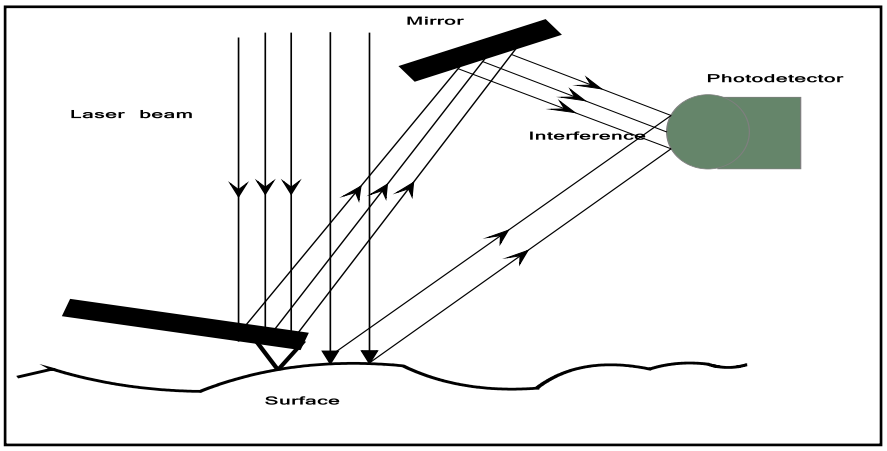

FIG.3.20 Interference of the laser beam reflected of the cantilever with that reflected of the sample surface.

The contribution of interference can be minimized by reducing laser power incident on the surface and the laser spot size on the cantilever. The diameter of laser spot dependence of the measured intensity of laser spot is illustrated in Figure 3.21. The optics used in the CD-AFM head shows that 85% of power falls away within 10 μm from the center of focus. Taking into account the width of the cantilever, 30-50 μm, and the experimental setup, which enables us to control the size of laser spot, the amount of power reaching to the sample surface is negligibly small so the additional improvement of SNR can be achieved by adjusting the size of spot to fit the width of the cantilever.

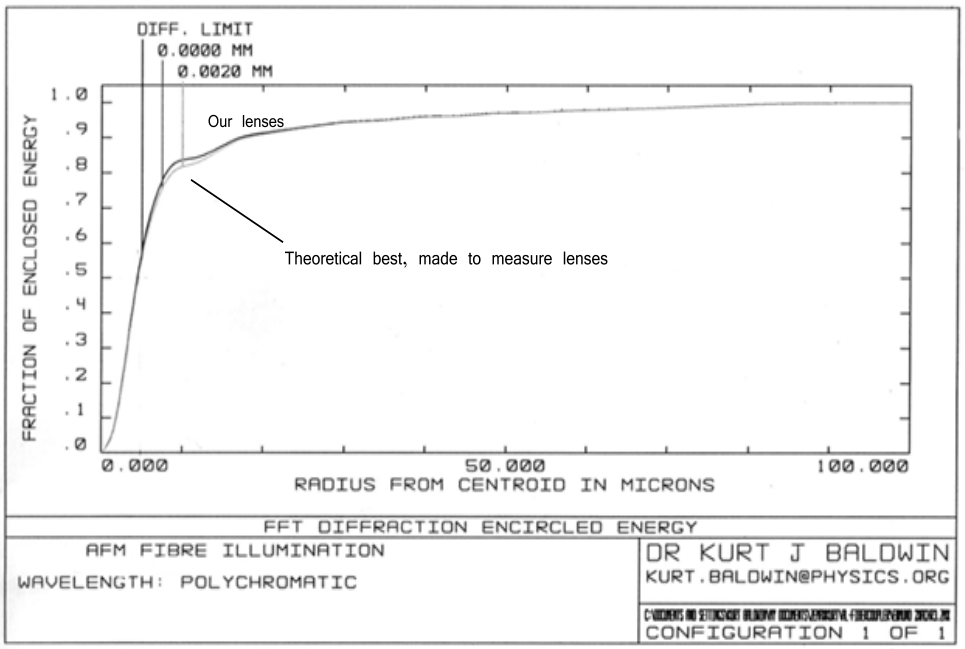

FIG.3.21 Laser spot radius dependence of the power loss of the laser spot on the cantilever. 85% of the spot power falls away at radius of 10μm.

Finally, to demonstrate the effect of reducing the noise related to the detection system, we have acquired PSD curves of a microcantilever, Figure 3.22, with different Multimode AFM heads, 1819EX, 1477EX and the modified CD-AFM. In order to cancel out the large effect of cantilever deflection sensitivity on noise level (see preceding section) the deflection sensitivity was adjusted to be constant as possible between experiments (in the range 90-100 nm/V). All the AFM heads show an identical level of thermal noise as expected but a variation of white noise level. The thermodynamic noise is independent of the AFM head used in the experiment, but the white noise is a measure of the system floor noise that depends upon the AFM head components. Since the CD-AFM head has the lowest level of the white noise compared to the others, the steps have been taken to decrease the noise are effective. The figure shows clearly the white noise level does not only depend on the deflection sensitivity.

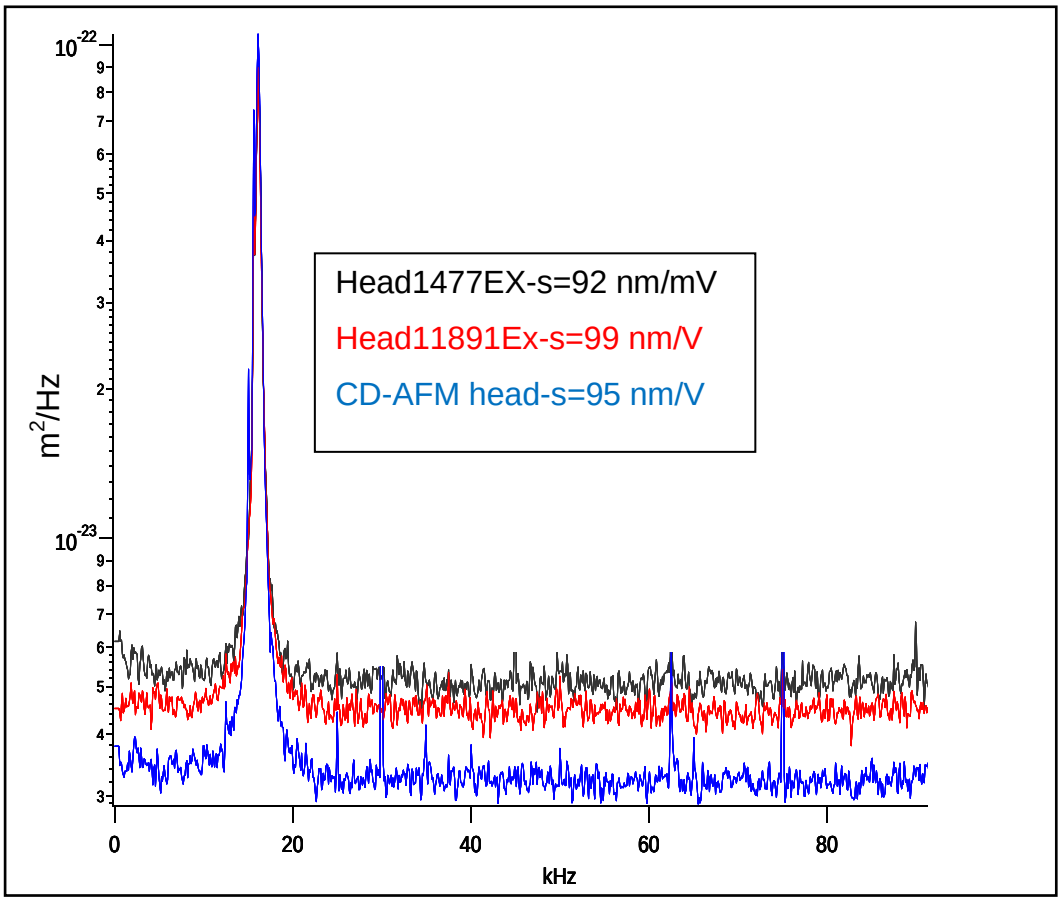

FIG.3.22 The deflection density noise of detection systems acquired by three AFM heads. The level of thermal nose is identical for all the heads under investigation. However, the CD-AFM head has the lowest level of floor noise among them.

3.9 Effect of white noise level on efficiency of the damping level of thermal noise.

Keeping a high signal to noise ratio (SNR) is essential for a number of reasons. Firstly, the resolution of AFM is not just limited by the thermodynamic noise generated by Brownian motion of the AFM cantilever. The floor noise (white noise) of the AFM detection system can set a limit on force resolution(*44*). In the case of a stiff cantilever the floor noise is the most predominant noise source but when the stiff cantilever is replaced by a softer one the thermodynamic noise becomes the dominant source.

Secondly, the 780 nm diode laser exploited to suppress the thermal oscillations of the cantilever relies on the output of a 670 nm diode laser used in the optical lever detection system, which is then fed into the feedback circuit to control damping levels. Therefore, if the deflection output signal of the 670 nm laser is contaminated with other noise arising from the deflection sensor (the random white noise background), the achievable damping level will be limited by this noise. The feedback system is therefore working to reduce noise that is not present mechanically, thereby inducing actual deflection fluctuations across the frequency spectrum where none previously existed. We cannot just filter out this random noise from the final data because we will be driving the lever with real fluctuations, and we cannot filter out the noise in the feedback circuit, because filters introduce phase lags in the system, particularly around the cut-off frequency, and phase lags are extremely detrimental to high speed feedback circuits. The white noise must therefore be reduced in the feedback system by increasing the SNR of the optical level detection system. Thus, optimization of the SNR improves the efficiency of the damping mechanism. As can be seen in preceding sections the white noise was improved, so the damping efficiency will increase.

In order to prove this idea, the damping level of the fundamental resonant peak of the cantilever, induced by thermal oscillation, has been obtained at different levels of white noise. The thermal noise of microlever-C was dampened by the radiation feedback force system. The same setup of the cancellation system, and the level of white noise as described in section 3.4-3.8, were used. It is clear that the efficiency of the cancellation system used to suppress the thermal variations of the cantilever depends on the noise of the deflection system, Figure 3.23 and 24.

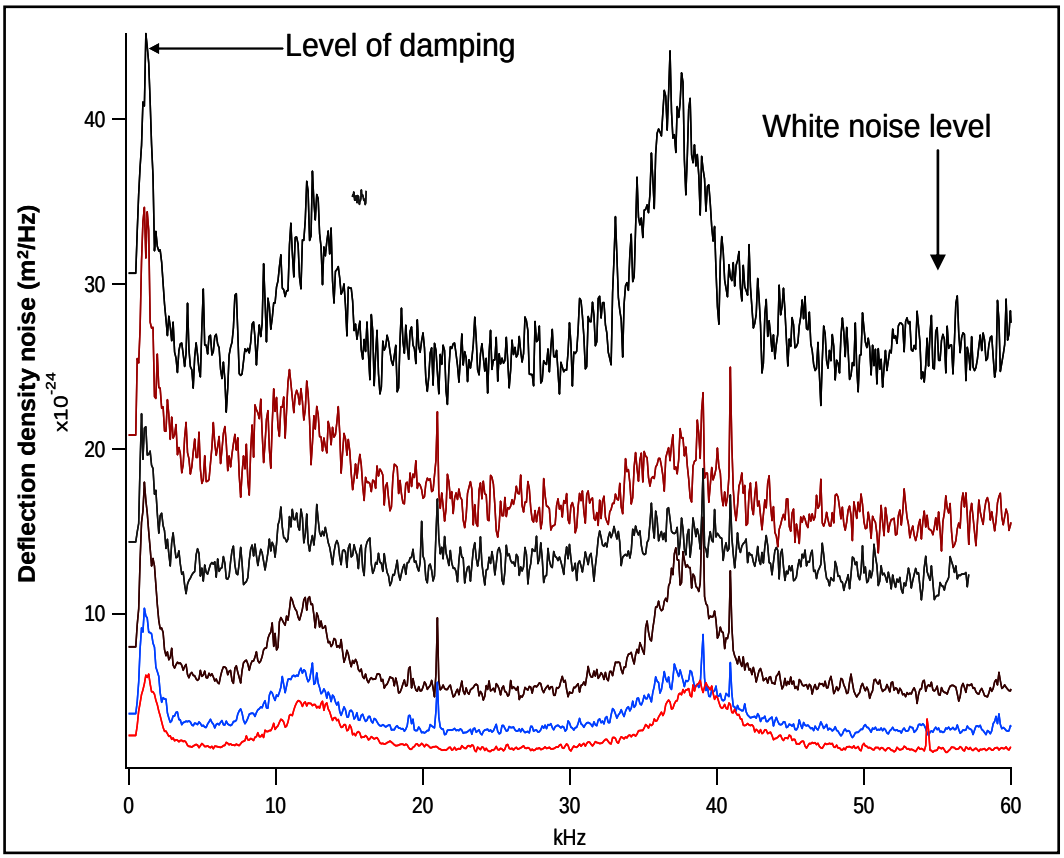

FIG.3.23. Power spectral density of a damped microlever C in water at different levels of floor noise of the CD-AFM head. The first peak represents the damped fundamental mode of the cantilever thermal noise and the flat line corresponds floor noise of the CD-AFM head (white noise). The level of damping of the thermal noise improves as a result of reducing the level of white noise.

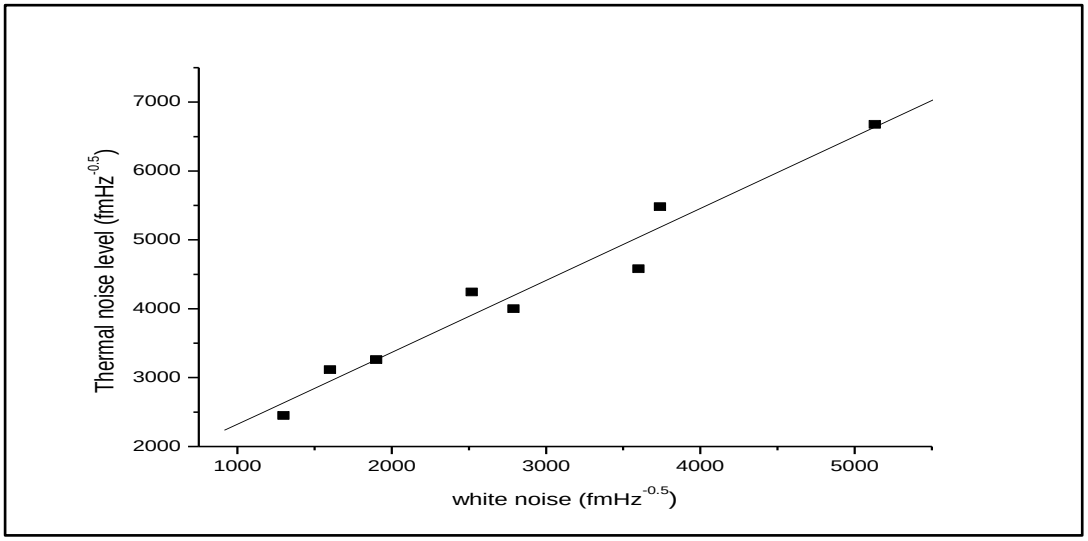

FIG.3.24 White noise dependence of the level of damping of the thermal peak of microlever-C, in water, measured using Figure 3.23.

In principle, the floor noise of the system sets a limit for the maximum achievable reduction of the thermal noise. Our study on different cantilevers confirms that conclusion and the limit of damping level would be optimized more if the system white noise is further minimized. For example, the diode laser (LD1) can be replaced by a more powerful one. Moreover, we could change the PSPD so that it works more efficiency with a smaller laser spot size.

3.10 Effect of PI parameters on the damping level

The feedback control system is at the heart of any system built for process control techniques. Despite the diversity of process control systems, most feedback systems are based on proportional-integral (PI) control due to its effectiveness and ease of use (*45*). The optimal values of PI are required to keep the system stable and to achieve the best performance of the system and then the optimum level of damping. Too high values of PI result in unstable oscillation of the cantilever and the lower ones may weaken system performance (section 3.11). Thus, to maintain the chosen setpoint constant and to achieve the best feedback performance the PI values should be chosen or adjusted carefully.

Cantilever motion may be damped through the selection of an appropriate value of gains. Therefore dozens of microlevers and Bio-levers have been studied and hundreds of P and I values were investigated, on a trial and error basis, in order to find the optimal values of PI. It was found that values of proportional gain (P) must be tenfold greater than the measured values of integral gain (I).

$$I = 0.1P \qquad [3.23]$$

This finding helps to save time during experimental setup, which takes between 1 and 2 hours. Moreover, the PI values were found to vary depending upon the cantilever. The optimal PI values for cantilever type C in water are P=21 and I=2.1, whereas they are P=26, I=2.6 for cantilever-D and P=24, and I=2.4 for the Bio-lever.

3.11 Cooling cantilevers using radiation force controlled via PI controller

Reducing the thermal vibration of an AFM cantilever by an active feedback system can be considered as identical to cooling, where the thermal vibration of a cantilever is proportional to its temperature. According to the equipartition theorem, a reduction of the lowest mechanical vibration mode of the cantilever is equivalent to decreasing the energy associated with the thermal motion of the cantilever, thereby decreasing its temperature.

The mechanism of cooling using optical force is based on the concept that light exerts a force when it is reflected or refracted by an object. In the case of 100% reflection, the force applied by optical force would be 7 pN/mW. For the cantilevers used in this experiment this force is sufficient, Table 3.1.

Table 3.1 Amplitude of thermally induced oscillations and equivalent noise on force measurements for three cantilevers (obtained experimentally).

Cantilever	Spring constant, k (pN/nm)	RMS amplitude thermal oscillations (nm)	Peak-peak Amplitude (nm)	RMS noise on measured force (pN)
D	30	0.37	1.3	11
C	10	0.64	3	6.4
Biolever-A	6	0.83	5	5

Eq.3.5 presents a simple description of cantilever motion. For simplicity, we consider the cantilever as a simple harmonic oscillator immersed in a viscous fluid and excited by thermal noise. In the case of an external force exerted onto the cantilever to counteract its thermal displacement, Eq.3.5 can be rewritten by taking into account the magnitude of the resultant forces, Λ, that represents the external force and the exciting thermal force so the motion of the cantilever is approximated by

$$m\frac{d^2Z(t)}{dt^2}+\frac{m\omega_0}{Q}\frac{dZ(t)}{dt}+kZ(t)=\Lambda \qquad [3.24]$$

The value of Λ relies on the amount of power deposited onto the backside of the cantilever to minimize the Brownian motion of the cantilever. Thus, a decrease or an increase in laser power depends on positional changes of the cantilever. The solution of Eq.3.24 is that of Eq.3.6 with modified resonance frequency and quality factor due to the impact of the external force. Assuming that Λ is frequency independent, the mean square of the damped amplitude of the cantilever for frequencies in the vicinity of the resonance frequency is

$$\delta z^2 = \frac{Q^2 \left\langle \left| \Lambda^2 \right| \right\rangle}{\kappa^2} \Delta \nu \qquad [3.25]$$

Here, $\frac{Q^2 \left\langle \left| \Lambda^2 \right| \right\rangle}{\kappa^2}$ represents the value of power spectral density of the cantilever oscillations at its resonance peak in frequency domain.

In this experiment, the thermal noise amplitude of higher vibration modes of the cantilever is neglected with respect to its first mode thermal noise. This assumption is justified due to the thermal noise of the second flexural mode being smaller than the first flexural mode noise by 250 times(*7*). Therefore, our measurements will be focused on the first mode. The magnitude of the thermal oscillation of the cantilever can be determined by integrating the area under the first peak corresponding to the first mode of the power spectrum curve.

Figure 3.25 shows the thermal noise spectra obtained for the free end of the microcantilever C (k=10 pN/nm) in water. The red curve corresponds to the free thermal oscillation of the microlever whereas the curves (blue to black) are obtained for damped thermal noise at different PI gains. The variations of the damping level of thermal noise amplitude show the importance of choosing adequate PI gains. Obviously, the magnitude of thermal noise depends on gain values.

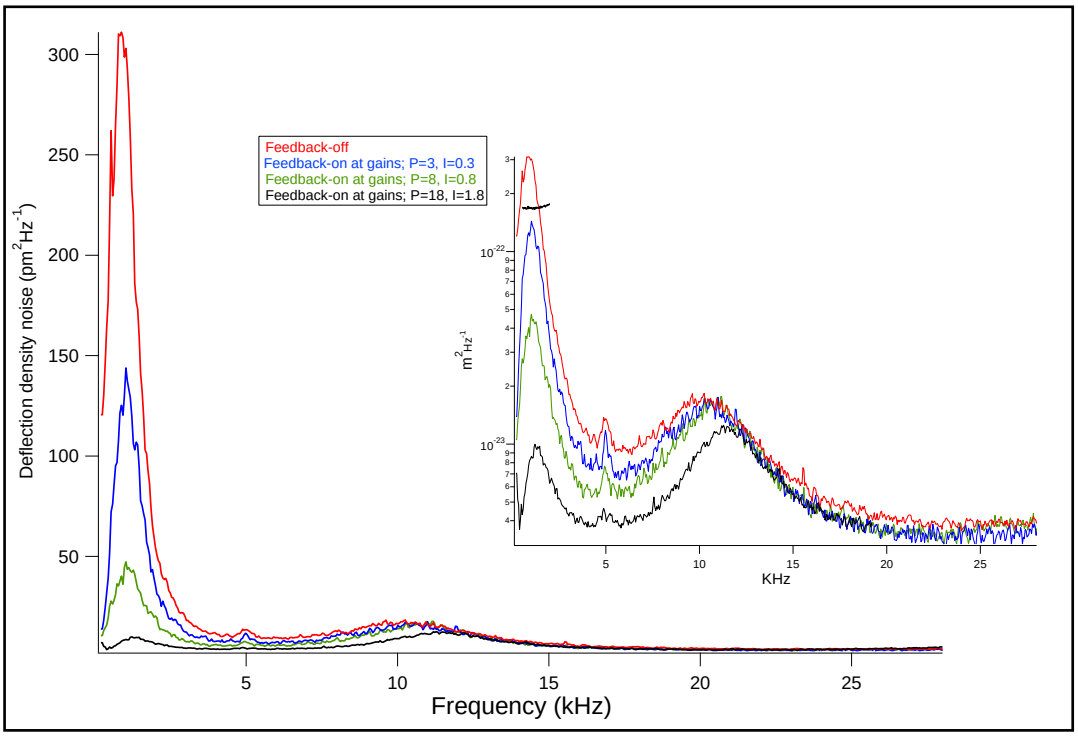

FIG.3.25 Power spectral density of the thermal noise of microcantilever C, 10pN/nm, in water. Red color corresponds to undamped oscillations of the microlever, feedback circuit is off. Others colored spectra correspond to the feedback circuit tuned at different PI gains. The inset shows the log scale of the curves

The thermal oscillation of the microlever is reduced when the feedback force is turned on. The value of the main peak of the power spectrum curve of thermal noise reflects the magnitude of the cantilever's thermal oscillation that decreases significantly from $17\times10^3 \, fm/\sqrt{Hz}$ to $2.3\times10^3 \, fm/\sqrt{Hz}$. The RMS value of that oscillation can be calculated by integrating the area under the peak. The measurements show that the RMS is minimized by a factor of 7, from ~6 Å to ~0.9 Å. Thus, the temperature corresponding to the measured RMS falls from room temperature of 300 K to ~5 K.

Figure 3.25 exhibits a slight shift in the resonance frequency of the fundamental vibration mode when applying the feedback. The frequency

shift increases upon decreasing the thermal oscillation of the cantilever. This is due to asymmetric damping. One side of the thermal peak is damped slightly more than the other. The system damps lower frequencies more efficiently than higher frequencies, hence an apparent shifts to higher frequencies.

The direct amplitude of thermal fluctuations of the cantilever in real time is displayed in Figure 3.26. The uncertainty of the microlever position before applying the feedback force was ~3 nm, peak to peak. However, this value declines to ~ 0.4 nm when the feedback circuit is turned on. The noise is filtered at a cut-off frequency of 4 kHz to eliminate high electronic noise. The filtration of the output of deflection signal excited thermally is crucial in order to extract the actual vibrations of the microcantilever.

If force sensitivity of a cantilever is just limited by thermal noise, the minimum detectable force is given by

$$\delta F = \sqrt{\frac{2k_B T k \Delta \nu}{Q \pi \nu_0}} \qquad [3.26]$$

Thus the RMS of force associated with thermal motion of the microlever C is ~6 pN which is in agreement with the value inferred from Figure 3.26. The RMS of force sensitivity is improved approximately more than six-fold to be <1 pN. On the other hand, the uncertainty of force, peak to peak, related to Brownian motion decreases more than seven folds to be ~4 pN, starting from approximately 30 pN.

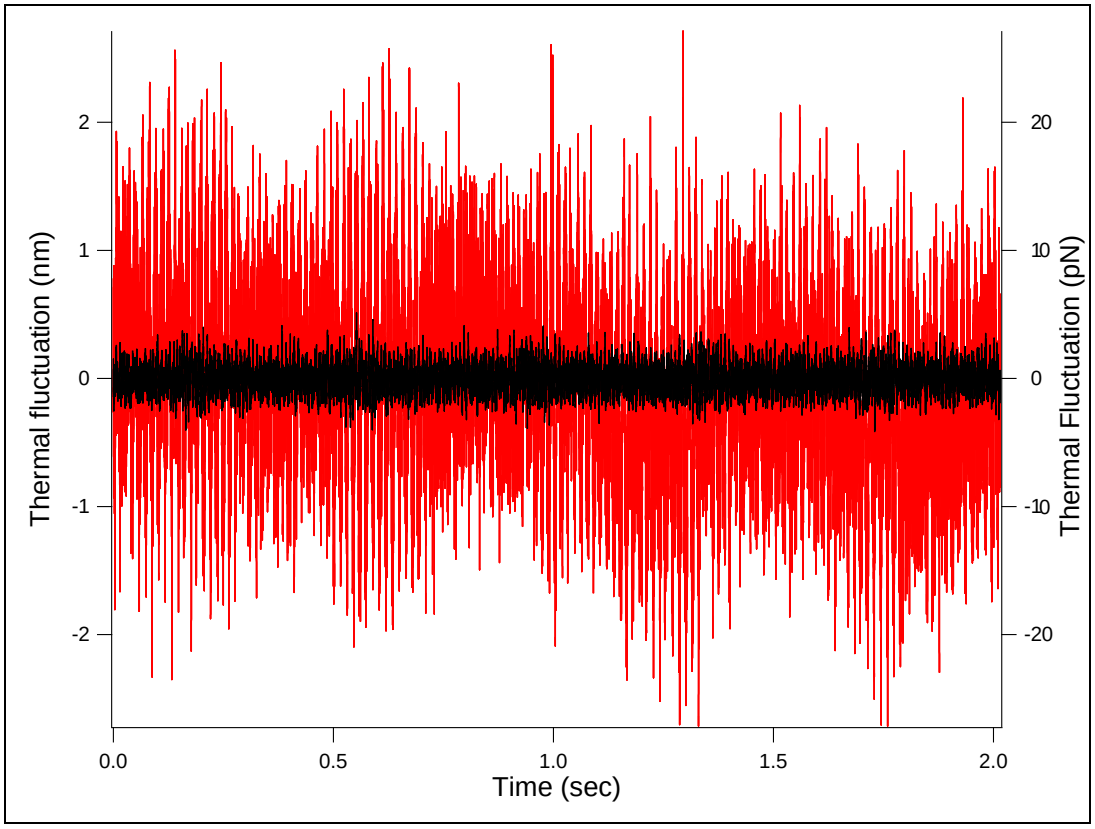

FIG.3.26 The noise in force and position of the microlever C after (black) and before (red) turning on the radiation force feedback unit.

Measurements of the Biolever-B (k=~6 pN/nm) thermal noise taken either via Figure 3.27 or 3.28 reveal similar behavior to microlever C. Fluctuations of the Biolever position, peak to peak, is considerably minimized from 5 nm to no more 0.3 nm. The root mean square of the Biolever thermal displacement, extracted from Figure 3.27 or 3.28, is ~0.1 nm and this corresponds to ~3 K.

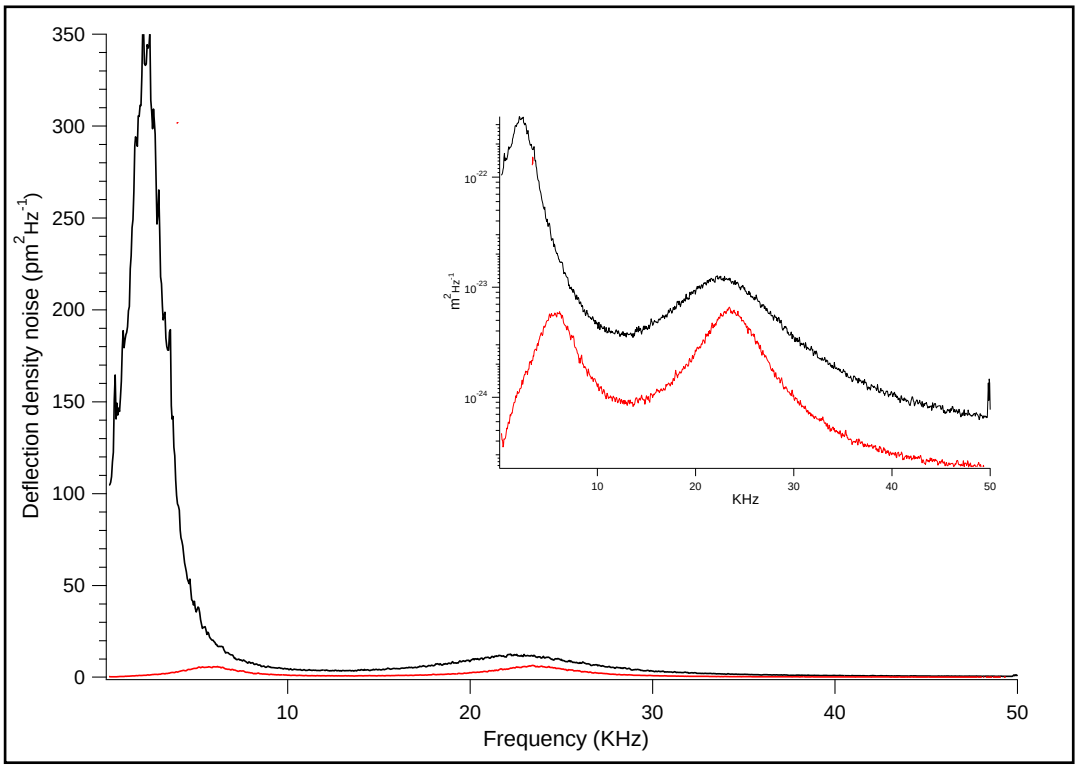

FIG.3.27 Power spectral density of thermal noise of the Biolever, ~6 pN/nm, in water, before (black) and after (red) turning on the thermal cancellation system.

Furthermore, the uncertainty of position related to the Biolever is optimized. The uncertainty of force resulting from thermal fluctuations of the free end of the Biolever, peak to peak, is 40 pN and 4.5 pN in RMS, but, these values are improved by using our system to be ~2 pN peak to peak and ~0.8 pN in RMS.

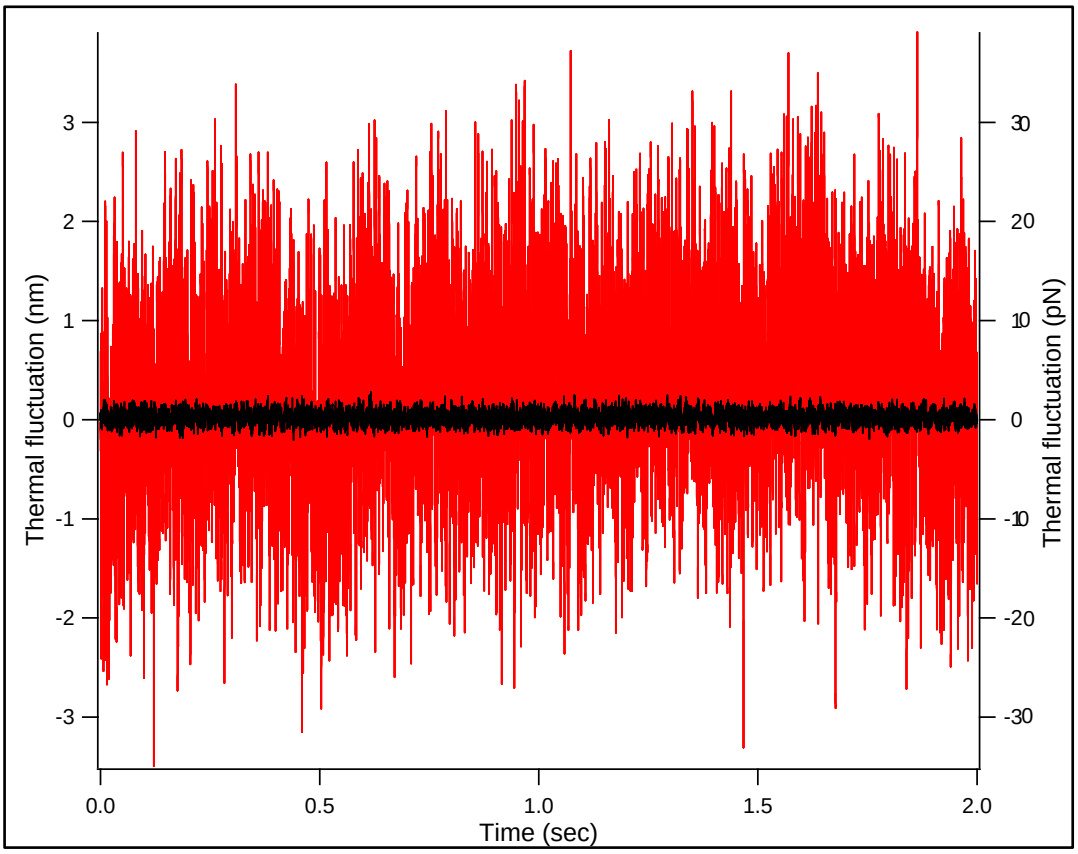

FIG.3.28 The noise force and position of the Biolever after (black) and before (red) turning on the radiation force feedback unit.

A microlever with higher resonance frequency and stiffness was also studied. Microlever D (k=~30 pN/nm) is less prone to thermal noise due to its high stiffness compared to the previously studied cantilevers. However, we applied feedback radiation force to it in order to widen the range of studied cantilevers.

Figure 3.29 shows that the PSD of cantilever D has dropped from $5.8\times10^{3}\ fm/\sqrt{Hz}$ to $2.3\times10^{3}\ fm/\sqrt{Hz}$ using radiation feedback.

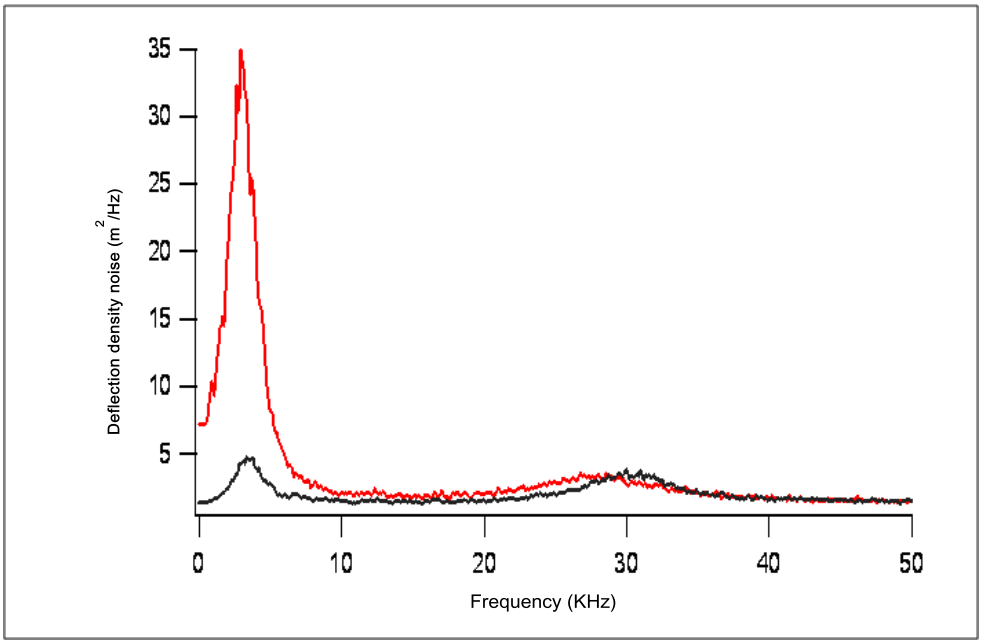

FIG.3.29 The PSD of thermal noise of microlever-D in water, before (red) and after (black) turning on the thermal cancellation system.

The fluctuation of position and force was minimized to be ~0.3 nm and 11 pN, peak to peak, respectively, Figure 3.30. The RMS of force noise was around 7 pN.

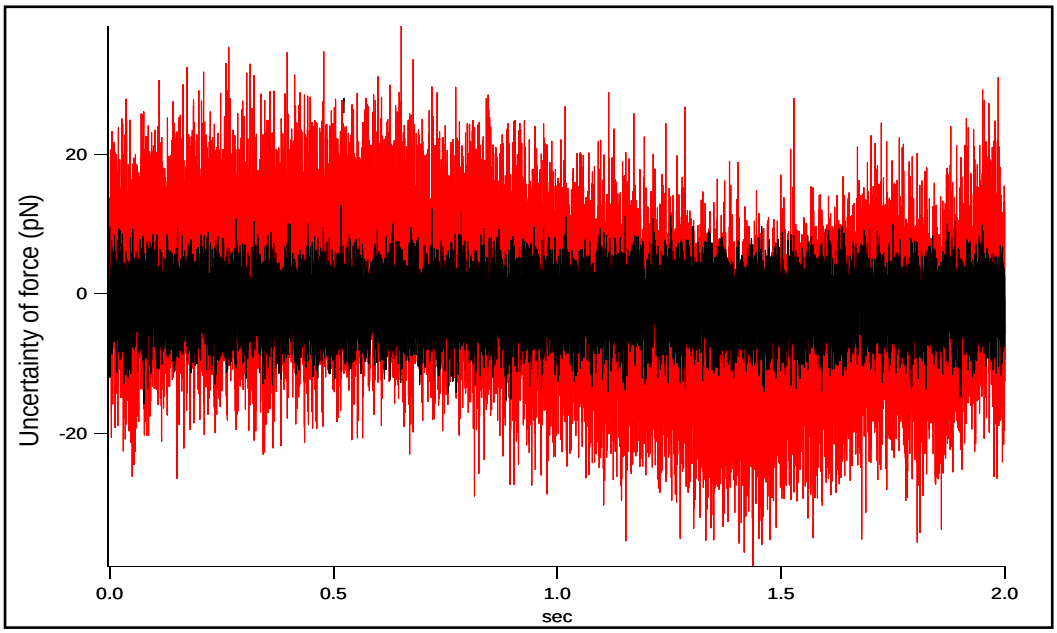

FIG.3.30 The noise force of microlever-D after (black) and before (red) turning on the radiation force feedback unit.

The ultimate performance of the feedback damping in terms of reduction of fluctuation amplitude is almost the same as with the Biolever and microlever C, reducing to a peak to peak amplitude of around 3 Å.

Figure 3.31 illustrates the noise spectrum of the laser signal used to damp the thermal oscillation of cantilever C. Comparison between the noise spectrum of the laser signal and noise spectrum of the cantilever motion shows that our feedback system has improved its ability to follow properly the changes of the cantilever position acting to maintain the setpoint constant. PSD of cantilever motion and laser power fluctuations shows two peaks corresponding to the first and second flexural mode of the cantilever, ~1 KHZ and 12 KHz respectively.

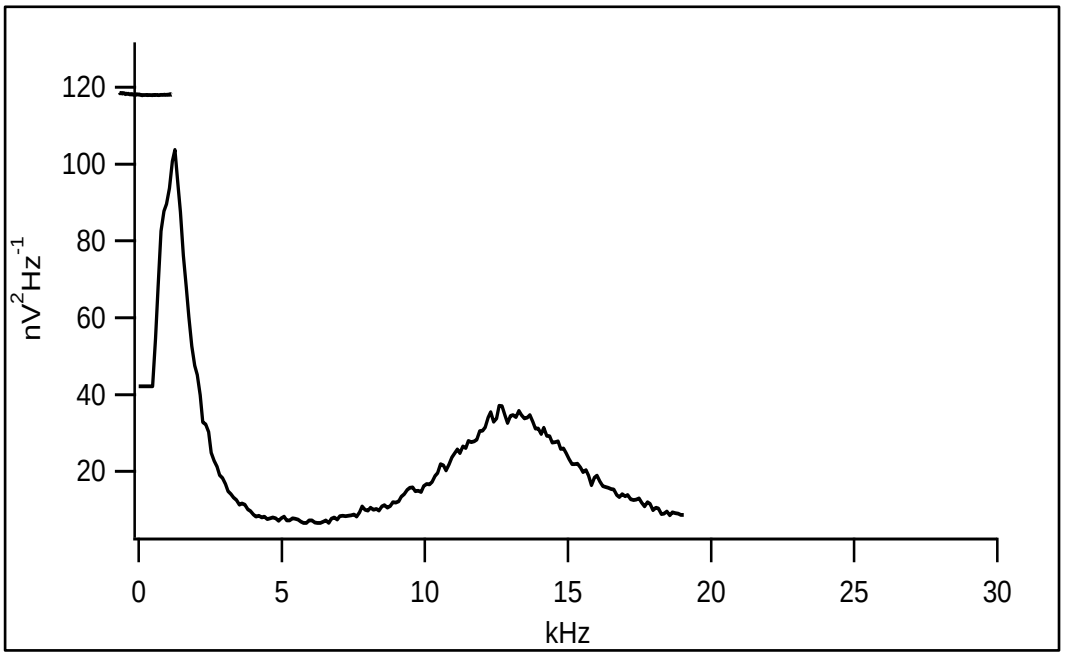

FIG.3.31 PSD of laser signal used to damp the thermal noise of the mircolever C.

3.12 Conclusion

The central motivation behind the system is to reduce the effect of the thermal noise and deflection instabilities, on both spatial and force measurement of soft AFM cantilevers. The improvement in a spatial or force resolution could open up the door for more applications of the AFM cantilever. For example, in order to gain a full dynamic force spectrum, the force must be applied at differing loading rates. Unfortunately, the compliance of the cantilever will limit the maximum accessible rate at which the force is loaded onto the construct (detailed discussion in the following chapters).

Using the CD-AFM system, we have directly demonstrated that the thermal noise related to a cantilever Brownian motion in water is effectively minimized to approximately 0.3 nm, peak to peak, and the force uncertainty resulting from the thermal noise has been reduced to 2 pN,

peak to peak, whereas RMS is less than 1pN. This high level of damping has been achieved as a result of the improvements in the system floor noise. As far as we know, this experimental setup is the first successful attempt to cool the softest two available cantilevers commercially in a liquid ambient by using just the optical beam deflection system to less than 3 K.

3.13 References

(1) Jianhua, W., Ying, F., Dong, Y., and Cheng, Z. (2005) Thermo-Mechanical Responses of a Surface-Coupled AFM Cantilever. *Journal of Biomechanical Engineering 127*, 1208-1215.

(2) Brockwell, D. J. (2007) Probing the mechanical stability of proteins using the atomic force microscope. *Biochemical Society Transactions 35*, 1564-1568.

(3) Hann, E., Kirkpatrick, N., Kleanthous, C., Smith, D. A., Radford, S. E., and Brockwell, D. J. (2007) The Effect of Protein Complexation on the Mechanical Stability of Im9. *Biophysical Journal 92*, L79-L81.

(4) Tokunaga, M., Aoki, T., Hiroshima, M., Kitamura, K., and Yanagida, T. (1997) Subpiconewton Intermolecular Force Microscopy. *Biochemical and Biophysical Research Communications 231*, 566-569.

(5) Brown, R. (1828) A brief account of microscopical observations made in the months of June, July and August, 1827, on the particles contained in the pollen of plants; and on the general existence of active molecules in organic and inorganic bodies. *Phil. Mag 4*, 161–173.

(6) Passian, A., Muralidharan, G., Mehta, A., Simpson, H., Ferrell, T. L., and Thundat, T. (2003) Manipulation of microcantilever oscillations. *Ultramicroscopy 97*, 391-399.

(7) Alvarez, M., Tamayo, J., Plaza, J. A., Zinoviev, K., Dominguez, C., and Lechuga, L. M. (2006) Dimension dependence of the thermomechanical noise of microcantilevers. *Journal of Applied Physics 99*, 024910.

(8) Florian, M., and Steve, M. G. (2009) Optomechanics. *Physics 2*, 40.

(9) Reif, F. (1965) *Fundamentals of Statistical and Thermal Physics.*, McGRA W-HILL, New York.

(10) Norton, M., and Karczub, D. (2003) *Fundamentals of noise and vibration analysis for engineers*, 2nd ed., Cambridge University Press, Cambridge.

(11) Viani, M., Schaffer, T., Chand, A., Reif, M., Gaub, H., and Hansma, P. (1999) Small cantilevers for force spectroscopy of single molecules. *Journal of Applied Physics 86*, 2258-2262.

(12) Viani, M., Schaffer, T., Chand, A., Reif, M., Gaub, H., and Hansma, P. (1999) Small cantilevers for force spectroscopy of single molecules. *J. Appl. Phys. 86*, 2258-2262.

(13) Arthur, B., and Frederick, S. (2006) Microfabricated torsion levers optimized for low force and high-frequency operation in fluids. *Ultramicroscopy. 106*, 838-846.

(14) Ashby, P. D., Chen, L., and Lieber, C. M. (2000) Probing Intermolecular Forces and Potentials with Magnetic Feedback Chemical Force Microscopy. *Journal of the American Chemical Society 122*, 9467-9472.

(15) Liang, S., Medich, D., Czajkowsky, D. M., Sheng, S., Yuan, J.-Y., and Shao, Z. (2000) Thermal noise reduction of mechanical oscillators by actively controlled external dissipative forces. *Ultramicroscopy 84*, 119-125.

(16) Ng, T. N., Jenkins, N. E., and Marohn, J. A. (2006) Thermomagnetic Fluctuations and Hysteresis Loops of Magnetic Cantilevers for Magnetic Resonance Force Microscopy. *IEEE Trans. Magn 42*, 378–381.

(17) Bruland, K. J., Garbini, J. L., and Dougherty, W. M. (1998) Optimal control of ultrasoft cantilevers for force microscopy. *Journal of Applied Physics 83*, 3972.

(18) Brown, K. R., Britton, J., Epstein, R. J., Chiaverini, J., Leibfried, D., and Wineland, D. J. (2007) Passive Cooling of a Micromechanical Oscillator with a Resonant Electric Circuit. *Physical Review Letters 99*, 137205.

(19) Wineland, D. J., Britton, J., Epstein, R. J., Leibfried, D., Blakestad, R. B., Brown, K., Jost, J. D., Langer, C., Ozeri, R., Seidelin, S., and Wesenberg, J. (2006) Cantilever cooling with radio frequency circuits. *eprint arXiv:quant-ph/0606180.*

(20) Shi-Hua, O., You, J. Q., and Franco, N. (2009) Cooling a mechanical resonator via coupling to a tunable double quantum dot. *Physical Review B (Condensed Matter and Materials Physics) 79*, 075304.

(21) Hao, L., Gallop, J. C., and Cox, D. (2009) Excitation, detection, and passive cooling of a micromechanical cantilever using near-field of a microwave resonator. *Applied Physics Letters 95*, 113501.

(22) Braginskii, V. B., Caves, C. M., and Thorne, K. S. (1977) Laboratory experiments to test relativistic gravity. *Phys. Rev. D. 15*, 2047-2068.

(23) Braginsky, V. B., and Vyatchanin, S. P. (2001) Frequency fluctuations of nonlinear origin in self-sustained optical oscillators. *Physics Letters A 279*, 154-162.

(24) Dorsel, A., McCullen, J. D., Meystre, P., Vignes, E., and Walther, H. (1983) Optical Bistability and Mirror Confinement Induced by Radiation Pressure. *Physical Review Letters 51*, 1550.

(25) Constanze, M., Ivan, F., Alexander, O., and Khaled, K. (2008) Optical self cooling of a deformable Fabry-Perot cavity in the classical limit. *Physical Review B (Condensed Matter and Materials Physics) 78*, 035309.

(26) Höhberger, C., Metzger, and Karrai, K. (2004) Cavity cooling of a microlever. *Nature. 432*, 1002-1005.

(27) Kippenberg, T. J., and Vahala, K. J. (2008) Cavity Optomechanics: Back-Action at the Mesoscale. *Science 321*, 1172-1176.

(28) Arcizet, O., Cohadon, P. F., Briant, T., Pinard, M., Heidmann, A., Mackowski, J. M., Michel, C., Pinard, L., Francais, O., and Rousseau, L. (2006) High-Sensitivity Optical Monitoring of a

Micromechanical Resonator with a Quantum-Limited Optomechanical Sensor. *Physical Review Letters 97*, 133601.

(29) Cohadon, P. F., Heidmann, A., and Pinard, M. (1999) Cooling of a Mirror by Radiation Pressure. *Phys. Rev. Lett. 83*, 3174.

(30) Mancini, S., and Wiseman, H. M. (2000) Optomechanical tailoring of quantum fluctuations. *Journal of Optics B: Quantum and Semiclassical Optics*, 260.

(31) Pinard, M., Cohadon, P. F., Briant, T., and Heidmann, A. (2000) Full mechanical characterization of a cold damped mirror. *Physical Review A 63*, 013808.

(32) Poggio, M., Degen, C., Mamin, H., and Rugar, D. (2007) Feedback cooling of a cantilever's fundamental mode below 5 mK. *Phys Rev Lett. 99*, 017201.

(33) Kleckner, D., and Bouwmeester, D. (2006) Sub-kelvin optical cooling of a micromechanical resonator. *Nature. 444*, 75-78.

(34) Tamayo, J. (2005) Study of the noise of micromechanical oscillators under quality factor enhancement via driving force control. *Journal of Applied Physics 97*, 044903.

(35) Gröblacher, S., Gigan, S., Böhm, H. R., Zeilinger, A., and Aspelmeyer, M. (2008) Radiation-pressure self-cooling of a micromirror in a cryogenic environment. *EPL. 18*, 54003.

(36) Corbitt, T., Chen, Y., Innerhofer, E., Müller-Ebhardt, H., Ottaway, D., Rehbein, H., Sigg, D., Whitcomb, S., Wipf, C., and Mavalvala, N. (2007) An All-Optical Trap for a Gram-Scale Mirror. *Physical Review Letters 98*, 150802.

(37) Schliesser, A., Delâ€™Haye, P., Nooshi, N., Vahala, K. J., and Kippenberg, T. J. (2006) Radiation Pressure Cooling of a Micromechanical Oscillator Using Dynamical Backaction. *Physical Review Letters 97*, 243905.

(38) Gigan, S., Böhm, H., Paternostro, M., Blaser, F., Langer, G., Hertzberg, J., Schwab, K., Bäuerle, D., Aspelmeyer, M., and Zeilinger, A. (2006) Self-cooling of a micromirror by radiation pressure. *Nature. 44*, 67-70.

(39) Favero, I., Metzger, C., Camerer, S., Konig, D., Lorenz, H., Kotthaus, J. P., and Karrai, K. (2007) Optical cooling of a micromirror of wavelength size. *Applied Physics Letters 90*, 104101.

(40) Jeffrey, L. H., and John, B. (1993) Calibration of atomic-force microscope tips. *Review of Scientific Instruments 64*, 1868-1873.

(41) Fukuma, T., and Jarvis, S. P. (2006) Development of liquid-environment frequency modulation atomic force microscope with low noise deflection sensor for cantilevers of various dimensions. . *Review of Scientific Instruments 77*, 043701.

(42) D'Costa, N., and Hoh, J. (1995) Calibration of optical lever sensitivity for atomic force microscopy. *Rev. Sci. Instrum. 66*, 5096-5097.

(43) Acsente, T. (2007) Laser diode intensity noise induced by mode hopping. *Romanian Reports in Physics. 59*, 87-92.

(44) Fukuma, T., Kimura, M., Kobayashi, K., Matsushige, K., and Yamada, H. (2005) Development of low noise cantilever deflection sensor for multienvironment frequency-modulation atomic force microscopy. *Review of Scientific Instruments 76*, 053704

(45) Chen, D., and Seborg, D. E. (2003) Design of decentralized PI control systems based on Nyquist stability analysis. *Journal of Process Control 13*, 27-39.

Chapter 4
Calibration of laser power

4.1 Introduction

Force distance curves are normally acquired by measuring the deflection of a cantilever as it interacts with a surface. Calibration of the force is a relatively straightforward matter, involving measuring the spring constant of the cantilever and multiplying by the measured deflection.

In section 3.1 we introduced the concept of locking a cantilever. CD-AFM was used to damp the thermodynamic noise associated with the cantilever's Brownian motion. The change of LD2 intensity used to suppress the thermodynamic noise is proportional to changes of the cantilever position, so it can be employed to suppress not only the thermally driven deflection, but also lock ‘’any’’ cantilever motion experienced during a force distance curve. The CD-AFM system attempts to keep the cantilever deflection at the reference level by increasing or decreasing laser power. In other words, the microlever has zero

compliance. A method is therefore required to convert laser power into applied force. As discussed in the preceding chapter, the motion of the cantilever (10 pN/nm) is locked with root-mean square fluctuation (δz) of <0.1 nm. Therefore, forces cannot be acquired by the deflection signal as those forces were balanced by optomechanical forces leaving the magnitude of deflection zero.

In order to circumvent this problem we proposed taking advantage of changes in laser diode2 (LD2) intensity, employed to suppress the mechanical noise of the lever, instead of the deflection signal. Fluctuations in laser intensity reflect the locked cantilever fluctuations (in chapter 3 I showed that the oscillation of LD2 follows the deflection of the cantilever precisely).

One attraction of using the LD2 signal is that dealing with electronic noise associated with laser signal is much easier than mechanical noise arising from real instabilities of the cantilever position. Electronic noise masks the real signal which can be hidden beneath it. The signal is intact and can be recovered by reducing the level of electronic noise either by using a suitable filter or preventing the noise from being introduced. In contrast, mechanical noise such as instability in an AFM cantilever (thermodynamic noise illustrated in chapter 3 and the jump-in will be explained in chapter 5) may distort the signal. Force measurements using AFM depend on sensing the interactions by a flexible cantilever. If the amplitude of random fluctuations is comparable to the real signal, the real signal cannot be recovered.

The conversion of the laser power into force was a challenge due to the forces acting on the cantilever arising from two sources; photon and photothermal forces. The photon force (radiation force) relies on the principle that when a photon reflects from a surface, it undergoes a change

in its momentum (M_m). According to Newton's second law, a change in the momentum results in a force on the surface, which leads to the radiation force F_{rad}.

$$\vec{F}_{rad} = \frac{d\vec{M}_m}{dt} \qquad [4.1]$$

When a photon hits a surface, it may be absorbed or reflected. If a photon is reflected elastically, it will rebound with the same magnitude of momentum but in the opposite direction. Therefore, the momentum transferred to the surface is double that of the incoming photon.

$$M_{m-total} = 2M_m \qquad [4.2]$$

In practice, the radiation force exerted on a surface is less than that calculated theoretically because a fraction of the photons may be absorbed by the surface. If the quantum treatment of photon is taken into account, thus, the momentum (M_m) of photon can be described by

$$M_m = \frac{W}{c} \qquad [4.3]$$

Where W is the energy of photon and c is the speed of light.

Therefore, the exerted force on the surface by photon force with normal incidence of the laser beam and 100% reflectivity of the metal-coated backside surface of cantilever is given by

$$F_{rd} = \frac{2P}{c} \qquad [4.4]$$

Where P is the laser power.

Based on Eq.4.4 the applied force by laser power is 6.7 pN per milliwatt (6.7 pN/mW). In terms of a cantilever with stiffness 10 pN/nm, the laser radiation force applied by LD2 (maximum laser power= 50 mW) can be enough to oppose the force generated by Brownian motion of the cantilever, ~30 pN .

The second source of the force acting upon the cantilever is that resulting from the absorbed fraction of photons. When the metal-coated backside of the cantilever is illuminated by a radiation source, a small fraction of radiation energy is absorbed by the surface, which results in a rise in temperature. This in turn, causes the cantilever to bend because of inhomogeneous thermal expansion of the coating film and the material of the cantilever, the bimetallic effect. The force resulting from a bimetallic effect is called photothermal force which is due to the fact that the optical energy is transformed into mechanical energy via thermal energy.

In this chapter we will explain how the LD2 signal can be transformed into force. In addition, the advantages of using the LD2 signal will be demonstrated with applications in the following chapters. From now on, all force curves will be acquired using the laser signal instead of the deflection. Thus, the force calibration of laser signal is a prerequisite procedure for force measurements.

4.2 Experimental setup and details

A schematic illustration of the experiment setup is shown in Figure 4.1. The AFM used in the experiment is a PicoForce microscope with the CD-AFM head and a Nanoscope IIIa controller (Digital instruments, Santa Barbara, California). The cantilevers used are Silicon Nitride V-shaped Veeco

cantilevers; four microcantilevers (C, D, E and F) and Four NP (A, B, C and D). All cantilevers are coated on backside with a gold layer of 60 nm in order to enhance the reflectivity of the surface, for manufacture's specifications see Table 1. Since force measurements using CD-AFM will be taken in aqueous solution, all calibration measurements are performed in Phosphate Buffered Saline (PBS) buffer at room temperature.

Two diode lasers are used. Laser diode 2 (LD2) (HL7851G, 50 mW, 780 nm, Hitachi) is for driving the cantilevers at different frequencies and amplitudes whereas Laser diode 1 (LD1) (HL6722G-Hitachi 5mW, Edwards Optics, 670 nm) with a constant intensity is for position sensing. The laser beams were directed into the CD-AFM head using a single mode optical fiber and then focused on the back side of the cantilever with a radius of $20\mu m$ using an adjustable pair of lenses, explained in chapter 3.

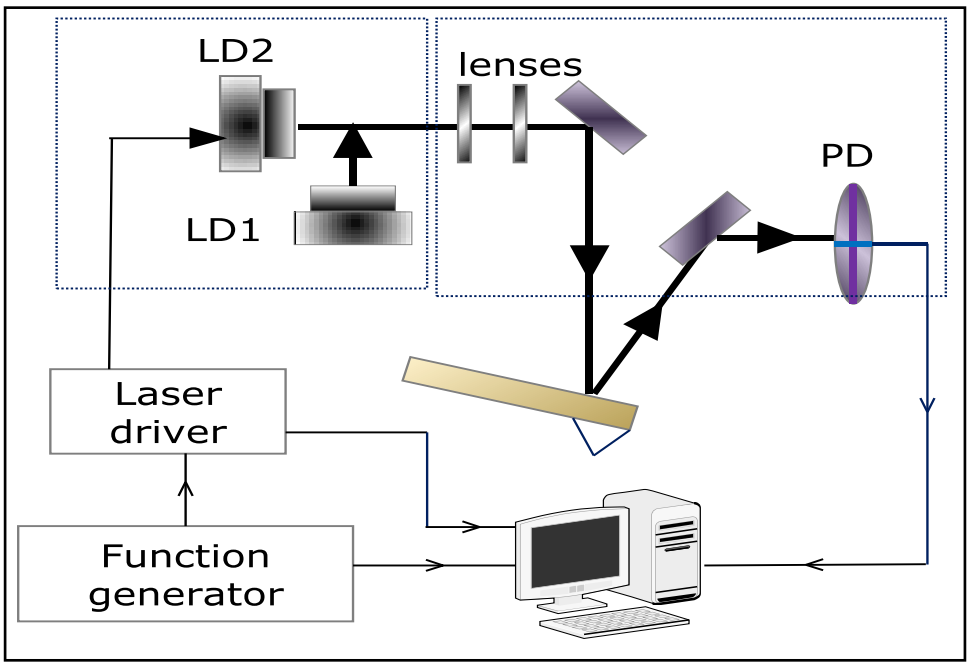

FIG.4.1 Experimental setup; see the text for details.

The intensity of LD2 laser was modulated using a laser driver (DBDL 200 T/S, Microlaser Systems) capable of modulating LD2 up to 50 mW and with frequency ranging from 0 to 2 MHz. Despite the peak value of LD2 power being 50 mW, the laser power intensity measured at the tip is half of 50 mW due to attenuation along the optical path. The laser driver is directly driven by a sinusoidal voltage generated by a programmable function generator (Thurlby Thandar Instruments, TG1304) with peak voltages from 500 mV to 1300 mV. Consequently, the intensity of LD2 on the free end of the cantilever varies sinusoidally with the driving signal at different frequencies. All sinusoidal oscillations of the cantilevers were driven with a DC offset of 0.7 V at which the laser diode is driven at approximately half its maximum output.

The cantilever position was detected with the standard optical beam deflection method using LD1, and the resulting voltage measured with a PC equipped with a data acquisition card (National Instruments, Austin, Texas) controlled via a home-built software using Labview 6 software. The deflection signal of the cantilever is recorded with a sampling rate of 50 kHz and then converted from volts to meters using the deflection sensitivity (nm/V) obtained by LabView (explained in chapter 3 section 3.7). The data was analyzed using IgorPro software (Wavemetrics, Lake Oswego, Oregon,USA).

4.3 Result and discussion

It is the principle function of an AFM cantilever to deflect when a mechanical force acts upon it. The change of the cantilever position is detected and then converted into force via Hooke's law.

However, the deflecting force may originate from another source. For instance, the optomechanical force due to interaction of light with the cantilever beam, Figure 4.2.

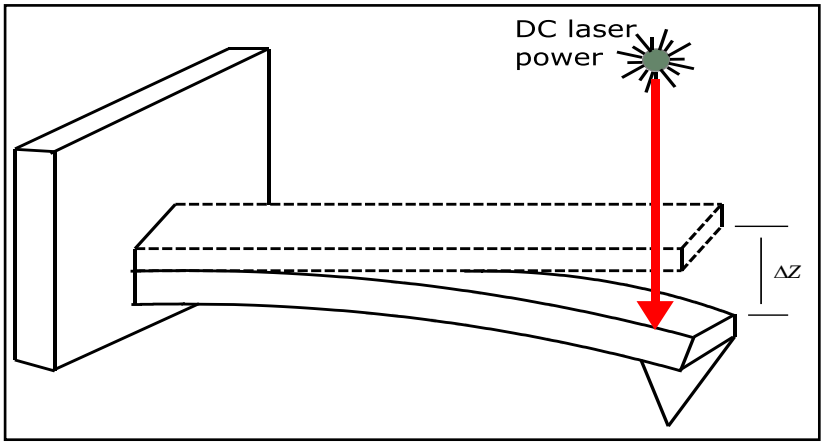

FIG.4.2 Deflection of a cantilever when its free end is subject to a constant load.

The interaction of laser radiation with the cantilever is through a mechanical response excited by both the reflected and absorbed photons. The absorbed photons raise the beam temperature and then movement occurs due to bimetallic effect (photothermal effect) (*1*). Figure 4.3 and Table 4.1 show that the cantilever bending induced by both reflected photons and bimetalic effect is proportional to laser power. For instance, microcantilever C with spring constant of 10 pN/nm deflects approximately 6 nm per mW of laser power. It is worth noting that 15 mV≡1 mW, Figure 4.4.

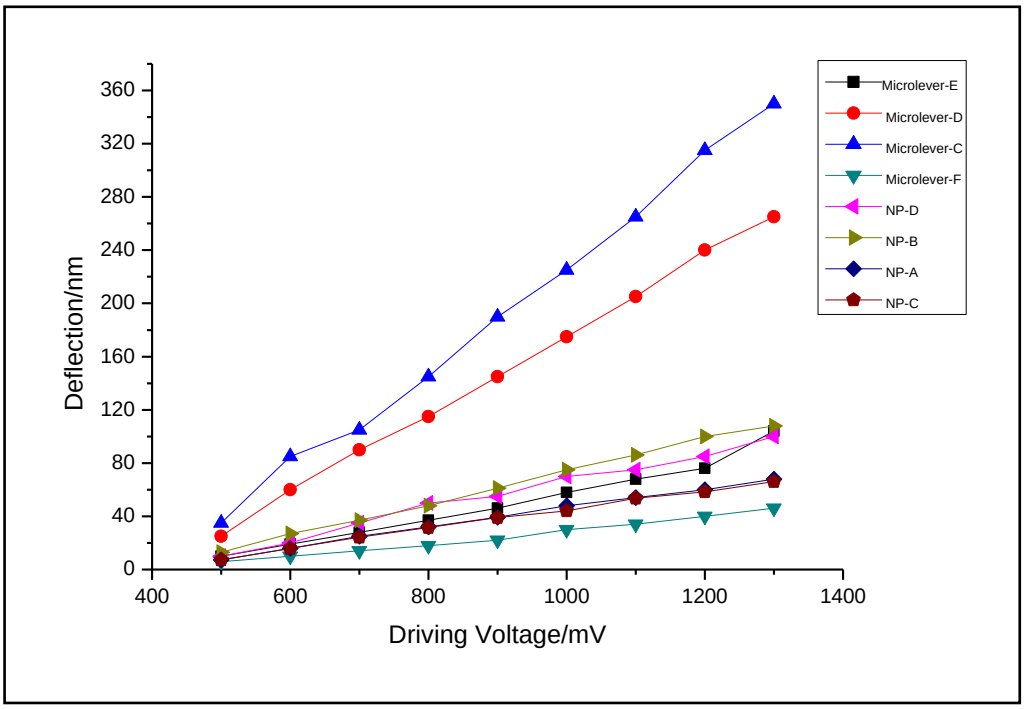

FIG.4.3 Deflection of cantilevers as function of DC driving voltage in PBS.

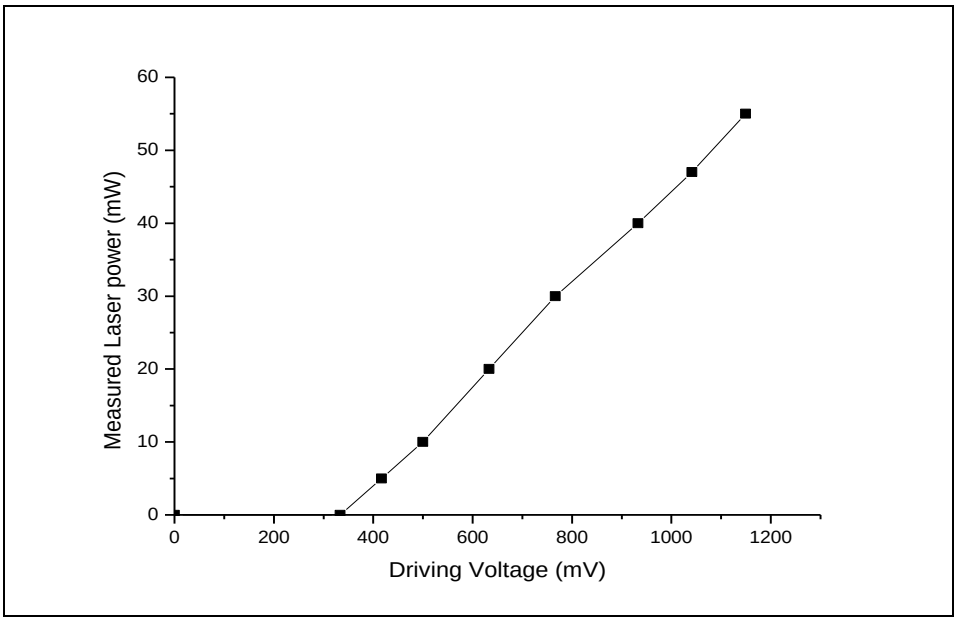

FIG.4.4 The relationship between the driving voltage and the output of laser power.

Table 4.1 Summary table of the results of eight cantilevers.

Probe	Manufacturer's nominal stiffness (Nm^{-1})	Manufacturer's nominal length (μm)	Deflection with respect to driving voltage (nm/mV)	Force sensitivity (pN/mV)
Microlever-C	0.01	320	0.4	4
Microlever-D	0.03	220	0.3	9
NP-D	0.06	196	0.109	6.5
Microlever-E	0.1	140	0.1	10
NP-B	0.12	196	0.12	14.4
NP-C	0.32	115	0.072	23
Microlever-F	0.5	85	0.05	25
NP-A	0.58	115	0.075	43.5

However, the higher than expected value of bending cannot be solely due to reflected photons (photon force) for a number of reasons. First, the cantilever deflection due to photon force should be proportional to the cantilever stiffness alone, as photon force is independent on the cantilever physical properties. A comparison of deflections of eight cantilevers used for the measurements with different stiffness and length illustrated in Figure 4.3 and Table 4.1 show that the bending of the cantilevers is not proportional to their stiffness. For instance, NP-D and NP-B cantilevers almost have a similar deflection, although NP-B is double the stiffness of NP-D.

Second, the force due to photon force, 6.7 pN/mW, is too small to cause such a deflection. Using Hooke's law for cantilever C, the deflection due to the reflected photons should be no more than 0.7 nm/mW≡ 0.5 Å/mV, contrary to results shown in Table 4.1.

Thirdly, the values of force sensitivity (applied force per driving voltage) show remarkable differentiation, although they should be similar due to the use of constant DC laser power.

It became apparent that the bimetallic deflection of the cantilever contributed the most to the bending of the cantilever. However, the force generated by the bimetallic effect at the end of a cantilever cannot be measured by Hooke's law. This poses a challenging problem in the calibration process because analysis of a cantilever deformation under thermal loading is problematic and complicated (*2*). To experimentally measure the force and overcome the obstacle associated with the thermal deflection, two approaches were proposed. Both of those approaches will be described in the following sections.

4.3.1 Static method

The schematic diagram of the static method is depicted in Figure 4.5. Two opposing cantilevers are used; bimetallic and non-bimetallic. The non-bimetallic cantilever (a reference lever), is uncoated, thus unaffected by bimetallic action. The use of this cantilever is to counteract the thermally induced deflection of the bimetallic one. The bimetallic cantilever is placed on the backside of the reference cantilever. The resulting force felt by the reference cantilever is the resultant of the photon and photothermal forces. The reference cantilever deflects in response to the bending of the bimetallic cantilever, Figure 4.5.

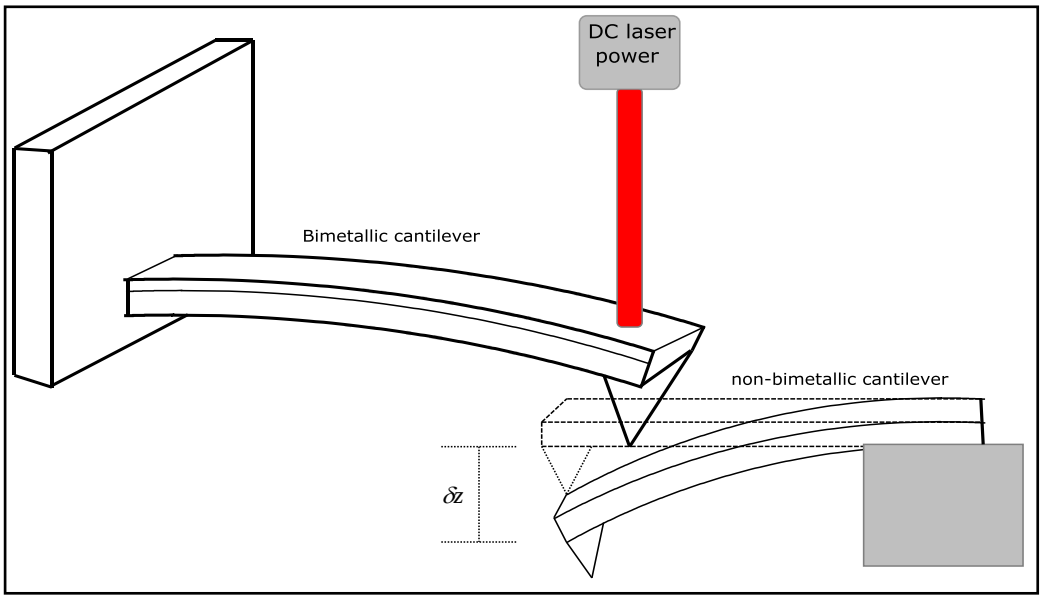

FIG.4.5 Schematic representation of the use of non-bimetallic cantilever to measure the thermal force acting on a bimetaliic cantilever.

The resistance of the reference lever to the applied loading (photothermal force) counteracts the bimetal cantilever deflection. The resistance is proportional to the loading applied and the reference lever stiffness. Thus, the photothermal force can be calculated by finding the countering force required to prevent the reference cantilever deflection (*3*). Therefore, Hooke's law is valid in an indirect way. For this, the effective force could be measured easily if the stiffness (k) and the deflection of the reference lever (Δz) are known. The true deflection of the reference cantilever due to the photothermal force is equal to (Δz) and found by subtracting the deflection of bimetallic cantilever with and without the reference cantilever. Consequently, the conversion factor from Volts to Newton can be found by plotting the driving voltage against the resulting force.

However, the use of a reference cantilever to measure the photothermal force has many difficulties. One of the disadvantages associated with this approach is that the use of a reference lever requires a tedious process of positioning the free end of the bimetallic lever onto the backside of the

reference cantilever. The free end of the bimetallic cantilever, which represents the load, may be applied far away from the end of the reference cantilever resulting in substantial error in the estimated force due to error in the reference cantilever spring constant(*4*) or torsional bending when the load is placed away from the cantilever midline(*5*). Due to this difficulty, the static method was abandoned and a more reliable method developed, as described in section 4.3.2.

4.3.2 Dynamic method

The excitation of a cantilever using an intensity- modulated laser beam is not new and has been demonstrated by several researchers (*6-10*). A particular vibration mode of a cantilever can be excited by focusing a power modulated laser on the cantilever. The laser illumination of the cantilever results in actuation of the cantilever mode either by photon or photothermal forces (*11*).

Here, we demonstrate for the first time, to our best knowledge, a V shaped cantilever actuation. One advantage of our system is that it allows us to modulate the AFM cantilevers with a wide spectrum of amplitudes and frequencies without the use of additional equipment. An example of application is to use the cantilever as a chemical sensor to detect masses in the range of 10^{-18} gm(*12*). In spite of the apparent advantage of using our system in applications that require cantilever actuation or modulation, we will focus on the calibration of the laser power.

The performance of the setup was demonstrated by actuating three V shaped cantilevers. Microcantilevers C, D and E. The cantilevers were immersed in PBS buffer. The modulated intensity laser acts at the free end, Figure 4.6. The effective force is the resultant of photon and

photothermal forces. Therefore, it is important to note that the effect we are interested in is the resulting oscillation of the cantilever regardless of the mechanism by which the laser actuates the cantilever. We need to determine the relationship between the laser power and the mechanical response of the cantilever and then model this relationship.

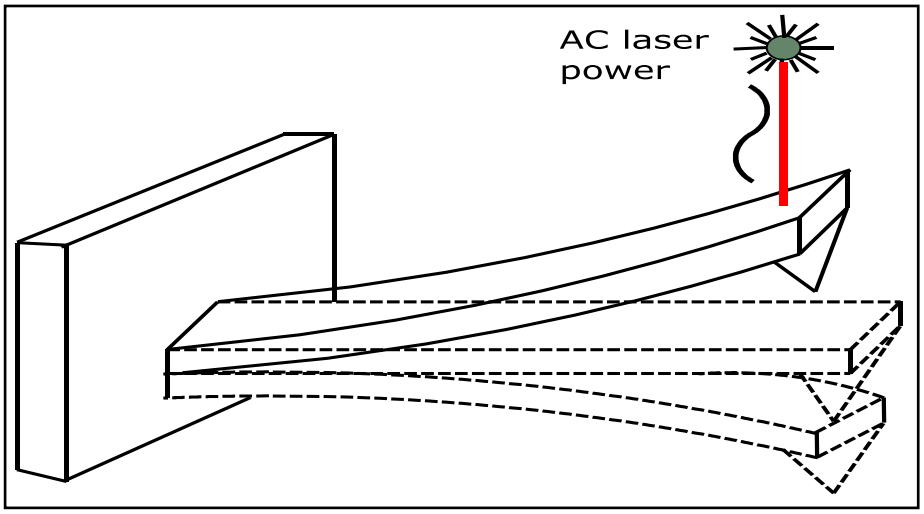

FIG.4.6 Cantilever is driven by a modulated-intensity laser focused on its free end.

The cantilever spring constant was independently measured using the thermal noise method (see chapter 2). The cantilever was irradiated by different constant (or DC) magnitudes of laser power, and each time the value of its stiffness was measured. This approach is valid as the DC laser power changes the position of cantilever and does not interfere with its dynamic motion due to thermal noise. The DC laser power causes a shift in the average position of the oscillating cantilever. The value of spring constant did not change and accordingly, the amount of LD2 power deposited on the cantilever does not modify its spring constant or resonant frequency, only its equilibrium position.

Figure 4.7 shows the mechanical response of mirocantilever C with stiffness of 10 pN/nm, excited by a sinusoidally modulated laser (LD2) at

different frequencies. Both the driving signal and the resulting motion of microlever C have the same frequency and can be modeled as a driven harmonic oscillator. The amplitude of the cantilever oscillation can be readily found using Figure 4.7.

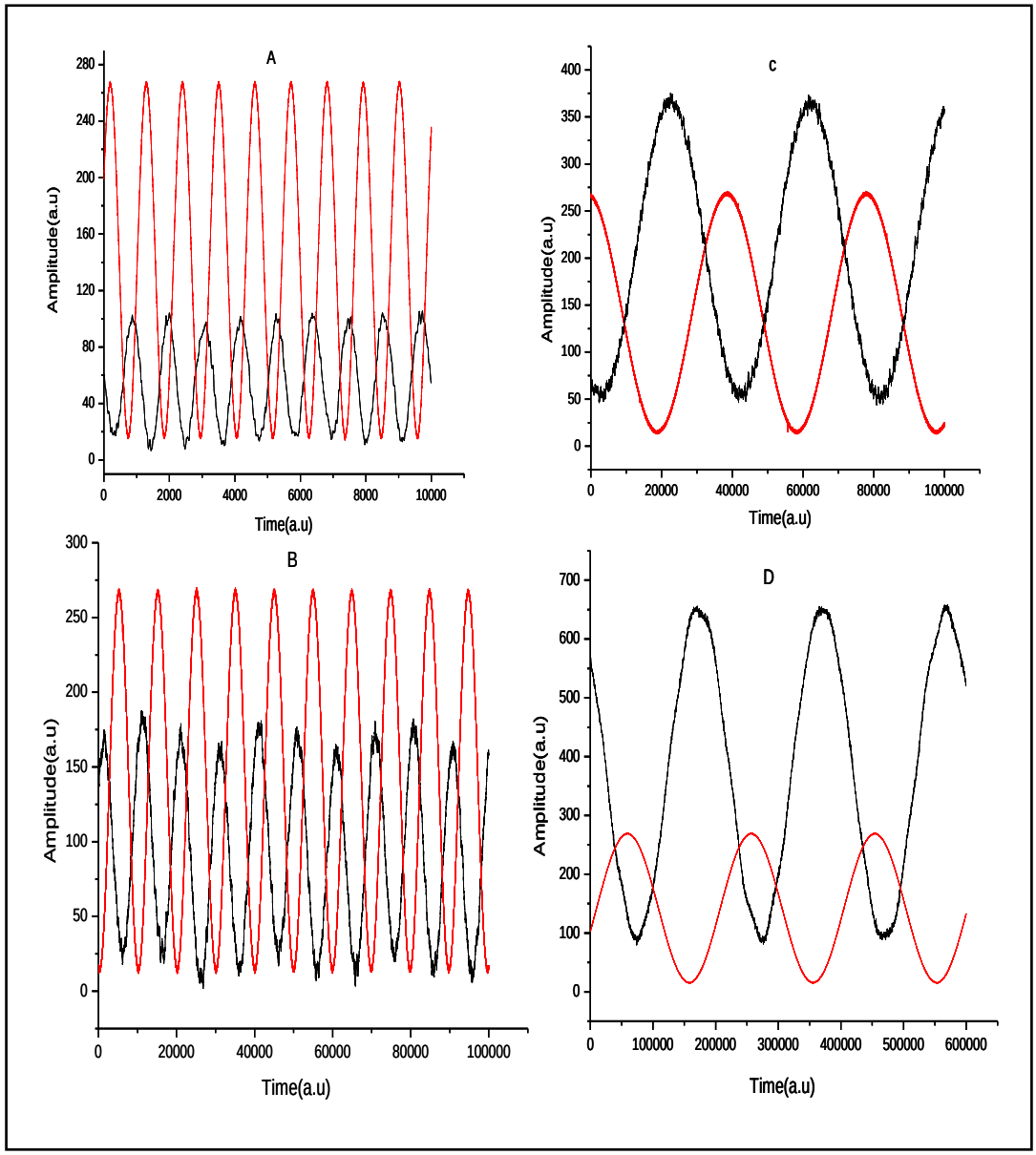

FIG.4.7 Cantilever C is actuated by intensity –modulated LD2, the driving signal of LD2 (red), 600 mV peak to peak, the resulting motion of the cantilever(black), at different driving frequencies: (A)900 Hz (B)100 Hz (c) 25 Hz (D) 5 Hz.

Figure 4.8 is a plot of the cantilever oscillation amplitude as a function of the driving voltage of LD2 at nine driving frequencies. It is obvious the resulting amplitude of the cantilever oscillation is frequency–dependent. For example, the resulting amplitude of the cantilever oscillation was found to be 0.23 nm/mV at a driving frequency of 1 Hz but this value drops to 0.08 nm/mV at 50 Hz.

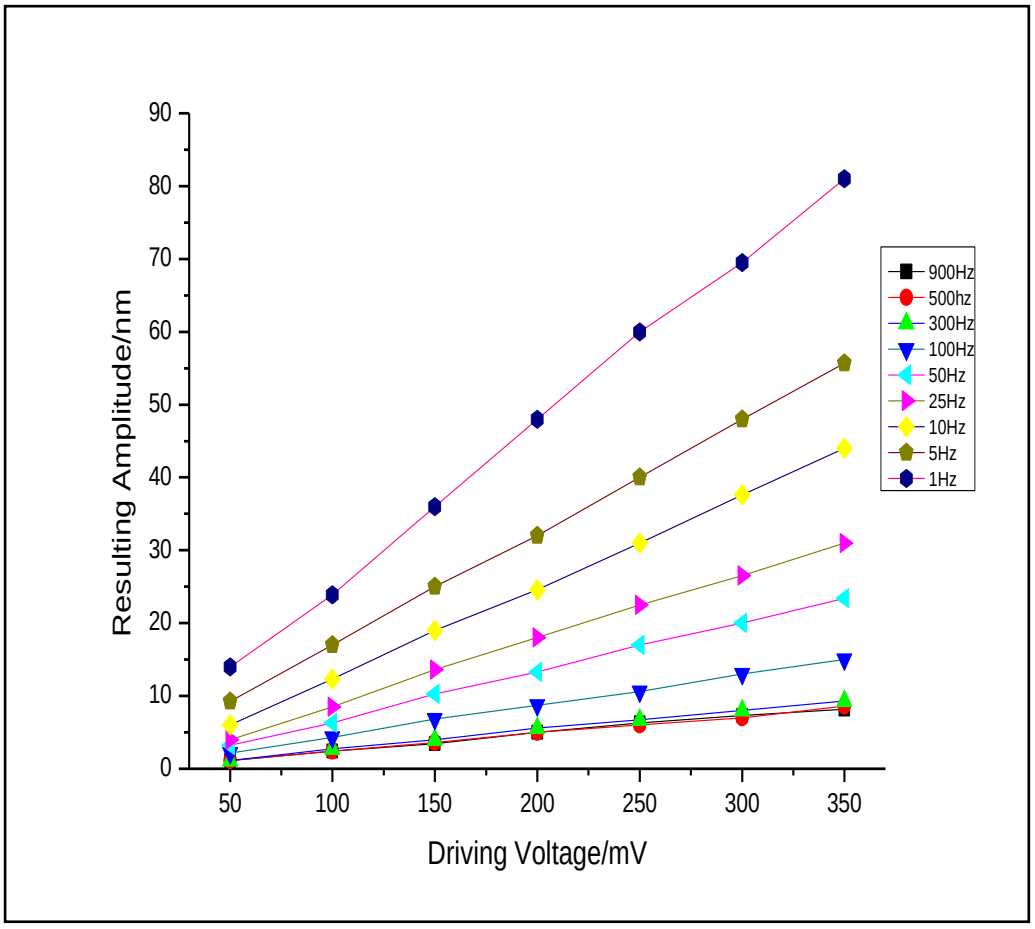

FIG.4.8 Dependence of the resulting amplitude on the driving voltage for the microlever

4.3.3 Modeling the cantilever oscillation

To model the cantilever oscillation in the light of a driven damped harmonic oscillator model, six approximations should be taken into account. First, the

effect of Brownian motion is not dominant and can be neglected in our calculations. Second, the two forces (photon and photothermal forces) acting on the cantilever are a periodic force. This assumption is reasonable because the forces originate from a modulated laser beam. The third approximation, the effect of hydrodynamic force can be neglected as the hydrodynamic effect is only detectable when the cantilever is actuated at velocities above 10 μm/s(*13*) which is higher than the most velocities (0.08-10 μm/s) at which the cantilever is driven. Fourth, the cantilever is far away from the surface so the tip-surface interactions have no effect on the cantilever dynamics. Fifth, the cantilever is assumed to be driven at its free end. Sixth, only the absolute motion of the cantilever can be considered regardless of the source of excitation.

Therefore, the governing equation of motion for the cantilever, depicted in Figure 4.6, can be written as

$$m\frac{d^2z(t)}{dt^2}+\gamma\frac{dz(t)}{dt}+\kappa z(t)=F\sin\omega t \qquad [4.5]$$

Here, F is the effective force acting at the free end of the cantilever, ω , γ, m and k are the angular driving frequency, the damping coefficient, mass and stiffness of the cantilever respectively. The right-hand side of Eq.4.5 is the frequency-dependent force due to the laser beam being modulated sinusoidally. Thus, both photon and photothermal forces at the tip show a sinusoidal-like oscillation.

In order to derive the oscillation amplitude (A) as a function of the driving force (F) and frequency (ω), Eq.4.5 can be rewritten using a complex exponential rather than sinϴ and dividing through by m.

$$\frac{d^2z(t)}{dt^2} + \frac{\omega_0}{Q}\frac{dz(t)}{dt} + {\omega_0}^2 z(t) = (F/m)e^{i\omega t} \qquad [4.6]$$

Where ${\omega_0}^2 = \kappa/m$ and $\gamma/m = \omega_0/Q$ here Q is the quality factor.

A particular solution could be in the form of $z(t) = Ae^{(i\omega t - i\theta)}$ which yields.

$$A = \frac{Fe^{i\theta}}{m(\omega_0^2 - \omega^2 + i\frac{\omega\omega_0}{Q})} \qquad [4.7]$$

Using, $e^{i\theta} = \cos\theta + i\sin\theta$, Eq.4.7 can be divided into two parts.

$$F\cos\theta = Am(\omega_0^2 - \omega^2) \qquad [4.8]$$

$$F\sin\theta = Am\frac{\omega\omega_0}{Q} \qquad [4.9]$$

Squaring and adding Eq.4.8 and Eq.4.9 to get rid of Θ gives

$$A = \frac{F\omega_0^2}{\kappa(\sqrt{(\omega_0^2 - \omega^2)^2 + \omega_0^2\omega^2 Q^{-2}})} \qquad [4.10]$$

Once the amplitude is determined (Figure 4.8) the driving force can be calculated from Eq.4.10.

4.3.4 Calibrating laser power

Figure 4.9 is a plot of the excitation force (computed using Eq.4.10 and the data from Figure 4.8) versus driving voltage. In Figure 4.9, the excitation force increases linearly with driving voltage, where the slope of this linear relationship gives the calibration of applied force with respect to driving

voltage (in unit of pN/mV), called from now on force sensitivity (F_s) which is constant for each driving frequency.

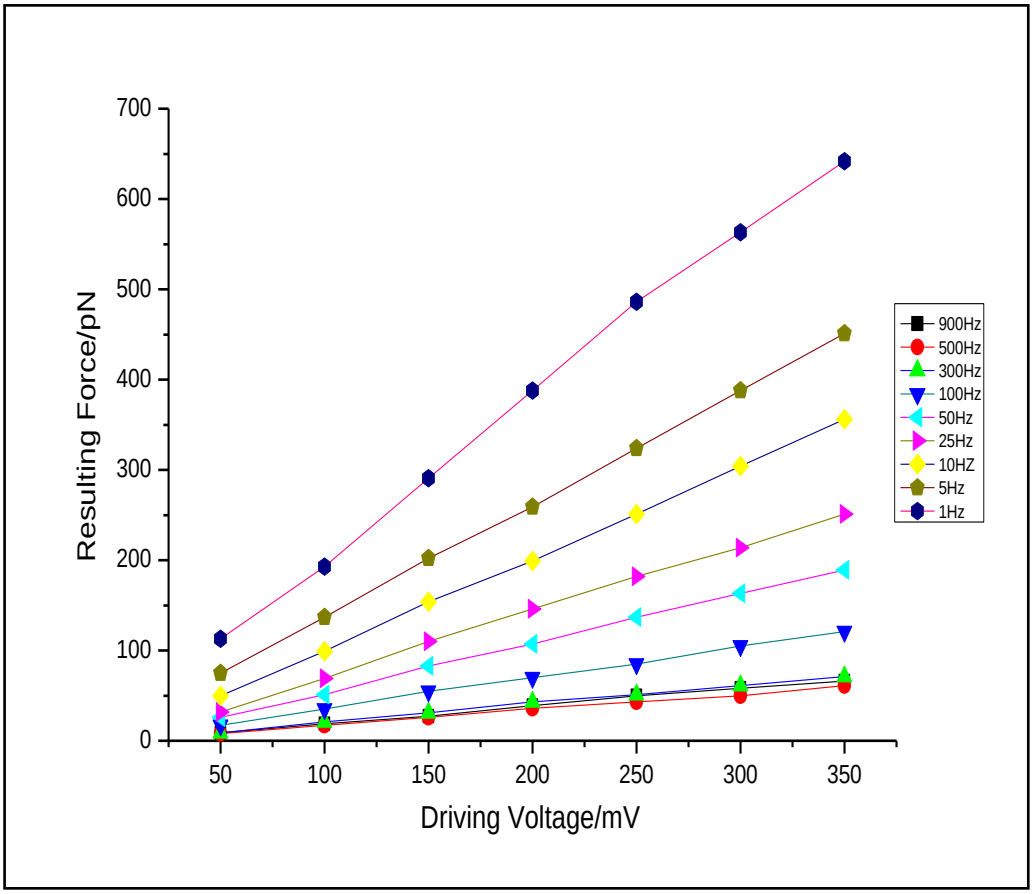

FIG.4.9 Dependence of the resulting force with the driving voltage for microlever-C.

According to Eq.4.10, if the excitation force is constant the resulting amplitude must decrease at driving frequencies less or higher than the cantilever resonance frequency (~900 Hz). However, Figure 4.8 shows that resulting amplitudes at driving frequencies less than the cantilever resonance frequency increases. This result seems paradoxical, if the excitation force is constant. To overcome this discrepancy, it should be assumed that the excitation force has more than one value and it is frequency-dependent.

In Figure 4.10, the force sensitivity (F_s) is plotted as a function of driving frequencies. The change in the driving frequency affects the force sensitivity non-linearly. It is clear that the force sensitivity of the microlever C can be divided into two frequency regions. In region 1, above 300 Hz, the magnitude of force sensitivity shows no change, ~0.2 pN/mV, leading to a conclusion that the source of the excitation force in this region is not frequency dependent. Later, this will be shown to be the photon force.

In region 2, below 300 Hz, the force sensitivity increases exponentially with decreasing driving frequencies leading to a conclusion that the excitation force in region 2 is frequency-dependent. The force sensitivity is ~0.5 pN/mV at 50 Hz and 1.5 pN/mV at 2 Hz. Later we will show the source of the excitation force in the region two is photothermal force. The two regions are more clearly defined when frequency is plotted using a log scale (Figure 4.10 inset).

.

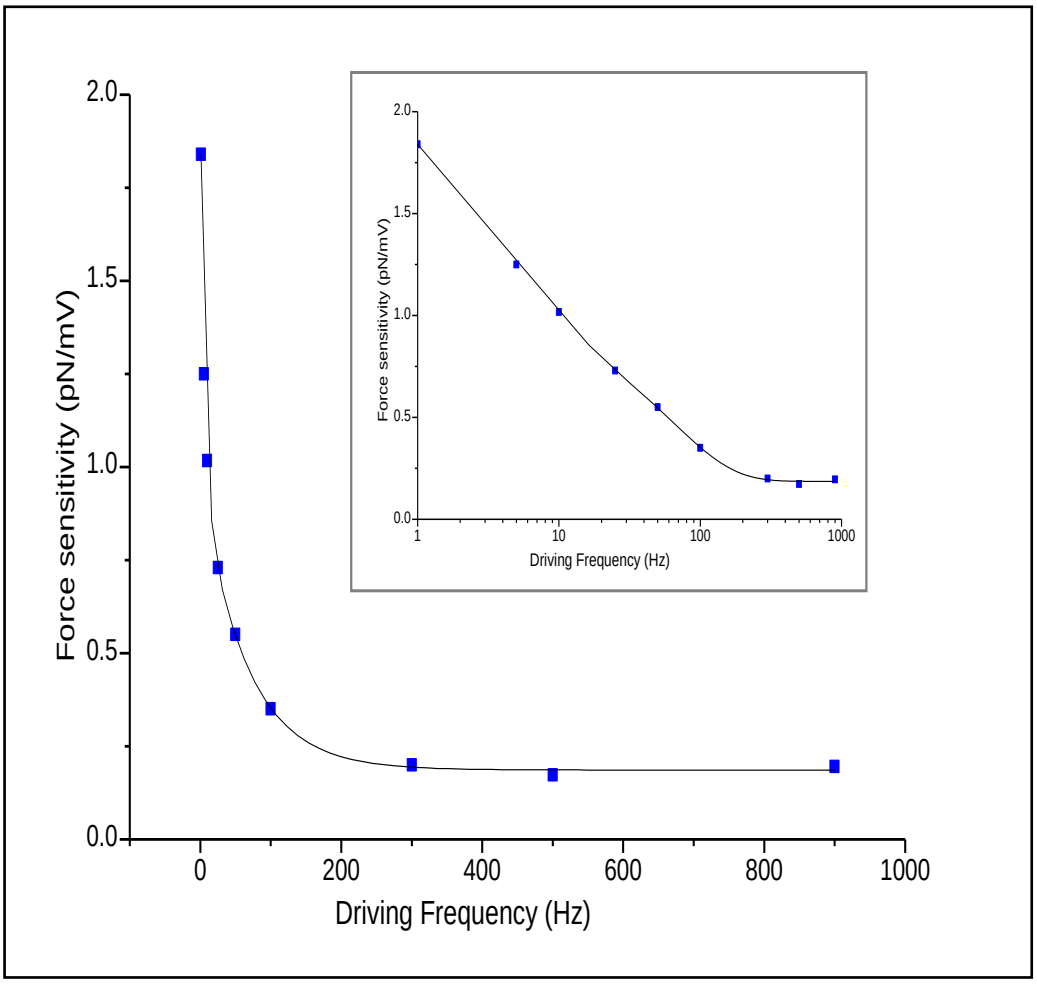

FIG.4.10 Dependence of force sensitivity with the driving frequency for microlever-C. The force sensitivity response to the driving frequencies is fitted to a triple exponential decay function $F_s = r_0 + r_1 \exp(\frac{-(\nu+1.91)}{\upsilon_1}) + r_2 \exp(\frac{-(\nu+1.91)}{\upsilon_2}) + r_3 \exp(\frac{-(\nu+1.91)}{\upsilon_3})$ **where r0=0.2 pN/mv, r1=762.7 pN.mv, r2=0.964 pN/mv, r3=0.798 pN/mv, υ1=0.365 Hz, υ2=6.74 Hz, υ3=65 Hz and the driving frequency υ. Inset shows the figure in log scale.**

4.3.5 Photon force limit

As discussed at the beginning of this chapter, the magnitude of force applied by photon force with respect to laser power is ~ 6.7 pN/mW. Taking into consideration the laser power output to driving voltage is 15 mV/mW, and the actual power incident on the cantilever is approximately half its

initial value (see chapter 3) the force sensitivity due to photon force theoretically should be approximately 0.22 pN/mV.

In the previous section, the deflection sensitivity of the cantilever C with respect to driving frequency was shown to exhibit two regions. In Figure 4.11 the cantilevers D and E both show a similar behavior. In region 1 the force sensitivity is constant and then in region 2 the force sensitivity increases exponentially with decreasing the driving frequency. The force sensitivity in region 1 is ~0.2 pN/mV. This value agrees very well with the calculated force sensitivity of photon force, 0.22 pN/m. This gives an indication that the force sensitivity limited by photon force is ~0.2 pN/mV.

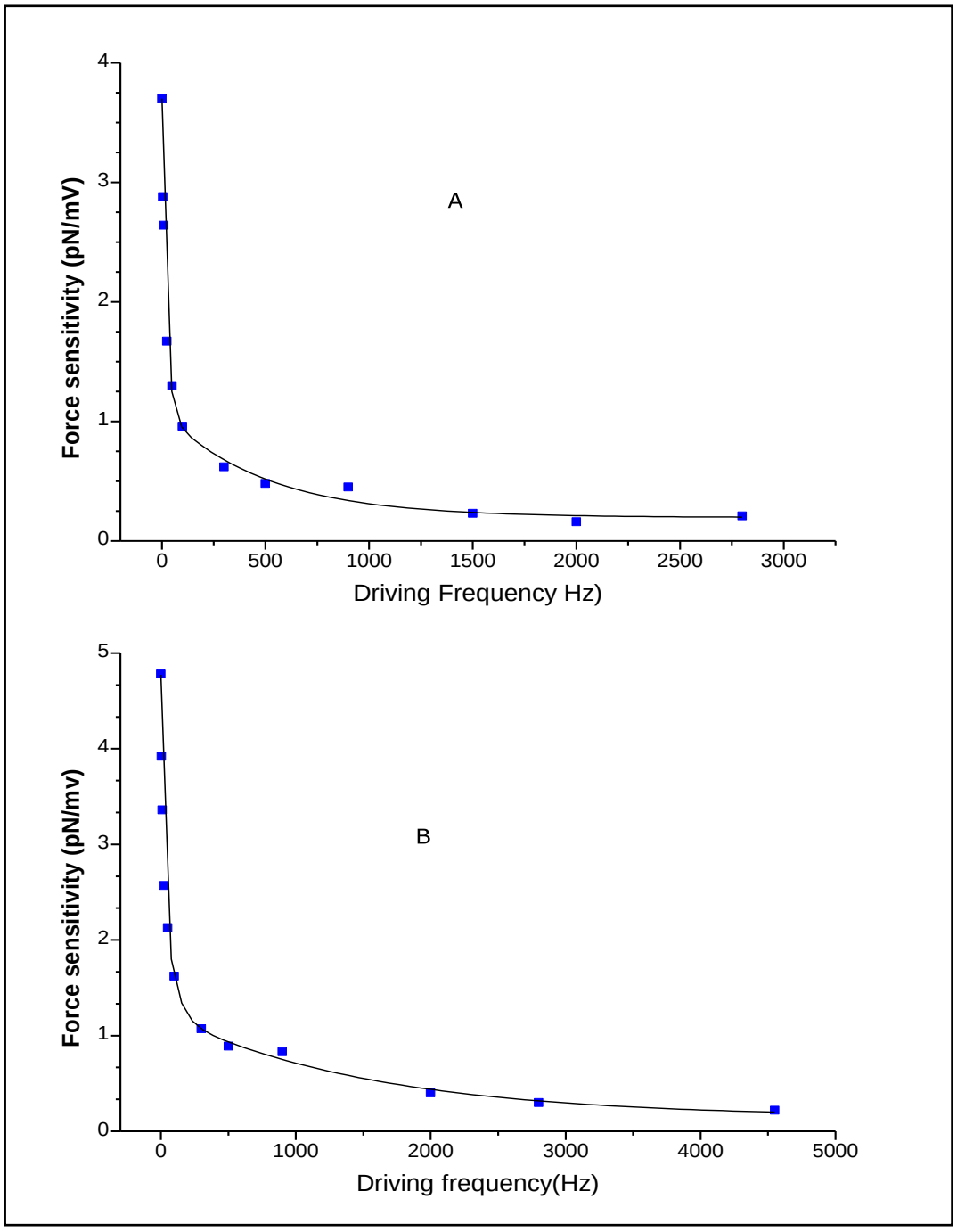

FIG.4.11 Dependence of force sensitivity with the driving frequency for microlever-D (A) and microlever-E(B)

Moreover, if the source of the deflecting force is just the photon force, the force sensitivity value must be similar for all cantilevers because it does not depend on the properties of the cantilever, it just relies on laser power.

Figure 4.11 shows the driving frequency dependence of force sensitivity for two cantilevers; cantilever D and cantilever E. In region1, both cantilevers have constant force sensitivity (~ 0.2 pN/nm).

However, the effect of photothermal force of cantilevers D and E starts earlier than that of microlever C. For instance, the force sensitivity of the microcantilever D (the resonance frequency in water is 2700 Hz) increases at the driving frequency of 1300 Hz and at 3000 Hz for cantilever E (the resonance frequency in water is 4600 Hz). This difference is reasonable due to the variation of thermal properties of the cantilevers.

As follows from the above results, the value of force sensitivity in the vicinity of their resonance frequency was similar for all cantilevers. This agreement leads to a conclusion that at particular driving frequencies close to and above the resonance frequency of a cantilever the exciting force is just photon force.

4.3.6 Photothermal force limit

In the above sections, we demonstrated that two forces cause the cantilever oscillations: photon and photothermal forces. Photothermal force has a detectable effect when the cantilever is actuated in low frequency regime, < 300 Hz for the microcantilever C. In this section, we will derive theoretically the frequency limit of the photothermal force, for cantilever C. For this purpose, the thermally derived deflection of cantilever C is related to frequency at which the heating source is modulated.

Theoretically, the bending of the bimetallic cantilever ($\Delta z_{heating}$) (*14, 15*), Figure 4.12, is given by

$$\Delta z_{heating} = \frac{3(\alpha_2 E_2 - \alpha_1 E_1)}{(h_1 + h_2)(E_1 E_2)} \frac{1 + \left(\frac{h_2}{h_1}\right)^2}{3\left(1 + \left(\frac{h_2}{h_1}\right)\right)^2 + \left(1 + \frac{E_2}{E_1}\frac{h_2}{h_1}\right)\left(\frac{h_2^2}{h_1^2} + \frac{E_1}{E_2}\frac{h_1}{h_2}\right)} l^2 \Delta T (E_1 + E_2)$$

[4.11]

Where α is the thermal expansion coefficient, E is Young's modulus, h is the thickness of the layer, ΔT is the change of the temperature and the subscript 1 and 2 denote silicon nitride (Si_3N_4) and the gold layer (Au) respectively.

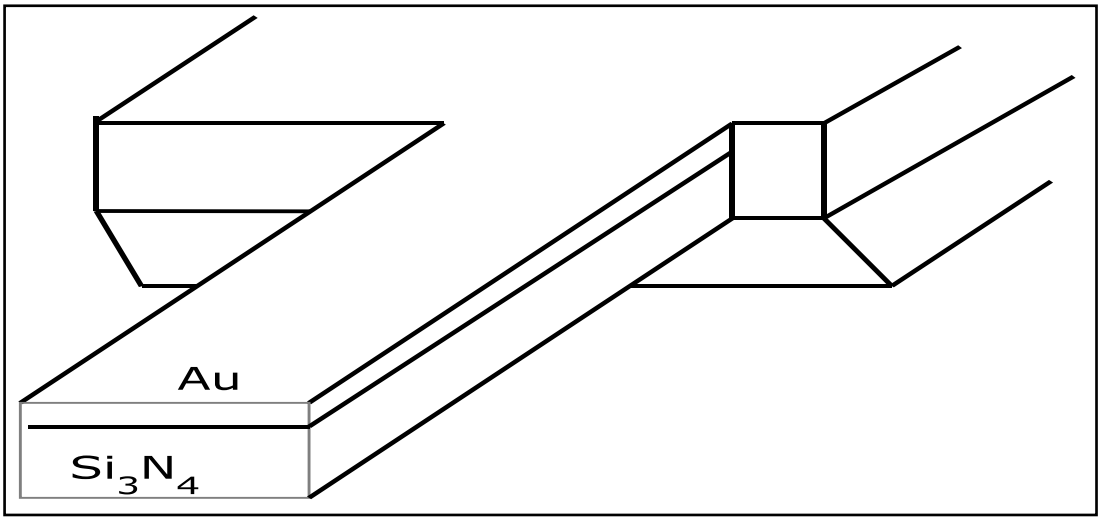

FIG.4.12 A schematic of a bimetallic cantilever used in the experiment.

According to Eq.4.11 the thermal bending ($\Delta z_{heating}$) of a cantilever depends on the change of the cantilever temperature, the mechanical and thermal properties of the cantilever. For a particular cantilever, the mechanical and thermal properties are constant. However, in the case of modulated-frequency heating source focused on the backside of a cantilever, the change of temperature (ΔT) is frequency-dependent(*16*).

The temperature distribution (T) within a cantilever can be described by the heat diffusion equation(*16, 17*).

$$\nabla^2 T - (\frac{\rho_1 C_1 + \rho_1 C_1}{\lambda_1 + \lambda_2})\frac{\partial T}{\partial t} = 0 \qquad [4.12]$$

Where ρ is the density, C is the specific heat (heat energy required to raise 1kg of a substance 1K) and λ is thermal conductivity (ability to conduct heat), the subscript 1 and 2 denote silicon nitride (Si_3N_4) and the gold layer (Au) respectively.

As shown in Figure 4.13, the temperature distribution along the cantilever is a one-dimensional propagation (X-direction) due to a) the temperature along the cantilever width (Y-direction) being constant because the laser spot size is comparable with the cantilever width and b) in the z dimension, the thickness of the cantilever, is much smaller than the length of the cantilever(*16*). Therefore, the heat diffusion equation can be written as

$$\frac{\partial^2 T}{\partial x^2} - (\frac{\rho_1 C_1 + \rho_1 C_1}{\lambda_1 + \lambda_2})\frac{\partial T}{\partial t} = 0 \qquad [4.13]$$

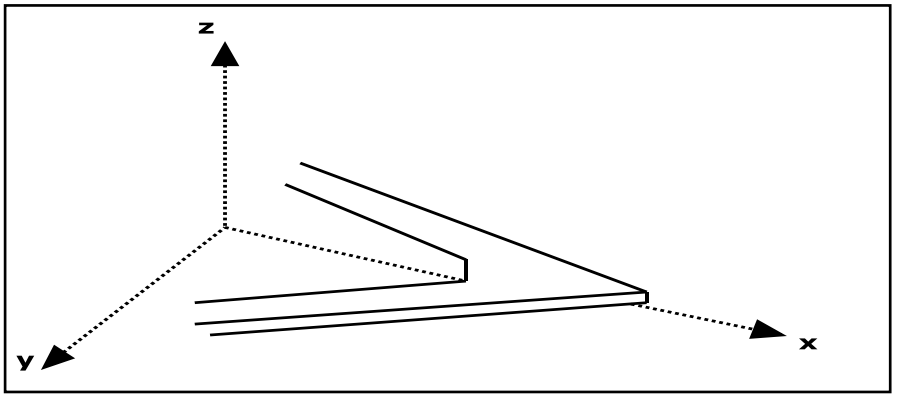

FIG.4.13 Model geometry of a V shaped cantilever.

However, Eq.4.13 cannot be a complete description of the temperature distribution in the cantilever. A simple conclusion drawn from Eq.4.13 is that the speed of heat propagation is infinite. As a consequence, if, for example, an end of a rod is heated, the temperature of the second end increases simultaneously(*18*). In reality this not true, so to overcome this drawback Cattaneo proposed a modification to Eq.4.13 by introducing the relaxation time (τ)(*19, 20*) leading to

$$\frac{\partial^2 T}{\partial x^2} - \left(\frac{\rho_1 C_1 + \rho_1 C_1}{\lambda_1 + \lambda_2}\right)\frac{\partial T}{\partial t} - \left(\frac{\rho_1 C_1 + \rho_2 C_2}{\lambda_1 + \lambda_2}\right)\tau \frac{\partial^2 T}{\partial t^2} = 0 \qquad [4.14]$$

The form of Eq.4.14 has a similarity to the wave equation ($\frac{\partial^2 y}{\partial x^2} + \frac{1}{\upsilon^2}\frac{\partial^2 y}{\partial t^2} = 0$). The parameters υ in the wave equation is the wave propagation speed. By introducing the term $\left(\frac{\rho_1 C_1 + \rho_2 C_2}{\lambda_1 + \lambda_2}\right)\tau$ in Eq.4.14 Cattaneo solved the paradox of infinite speed of heat diffusion for the thermal wave.

The relaxation time or thermal diffusion time of a cantilever can be given by(*21, 22*)

$$\tau = \frac{l}{2}^2 \frac{\rho_1 h_1 C_1 + \rho_2 h_2 C_2}{\lambda_1 h_1 + \lambda_2 h_2} \qquad [4.15]$$

Where ι is the length of the cantilever, C is the specific heat, λ is the thermal conductivity and h is the thickness. The subscript 1 and 2 denote silicon nitride (Si_3N_4) and the gold layer (Au) respectively.

The predicted value of τ for microcantilever C based on Eq.4.15 and Table 4.2 is ~2 ms, for microcantilver D and E are ~0.8 ms and ~0.4 ms

respectively. The conclusion that the temperature could propagate inside the cantilever as a physical wave when excited by a periodic heat source has been confirmed by many authors (*23-26*). Ramos et al(*16*) proposed that the distribution may be considered as a heavily damped wave in which the amplitude of the temperature decays along the cantilever exponentially, Figure 4.14, with decay constant equal to the thermal diffusion length (the distance along the cantilever at which the amplitude of temperature falls to 1/e of its origin value).

The response of the cantilever to the photothermal force is subject to the time taken to diffuse the thermal energy along the cantilever (τ). Therefore, if the time taken to modulate the heating source is less (i.e., higher frequency) than the time for the thermal wave to propagate along the lever, the physical effect of the photothermal force will be negligible(*24, 27*).

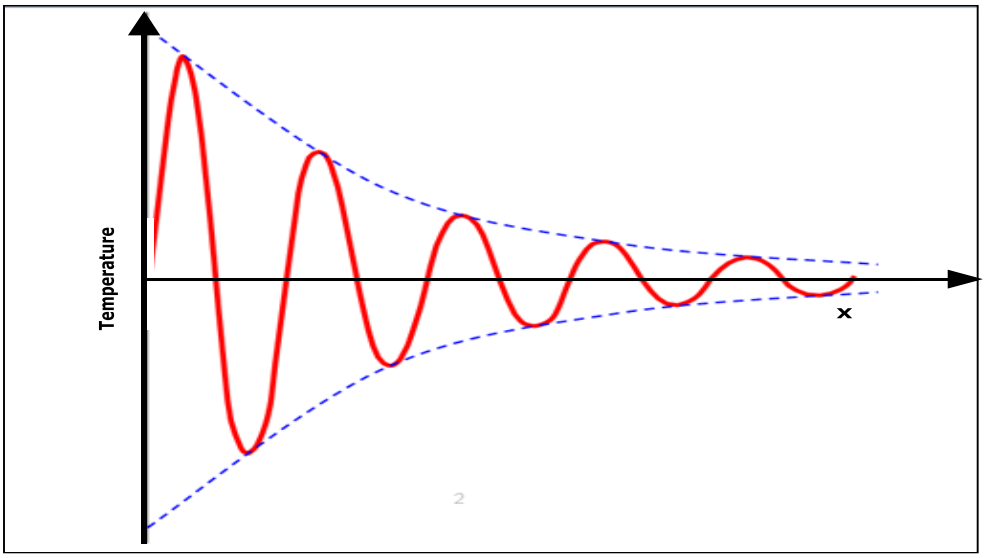

FIG.4.14 Propagation of thermal wave along a cantilever as a damped harmonic wave.

Table 4.2 Thermophysical properties of the materials used in cantilevers C, D and E(*16, 17, 21*)

	ρ(kg/m$^{)}$	λ(W/mK)	C(J/kg.K)	α (K^{-1})	E(Nm^{-2})	h(nm)
Si_3N_4	3400	32	750	3×10^{-6}	1.8×10^{11}	600
Au	19300	317	130	14.2×10^{-6}	0.8×10^{11}	60

The assumption that the distribution of temperature through the lever behaves as a wave leads to the solution of the equation being a function of the modulation frequency. Thus, when the cantilever is irradiated by a sinusoidally modulated laser beam with amplitude P_0 the change in the cantilever temperature can be described by (*28*)

$$\Delta T(x,t) = \frac{\beta P_0}{H_C\sqrt{1+\omega^2\tau^2}} \qquad [4.16]$$

Where β is the absorbed fraction of the radiant power and H_C is the heat capacity.

According to Eq.4.16 the change of the cantilever temperature is frequency dependent. By substituting Eq.4.16 into Eq.4.11, the thermal bending of the cantilever can be expressed as

$$\Delta z_{heating} = \frac{3(\alpha_2 E_2 - \alpha_1 E_1)}{(h_1 + h_2)(E_1 E_2)} \frac{1 + \left(\frac{h_2}{h_1}\right)^2}{3\left(1 + \left(\frac{h_2}{h_1}\right)\right)^2 + \left(1 + \frac{E_2}{E_1}\frac{h_2}{h_1}\right)\left(\frac{h_2^2}{h_1^2} + \frac{E_1}{E_2}\frac{h_1}{h_2}\right)} l^2 \frac{\beta P_0}{H_C \sqrt{1 + \omega^2 \tau^2}} (E_1 + E_2)$$

[4.17]

Eq.4.17 reveals that the thermal deflection of the cantilever is frequency-dependent. For a specific cantilever, the thermal deflection could increase more than tenfold when the modulation frequency of the heating source decreases from 900 Hz to 1 Hz. In order to relate the thermal deflection of the cantilever to the driving frequency, we introduce the relative bending which is the thermally normalized deflection to the deflection at 900 Hz. Figure 4.15 is a plot of relative bending of cantilever C versus frequency. The relative bending of the cantilever starts to increase exponentially with decreasing the driving frequency below 400 Hz. These results are in a good agreement with the experimental results. Therefore, the deflection of the cantilever at frequencies less than 400 Hz is due to photothermal force.

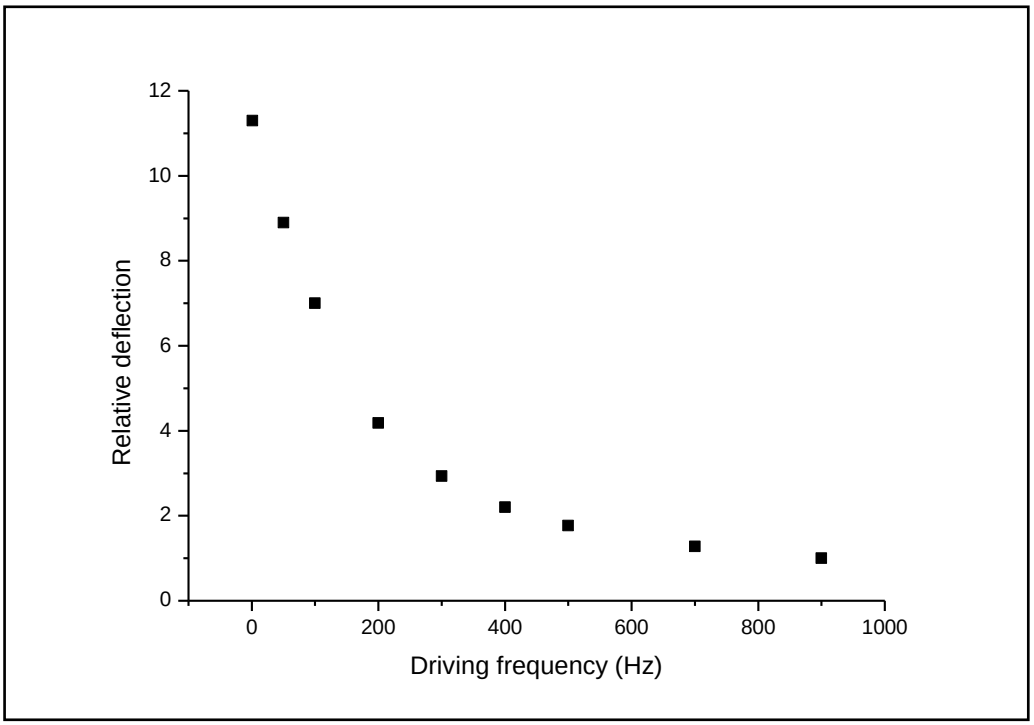

FIG.4.15 Theoretical relative deflection of cantilever C as function of laser beam modulation frequency, calculated using Eq.4.17 and normalized to the bending of the cantilever at 900 Hz.

4.4 Conclusion

Here, a method to convert laser power to force was presented. The calibration is based on relating the force sensitivity (converting the driving voltage of laser intensity into force) to the frequency at which the cantilever is driven. Therefore, the force sensitivity can be used as a conversion factor. Furthermore, it has been shown that the cantilever driven harmonically using laser intensity modulated sinusoidally can be treated as forced harmonic system and all equations of the harmonic system are applicable.

We have demonstrated that the force sensitivity depends upon mechanical properties of the cantilever by calculating it for three cantilevers. In

addition, we have shown the excitation force acting on a cantilever modulated using a periodic heat source (for example a laser beam) is not constant. They are frequency-dependent. The impact of photothermal force is dependent upon the modulation frequency of heating source, and thermal properties of cantilevers. So, the photothermal force becomes more distinct at lower modulation frequency resulting in an increase of the oscillation amplitude of the microlever.

Using the concept that the distribution of temperature along cantilevers can take wave-like form, we demonstrated that the theoretical results agree well with the experimental results. Finally, it is worth noting that cantilever C, based on Eq.4.17 and Table 4.2 shows a deflection of 188 nm per Kelvin. Usually AFM cantilevers show a measurable deflection when its temperature changes by just 10^{-5} K(*21, 22, 29*). Therefore, the effect of using laser power to control the cantilever deflection on the sample temperature investigated by CD-AFM may be negligible.

4.5 References

(1) Tamihiro, G. (2009) Photothermal technique using individual cantilevers for quality monitoring in thin film devices. *Review of Scientific Instruments 80*, 074902.

(2) Tsai, H. H., and Hocheng, H. (1998) Investigation of the transient thermal deflection and stresses of the workpiece in surface grinding with the application of a cryogenic magnetic chuck. *Journal of Materials Processing Technology 79*, 177-184.

(3) Wen-Hwa, C., Mehregany, M., and Mullen, R. L. (1993) Analysis of tip deflection and force of a bimetallic cantilever microactuator. *Journal of Micromechanics and Microengineering*, 4.

(4) John, E. S., Ian, L., Paul, M., and Lee, R. W. (1995) Method for the calibration of atomic force microscope cantilevers. *Review of Scientific Instruments 66*, 3789-3798.

(5) Peter, J. C., Charles, A. C., and John, H. (2004) Quantitative analytical atomic force microscopy: a cantilever reference device for easy and accurate AFM spring-constant calibration. *Measurement Science and Technology*, 1337.

(6) Glenn, C. R., Dorothy, A. E., and Richard, S. (1998) Photothermal modulation for oscillating mode atomic force microscopy in solution. *Applied Physics Letters 72*, 1911-1913.

(7) Shuhei, N., Dai, K., Takeo, S., Tomonori, N., Yasuo, H., and Hideki, K. (2008) Photothermal excitation and laser Doppler velocimetry of higher cantilever vibration modes for dynamic atomic force microscopy in liquid. *Review of Scientific Instruments 79*, 123703.

(8) Umeda, N., Ishizaki, S., and Uwai, H. (1991) pp 1318-1322, AVS.

(9) Nickolay, V. L., and Panos, G. D. (2003) Femtogram mass detection using photothermally actuated nanomechanical resonators. *Applied Physics Letters 82*, 2697-2699.

(10) Ilic, B., Krylov, S., Aubin, K., Reichenbach, R., and Craighead, H. G. (2005) Optical excitation of nanoelectromechanical oscillators. *Applied Physics Letters 86*, 193114.

(11) Hayato, Y., Noriyuki, K., Atsushi, M., Takayuki, U., Daisuke, Y., and Toshio, A. (2007) Tip-sample distance control using photothermal actuation of a small cantilever for high-speed atomic force microscopy. *Review of Scientific Instruments 78*, 083702.

(12) Soren, D., Rasmus, S., Winnie, S., and Anja, B. (2005) Enhanced functionality of cantilever based mass sensors using higher modes. *Applied Physics Letters 86*, 233501.

(13) Janovjak, H., Struckmeier, J., and Müller, D. J. (2005) Hydrodynamic effects in fast AFM single-molecule force measurements. *European Biophysics Journal 34*, 91-96.

(14) Wachter, E. A., Thundat, T., Oden, P. I., Warmack, R. J., Datskos, P. G., and Sharp, S. L. (1996) Remote optical detection using microcantilevers. *Review of Scientific Instruments 67*, 3434-3439.

(15) Shaver, P. J. (1969) Bimetal Strip Hydrogen Gas Detectors. *Review of Scientific Instruments 40*, 901-905.

(16) Ramos, D., Tamayo, J., Mertens, J., and Calleja, M. (2006) Photothermal excitation of microcantilevers in liquids. *Journal of Applied Physics 99*, 124904.

(17) Almond, D. P., and Patel, P. M. (1996) *Photothermal science and techniques*, Vol. 10, First ed., Chapman and Hall, London.

(18) Alvarez-Ramirez, J., Fernandez-Anaya, G., Valdes-Parada, F. J., and Alberto Ochoa-Tapia, J. (2006) A high-order extension for the Cattaneo's diffusion equation. *Physica A: Statistical Mechanics and its Applications 368*, 345-354.

(19) Mandelis, A. (1992) in *Progress in photothermal and photoacostic science and technology.* pp 160-250, Elsevier., New York.

(20) Barnes, J. R., Stephenson, R. J., Woodburn, C. N., Shea, S. J. O., Welland, M. E., Rayment, T., Gimzewski, J. K., and Ch, G. (1994) A femtojoule calorimeter using micromechanical sensors. *Review of Scientific Instruments 65*, 3793-3798.

(21) Gimzewski, J. K., Gerber, C., Meyer, E., and Schlittler, R. R. (1994) Observation of a chemical reaction using a micromechanical sensor. *Chemical Physics Letters 217*, 589-594.

(22) Rohsenow, W. M., Hartnett, J. P., and Cho, Y. I. (1997) *Handbook of Heat Transfer*, McGraw-Hill, London.

(23) Agustin, S. (2006) Energy propagation of thermal waves. *European Journal of Physics*, 1349.

(24) Galovic, S., Kostoski, D., Stamboliev, G., and Suljovrujic, E. (2003) Thermal wave propagation in media with thermal memory induced by pulsed laser irradiation. *Radiation Physics and Chemistry 67*, 459-461.

(25) Marin, E., Marin-Antuna, J., and Diaz-Arencibia, P. (2002) On the wave treatment of the conduction of heat in photothermal experiments with solids. *European Journal of Physics*, 523.

(26) Metzger, C., Favero, I., Ortlieb, A., and Karrai, K. (2007) Opto-Mechanics of deformable Fabry-Perot Cavities. *arXiv e-print. arxiv:0707.4153*.

(27) Datskos, P. G., Lavrik, N. V., and Rajic, S. (2004) Performance of uncooled microcantilever thermal detectors. *Review of Scientific Instruments 75*, 1134-1148.

(28) Watcher, E. A., Thundat, T., Oden, P. I., Warmack, R. J., Datskos, P. G., and Sharp, S. L. (1996) Remote optical detection using microcantilevers. *Rev. Sci. Instrum. 67*, 34343439.

Chapter 5
Interpretation of force-distance curves acquired from the laser power required to lock a cantilever

5.1 Overview

AFM force-distance curves have become a powerful tool to analyze and study surface forces and materials properties. Valuable information related to the nature of intermolecular forces, generated between the tip and the surface, and mechanical properties of surface such as elasticity have been characterized and measured by force-distance curves. As described in the previous chapters, the atomic force microscope can be used to acquire force-distance curves by means of plotting the cantilever deflection converted to force as a function of the tip-surface separation.

However, due to the increasing interest in small force measurements, the stiffness of the cantilever is getting smaller. Achieving high force resolution involves using softer cantilevers. However, the increase in the force resolution comes at the expense of cantilever instability. Two major sources of cantilever instability can cause uncertainty or discontinuity in force –distance curves: thermodynamic noise (Brownian motion) and non-equilibrium or transient events close to the surface, such as jump-to-contact or jump-off.

In chapter 3, it has been demonstrated the effect of thermodynamic noise (Brownian motion) on cantilever stability. For example, a cantilever with stiffness of 0.01 N/m could suffer from a spatial fluctuation of ~3 nm that can cause an uncertainty in force resolution by ~30 pN. Thus, the zero line could oscillate by approximately 30 pN causing an uncertainty in the force measured. Furthermore, due to the gradient of attractive force in the proximity of the surface exceeding the cantilever spring constant, the cantilever becomes unstable and the tip jumps to the sample surface leaving a discontinuity in the force-distance curve, which may be a few or hundreds of Å(*1*) depending on the stiffness of the cantilever, the lower the cantilever stiffness the higher the tip-surface separation (*1-4*). Thus, valuable information about the interaction between the cantilever tip and the sample surface may be lost.

The problem of jump-to-contact and thermodynamic noise can be minimized by increasing the cantilever stiffness, thus allowing the cantilever tip to approach close to the surface further. However, the use of a stiffer cantilever comes at the expense of the force sensitivity(*5*).

These instabilities can be avoided without using a stiffer cantilever. The cantilever position can be fixed by applying a balancing force while the sample surface is moved towards the cantilever. Methods based on force-

feedback control have been employed. These methods have proven capable of preventing such instabilities and increasing the accuracy in force-distance curves. The balancing force can be, for example, electrostatic or magnetic forces, and more details about these methods can be found in chapter 3.

Although CD-AFM can be used to deal with difficulties associated with cantilever instabilities, the focus of this chapter is to obtain and interpret the force-distance curves using the laser power signal instead of the cantilever deflection. In this chapter, it will be shown that CD-AFM can provide similar force and spatial resolution to those obtained by the softest V-shaped cantilever available in market but without disadvantages associated with instability of this cantilever.

5.2 Experimental setup

Figure 5.1 shows the experimental configuration used to obtain the force distance curves. The experiments have been carried out using CD-AFM illustrated in chapter 3. The cantilever used is commercial available microcantilever C (Veeco, k= 0.01 N/m).

In order to acquire the curves, CD-AFM is first operated in the standard force spectroscopy mode by switching the feedback force off. Then the cantilever is retracted a sufficient distance from the surface to minimize tip-surface interactions. This procedure is necessary as the tip-surface interactions may affect the locking process (see chapter 3). At this point, the feedback force is switched on and the cantilever deflection is locked to ~0.3 nm. The range of the force curve is controlled automatically using the "trigger threshold" feature of the AFM, where the tip is retracted when it

achieves a set deflection. As the lever is locked, a positive deflection represents a loss of lock. Therefore, to minimize the duration of this off-lock, the trigger is set at 2nm (the lowest stable trigger threshold). Thus, the 2 nm limit will be used for all force measurements by CD-AFM.

The surface is moved towards the locked cantilever using the piezoscanner. Since the cantilever deflection is no longer available, the tip-surface interactions are read out by the laser signal used to lock the position of the cantilever.

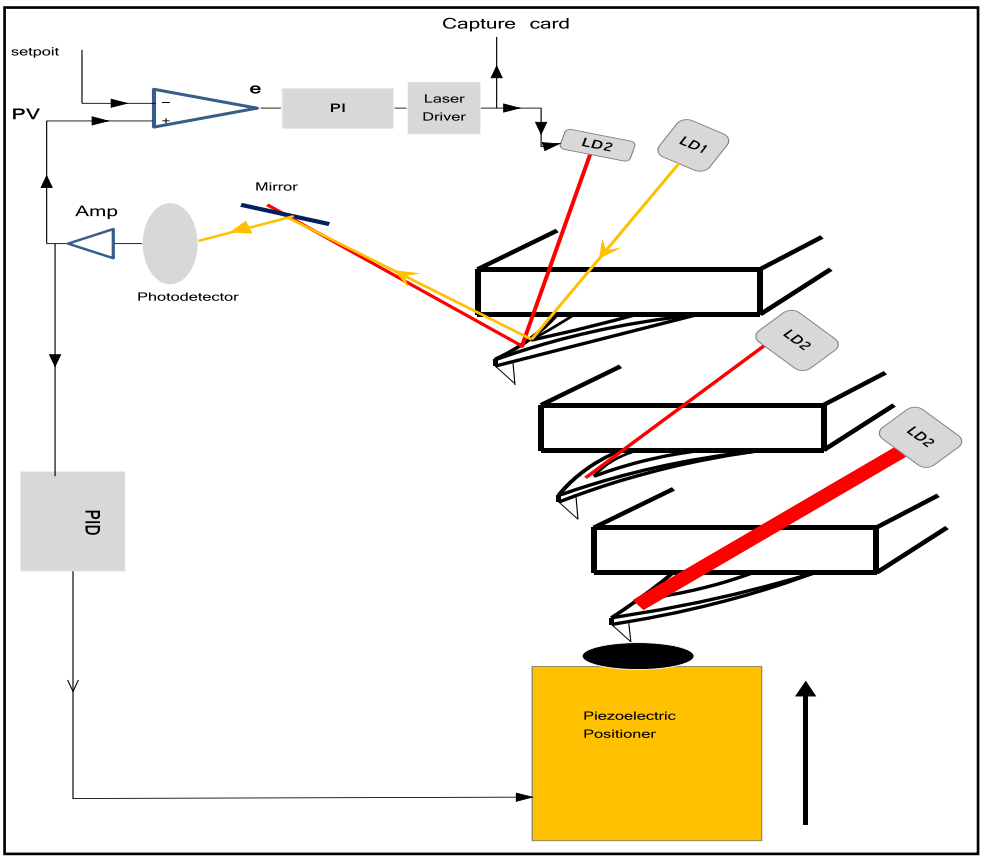

FIG.5.1 Experimental setup used to obtain force-distance curves using CD-AFM. The cantilever deflection is locked a sufficient distance from the surface and then the surface is moved towards the cantilever. Due to the change of surface force the laser power increases and decreases.

5.3 Acquisition of Force-distance curve

5.3.1 Laser power signal versus time

Figure 5.2(A) shows the deflection signal versus time measured with the microlever C on a mica substrate moved up and down a defined distance, known as ramp size, by the piezoscanner, Figure 5.(B). The experiment is performed with the feedback force off.

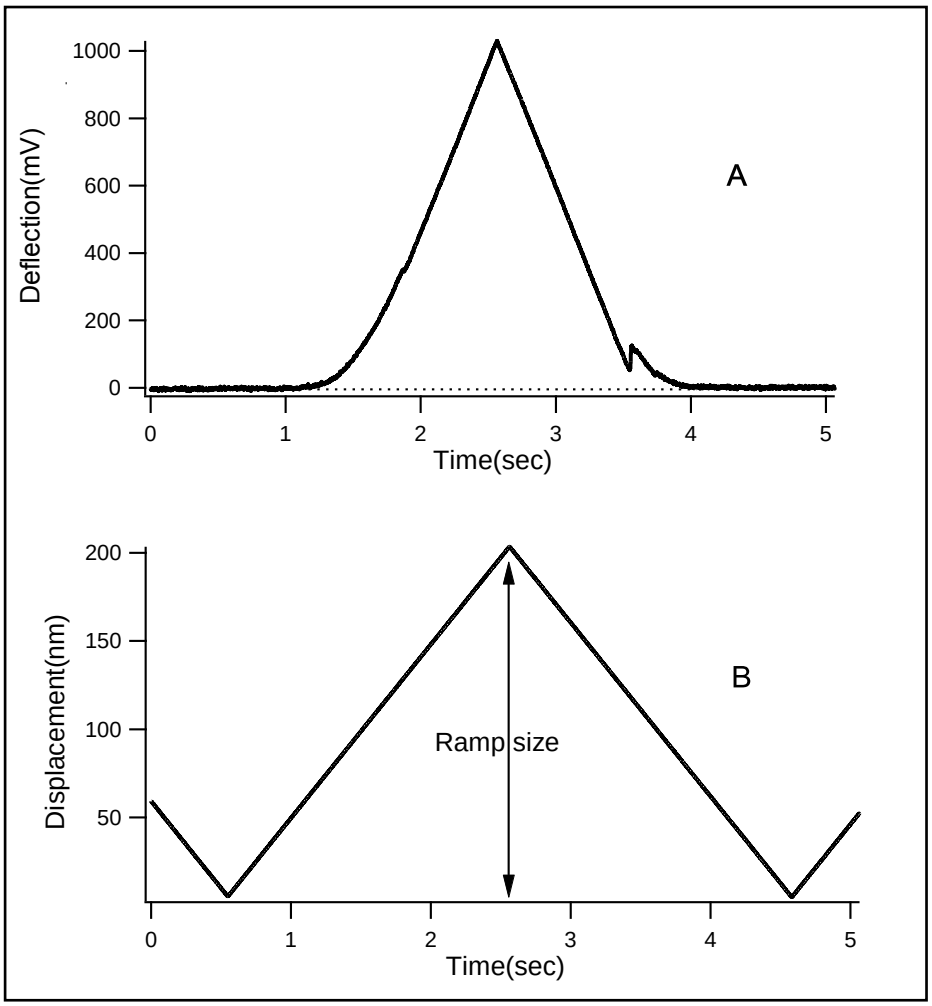

FIG.5.1 The top graph represents the cantilever deflection vs time in response to the piezoscanner motion whereas the bottom shows one cycle of the piezoscanner displacement. The surface used is mica and the cantilever is a Veeco- microlever C and both are immersed in an aqueous solution.

The same experiment was performed with the feedback system on. Figure 5.3 shows three signals acquired simultaneously and plotted versus time; laser, deflection and piezoscanner signals. Figure 5.3(A) is a close replica of the deflection signal illustrated in Figure 5.2(A) using the laser signal employed to lock the cantilever deflection. Note that, at point far away from the surface, the change in laser signal remains zero indicating that there are no detectable surfaces forces, Figure 5.3(A). Thus, this region can be used to define the zero force point in the laser signal.

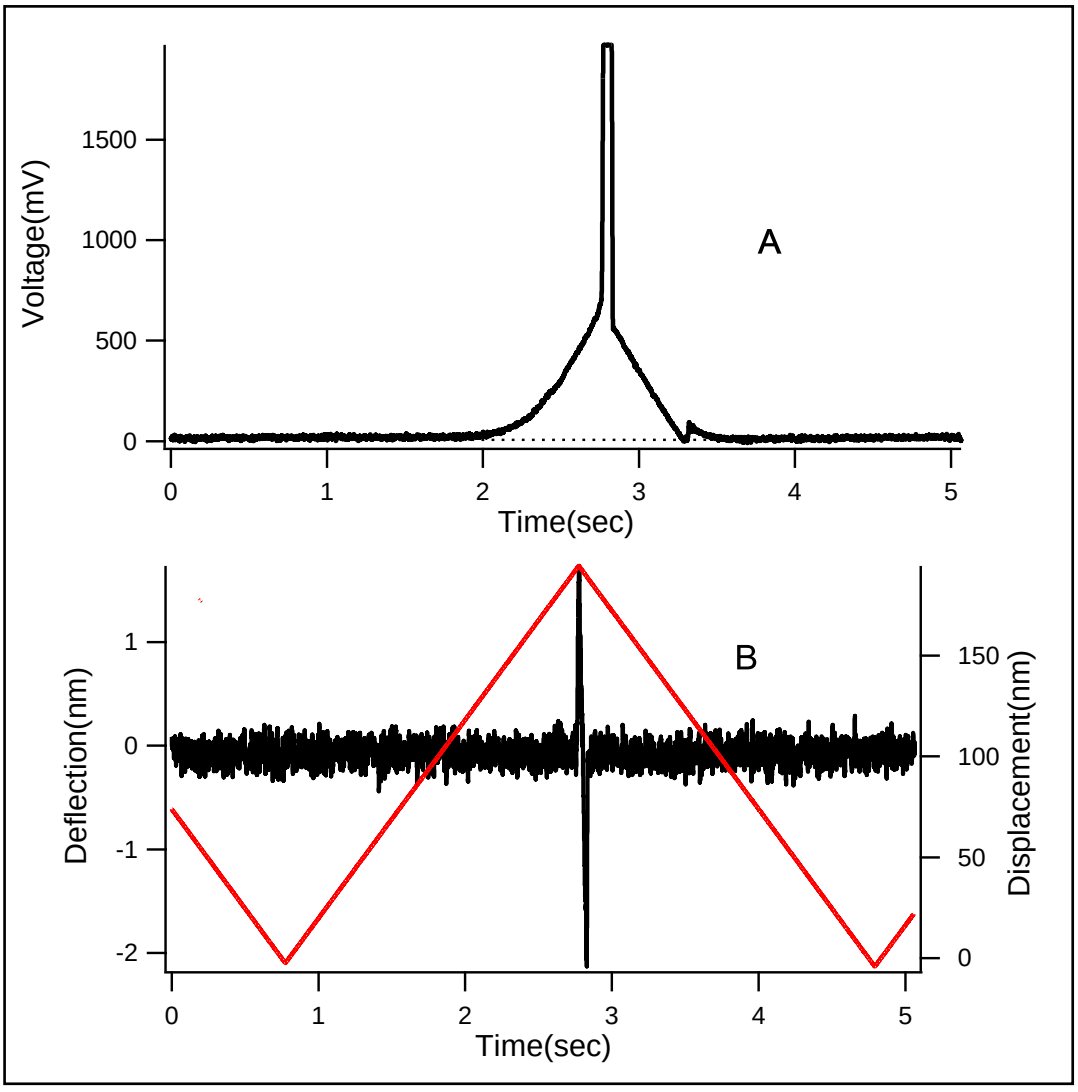

FIG.5.3 (A) Changes of laser signal in response to ramping mica surface along z-direction using a piezoscanner (B) the deflection of the locked cantilever (black) during the motion of the piezoscanner (red).

As the surface approaches the locked cantilever and begins to enter the area where tip-surface interactions become effective, the laser signal starts to change while the deflection of the locked cantilever acquired simultaneously remains constant, Figure 5.4.

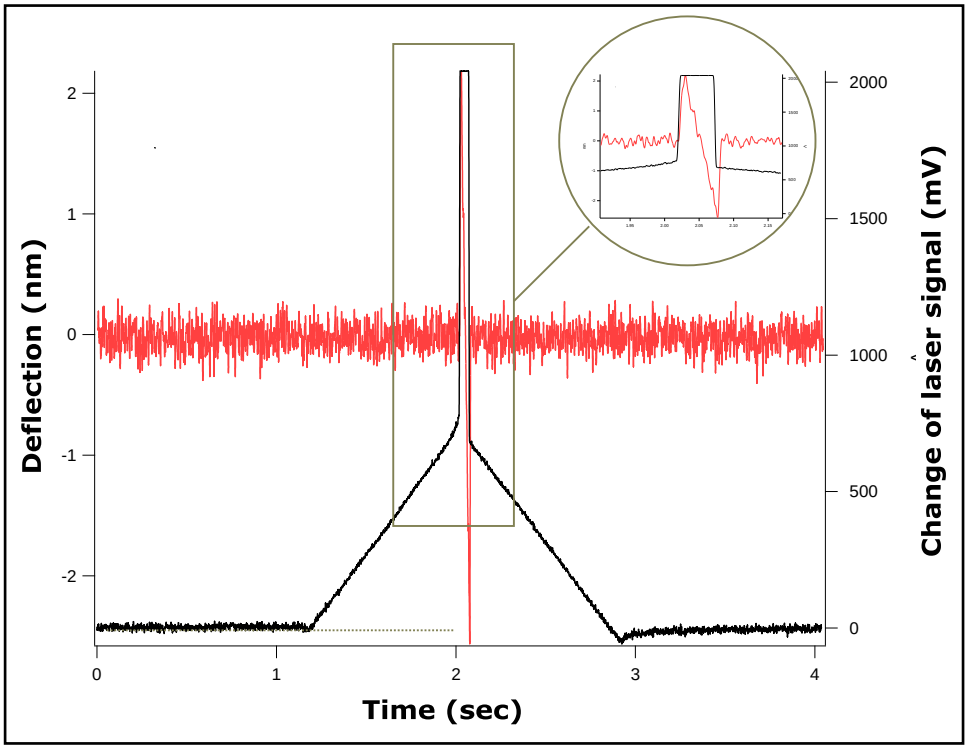

FIG.5.4 Simultaneous acquisition of the deflection of the locked cantilever (red) and the laser signal (black) used to lock the cantilever versus time using a Veeco-microlever-C on mica surface in an aqueous solution.

In order to keep constant deflection of the cantilever, the intensity of laser power is varied in response to the change of surface forces. Beyond this region, a significant linear increase in laser signal can be observed. At some point, movement of the piezoscanner pushes the cantilever back leading to an increase in cantilever deflection. In other words, the force applied by laser power can no longer withstand the movement of the piezoscanner.

It is clearly seen that the motion of the piezoscanner acquired simultaneously with the cantilever deflection and the laser signals

(Figure 5.3) continues in a linear fashion, so is not the cause of the loss of lock. The cantilever starts to deflect when the voltage used to drive the diode laser 2 (LD2) reaches its maximum limit. The cantilever deflection indicates that the force feedback has failed in what is known as "off-lock".

The achievable power range of the laser signal is limited. The operation range of LD2 is between 350 to 1300 mV. It is worth noting that although the maximum limit is ~ 1300 mV, this does not relate to a fixed force limit as the laser power to force conversion is rate dependent (chapter 4).

Primarily, the laser power was set at its half maximum which corresponds to ~ 600 mV that limits the maximum increase in laser signal to ~ 700 mV and the maximum decrease to approximately 250 mV. In Figure 5.5, the adhesive force is too large, and takes the laser power beyond 250 mV limit, therefore resulting in loss of laser lock. The force limit may be increased by using more powerful lasers.

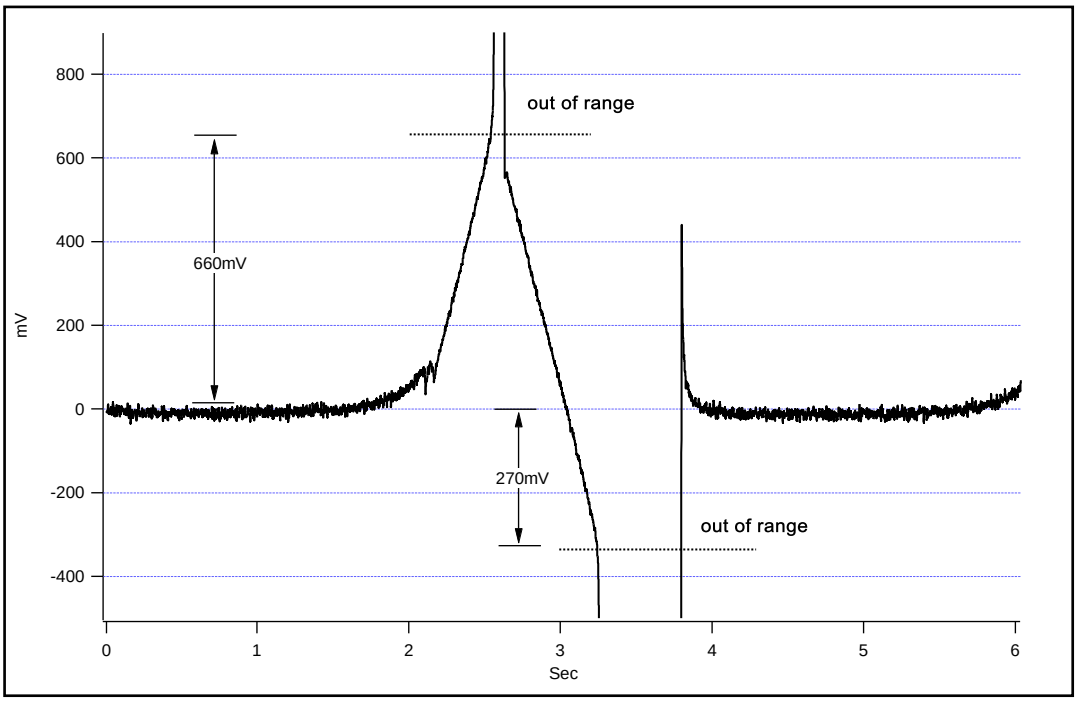

FIG.5.5 The upper and lower variation voltage limit of laser signal used to lock the cantilever deflection.

5.3.2 Laser power signal versus piezo displacement

Figure 5.6 depicts a common relationship between the cantilever deflection and the surface position. Usually, in order to relate the deflection signal to the surface position, the deflection is plotted versus the piezoscanner displacement. Such a figure is called deflection-displacement curve.

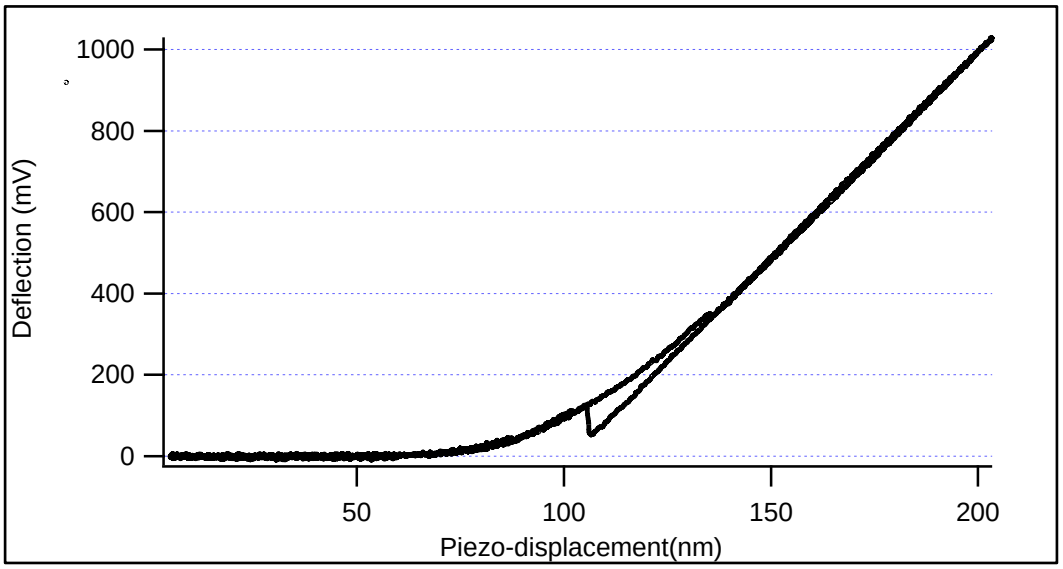

FIG.5.6 Deflection-displacement curve of microlever-C on a mica surface in water obtained using standard AFM.

The deflection-displacement curve is reproducibly obtained using the laser signal, Figure 5.7. The laser signal is plotted against the piezoscanner displacement, from now on it will be called the laser-displacement curve. Direct comparison between the deflection-displacement curve (Figure 5.6) and the laser-displacement curve (Figure 5.7) shows the same behavior.

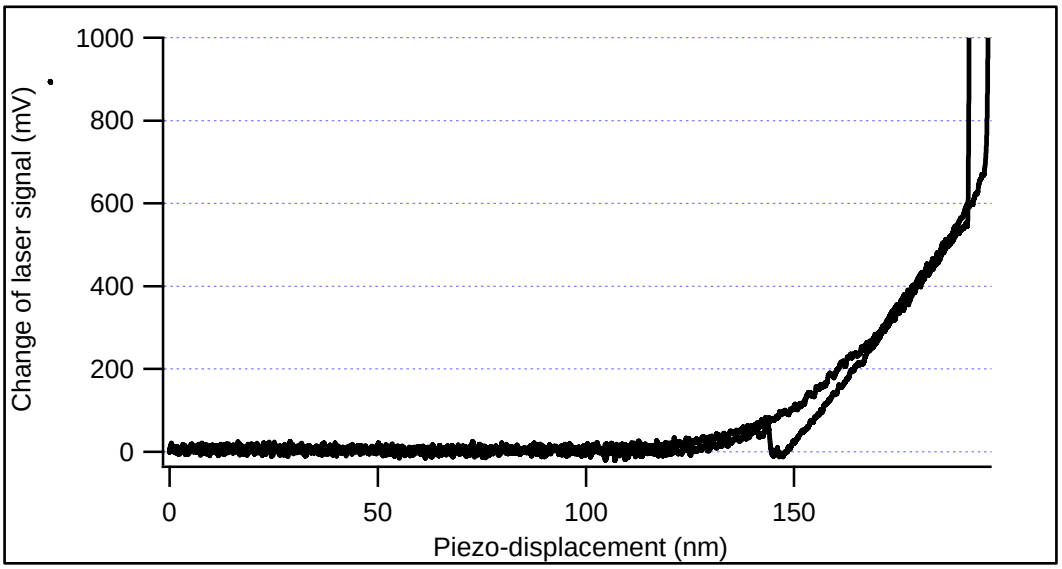

FIG.5.7 Laser-displacement curve of microlever-C on a mica surface in water obtained using CD-AFM.

5.4 Calibration of laser-displacement curves

In order to convert the deflection-displacement or a laser –displacement curve to a force-separation curve, the curves must be scaled in force and the piezoscanner displacement is converted to the tip-surface separation. In chapter 2, we showed how the deflection-displacement curve can be converted to the force-separation curve. In the following, we will first discuss force calibration in the laser signal curves and then introduce an approach to compute the tip-sample separation.

5.4.1 Force calibration

In order to convert the deflection into force, the cantilever deflection is just multiplied by the cantilever stiffness. However, scaling laser- displacement curves in force is quite complicated involving multiple steps. First, the relationship between laser power and the resulting force acting on the cantilever must be established. Such a relationship was introduced in

chapter 4. However, the relation between force and laser power is not enough to scale laser displacement curves in Force. Figure 5.8 shows a conversion factor, or force sensitivity, (F_s) as function of driving frequency for cantilever C with stiffness of 0.01 N/m. However, it is not straightforward to apply this conversion factor to a force curve because the rate of change of cantilever is *not constant*.

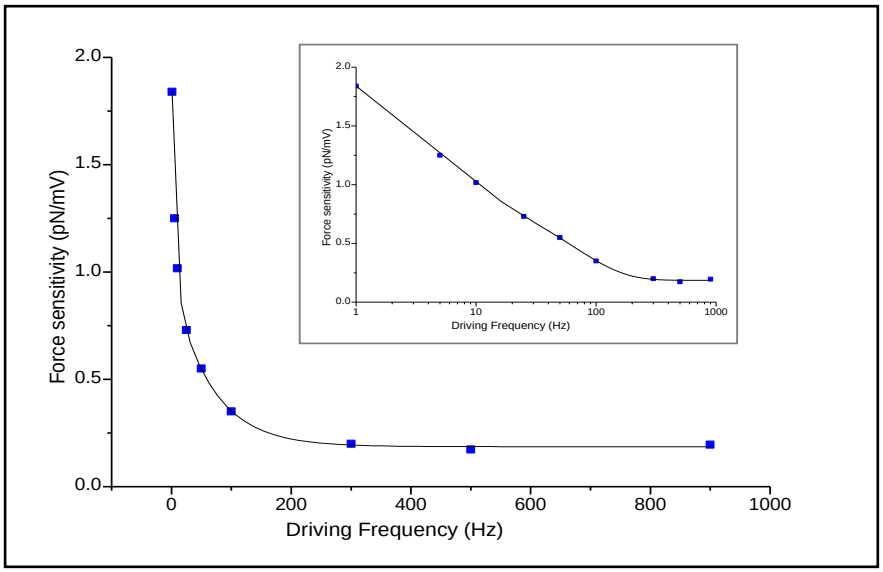

FIG.5.8 Dependence of force sensitivity with the driving frequency for microlever-C. The force sensitivity response to the driving frequencies is fitted to a triple exponential decay function. Inset shows the figure in log scale.

To overcome this drawback I proposed to relate F_s to the rate of change of the laser signal instead of the driving frequency. The rate of change of the laser signal means the change of laser signal as a function of time. In chapter 4, the laser power is changed by means of modulating the laser driver at different frequencies and then measuring the resulting force by monitoring the cantilever response. Instead of relating the force sensitivity to the modulating frequency, it will be helpful if it is related to the rate of change of the laser power used to drive the cantilever.

Figure 5.9 shows the laser power signal used to drive the cantilever as function of time. The rate of change can be defined as the slope at the point where the wave crosses the zero-axis.

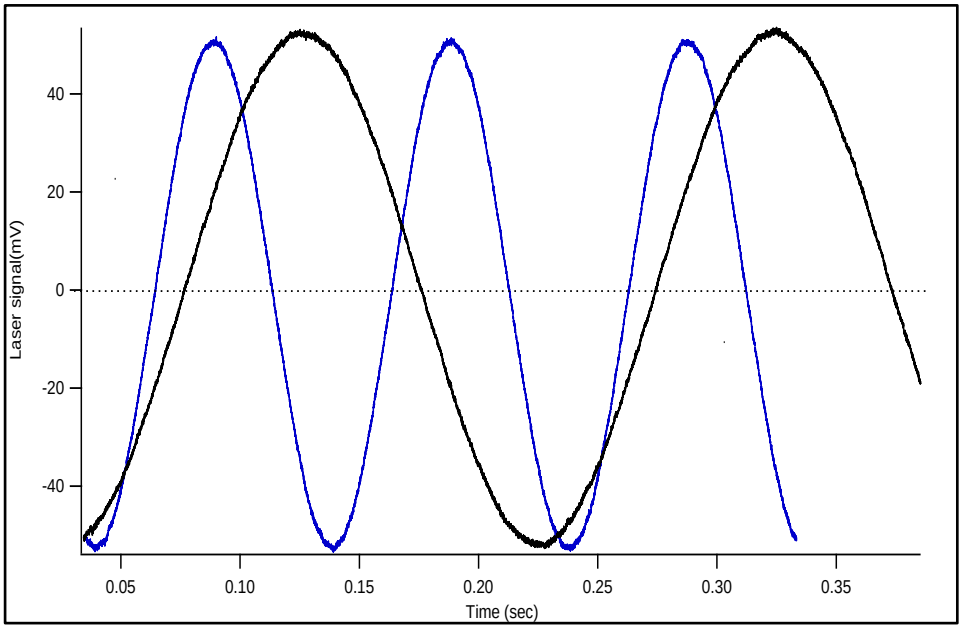

FIG.5.9 The change of output of laser diode as function of time. The laser diode is driven at different frequencies, 5 Hz (black) and 10 Hz(blue).

Figure 5.10 illustrates a plot of the rate of change of the laser power signal versus the corresponding driving frequency. The slope of the linear fit represents the conversion factor (R_H) from the changing rate sensitivity to the driving frequency.

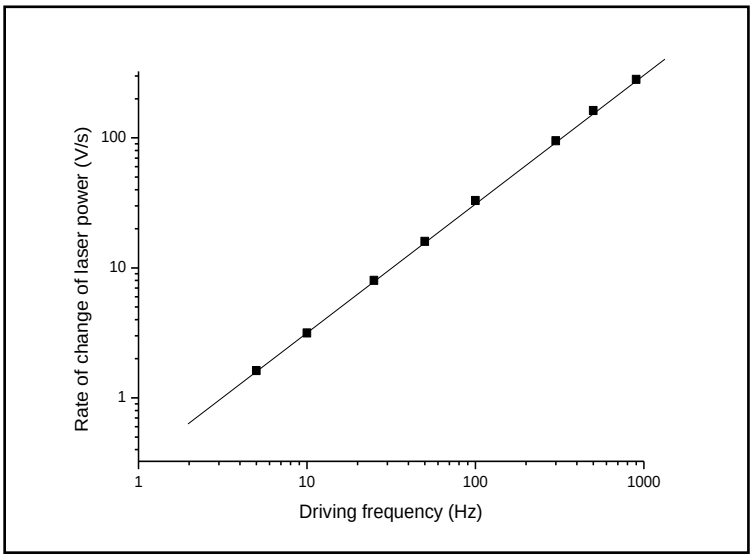

FIG.5.10 Rate of change of laser power as function of the driving frequency at driving voltage of 100mV.

To estimate R_H at different driving voltages, $(R_H)^{-1}$ is plotted against the driving voltage, Figure 5.11.

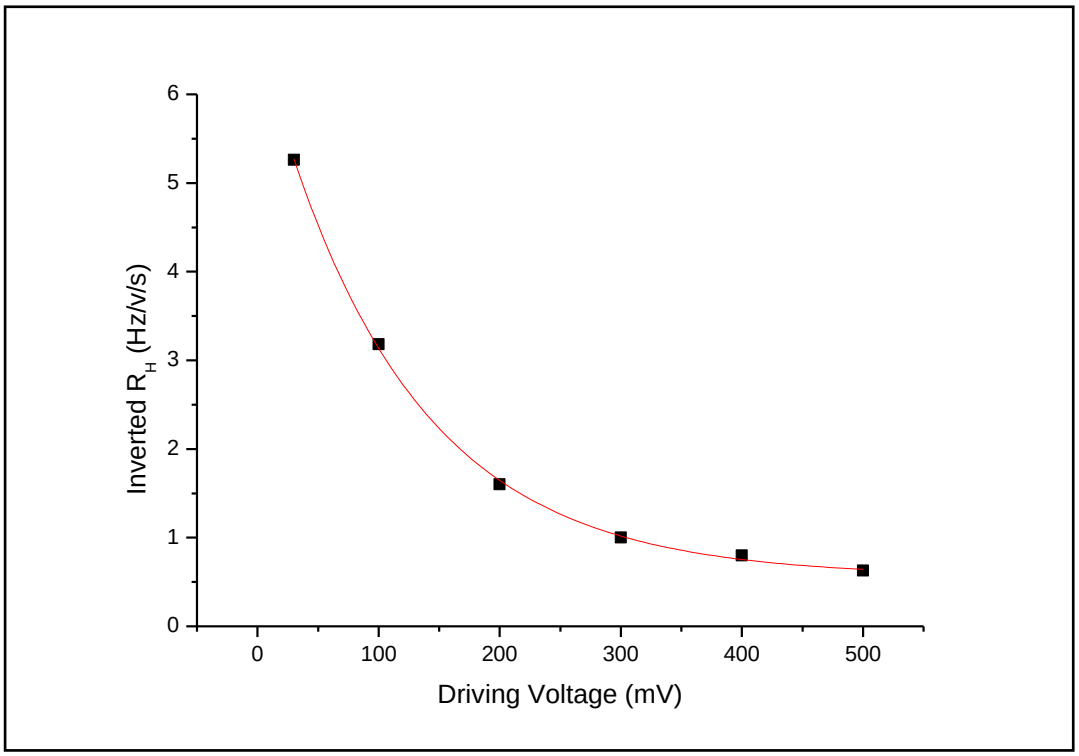

FIG.5.11 $(R_H)^{-1}$ versus the driving voltages. The continuous line corresponds to the fit to exponential function.

In order to scale the laser curve, firstly the curve should be obtained as a function of time, Figure 5.12. The second step is to divide the laser curve into different segments of constant rate of change of the laser signal. The maximum voltage for each segment is used to define the corresponding $(R_H)^{-1}$ using Figure 5.11. By multiplying the rate of change of laser signal for each segment by $(R_H)^{-1}$, the frequency at which the laser diode is modulated can be calculated. In order to find the corresponding force sensitivity (F_s) we use Figure 5.8. Finally, multiply each conversion factor by the height of the segment, in unit of mV, to find the corresponding force. By adding the regions to each other, the magnitude of the applied force can be computed. In the section 5.5 we will demonstrate the validity of this method to scale the laser curve in force by comparing it to those obtained by means of the cantilever deflection.

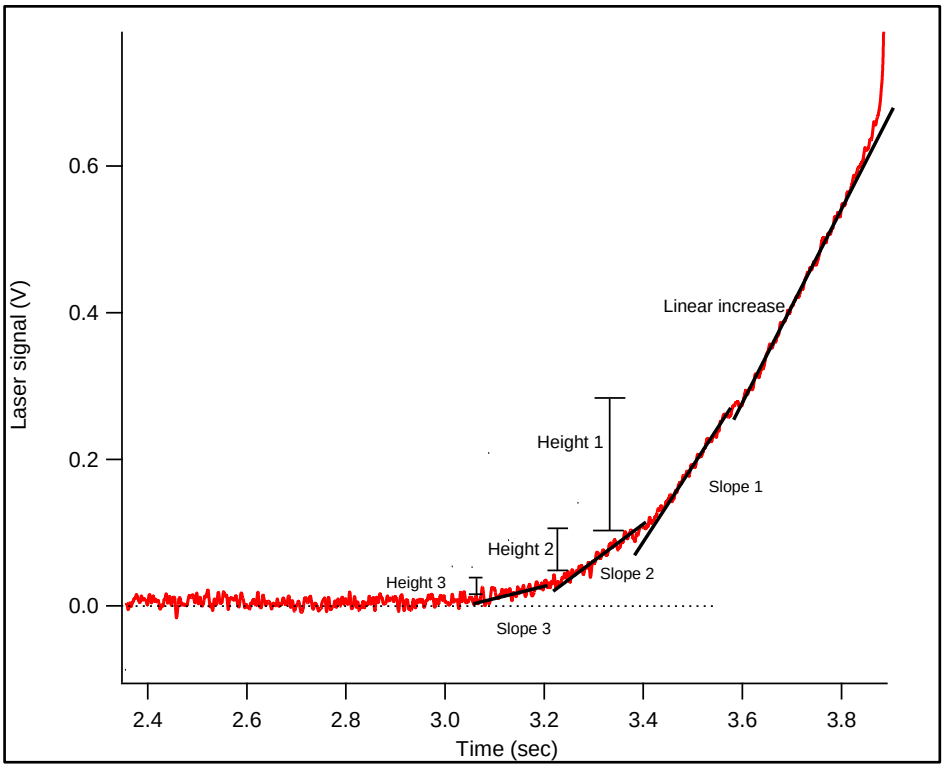

FIG.5.12 The approach laser curve versus time measured with cantilever C in aqueous solution on a mica surface. Before the jump-to-contact the curve shows the effect of surface forces on the laser power. The change of laser power due to the surface forces can be divided into few regions depending on the rate of change of the laser signal. Each region has its own conversion factor which is multiplied by its height to get the force. By adding the forces of the regions to each other the maximum force can be determined.

5.4.2 Tip-sample separation

Usually, it is instructive to describe the surface forces as a function of the tip-surface separation. Therefore, it is more informative if the laser signal is plotted versus the tip-sample separation.

The laser (LD2) output changes in response to the cantilever deflection. It is clear that the laser output is simply a proportional amplification of the cantilever deflection. Thus, the procedures followed when using the deflection signal to convert the piezo-displacement to tip-surface separation (chapter 2) are still valid for the laser (LD2) output. In the deflection signal, the linear increase in the cantilever deflection (contact region) was used to define the zero separation. Likewise, the linear increase in laser single can be used as a reference line to define the zero separation due to both increases occuring after the jump-to-contact event, justification for which can be found in section 5.6.

Figure 5.13(A) illustrates the output of the laser diode (LD2) and the piezoscanner in volts. Both signals are plotted against time. The slope of linear increase of laser signal is substantially higher than that of the piezoscanner signal. These results illustrated in Figure 5.13(A) are similar to those obtained for the deflection signal (chapter 2). In order to correct the output of the laser diode (LD2) to follow exactly the piezoscanner output, the laser output curve is multiplied by the slope of the linear increase of the laser –displacement curve, both scaled in volt. As a result, the laser output and the piezoscanner curves overly perfectly in the linear increase region, Figure 5.13(B).

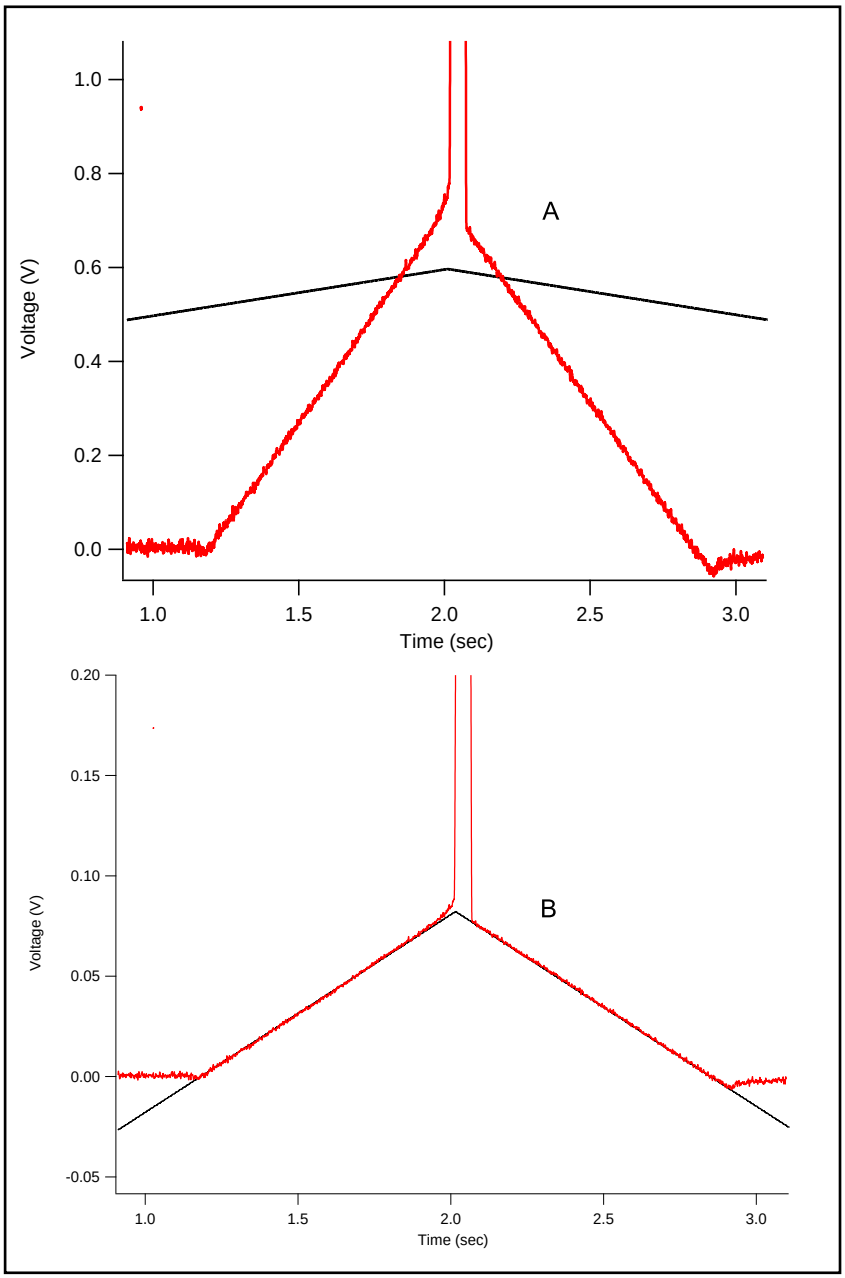

FIG.5.13 Laser output (red) and the piezoscanner output (black) plotted as function of time. (A) Before and (B) After correction.

Subtraction of the corrected laser signal from the piezoscanner signal results in the tip-surface separation. To obtain force-separation (force-distance) curves, the laser signal scaled in Newton is plotted against tip-surface separation, as illustrated in Figure 5.14.

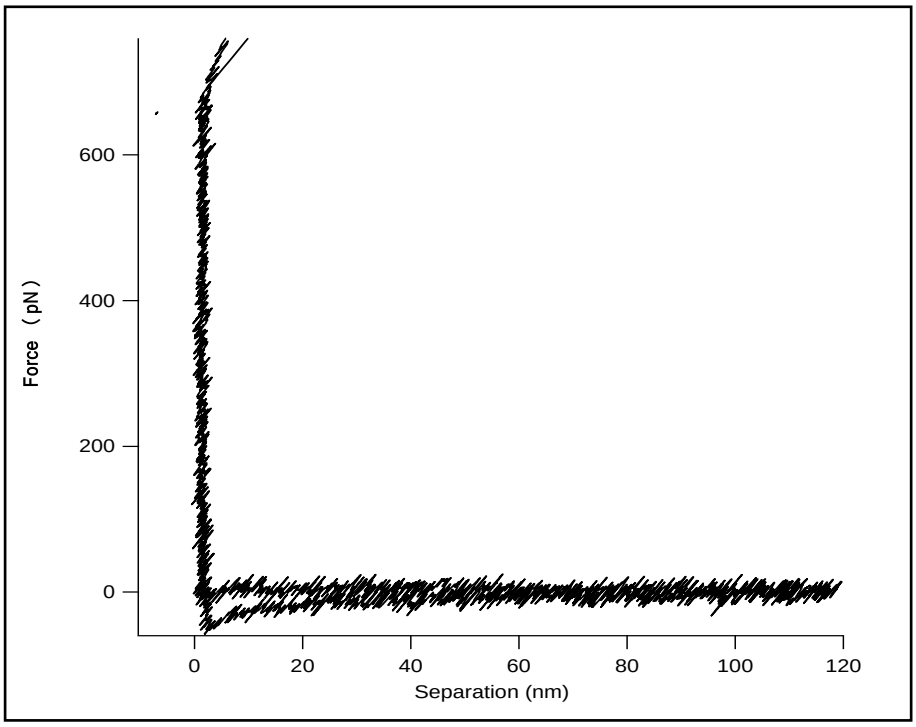

FIG.5.14 Force distance curve measured by CD-AFM on mica surface with cantilever C (0.01N/m) in water

5.5 Further investigation and analysis on force-distance curves obtained by CD-AFM

In the above sections we demonstrated the ability of the force-distance curve acquired by laser signal to mimic the conventional force-distance curve obtained by the deflection signal. In Figure 5.15, both curves show an increase in force surface when the tip is ~30 nm from surface and the maximum force before contacting with surface is ~380 pN.

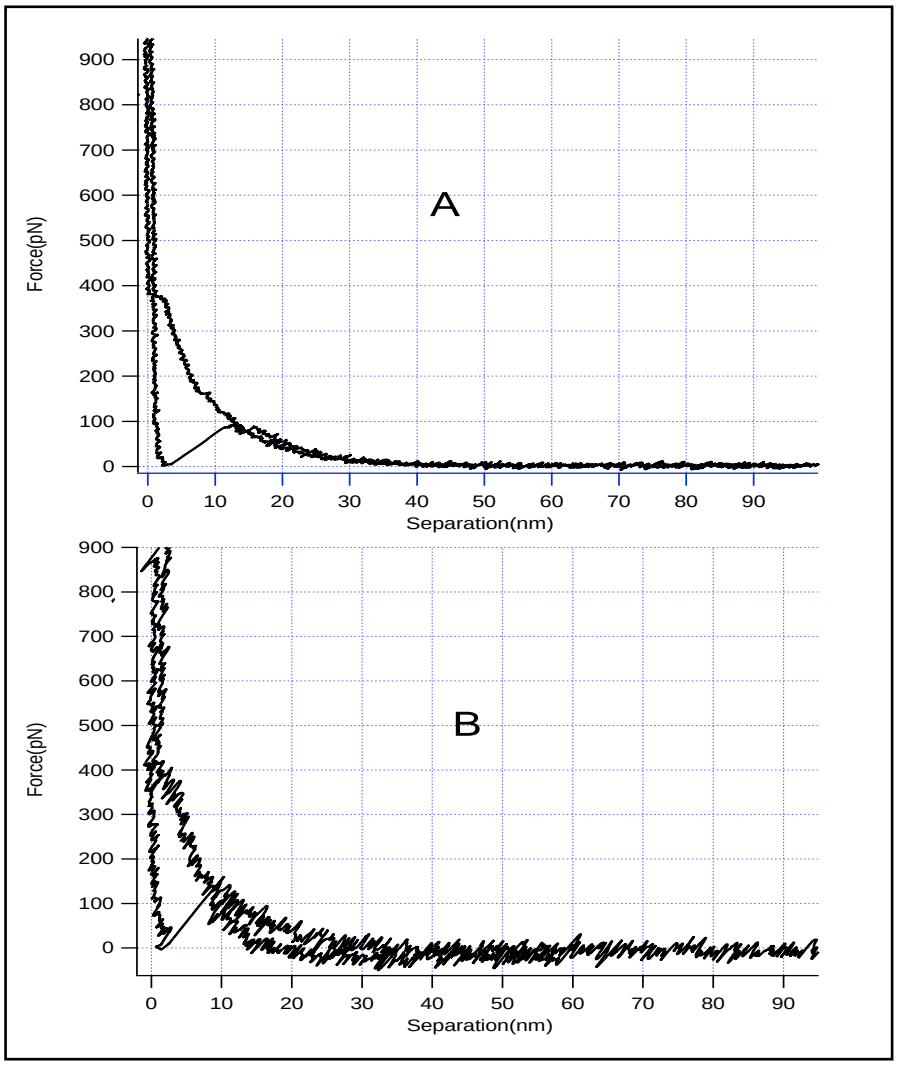

FIG.5.15 Force distance curve measured with microcantilevre C on a mica surface in an aqueous solution (A) by deflection signal (B) by laser signal.

However, further quantitative measurements are required to validate the laser signal as an alternative to the deflection signal. To interpret force-distance curves obtained by CD-AFM it is necessary to characterize the forces acting between tip and surface. Moreover, the accuracy of the methods illustrated above to translate the laser-displacement curve to a force-distance curve need to be verified. In the following section, we will demonstrate the capability of the system to reproduce similar measurements to those obtained by conventional AFM through

investigating repulsive electrostatic forces as a function of salt concentration and indentation of a soft surface on the force-distance curve.

5.5.1 Measuring long range electrostatic forces in aqueous solution

To study the electrostatic force generated between an AFM tip and a mica surface (for explanation see section 1.3), force-distance curves were acquired at different salt concentrations. The tip experiences a repulsive force due to electrostatic forces as a function of salt concentration. The repulsive force decreases exponentially as function of increasing tip-surface separation, with a decay length depending on ionic strength and such results have been reported using standard AFM(*6-11*).

Figure 5.16 represents force-distance curves (approach curves only) measured with microcantilever C (0.01N/m) on a mica surface at different NaCl concentrations using conventional AFM, while Figure 5.17 reproduces the same experiment using CD-AFM. The repulsive force maximum measured by conventional AFM or CD-AFM at each concentration is the average maximum force measured from 13 curves.

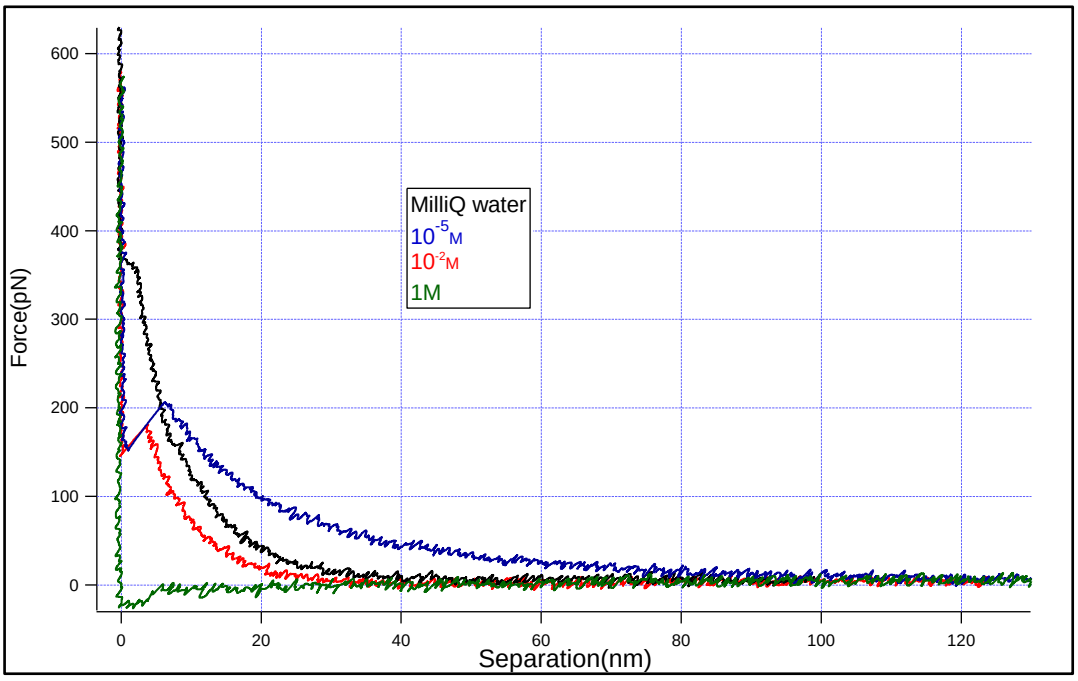

FIG.5.16 Force versus separation between the microcantilever C and mica surface in aqueous solution at different NaCl concentrations obtained by the deflection signal (only approch curve).

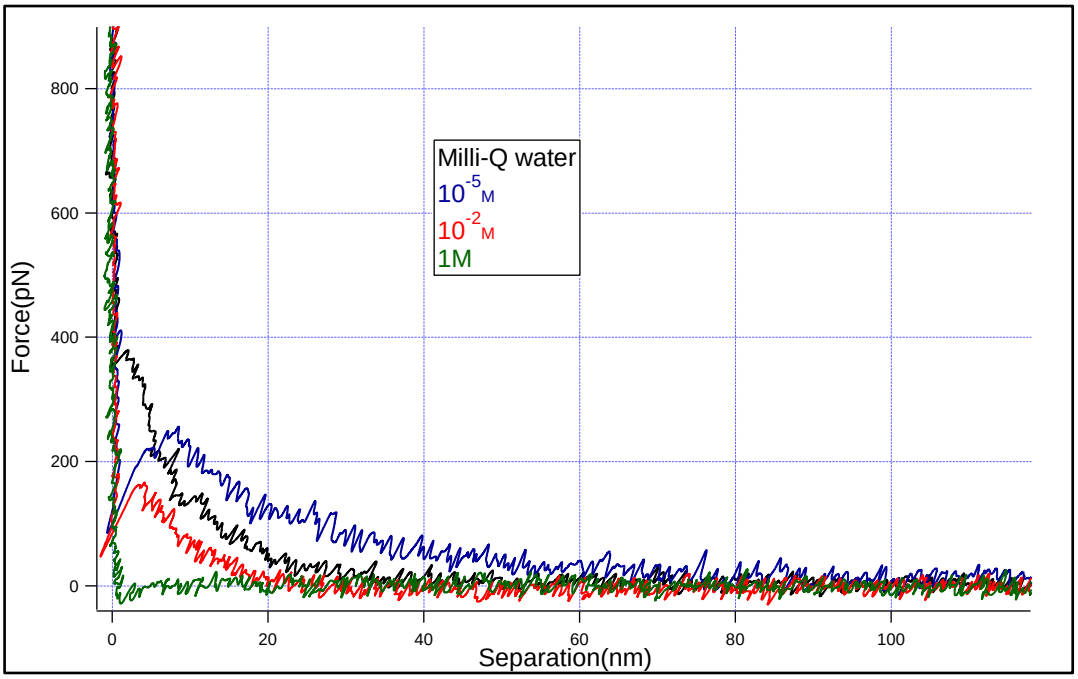

FIG.5.17 Force versus separation between microcantilever C and mica surface in aqueous solution at different NaCl concentrations obtained by the laser signal (only approach curve).

In Milli-Q water, the measured repulsive force by standard AFM is 416±28 pN and 424±33 pN using CD-AFM. As the salt concentration increases, the repulsive force decreases. For example, using standard AFM, it is 206±11 pN at 10^{-5} M and 184±11 pN at 0.01 M. The use of CD-AFM shows a slight difference in measured repulsive forces. For instance, at 10^{-5} M it is 222±16 pN and 178±14 pN at 0.01M. However, at higher salt concentration, 1M, the repulsive force diminishes and attractive forces dominate. Within the error of the measurements, the repulsive force measured in different NaCl concentrations by means of standard AFM or CD-AFM are similar. A key result in above comparison is the validity of the force calibration method discussed in section 5.4.

Moreover, for example, at 10^{-5} M, the cantilever starts to deflect upward at approximately 90 nm from the surface. An increase of salt concentration to 0.01 M leads to the range of the repulsion force decreases to ~30 nm. Similar to the trend of the cantilever deflection, the laser signal shows a detectable change at a distance of approximately 90 nm from the surface at10^{-5} M and of 30 nm at 0.01M.

Moreover, the decay length of the repulsive force decreases with increasing the salt concentrations. In order to measure the decay length, the repulsion part of the force-distance curves of those obtained by either the cantilever deflection or the laser signal is fitted to the exponential function ($Ae^{\frac{-x}{\varsigma}}$), where A is the amplitude and ς is the decay length, Figure 5.18. For the unlocked cantilever the decay length is 7.4 nm in Milli-Q water, 21 nm at 10^{-5} M and 7 nm at 0.01M. Using CD-AFM the measured decay length in Milli-Q water is 8.7 nm, 19.8 nm at 10^{-5} M and 7.6 nm at 0.01 M. The constancy of tip-surface separation shows undoubtedly the method used to determine the tip-surface separation in the curves obtained using the laser signal is correct. It is worth noting that

the decay length measured here is not the Debye length, which requires a well defined shape of the tip for true quantitative measure (beyond the scope of this chapter). Our aim is to compare the behavior of force – distance curves obtained by standard AFM to those obtained by CD-AFM, which is valid when the same tip is used for each experiment.

Furthermore, as for the average jump-to-contact distances measured by conventional AFM or CD-AFM, no significant differences were found. In 10^{-5} M NaCl the cantilever jumps to surface at ~ 6.3 nm from surface. The distance is reduced to ~ 4 nm in 0.01 M NaCl.

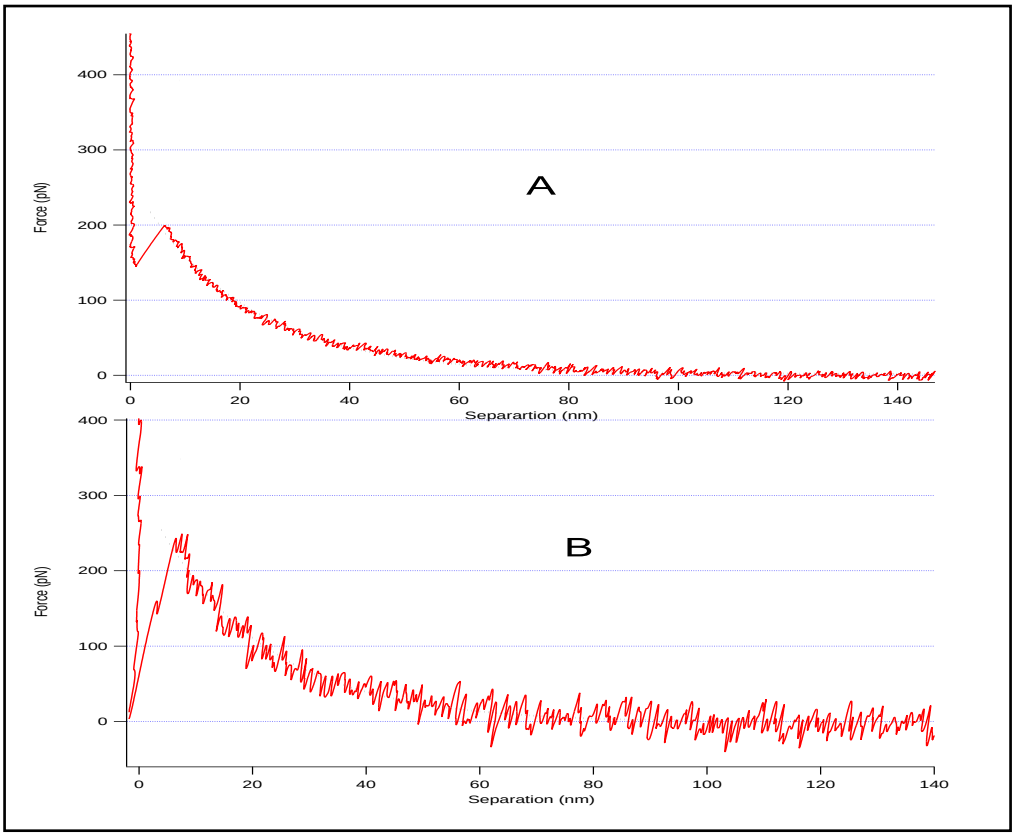

FIG.5.18 Force distance curve at 10^{-5} M NaCl concentration (red) is fitted to exponential function (dashed line). Deflection signal (A) and laser signal (B).

A direct comparison between measurements presented above and obtained by the two methods show firmly that the force-distance curves obtained by the laser signal looks like those curves acquired using the

conventional AFM (Figure 5.18). However, in the conventional AFM, the distance between the jump point and surface appears as a straight line without any real signal, Figure 5.19. Using CD-AFM, it was observed a slight fluctuation along the jump to contact distance that could be a force profile but due to smoothing the curve the force profile diminishes, Figure 5.20. Although exploring the force profile between the jump-to-contact point and the surface could reveal valuable information about the tip-surface interactions close to surface, it is out of the scope of this chapter.

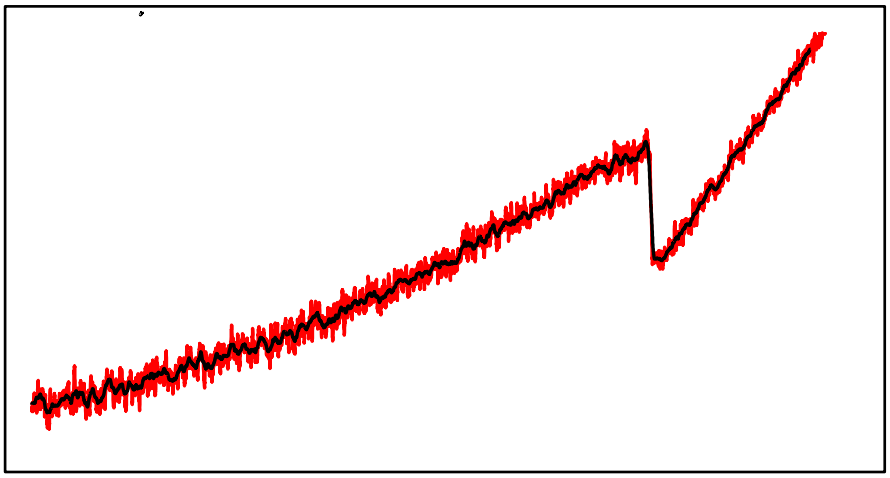

FIG.5.19 Force curve is obtained by a conventional AFM without (red) and with (black) smoothing. No real signal can be detected in the gap between the jump point and the surface.

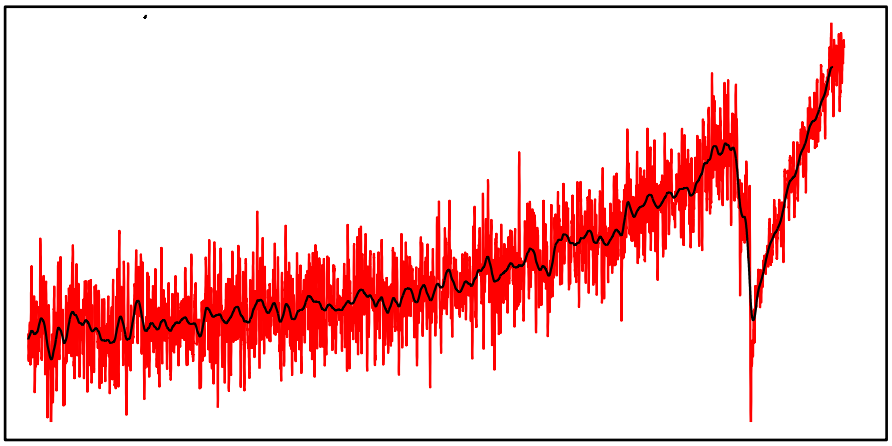

FIG.5.20 Force curve is obtained by CD-AFM without (red) and with (black) smoothing. A small peak can be detected in the gap between the jump point and surface in the unsmoothed curve.

5.5.2 Force- distance curve on lipid bilayer

In previous sections, we demonstrated the capability of CD-AFM to reproduce the measurements acquired by conventional AFM on a hard surface and in different salt concentrations. The measurements obtained by means of the laser signal agree with those measured by standard AFM. Such measurements were performed using the non-contact part of force-distance curves. When it comes to the contact part of the force-distance curve, the interpretation becomes complicated. The contact part of the force curve obtained by the deflection signal (standard AFM) shows a linear and constant compliance and can be used to define the zero tip-surface separation point. However, interpretation of the linear part in the force-distance curve obtained using CD-AFM is quite complicated (see section 5.6).

In order to demonstrate the system's capability to reproduce the measurements performed on the contact part of the force curve, we used a soft surface. The main reason for this choice is that a soft cantilever, such as that used in this experiment, is insensitive to indentations of a hard surface(*12*) so any change of the cantilever deflection is hard to observed by the deflection system and hence by the feedback system. Here we focus on the use of a lipid bilayer as a soft surface. The lipid bilayer formed from double lipid layers is the universal components for the cell membrane structure whose role is to mark the cell boundaries and to surround the cell(*13*). Typically, the thickness of the lipid bilayer is ~5 nm(*14*).

Figure 5.21 show schematic description of the force-distance curve on a lipid bilayer deposited on a mica substrate. When the cantilever tip is far away from the bilayer no interactions are observed. Once the tip contacts the bilayer, the cantilever deflects upward. Further motion of the piezo

results in the lipid bilayer is elastically compressed (*15*) and the cantilever deflects upward. At a certain point, when the applied force exceeds the rupture force of the bilayer, the tip jumps to contact with mica surface penetrating the lipid bilayer film.

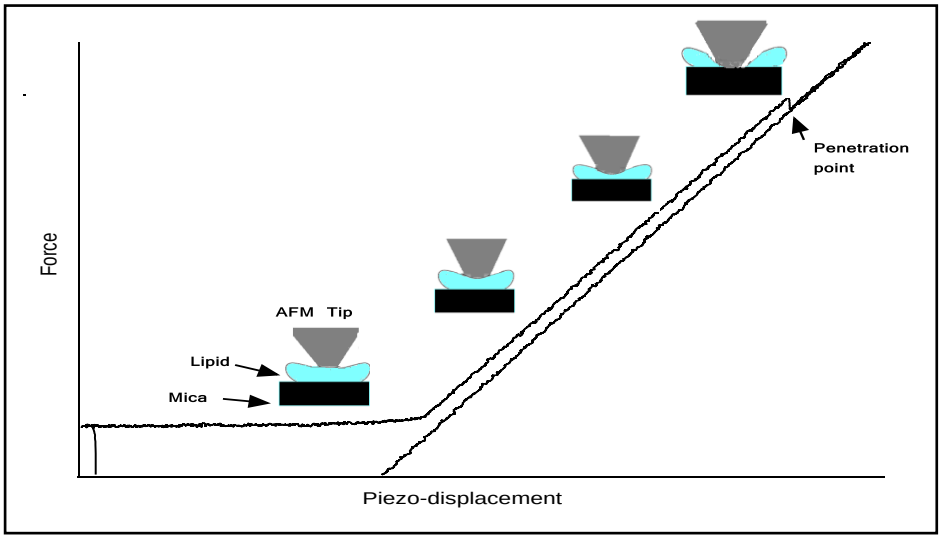

FIG.5.21 Schematic diagram describing the cantilever tip penetration in a lipid bilayer using atomic force microscopy.

Figure 5.22 shows a typical force distance curve recorded on a lipid bilayer of ~5 nm thickness using a cantilever with stiffness of 0.01N/m. The approaching curve shows that the tip comes to contact with lipid bilayer at a distance of 7 nm from the support surface (mica). Further motion of the piezoscanner results in compressing the bilayer by 2 nm prior to breaking through. Although the figure shows the breakthrough force is 1.3 nN and the breakthrough distance is 5 nm, there is no one definite value for the breakthrough distance and force. Butt et al demonstrated the bilayer film breakthrough is an activated process, an energy barrier must be surmounted (*16, 17*). In this process, the energy increases as the tip applies more pressure on the bilayer film. Thus, the breakthrough force and distance show a Gaussian-like distribution(*18*).

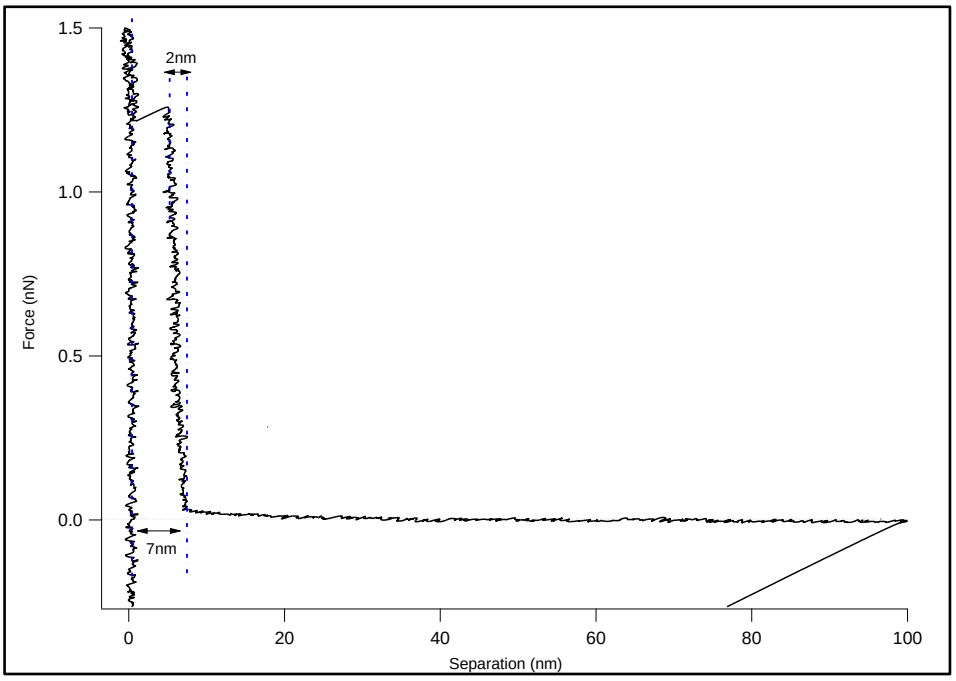

FIG.5.22 A typical force distance curve acquired by standard AFM on a lipid bilayer using an AFM cantilever with stiffness of 0.01 N/m and an approaching speed of 200 nm/s.

Figure 5.23 shows the force curve on the lipid bilayer obtained by CD-AFM. Similar behavior to the deflection signal (conventional method) can be observed. The laser signal shows no change when the locked cantilever is far away from the lipid bilayer. At closer distance, the laser power starts to increase in response to the compression of the lipid bilayer which results in deflecting the cantilevers upward. At a certain point the laser power drops quickly indicating the tension on the cantilever was eased because the tip has broken through the lipid film. The breakthrough force and distance measured by the laser signal are similar to those obtained by the cantilever deflection, within error range.

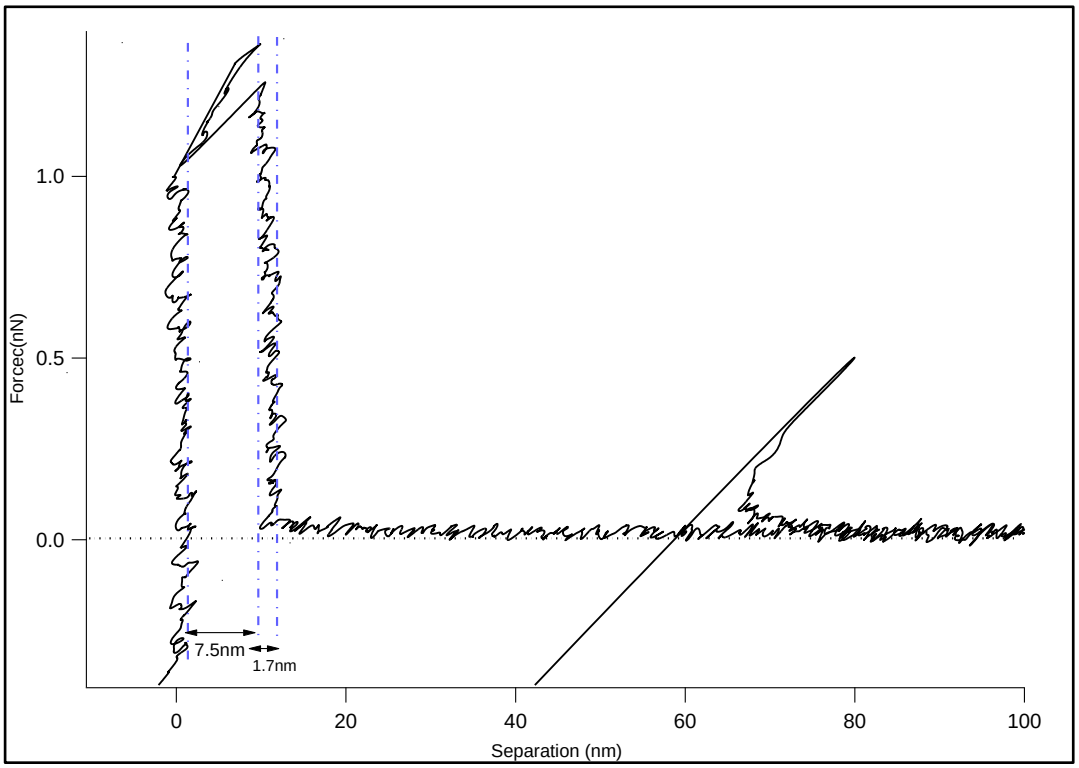

FIG.5.23 Force curve on lipid bilayer obtained by CD-AFM using an AFM cantilever with stiffness of 0.01 N/m and an approaching speed of 200 nm/s.

During acquisition of the force curve using CD-AFM, the cantilever is kept locked to ~0.3 nm, Figure 5.24. The cantilever only deflects once the laser power has gone out of range and the feedback loop is no longer active.

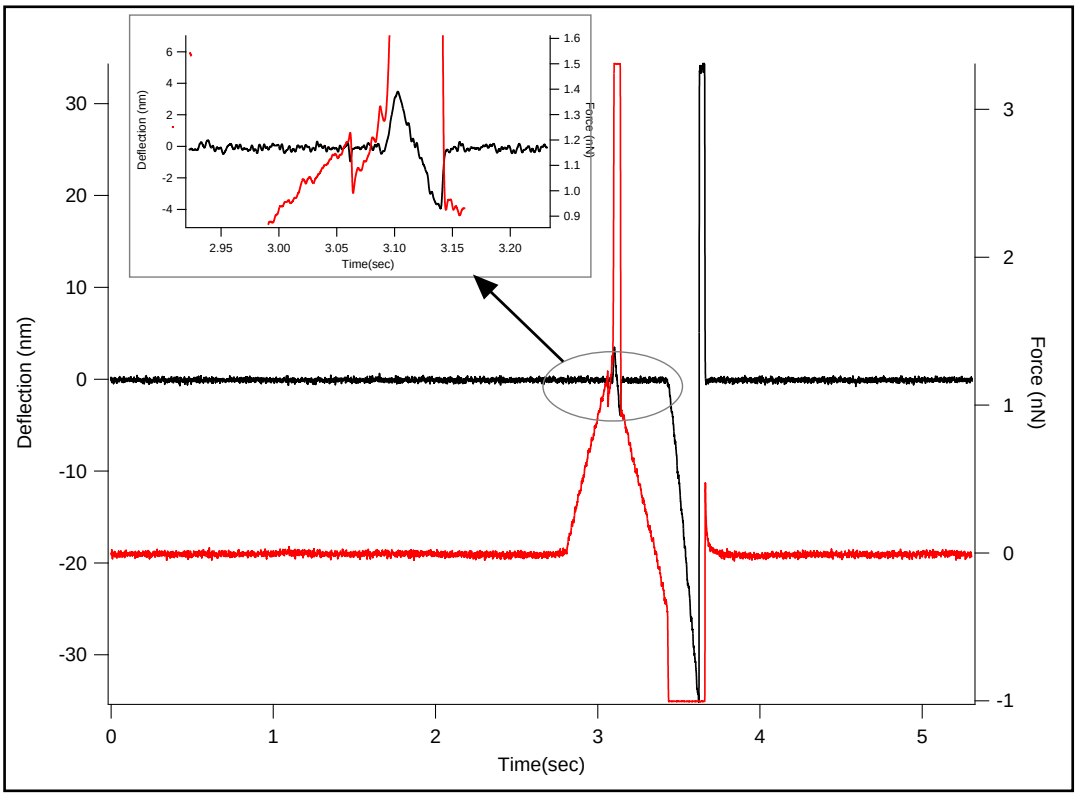

FIG.5.24 Simultaneous acquisition of laser signal and the deflection of the locked cantilever during measuring the force curve on lipid bilayer. Inset shows the cantilever is kept locked even during the lipid penetration.

If the tip is retracted before rupturing the lipid bilayer, the retract curve is identical to the approach curve, so the region before the rupture point can be described as elastic(*16*). Therefore, the Young modulus value (E) of the lipid bilayer can be evaluated from fitting the indentation of the lipid bilayer versus the applied force to Hertz's model (see chapter 1 section 1.3.3). Figure 5.25 shows Hertz`s model fits the indentation-force curve well. The elastic behavior measured using CD-AFM and standard AFM techniques shows a very good agreement.

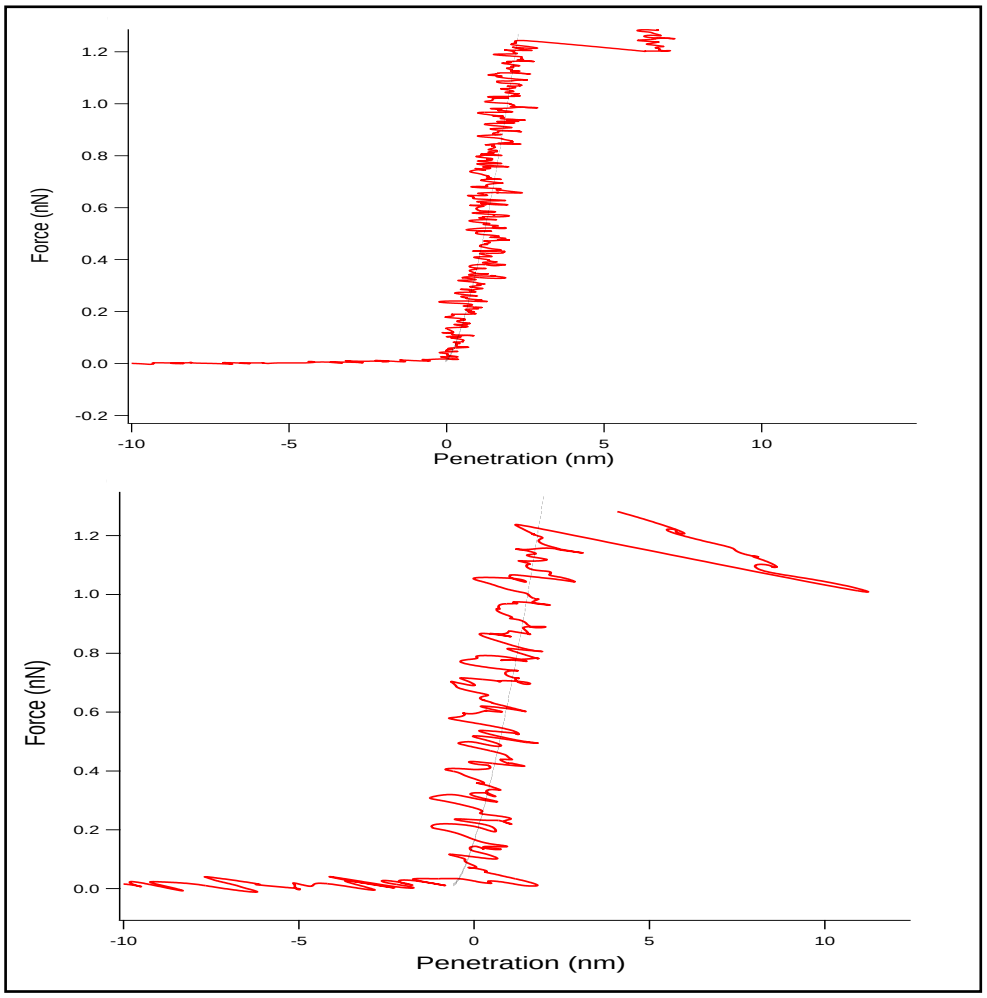

FIG.5.25 Nanoindention curve obtained on a lipid bilayer using microcantilever C (k=0.01 N/m). The dashed line corresponds to the fit to Hertz`s model (see chapter 1) with fitting parameters: the Poisson's ration=0.4, the radius of the tip curvature=25nm and Young's modulus=120MPa (10-100MPa for rubber). (Top) the cantilever deflection (Bottom) the laser signal.

5.6 Scenarios proposed to explain the linear increase in laser signal

Figure 5.26 shows the deflection of locked cantilever obtained simultaneously with the laser signal as function of the piezo displacement. One of the key features in Figure 5.26 is that beyond the jump-to-contact

point, the laser signal shows a linear increase whereas the cantilever remains locked and the piezoscanner keeps moving.

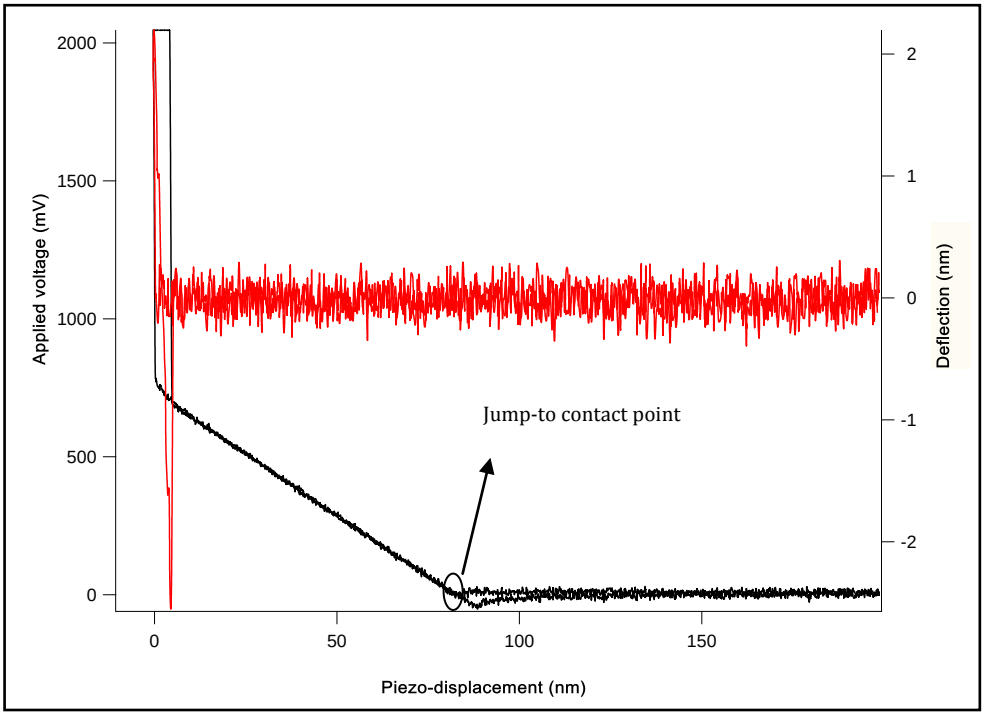

FIG.5.26 Laser signal in millivolt (black) and the deflection of the locked cantilever in nm (red) acquired simultaneously versus the piezoscanner displacement.

The source of the linear increase in the laser signal upon contact is one of the drawbacks related to force-distance curves acquired using CD-AFM. To find out the origin of such an increase, two potential scenarios are proposed. The first scenario is based on assuming that the tip of the unlocked cantilever does not snap into contact. Instead the tip is in a region above the true surface contact where the attractive force are balanced by other repulsive forces so the tip appears as if in physical contact with surface. Further motion of the piezoscanner pushes the cantilever back until the maximum deflection limit is reached. When the cantilever is locked using CD-AFM the cantilever tip is allowed to dive further in this region until the feedback system cannot lock the cantilever any more. However, the scenario cannot explain the substantial motion of the piezoscanner in this region by several tens of nanometre.

In the second scenario, the linear increase is attributed to the friction effect as the tip slides on the surface. The occurrence of sliding is more likely to happen when the tip is tilted an angle to the surface(*19*). In CD-AFM experiments, when the tip contacts a hard surface, the cantilever is not allowed to deflect upwards because of the locking forces, but it is possible that the cantilever tip slides forward on the surface. The sliding of the cantilever together with friction may cause the cantilever to bow resulting in an offset in the laser spot on the photodiode. Due to the linear motion of the piezoscanner, the deformation of the cantilever can be also linear. Such an offset induces the laser diode to pump more power to suppress such a shift. Hence, the vertical deflection is kept constant, but the laser power increases linearly. Likewise, the converse happens as the tip is retracted. Such a scenario could raise questions about the effect of the sliding on the sample and the positional accuracy of the tip. Previously, we demonstrated the system's capability to reproduce force curves on a soft surface such as a lipid bilayer. The lipid bilayer was imaged after acquiring the force curve and no damage was observed. However, further investigation is required.

5.7 Conclusion

Here, we have demonstrated an efficient use of CD-AFM to obtain similar force curves but with a locked cantilever to those obtained by standard AFMs. The cantilever is kept locked even on the surface. Such a conclusion was supported by several measurements performed on a hard and a soft surface. Moreover, an explanation is proposed as to how the system withstands the motion of the piezoscanner by introducing the concept of a friction effect. All curves and measurements are consistent with those obtained by the cantilever deflection (conventional AFM).

In this chapter we used two methods to calibrate force curves and to correct the tip-sample separation. Both methods have been proven accurate by comparing the results obtained using CD-AFM to those obtained using standard AFM.

A key feature of CD-AFM is its capability to perform force experiments without the disadvantages of cantilever mechanical instability. CD-AFM does not require tedious setup allowing the user to perform force experiments without additional preparations and using standard cantilevers. Moreover, the system can be operated in the standard force spectroscopy mode by just switching off the feedback circuit. These give our system versatility over other methods used to control AFM cantilever instabilities, such as magnetic and electrostatic force feedback (more details in chapter 3 section 3.3).

5.8 References

(1) Joyce, S. A., and Houston, J. E. (1991) A new force sensor incorporating force-feedback control for interfacial force microscopy. *Review of Scientific Instruments 62*, 710-715.

(2) Martin, Y., Williams, C. C., and Wickramasinghe, H. K. (1987) Atomic force microscope–force mapping and profiling on a sub 100-Å scale. *Journal of Applied Physics 61*, 4723-4730.

(3) Pethica, J. B., and Sutton, A. P. (1988) On the stability of a tip and flat at very small separations. *Journal of Vacuum Science & Technology A: Vacuum, Surfaces, and Films 6*, 2490-2494.

(4) Soma, D., Raychaudhuri, A. K., Sreeram, P. A., and Dietzel, D. (2009) The effect of intrinsic instability of cantilever on static mode atomic force spectroscopy. *Nanotechnology 21*, 045706.

(5) Kato, N., Suzuki, I., Kikuta, H., and Iwata, K. (1997) Force-balancing microforce sensor with an optical-fiber interferometer. *Review of Scientific Instruments 86*, 2475-2479.

(6) Butt, H.-J. (1991) Measuring electrostatic, van der Waals, and hydration forces in electrolyte solutions with an atomic force microscope. *Biophysical Journal 60*, 1438–1444.

(7) Bowen, W. R., and Jenner, F. (1995) Dynamic ultrafiltration model for charged colloidal dispersions: a Wigner-Seitz cell approach *Chemical Engineering Science 50*, 1707-1736.

(8) Faibish, R. S., Elimelech, M., and Cohen, Y. (1998) Effect of Interparticle Electrostatic Double Layer Interactions on Permeate Flux Decline in Crossflow Membrane Filtration of Colloidal Suspensions: An Experimental Investigation. *Journal of Colloid and Interface Science 204*, 77-86.

(9) Cappella, B., Baschieri, P., Frediani, C., Miccoli, P., and Ascoli, C. (1997) Force-distance curves by AFM. *IEEE Engineering in Medicine and Biology 16*, 58-65.

(10) Ducker, W. A., and Senden, T. J. (1992) Measurement of force in liquids using a force microscope. *Langmuir 8*, 1831-1836.

(11) Weisenhorn, A. L., Maivald, P., Butt, H. J., and Hansma, P. K. (1992) Measuring adhesion, attraction, and repulsion between surfaces in liquids with an atomic-force microscope. *Physical Review B 45*, 11226.

(12) Fraxedas, J., Garcia-Manyes, S., Gorostiza, P., and Sanz, F. (2002) Nanoindentation: Toward the sensing of atomic interactions. *Proceedings of the National Academy of Sciences of the United States of America 99*, 5228-5232.

(13) Martin, D. K. (2007) in *Fundamental biomedical technologies* (Ferrari, M., Ed.), Springer, New York.

(14) Liu, A. L. (2006) in *Advances in Planar Lipid Bilayers and Liposome*, Academic Press, London.

(15) Butt, H.-J., Cappella, B., and Kappl, M. (2005) Force measurements with the atomic force microscope: Technique, interpretation and applications. *Surface Science Reports 59*, 1-152.

(16) Butt, H.-J., and Franz, V. (2002) Rupture of molecular thin films observed in atomic force microscopy. I. Theory. *Physical Review E 66*, 031601.

(17) Loi, S., Sun, G., Franz, V., and Butt, H.-J. (2002) Rupture of molecular thin films observed in atomic force microscopy. II. Experiment. *Physical Review E 66*, 031602.

(18) Künneke, S., Krüger, D., and Janshoff, A. (2004) Scrutiny of the Failure of Lipid Membranes as a Function of Headgroups, Chain Length, and Lamellarity Measured by Scanning Force Microscopy. *Biophysical Journal 86*, 1545-1553.

(19) Hoh, J. H., and Engel, A. (1993) Friction effects on force measurements with an atomic force microscope. *Langmuir 9*, 3310-3312.

Chapter 6
Studying mechanical properties of I27 using CD-AFM

6.1 Introduction

Using AFM, the mechanical properties of approximately 50 proteins to date (*1, 2*), have been unveiled since the seminal work of Mitsui (*3*).The most extensively studied protein by AFM is the giant muscle protein titin, which is the biggest single chain protein discussed so far and mainly composed of roughly 300 repeats of Immunoglobulin (Ig) and Fibronectin type III (FNIII) domains(*4*). Each folded domain of titin is approximately 4nm long and that gives titin a length of more than 1μm and a width of 3nm (*5*). Titin is one of the most abundant proteins in striated muscle and spans almost half of the muscle sarcomere and contributes greatly to muscle elasticity. It

is involved in maintaining the structural integrity of sarcomere by developing what is called passive force, responsible for restoring muscle length after stretching. This process protects muscle from damage(*6*).

Titin is mainly divided into two regions, the A-band and the I-band, Figure 6.1. The A-band is mostly composed of FNIII (65%) and Ig repeats (30%), in addition to a kinase domain and unique sequences(*7*). Unlike the A-band, I-band contains Ig domains (proximal and distal regions), a PEVK segment (containing a high frequency of proline(P) , glutamic acid(E), valine(V) and lysine residues(K)) and unique sequences. The I-band of titin is the extensible region; therefore it is responsible for elasticity of titin and muscle (*8*). Ig domains are structurally similar, consisting of 8-9 strands of β-sandwich arranged in two anti-parallel sheets(*9*).

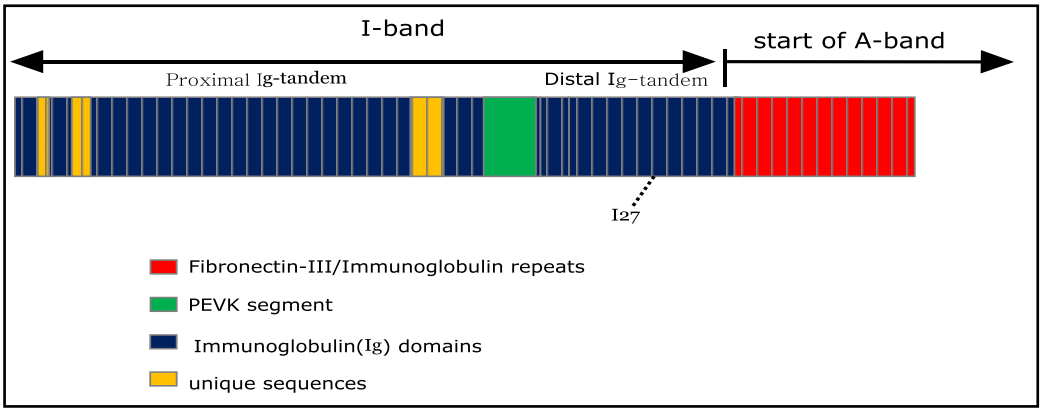

FIG.6.1 Scheme for titin structure.

The 27th Ig domain (I27) of the distal region of the I-band of human cardiac titin was one of the first domains with a known structure, in this case studied by NMR techniques(*10*). The architecture of I27 is similar to other Ig domains and consists of 8 strands of β-sandwich packing in two sheets against each other(*11-13*). Each sheet is composed of four strands; A`GFC sheet and DEBA sheet, Figure 6.2. Unlike other strands which are anti-parallel, the strand A` and G are parallel and linked to each other by six

hydrogen bonds, whereas the stands A and B are linked by three hydrogen bonds(*14*).

Although Ig domains, such as I27 and I1, have a similar structure, it has been observed that they show different response to applied forces(*4, 15*) indicating that the protein structure has a small role to play in the stability and resistance of proteins to deformation factors. However, experimental and theoretical studies have suggested that the stability could stem from difference in the positions and the number of hydrogen bonds between the β- strands which resist deformation (A' and G strands) (*16, 17*).

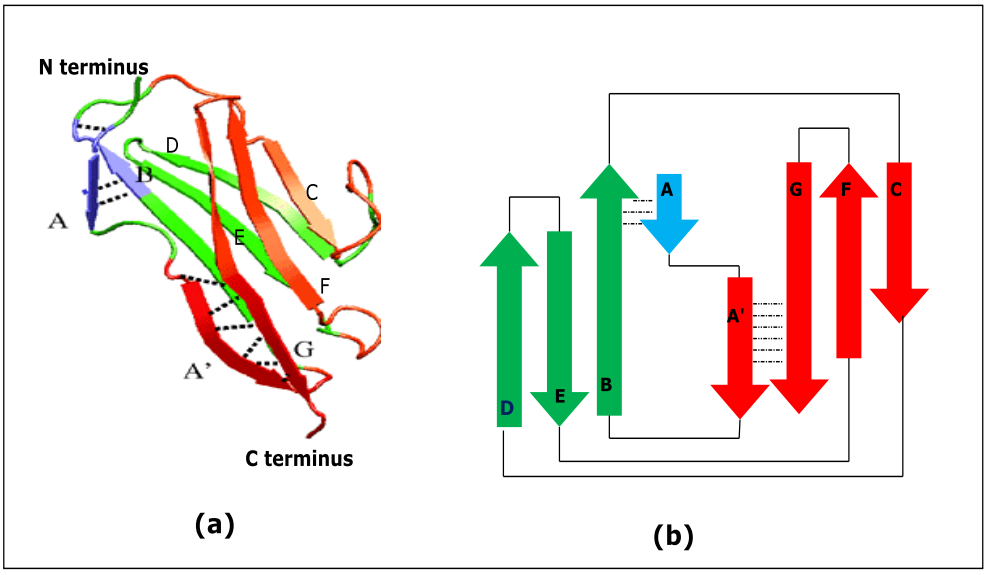

FIG.6.2 a) Structure of I27, b) topology diagram of I27. Dotted lines indicate hydrogen bonds positions. A`GFC sheet is colored in red and DEBA sheet in green.

I27 has become a paradigm for AFM experiments due to the huge number of experimental(*14, 17-22*) and theoretical(*23-25*) studies directed to explore its mechanical properties. Typically, the mechanical unfolding of a protein by AFM is performed by tethering the protein between the AFM cantilever tip and a substrate mounted on an AFM piezoscanner. Thus, the unfolding of the protein is triggered by applying a stretching force on it. At a certain force, the protein domains unfold subsequently providing a

sawtooth pattern. Unfolding tandem repeats of identical domains reveal a saw-toothed pattern with evenly spaced force peaks, where each peak represents the unfolding of a domain, Figure 6.3. The use of only a single domain is not feasible due to surface-tip interactions that obscure the interpretation of the force curve and titin cannot be used as it is difficult to identify which domain is unfolding (*3, 26-28*). Thus, an identical tandem repeats of a single domain is necessary to overcome the drawbacks associated with the ambiguity of the force curve. Protein engineering techniques have allowed the building of a construct of identical tandem repeats of a single domain(*29-31*). Therefore, obtaining a force-extension curve of a polymer of five, seven or even twelve I27 domains has become a routine experiment in many laboratories(*14, 32, 33*).

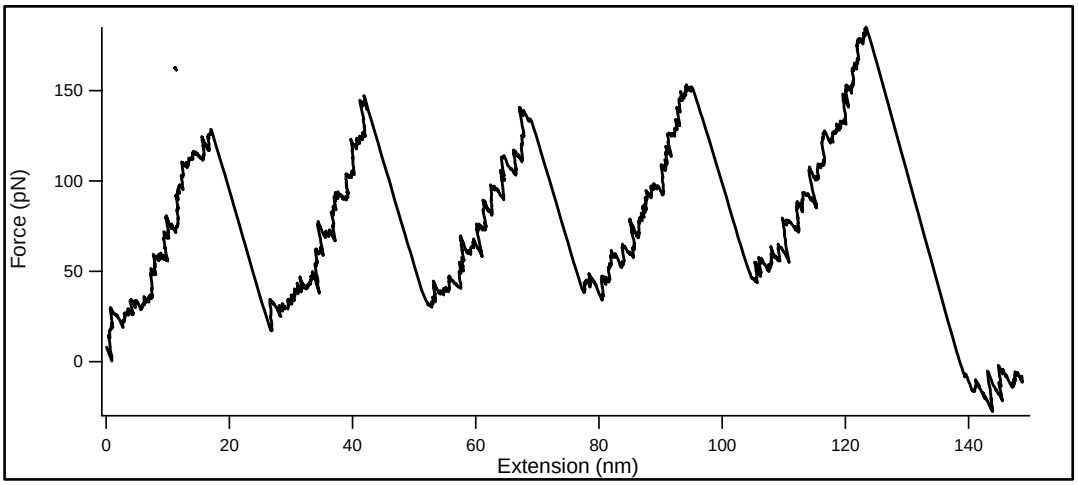

FIG.6.3 Force-extension curve of four domains of I27 acquired by conventional AFM using a microlever C at pulling speed of 400nm/s shows four equally distanced peaks. Each peak represents an unfolding domain of I27.

Based on numerous experiments and theoretical studies, such as Steered Molecular-Dynamic simulation (MD), the high structured stability of I27 domain is thought to be due to a patch of hydrogen bonds between four of its strands, A`-G and A-B(*23, 34*), Figure6.2.

The average unfolding forces of I27 vary between ~100pN and ~250pN, depending on the stretching rate(*1, 35*). Furthermore, AFM experiments have shown that the full contour length of I27 domain is on order of 28.1nm(*14, 36*). On the other hand, close examination of the I27 unfolding force-extension curve shows a deviation of its contour length that resembles a hump preceding the major unfolding peak. The deviation of the domain contour length was attributed to the intermediate of the unfolding pathway of I27 domain, Figure 6.4(*18*).

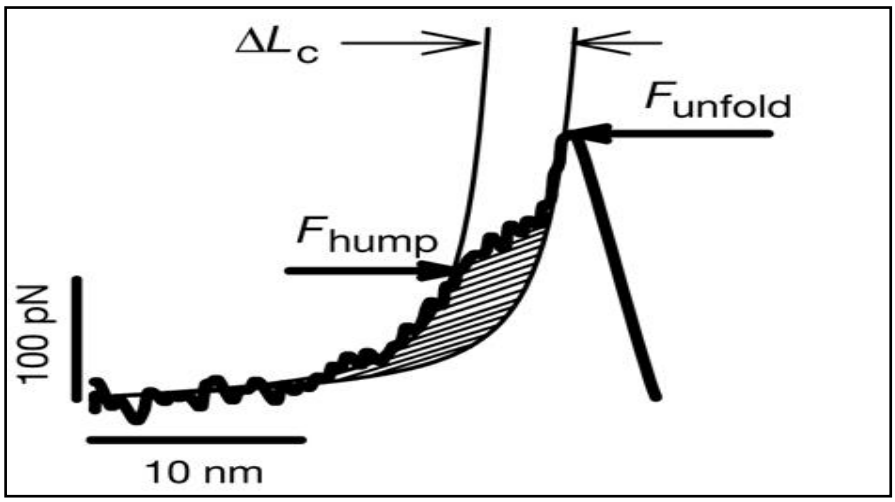

FIG.6.4 Plot of the first peak of I27 force-extension curve illustrates a deviation or hump prior the main peak. The hump is called intermediate unfolding peak (*18*)

According to molecular dynamic simulation (MD) prediction, when I27 domain is stretched by applying a force along its N and C termini, the greatest resistance to unfolding is created by the hydrogen bonds between A` and G strands and the intermediate peak observed on the I27 force-extension curve is due to breaking of a patch of hydrogen bonds between A and B strands that has lower resistance, this increases the end to end length of each domain by 0.6 nm, leading to the observed change in contour length (*18, 23*). Thus I27 has three phases; native, intermediate unfolding and complete unfolding.

In chapter 3, we have demonstrated the capability of CD-AFM of damping standard cantilever oscillations associated with its Brownian motion to a level that has never been achieved. The system allows us to perform force measurements for a biological sample in its physiological conditions without the limitation of thermal noise. Usually, recording unfolding events of proteins stretching by force below their thermal noise limit is impossible due to that the force amplitude of thermally induced cantilever oscillations is more enough to unravel the protein domain (detailed discussion in chapter 3). In addition, a calibration method to quantify force associated with using laser power, as a feedback force, has been developed (chapter 4 and 5), though it was a complex process involving measuring and studying the link between radiation and photothermal force and their impact upon the lever.

The use of the technique, described in this chapter, to unfold I27demonstrates that force-extension curves of protein can be obtained using CD-AFM. In contrast to the conventional method, a change of laser power used to suppress the deflection of the cantilever is used to record the force-extension curve of I27. Theoretically, CD-AFM is capable of measuring force as low as ~3 pN (using microlever C) limited by thermal noise (see chapter 3). This extends the ability of AFM to explore the mechanical properties of more proteins. Moreover, some of the drawbacks associated with the current use of AFM cantilevers to mechanically unfold proteins will be eliminated or minimized. These include the cantilever recoil after unfolding and the limited dynamic range achievable using standard AFM techniques.

6.2 Materials and methods

6.2.1 CD-AFM

The setup used to unfold a polymer of I27 domains is depicted in Figure 6.5. The key element of the system is a combination of two diode lasers; diode laser 1 (LD1) is exploited to provide the position of the cantilever through the deflection signal whereas the second diode laser (LD2) provides a feedback force. The CD-AFM configuration is based on a Veeco Picoforce microscope controlled by a Nanoscope IIIA controller (Digital Instruments, Santa Barbara, California) to permit standard force spectroscopy to be performed when the feedback circuit of CD-AFM is off.

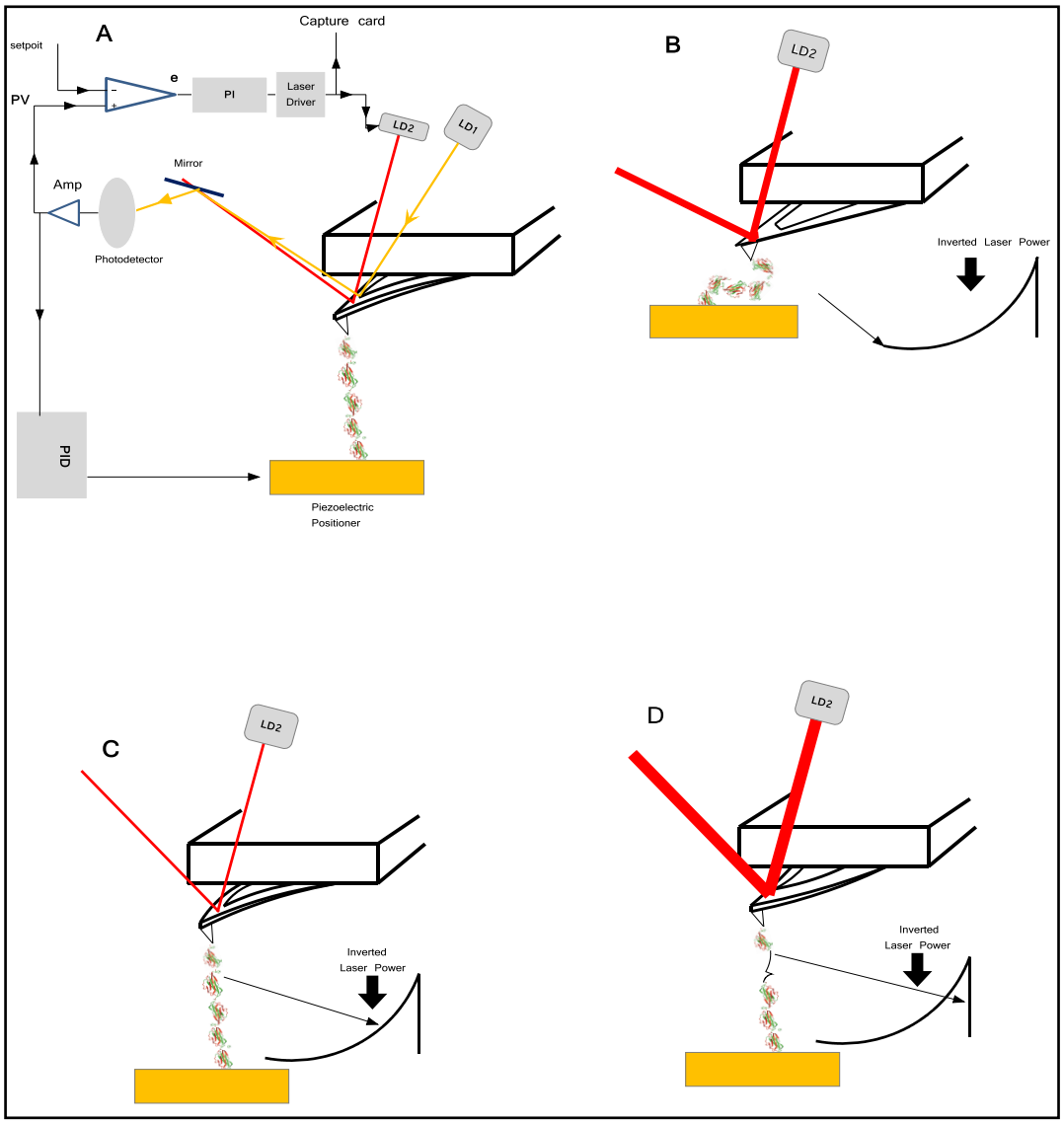

FIG.6.5 Schematic diagram of the I27 unfolding experiment using CD-AFM (A). Extension of an I27 domain results in deflection the cantilever that is corrected by increasing or decreasing the laser power to maintain the setpoint (B-D). The change of laser power reflects the cantilever change that results in the well known sawtooth pattern observed in the conventional experiment. The red line represents the LD2 radiation and its thickness reflects laser intensity.

6.2.2 Recording an unfolding of a single I27 domain

In this experiment, we use a construct consisting of five copies of I27 domain (C47S, C63S I27)$_5$ suspended in a PBS buffer at a concentration of 100 μgml^{-1}, for more details see chapter 2. All pulling experiments (unfolding of protein) have been performed using a Veeco microcantilever C, with a stiffness of 10 pN/nm. The stiffness of the microcantilever C was calibrated prior using the thermal noise method(*37*).

The CD-AFM system relies on an external capture card and softwares (for example, Labview) not designed for force spectroscopy measurements this increases the acquisition time for one force-extension curve comparing to standard AFM force spectroscopy. Consequently, force-extension curves are measured off-line. The time taken by CD-AFM is then longer than that is taken by standard AFM techniques. Thus it is necessary to make sure the cantilever tip is in the right place to pick up a protein construct with high probability prior to commencing the unfolding experiment.

To achieve this, the system is operated in the standard force spectroscopy mode by switching off the feedback circuit, until the cantilever tip starts picking up protein constructs with high ratio, normally two clear force-distance curves out of 100 hits. Thereafter, the cantilever is retracted an adequate distance from the surface so as the deflection of the cantilever is not influenced by the tip-surface interaction and the offset of the cantilever position resulting from the radiation force is much smaller than the separation between the tip and the surface. Otherwise, the cantilever may hit the surface.

The feedback circuit is switched on to lock the cantilever deflection at the chosen setpoint prior to approaching the cantilever again to the surface on

which I27 protein constructs are immobilized. To pick up the protein, the locked cantilever is pressed down onto the surface.

The loss in the feedback force lasts for less than 70 ms prior to the system restoring zero deflection (see chapter 5). This has no effect on the pulling experiment as the system regains the signal lock long before the tip leaves the surface.

Since the motion of the microlever is frozen, the unfolding of a domain is induced by the retraction of the piezoelectric positioner. The I27 construct is retracted via a piezoscanner at a constant velocity, Figure 6.5A. Retraction of the cantilever leads to an elongation of the poly protein leading to an increase in force and a gradual deflection of the cantilever. Bending of the lever is recorded as an error signal and sent to the feedback system which drives the second laser to decrease the amount of laser power incident on the cantilever in order to sustain the setpoint, Figure 6.5B-C. Once the protein domain unfolds the tension on the protein domain drops and hence the cantilever springs back, due to the restoring force, causing the laser power to increase to oppose the cantilever recoil keeping the deflection constant, Figure 6.5D. Thus, changes of lever deflection will be simultaneously transformed to changes in the laser power leaving the cantilever bending constant.

The deflection, z-piezo voltage and the laser power signals are captured by a capture PC card (National Instruments, Austin, Taxis) at a sampling rate of 10 kHz on a separate PC using a custom Labview program. The raw data recorded by Labview were exported as files to IgorPro software (Wavemetrics, Lake Oswego, Organ). Hence, the data were converted into volts using the Labview conversion factor (0.00244 V/bit) and filtered in order to remove electronic and thermal noise and analyzed offline using IgorPro.

6.2.3 Criteria applied for selection of force-extension curves

Best et al(*35*) introduced useful criteria to analyze unfolding force curves of proteins. Here, we follow the same criteria with some modifications to suit the CD-AFM system.

1. The force peaks should be evenly spaced.
2. The last peak represents the detachment of the protein either from the tip or surface.
3. Each curve should have at least three peaks without counting the last peak. Any force-extension curve containing less than three unfolding peak should be rejected.
4. The detachment peak has a larger drop in the laser power than the other unfolding peaks.
5. The zero force is determined by the region in which the change of the laser power is constant.
6. The unfolding force is the maximum force measured just before a sharp drop in the tension on the protein.
7. The cantilever should pick up a single protein. If the unfolding trace shows more than one protein attached, in series or in parallel, to the cantilever tip the trace should be rejected. For example, in the construct used in this experiment the number of domains is five, if the trace shows more than five peaks that means the tip picks more than a single construct.

6.2.4 Unfolding force vs the tip-sample separation

In chapter 5 we showed how the laser-displacement curve can be converted to the laser-separation curve. In this chapter we will follow the same approach. As for force calibration, in chapter 4 and 5 we introduced

a method to calibrate laser signal which demonstrated capability of measuring force precisely. The method used to convert the laser power into force depends on the rate of change of the laser signal during force measurements.

Figure 6.6 shows an unfolding peak of I27 domain recorded by laser signal as a function of time. In order to measure the unfolding force for each peak, the rising edge of the peak during the unfolding process is divided into different segments based on the rate of change of the laser signal. Each segment height is multiplied by computed conversion factor, see chapter 5 section 5.4.1. By adding the segment, in Newton, to each other, the unfolding force can be found.

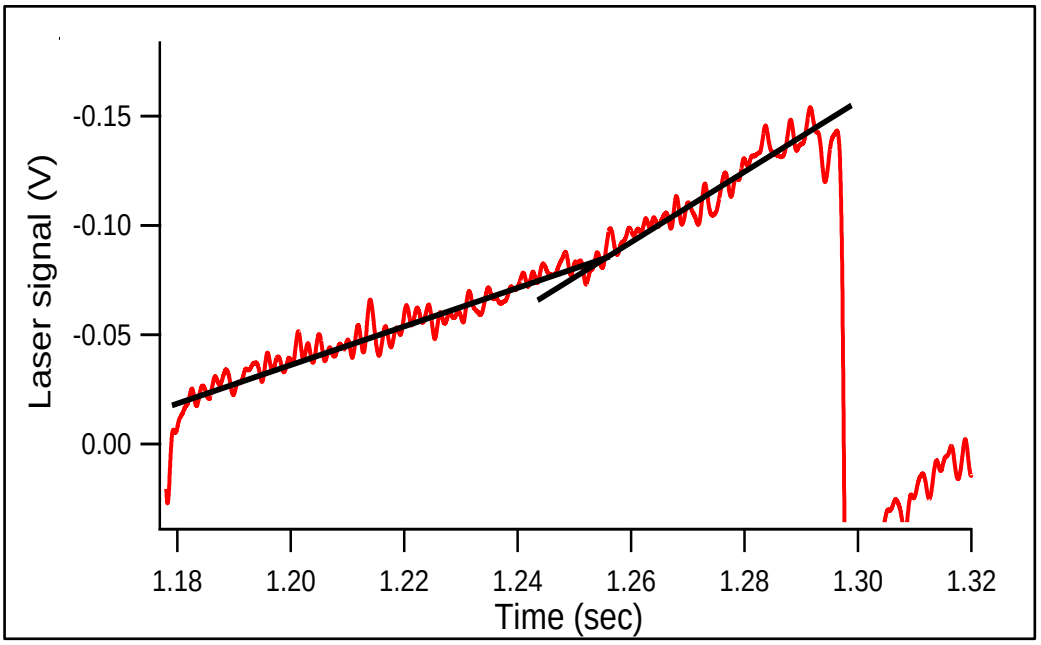

FIG.6.6 The rising edge of the unfolding peak of the protein obtained by laser signal displays variation in its steepness (black lines) that can be divided into two regions.

6.3 Results and discussion

6.3.1 Sawtooth fingerprint of the I27 construct

Figure 6.7 shows a force-extension curve of the mechanical unfolding of $(I27)_5$ using CD-AFM in which I27 domains are unraveled in series. The force-extension curve is obtained by monitoring the laser power while unfolding the protein. The peaks are equally spaced by a constant distance with a slight varying of the force around 170 pN. Each peak represents an unfolding of domain in the construct and the last peak in the trace is the detachment of the protein from either the tip or the surface. The most familiar force-extension profile of $(I27)_5$ concatamer was reproduced using a locked cantilever. The change of the laser power, used to damp the cantilever deflection, is successively utilized to reflect the change of the cantilever deflection caused by the unfolding events of I27. It is readily observed that the force-extension curve of the I27 construct obtained by the CD-AFM system is quite similar to that of conventional AFM.

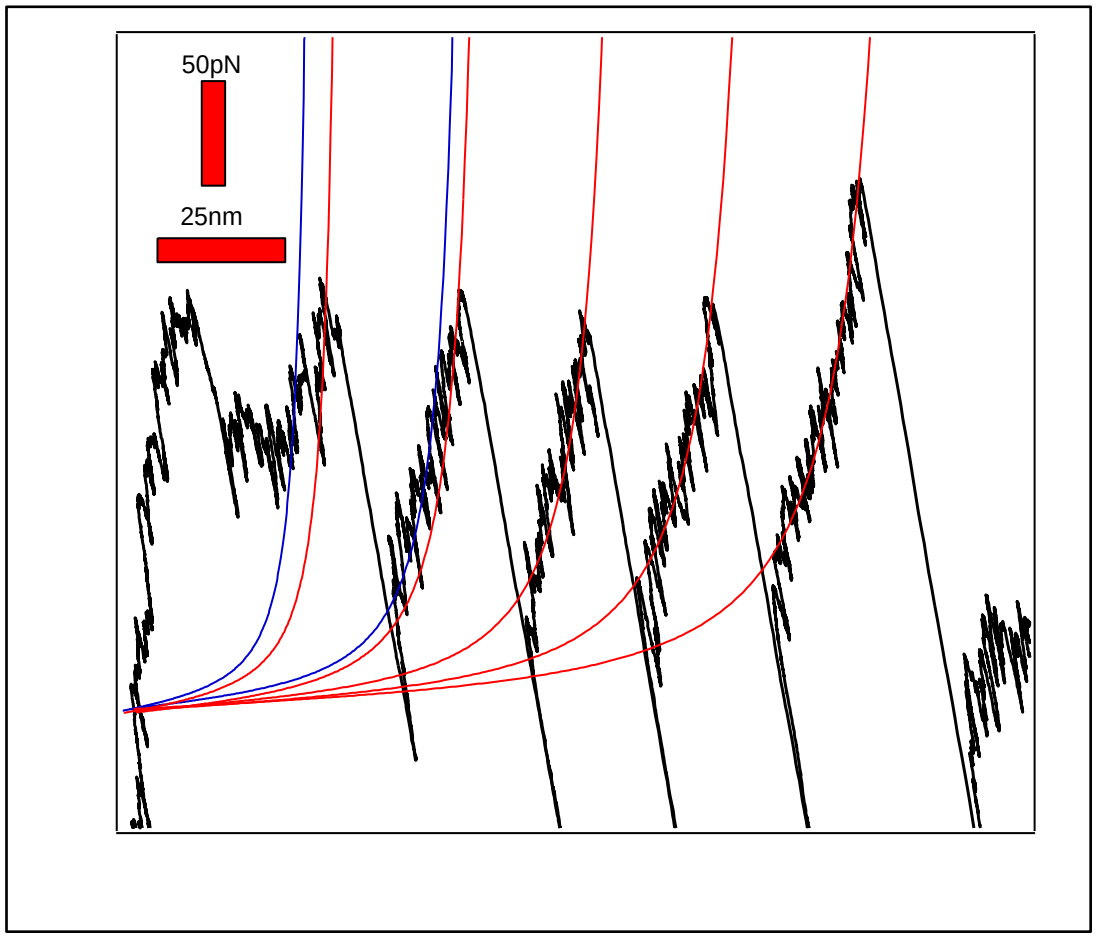

FIG.6.7 Mechanical unfolding curve of a concatamer of $(127)_5$, captured with CD-AFM at a pulling speed of 400 nms^{-1}. Four unfolding events recorded by the change of the laser power instead of the deflection with Veeco microcantilever C. The rising edge of the peaks can be fitted satisfactorily by WLC using a persistence length of 0.32 nm.

The rising edge of the unfolding of peaks can be described by the Worm - like chain model (WLC) used to describe the change in the length of a protein stretched via mechanical force(*38*). The relationship between the stretching force and the extension of a protein using WLC model is given by Eq.6.1

$$F(x) = \frac{K_B T}{p}\left[0.25\left(1-\frac{x_t}{L}\right)^{-2} - 0.25 + \frac{x_t}{L}\right] \qquad [6.1]$$

Where F is the applied force, x_t the extension, L is the contour length (the full extension length of each domain), p is the persistence length.

The second and third peaks were not well described by WLC. The first peak represents tip-surface interactions. Two WLC fits are used to describe the second and third unfolding peaks which may provide an evidence for the existence of the unfolding intermediate, previously described. Although, the deviation on the second peak is evident, it was not quite clear on the third peak due to the high electronic noise level associated with the laser power output. The deviation on the second peak is approximately 4 nm from the main peak and decreases to ~2 nm on the third peak. The evident deviation (small peak) on the second peak cannot be attributed to non-specific interactions between the AFM tip and the surface because the small peak is ~30 nm above the surface and the force interactions become ineffective at 30 nm above the surface(*14*).

To interpret the intermediate peak, one can imagine the I27 domain is composed of two regions, one is weaker than the other and less resistance to the unfolding force. The weaker regions unfold first throughout the I27 construct accumulating to form the intermediate peak(*12, 39*). The unfolding intermediate diminishes as more peaks unfold. Upon relaxation the tension force after unfolding the main peak, the weaker regions refold partially allowing the appearance of the intermediate peak on the consecutive peaks with decreasing strength (*18*).

One disadvantage related to the use of CD-AFM is that only four out of five domains in the poly protein are observed to unfold. This may attribute to the sliding of the cantilever tip when contacting the surface. In section 5.6, we proposed that when the tip contacts a hard surface and the cantilever is not allowed to deflect upwards because of the locking forces, the cantilever

tip slides forward on the surface. Such a slide may cause the first domain to unfold.

6.3.2 Determining the unfolding length of I27 module

In Figure 6.7 each force peak represents unfolding of an I27 domain and is separated from the next one by an equal space which is the contour length difference between a folded and unfolded I27 domain (ΔL).

ΔL is measured by fitting the rising edge of consecutive unfolding peaks to the WLC (Eq.6.1). Figure 6.8 illustrates a histogram of ΔL for the unfolding length of I27 domain obtained by CD-AFM. The peak of the distribution is located at~26.7 nm. This value is in agreement with the expected value of 27.3 nm, calculated by multiplying the number of amino acids by the separation distance between sequential C_α atoms(*34*). The typical value of ΔL of I27 measured using standard AFM techniques is ~28 nm. Thus, within the expected range of error, ΔL is in good agreement with the expected value.

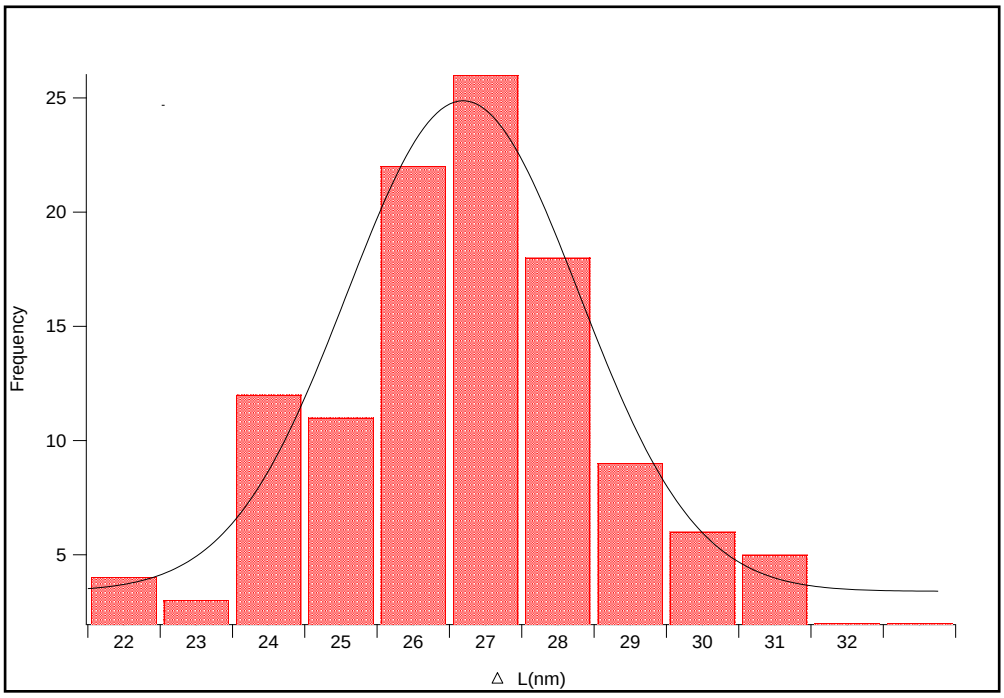

FIG.6.8 Distribution of ΔL for an I27 domain using CD-AFM.

6.3.3 The influence of loading rate on the measured unfolding force

The loading rate is an important determinant of the magnitude of the unfolding force. The loading rate is an expression used to describe the rate at which the mechanical force applied to the protein. The effect of the loading rate on the unfolding force was predicted by Bell's model (*40*)

$$F = \frac{k_B T}{x_u} \ln\left(\frac{x_u r_f}{k_B T \alpha(0)}\right) \qquad [6.2]$$

Where F represents unbinding force (unfolding force), x_u is the width of the potential for unfolding, k_B is Boltzmann constant, T is temperature and α(0) is the unfolding rate in the absence of the mechanical force.

According to the Bell model, the unfolding of a protein is a process in which the free energy landscape of the protein is deformed by applying force,

Figure 6.9. The protein settles at its native state (N) at the bottom of an energy well of depth of ΔG_u . The depth of the well represents the height of energy barrier that the protein has to cross to unfold. In forced unfolding experiments, the role of the mechanical force is to lower the energy barrier by Fx_u , where x_u represents the width of the energy transition barrier (*34, 38, 40, 41*). In the absence of an external force the unfolding of a protein is dominated by the thermal force whereas the presence of an external mechanical force creates a competition with the thermal force(*38, 42*). Thus, in the low loading rate regime the effect of the thermal force is the major determinant of the unfolding process but its role diminishes with increasing the loading rate where the mechanical force becomes dominant. Experimentally the loading rate can be given by

$$r_f = k_{eff}.u \qquad [6.3]$$

Where u is the pulling speed (which is the retraction velocity of the cantilever tip) and k_{eff} is the effective stiffness.

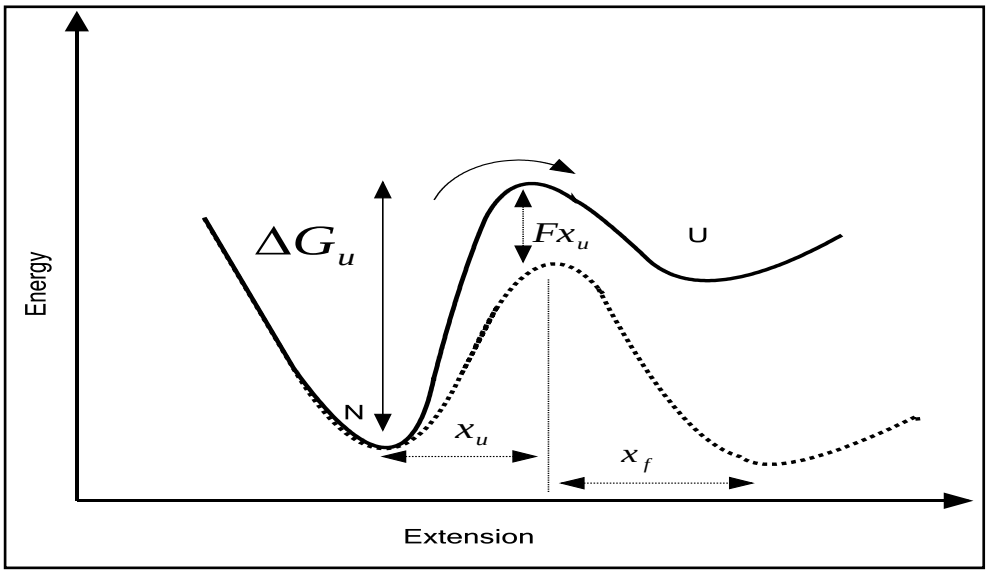

FIG. 6.9 Energy diagram of the unfolding of a protein. Solid line shows the energy diagram of the protein without applied force. The lowest energy level of the protein is its native state (N). ΔG_u is the height of energy barrier. Dashed line represents the energy path of unfolding of the protein after applying a force (F). The height of energy barrier is lowered by Fx_u that allows the protein to jump to unfolding state (U) where x_u is the distance between bound state and transation state (the width of the potential for unfolding) and x_f is the width of the potential for folding

k_{eff} describes a combined stiffness of the protein and the cantilever. Thus, during unfolding the protein construct the cantilever act as two springs linked in series(*43*)

$$\frac{1}{k_{eff}} = \frac{1}{k_c} + \frac{1}{k_p} \qquad [6.4]$$

Where k_c is the stiffness of the cantilever and k_p is the stiffness of the protein construct.

In pulling experiments using conventional AFM two parameters define the loading rate; the pulling speed and the cantilever stiffness. Although the use of a stiffer cantilever can increase the loading rate, the force resolution can be deteriorated. Therefore, an increase of the loading rate will be at the expense of the force resolution.

The loading rate can also be increased by increasing the pulling speed. The faster stretching the protein the higher unfolding force (*34, 44*). Eq.6.3 shows that the loading rate increases linearly with increasing the pulling speed. However, the maximal pulling speed is limited to <2-4 μm/s. Janovjak and et al(*45*) showed that if the pulling speed is above a few μm/s the effect of hydrodynamic force acting on the cantilever can be of the order of 100 pN that leads to a large deviation in force measurements.

As can be seen from Eq. 6.2 the force at which a protein unfolds is proportional to the loading rate of force application. This relationship has been demonstrated by a number of experimental studies (*12, 34, 38, 46*) and predicted by simulation methods such as Monte Carlo simulation (*14, 47*). Thus, the curves acquired by CD-AFM should follow the same trend.

To investigate the effect of pulling speed on unfolding forces using CD-AFM a concatamer of $(I27)_5$ is unfolded at four pulling speed 100 nm/s, 400 nm/s, 600 nm/s and 900 nm/s. The mean rupture force at each pulling speed is obtained by fitting the histogram of the forces distributions to a Gaussian function, Figure 6.10.

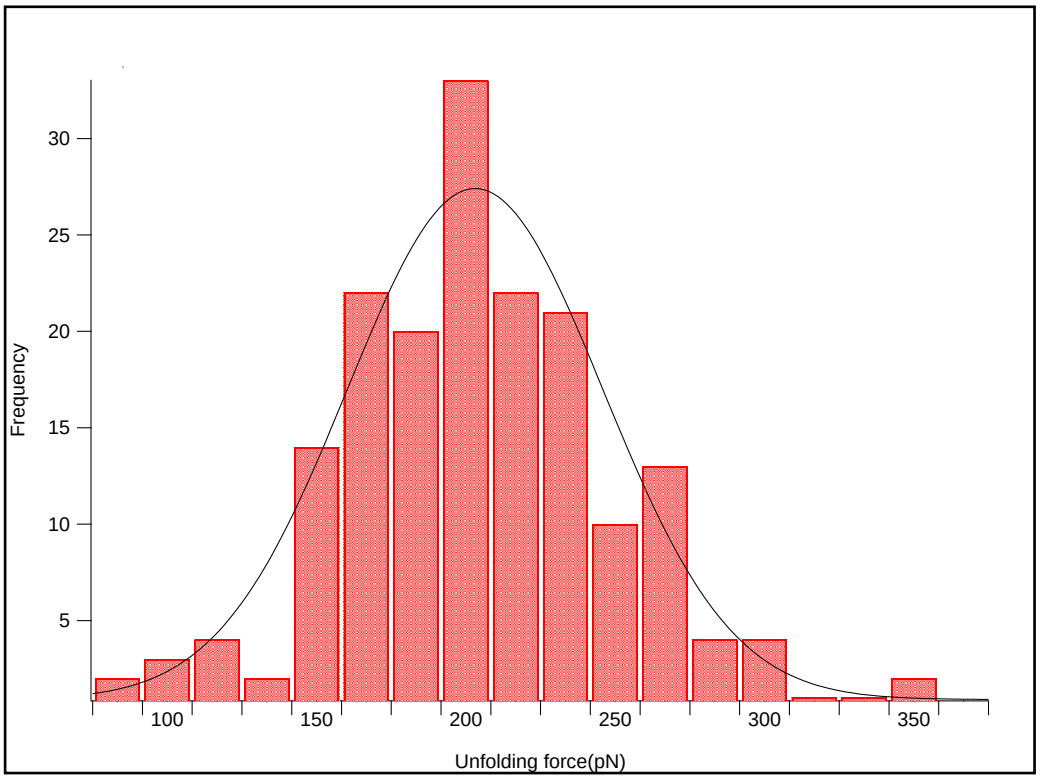

FIG.6.10 Histogram of the mechanical unfolding forces of $(I27)_5$ obtained by CD-AFM at pulling speed of 400 nms^{-1}

Figure 6.11 illustrates the pulling speed dependence of unfolding forces of $(I27)_5$ construct obtained by CD-AFM and conventional AFM using the same construct(*34*) at different pulling speeds. The increase of rupture force with pulling speed is observed, which is an evident proof that the force curves obtained by the CD-AFM system follow the predictions made by the Bell model.

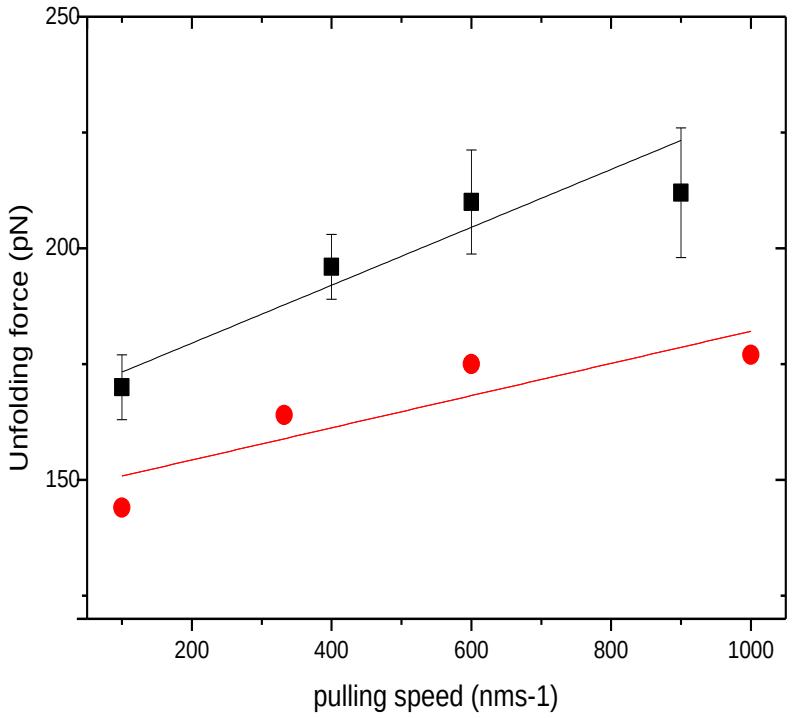

FIG.6.11 Pulling speed dependence of the unfolding force of $(I27)_5$ obtained by CD-AFM (black square), compared with published data (red circle) obtained by a Veeco microcantilevre (k=30 pN/nm) using standard AFM force techniques, taken from (*34*).

In contrast to the unfolding force obtained by conventional AFM (*34*) the unfolding force recorded by the CD-AFM system shows a significant increase at each pulling speed. For example, the unfolding force at a pulling speed of 400 nm/s is ~200 pN using CD-AFM whereas the value obtained for the same construct by conventional AFM is ~160 pN. The increase observed in the rupture force is expected. Bell's model predicts the unfolding force is affected by the system stiffness (k_{eff}) and hence the loading rate. Thus, the higher the effective stiffness the higher the unfolding forces(*47, 48*).

6.3.4 Effect of cantilever recoil on formation of refolding peaks

In the absence of tension, the unfolded domain can refold fully or partially. (*49-55*). Further extension then unfolds these fully or partially refolded domains. However, due to recoiling the cantilever after unfolding events further tension may be loaded on the protein that prevents the formation of refolding peaks.

The use of CD-AFM minimizes the effect of cantilever's recoil. Figure 6.12 shows the recoil of the cantilever is almost zero indicating that there is no tension loaded on the refolded domain. Thus the indirect observation of the fully/partially refolding events (if they exist) using a locked cantilever is more likely than by conventional AFM.

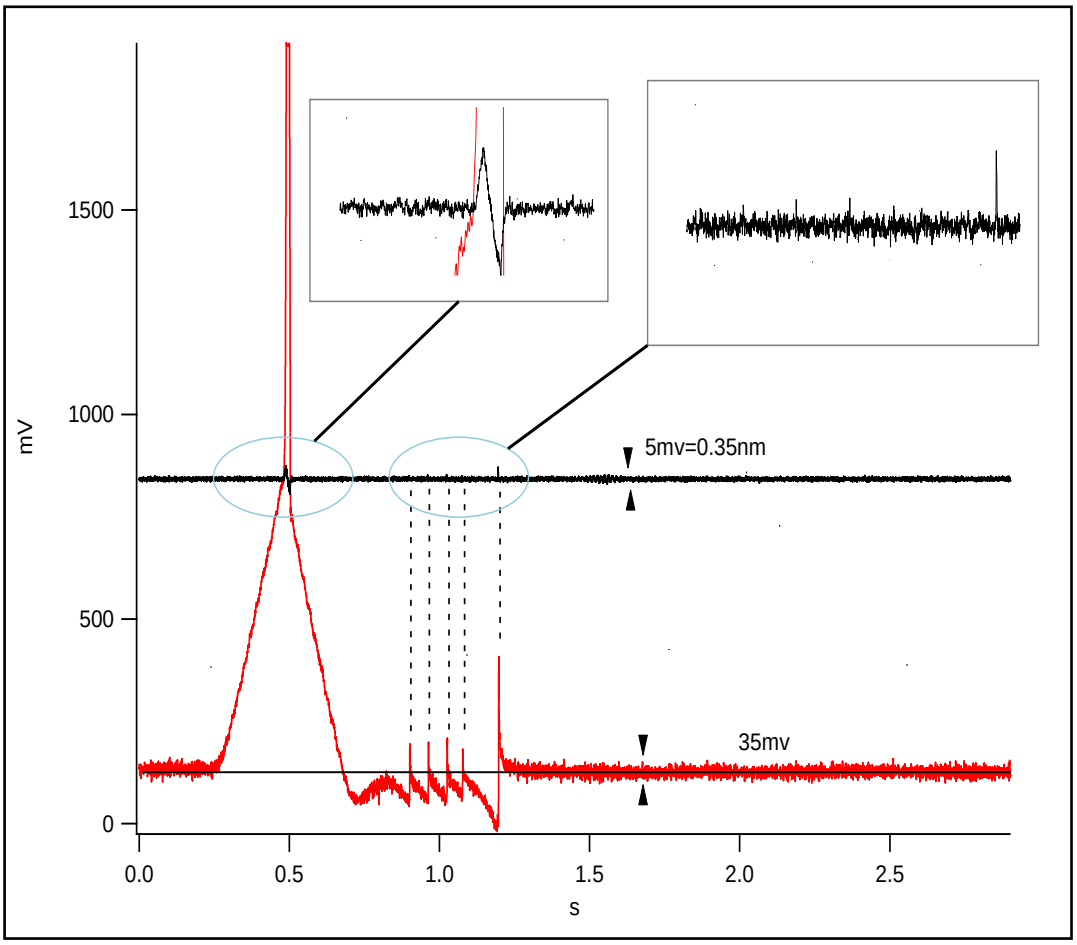

FIG.6.12 Change of the laser signal (LD2) during the mechanical unfolding of I27 domains (red) and the cantilever deflection signal (black) recorded simultaneously.

However, close inspection of all curves obtained using CD-AFM show no sign of refolding. This may be due to the slow folding rate in I27 domain, taking no less than 1s to refold that is longer than the pulling experiment time scale(*14, 53*). The long time refolding is due to the fact that the width of the potential for folding is 50 times larger than the width for unfolding(*39, 56*). Therefore the observation of such events is unlikely.

In contrast, protein L has a faster folding rate than I27(*57*), and it is more likely to observe refolding events. Figure 6.13 shows main unfolding peaks of protein L followed by secondary peaks which may be attributed to refolding events(*58*). The space between the main peak and the secondary

peak (refolding) is consistent through the trace at 5 nm. It is worth noting, in conventional pulling experiment, no refolding events are observed.

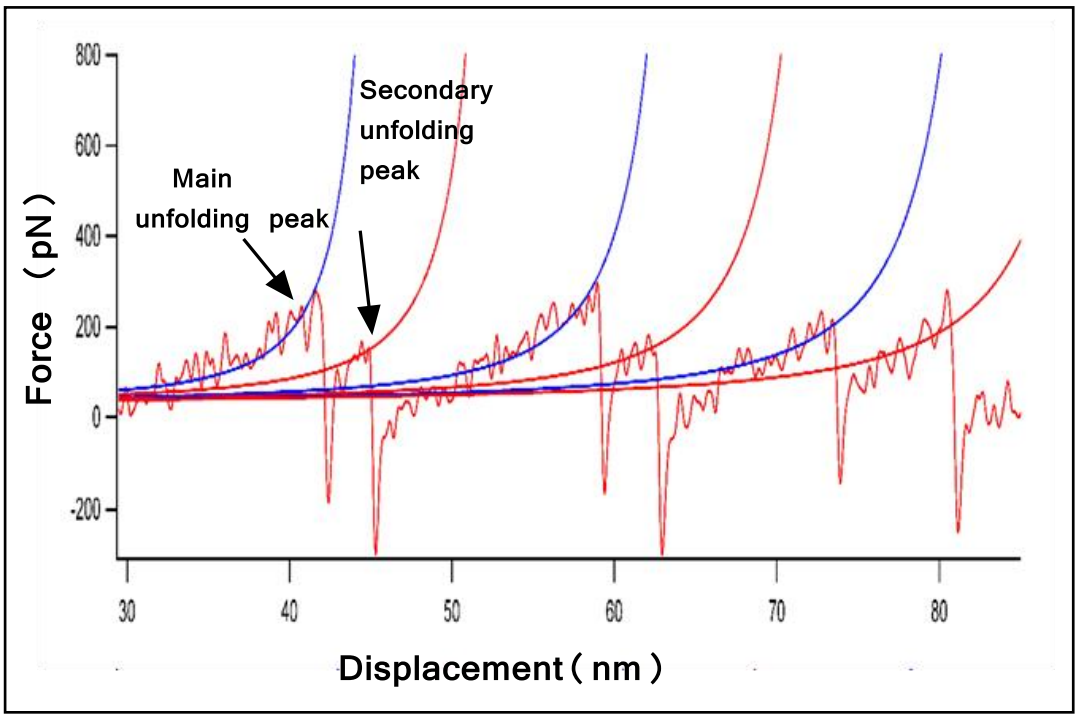

FIG.6.13 The presence of secondary unfolding peaks due to refolding events in the force – distance curve of protein L obtained by CD-AFM taken from(*58*).

The presence of the refolding peaks in the force curve of protein L supports the conclusion that CD-AFM minimizes the effect of the tension generated by the recoiling cantilever after unfolding the protein's domain.

6.3.5 The effect of the feedback system on the I27 unfolding trace

In contrast to the conventional pulling experiment, the force-extension traces acquired by CD-AFM show spikes after each unfolding event, Figure 6.14. The occurrence of the spikes is due to the overreaction introduced by the feedback system to compensate the rapid change in the cantilever deflection. The resistance of the protein to the stretching force

causes the cantilever to deflect downwards resulting in a gradual decrease in laser power in an attempt to maintain the system setpoint. A sudden increase in the molecule's length releases the stored energy in the deflected cantilever causing it to spring upwards. This causes the feedback system to apply more laser power to counteract such a quick change in the cantilever position. If the event occurs in time faster than the response time of the feedback system, due to its finite response (details in chapter 3), such spikes will be inevitable.

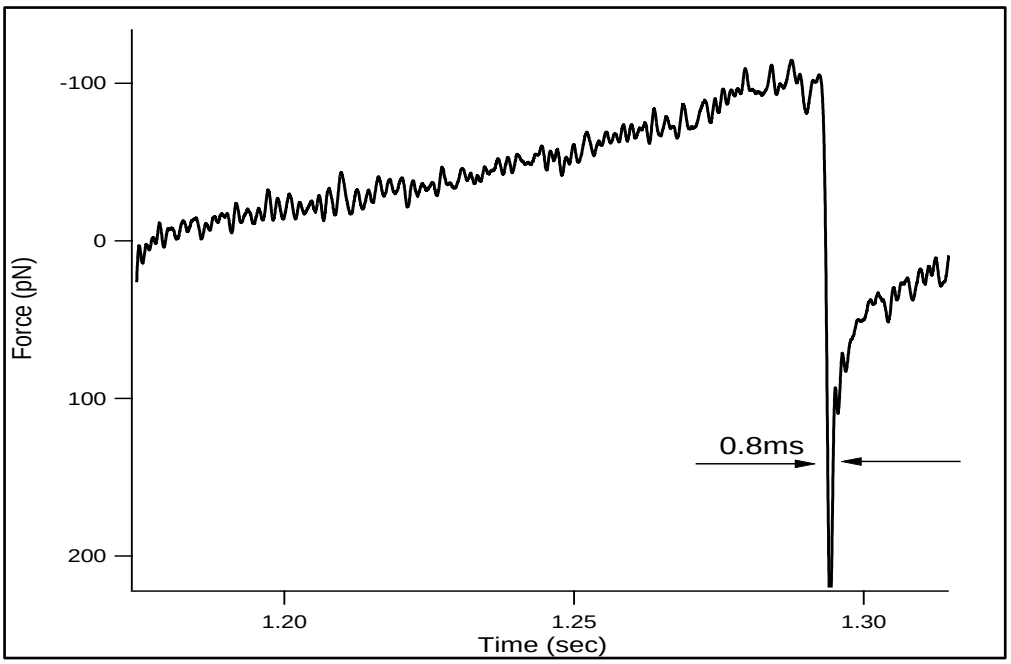

FIG.6.14 The mechanical unfolding curve for $(I27)_5$ obtained by CD-AFM shows a brief spike after unfolding the domain caused by the feedback circuit.

To show that the spikes are artifacts caused by the feedback loop and not real signal induced by unfolding the protein domain, I analyzed the effect of a sudden change in the cantilever deflection on the feedback signal using the same setup discussed in section 3.5.

In such a setup, the driving signal, a square-wave voltage, generated from a function generator is fed into the setpoint of the system causing an offset

in the cantilever deflection. The driving signal is abruptly changed from zero to maximum in order to mimic the abrupt change of the cantilever deflection following an unfolding event, Figure 6.15. The feedback system responds to that change by applying an appropriate force on the cantilever to maintain the setpoint.

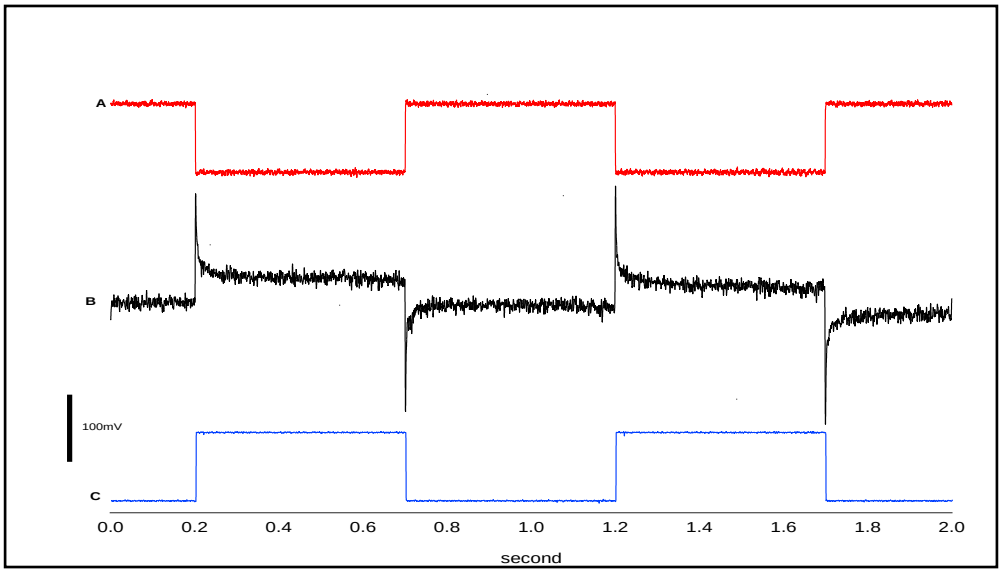

FIG.6.15 Response of the feedback system (black) to a sudden change in the deflection signal of the cantilever (red) driven by a square wave signal (blue) at 1Hz and an amplitude of 100mV.

Figure 6.15B shows similar spikes to those seen in Figure 6.14 or 6.12 leading to a conclusion that spikes are artifacts and caused by the feedback system. However, the system overreaction does not affect the damping process.

Figure 6.12 shows the cantilever deflection and change of laser power, used to suppress the cantilever deflection, both recorded simultaneously. The deflection of the cantilever contains a tiny spike following the detachment of the protein construct which have no impact on cantilever's stability. Although the response of the feedback system to an abrupt change of the cantilever position is not effective, the system overreaction

takes <1 ms to reestablish the setpoint and that time may be considered as a dead time of the feedback system, Figure 6.14. Hence, an event occurring within time <1 ms after unfolding the domain will not be resolved by the system.

6.3.6 Effect of temperature on unfolding force

An increase in temperature of a biological sample such as proteins may damage them. Proteins can be denatured or softened by increasing their temperature. Taniguchi et al. (*59*)reported that the unfolding force of I27 decreases by 1.5 pN/°C. In addition, it has been reported that the temperature of a lipid irradiated directly by an IR laser beam with a diameter of 0.8 μm and 100 mW rises by ~1.5°C(*60*).

In order to measure the increase in temperature during force measurements by our system, a thermocouple sensor type K is placed inside the fluid cell close to the probe. The rise in temperature is monitored for 40 minutes using a digital thermometer (Fluke 52.2-dual input) and is found to be <2°C. Therefore, the use of the IR laser has no significant effect on the unfolding force of protein.

6.3.7 Effect of electronic noise on force measurements

The level of electronic noise associated with the laser signal may mask the real signal. In order to determine the effect of the noise on the laser signal, we measured the double layer force generated between an AFM tip and a mica surface in ultrapure water (Milli-Q water, 18MΩ). As surface forces scale with area, the repulsive double layer force depends drastically on the radius of the cantilever tip (*61*). Using standard AFM techniques, we found

the maximum repulsive double layer force (before jump-to-contact point) resulting from interactions between silicon-nitride tip (Veeco-MLTC, stiffness of 10 pN/nm and nominal radius of 20-60 nm) and the mica surface is ~400 pN. However, the force drops to ~30 pN using a sharper silicon tip (Veeco-MSNL, stiffness of 10 pN/nm and nominal radius of 2-3 nm), Figure 6.16 (black trace). The laser signal (red trace) shows the same measured force. Both curves are smoothed at frequency equivalent to 400 Hz. However, due to electronic noise, deflection noise was limited to ~15 pN and for the laser signal to ~30 pN.

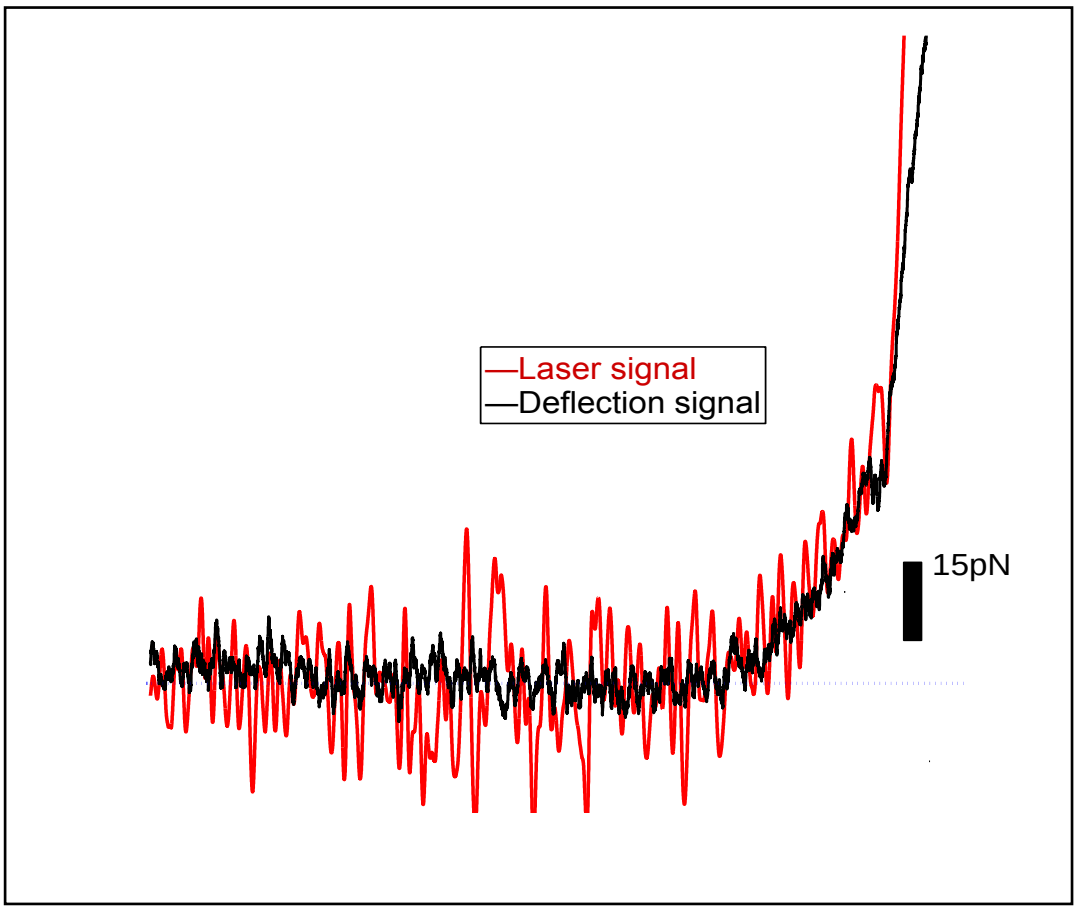

FIG.6.16 Force curves acquired using a cantilever tip ((Veeco-MSNL, stiffness of 10 pN/nm and nominal radius of 2-3 nm) on mica surface. Conventional AFM (black) and CD-AFM (red).

Further smoothing of the curve could reduce the level of noise leading to an increase in signal to noise ratio (SNR), but it could also degenerate the signal. For example, in the unfolding force curve of protein, the shape of the unfolding peak can be changed, Figure 6.17. Fast transient events, such as the tip recoil after unfolding, are averaged and smoothed if the smoothing is set to high.

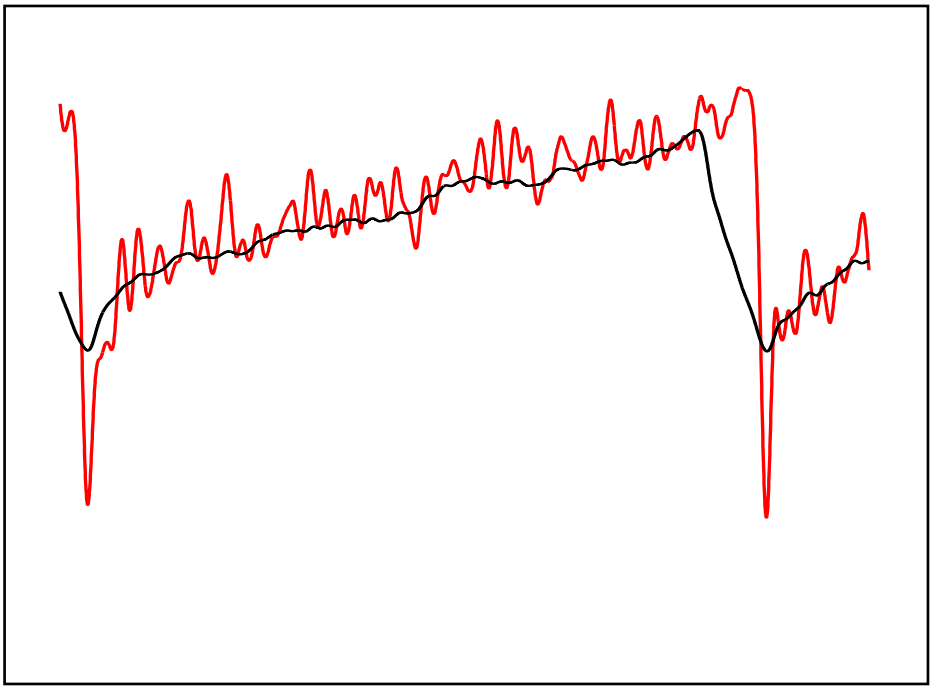

FIG.6.17 An unfolding peak of protein obtained by laser signal. The laser signal is filtered at 400 Hz (red) and at 200 Hz (black).

In chapter 3 we showed that the background noise density (white noise) of the optical beam deflection system is ~1000 fm/√Hz. This noise has a wide range of frequencies and can cause fluctuation in the output of the feedback system at all frequencies, including frequencies below 200 Hz. The output of the feedback system depends on the deflection system. Hence this noise manifests as broadband noise on the laser signal. Handling such noise is possible. However, Fukuma et al (*62*) demonstrated the density of the deflection noise can be reduced to less than 17 fm/√Hz

by using more sensitive detectors. Such low level of noise can improve the performance of the system and SNR of its output (discussed in chapter 3).

Noise related to the ground loop may also have a significant impact on the noise level. Such noise originates from variation in the ground potential of power outlets. Thus, if two or more electronic instruments are plugged into different power outlets noise of 50/60 Hz or their harmonics may appear in the output signal(*63*). For example, ground loop noise manifests itself as hum in audio systems. The CD-AFM system is composed of more than six electronic instruments each plugged into different power outlets, so the occurrence of such noise is inevitable.

Filtering the signal at low frequency is not an appropriate way to minimize the level of noise. The use of a low pass filter with cut off frequency around 50 Hz is not preferable as events at frequencies >50 Hz may be eliminated as well. A band pass filter is not adequate as the surrounding frequencies to the cut off frequency may be removed(*63, 64*). Therefore, the ideal solution is to connect all the earthing paths of the system to one outlet. This can be achieved by using an isolation transformer with enough outlets(*65*). The isolation transformer allows removing the effect of variation of the ground potential.

Such electronic noise can prevent observing unfolding force of proteins located beneath the noise limit. Figure 6.18 shows an unfolding force curve obtained using CD-AFM to an $(Im9)_3(I27)_4$ construct comprised of three Im9 domains alternating with four I27 domains. The presence of I27 domains acts as fingerprint of the construct and to facilitate the analysis. The unfolding domains of I27 can be readily observed. However due to the high level of electronic noise, no mechanical unfolding peaks of Im9 are recorded indicating that Im9 has very low unfolding force which is expected to be <20pN(*66*). The unfolding peak of Im9 is believed to be intact and

buried under the electronic noise. The deflection of the cantilever recorded during the unfolding shows that the thermal fluctuations induces unfolding force of ~3 pN. Therefore, if we ruled out the electronic noise CD-AFM would observe any force above ~3 pN.

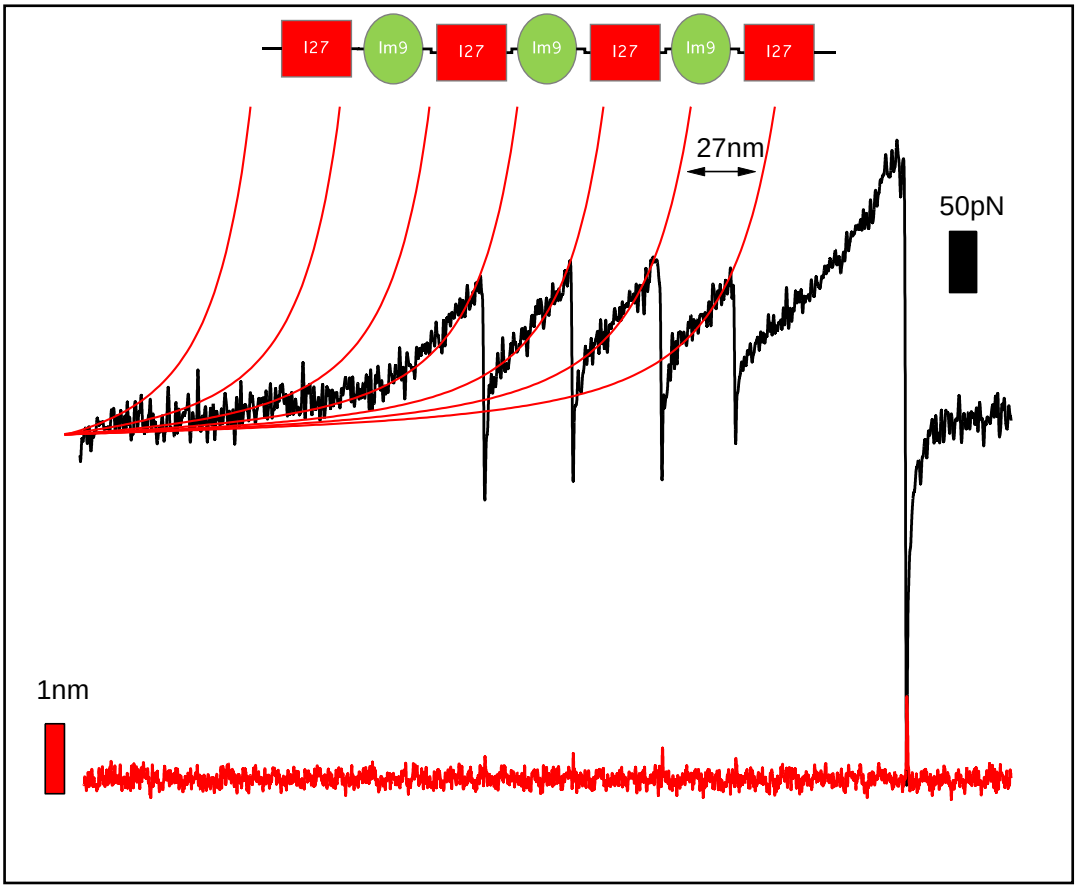

FIG.6.18 (Top) unfolding curve of $(Im9)_3(I27)_4$ construct obtained by laser signal. Four mechanical unfolding peaks of I27 can be observed and due to electronic noise no unfolding peak of Im9 can be observed. (Bottom) the deflection signal of the locked cantilever during acquisition of the force curve. The cantilever deflection is locked at ~0.35 nm equivalent to ~3 pN.

We hope the reduction of detection system and ground loop noise, will allow force resolution of the order of subpiconewton. However, introducing such improvements to our system was difficult due to the limited time we had.

6.4 Conclusion

In this chapter we demonstrate the implementation of CD-AFM for unfolding proteins. The use of I27 is only a proof of principle that unfolding force-extension curve of a protein could be obtained by using CD-AFM by which a very soft microcantilever is locked to a spatial fluctuation of approximately 0.3 nm peak to peak.

Here we demonstrated the use of CD-AFM minimizes effects of instabilities associated with the use of soft cantilevers such as the recoil of cantilever and thermodynamic noise. Moreover, we demonstrated the use of our system can increase the loading rate without deteriorating the force resolution. Due to the electronic noise the system's sensitivity is limited to ~30 pN. However, we proposed some solutions to solve the electronic noise by which the system's sensitivity would be improved further. Such solutions will be implemented later.

6.5 References

(1) Linke, W., and Grützner, A. (2008) Pulling single molecules of titin by AFM—recent advances and physiological implications. *Pflügers Archiv European Journal of Physiology 456*, 101-115.

(2) Sulkowska, J. I., and Cieplak, M. (2008) Stretching to Understand Proteins--A Survey of the Protein Data Bank. *Biophysical Journal 94*, 6-13.

(3) Mitsui, K., Hara, M., and Ikai, A. (1996) Mechanical unfolding of a2-macroglobulin molecules with atomic force microscope. *FEBS Letters 385*, 29-33.

(4) Li, H., and Fernandez, J. M. (2003) Mechanical Design of the First Proximal Ig Domain of Human Cardiac Titin Revealed by Single Molecule Force Spectroscopy. *Journal of Molecular Biology 334*, 75-86.

(5) Tskhovrebova, L., and Trinick, J. (2003) Titin: properties and family relationships. *Nat Rev Mol Cell Biol 4*, 679-689.

(6) Trombitas, K., Greaser, M., Labeit, S., Jin, J.-P., Kellermayer, M., Helmes, M., and Granzier, H. (1998) Titin Extensibility In Situ: Entropic Elasticity of Permanently Folded and Permanently Unfolded Molecular Segments. *J. Cell Biol. 140*, 853-859.

(7) Tskhovrebova, L., and Trinick, J. (2002) Role of titin in vertebrate striated muscle. *Philosophical Transactions of the Royal Society of London. Series B: Biological Sciences 357*, 199-206.

(8) Nagy, A., Cacciafesta, P., Grama, L., Kengyel, A., Malnasi-Csizmadia, A., and Kellermayer, M. S. Z. (2004) Differential actin binding along the PEVK domain of skeletal muscle titin. *J Cell Sci*, jcs.01501.

(9) Erickson, H. P. (1994) Reversible unfolding of fibronectin type III and immunoglobulin domains provides the structural basis for stretch and elasticity of titin and fibronectin. *Proceedings of the National Academy of Sciences of the United States of America 91*, 10114-10118.

(10) Improta, S., Politou, A. S., and Pastore, A. (1996) Immunoglobulin-like modules from titin I-band: extensible components of muscle elasticity. *Structure 4*, 323-337.

(11) Fisher, T. E., Marszalek, P. E., and Fernandez, J. (2000) Stretching single molecules into novel conformations using the atomic force microscope. *Nature Structural Biology 7*, 719–724.

(12) Rief, M., Gautel, M., Oesterhelt, F., Fernandez, J. M., and Gaub, H. E. (1997) Reversible Unfolding of Individual Titin Immunoglobulin Domains by AFM. *Science 276*, 1109-1112.

(13) Lu, H., and Schulten, K. (2000) The key event in force-induced unfolding of Titin's immunoglobulin domains. *Biophysical Journal 79*, 51-65.

(14) Carrion-Vazquez, M., Oberhauser, A. F., Fowler, S. B., Marszalek, P. E., Broedel, S. E., Clarke, J., and Fernandez, J. M. (1999) Mechanical and chemical unfolding of a single protein: A comparison. *Proceedings of the National Academy of Sciences of the United States of America 96*, 3694-3699.

(15) Marek, C., Annalisa, P., and Trinh Xuan, H. (2005) Mechanical properties of the domains of titin in a Go-like model. *The Journal of Chemical Physics 122*, 054906.

(16) Lu, H., Isralewitz, B., Krammer, A., Vogel, V., and Schulten, K. (1998) Unfolding of Titin Immunoglobulin Domains by Steered Molecular Dynamics Simulation. *Biophysical Journal 75*, 662-671.

(17) Brockwell, D., Paci, E., Zinober, R., Beddard, G., Olmsted, P., Smith, A., Perham, R., and Radford, S. (2003) Pulling geometry defines the mechanical resistance of a beta-sheet protein. *Nature Structural Biology 10*, 674-776.

(18) Marszalek, P. E., Lu, H., Li, H., Carrion-Vazquez, M., Oberhauser, A. F., Schulten, K., and Fernandez, J. M. (1999) Mechanical unfolding intermediates in titin modules. *Nature 402*, 100-103.

(19) Williams, P. M., Fowler, S. B., Best, R. B., Luis Toca-Herrera, J., Scott, K. A., Steward, A., and Clarke, J. (2003) Hidden complexity in the mechanical properties of titin. *Nature 422*, 446-449.

(20) Christian, A. B., Harald, J., Alexej, K., and Daniel, J. M. (2007) Digital force-feedback for protein unfolding experiments using atomic force microscopy. *Nanotechnology*, 044022.

(21) Garcia-Manyes, S., Brujic, J., Badilla, C. L., and Fernández, J. M. (2007) Force-Clamp Spectroscopy of Single-Protein Monomers

Reveals the Individual Unfolding and Folding Pathways of I27 and Ubiquitin. *Biophysical Journal 93*, 2436-2446.

(22) Perez-Jimenez, R., Wiita, A. P., Rodriguez-Larrea, D., Kosuri, P., Gavira, J. A., Sanchez-Ruiz, J. M., and Fernandez, J. M. (2008) Force-Clamp Spectroscopy Detects Residue Co-evolution in Enzyme Catalysis. *Journal of Biological Chemistry 283*, 27121-27129.

(23) Lu, H., and Schulten, K. (1999) Steered molecular dynamics simulation of conformational changes of immunoglobulin domain I27 interprete atomic force microscopy observations. *Chemical Physics 247*, 141-153.

(24) Marek, C., Trinh Xuan, H., and Mark, O. R. (2004) Thermal effects in stretching of Go-like models of titin and secondary structures. *Proteins: Structure, Function, and Bioinformatics 56*, 285-297.

(25) Pai-Chi, L., and Dmitrii, E. M. (2003) Theoretical studies of the mechanical unfolding of the muscle protein titin: Bridging the time-scale gap between simulation and experiment. *The Journal of Chemical Physics 119*, 9260-9268.

(26) Erickson, H. P. (1997) Protein Biophysics: Enhanced: Stretching Single Protein Molecules: Titin Is a Weird Spring. *Science 276*, 1090-1092.

(27) Kageshima, M., Lantz, M. A., Jarvis, S. P., Tokumoto, H., Takeda, S., Ptak, A., Nakamura, C., and Miyake, J. (2001) Insight into conformational changes of a single [alpha]-helix peptide molecule through stiffness measurements. *Chemical Physics Letters 343*, 77-82.

(28) Mitsui, K., Nakajima, K., Arakawa, H., Hara, M., and Ikai, A. (2000) Dynamic Measurement of Single Protein's Mechanical Properties. *Biochemical and Biophysical Research Communications 272*, 55-63.

(29) Li, H. (2007) Engineering proteins with tailored nanomechanical properties: a single molecule approach. *Organic & Biomolecular Chemistry 5*, 3399-3406.

(30) Li, H., Oberhauser, A. F., Fowler, S. B., Clarke, J., and Fernandez, J. M. (2000) Atomic force microscopy reveals the mechanical design of a modular protein. *Proceedings of the National Academy of Sciences of the United States of America 97*, 6527-6531.

(31) Carrion-Vazquez, M., Oberhauser, A. F., Fisher, T. E., Marszalek, P. E., Li, H., and Fernandez, J. M. (2000) Mechanical design of proteins studied by single-molecule force spectroscopy and protein engineering. *Progress in Biophysics and Molecular Biology 74*, 63-91.

(32) Kawakami, M., Byrne, K., Brockwell, D. J., Radford, S. E., and Smith, D. A. (2006) Viscoelastic Study of the Mechanical Unfolding of a Protein by AFM. *Biophysical Journal 91*, L16-L18.

(33) Smith, D. A., Brockwell, D. J., Zinober, R. C., Blake, A. W., Beddard, G. S., Olmsted, P. D., and Radford, S. E. (2003) Unfolding Dynamics of Proteins under Applied Force. *Philosophical Transactions: Mathematical, Physical and Engineering Sciences 361*, 713-730.

(34) Brockwell, D. J., Beddard, G. S., Clarkson, J., Zinober, R. C., Blake, A. W., Trinick, J., Olmsted, P. D., Smith, D. A., and Radford, S. E. (2002) The Effect of Core Destabilization on the Mechanical Resistance of I27. *Biophysical Journal 83*, 458-472.

(35) Best, R. B., Brockwell, D. J., Toca-Herrera, J. L., Blake, A. W., Smith, D. A., Radford, S. E., and Clarke, J. (`) Force mode atomic force microscopy as a tool for protein folding studies. *Analytica Chimica Acta 479*, 87-105.

(36) Carrion-Vazquez, M., Marszalek, P. E., Oberhauser, A. F., and Fernandez, J. M. (1999) Atomic force microscopy captures length phenotypes in single proteins. *Proceedings of the National Academy of Sciences of the United States of America 96*, 11288-11292.

(37) Jeffrey, L. H., and John, B. (1993) Calibration of atomic-force microscope tips. *Review of Scientific Instruments 64*, 1868-1873.

(38) Brockwell, D. (2007) Force Denaturation of Proteins - an Unfolding Story. *Current Nanoscience 3*, 3–15.

(39) Rief, M., Fernandez, J. M., and Gaub, H. E. (1998) Elastically Coupled Two-Level Systems as a Model for Biopolymer Extensibility. *Physical Review Letters 81*, 4764.

(40) Walton, E. B., Lee, S., and Van Vliet, K. J. (2008) Extending Bell's Model: How Force Transducer Stiffness Alters Measured Unbinding Forces and Kinetics of Molecular Complexes. *94*, 2621-2630.

(41) Evans, E., and Ritchie, K. (1997) Dynamic strength of molecular adhesion bonds. *72*, 1541-1555.

(42) Marek, C., Trinh Xuan, H., and Mark, O. R. (2002) Thermal folding and mechanical unfolding pathways of protein secondary structures. *Proteins: Structure, Function, and Genetics 49*, 104-113.

(43) Nitin, R., Qiliang, Y., and Juan, J. d. P. (2004) Molecular simulation of the reversible mechanical unfolding of proteins. *The Journal of Chemical Physics 120*, 5781–8.

(44) José Luis R.Arrondo, and Alonso, A. (2006) in *Springer Series in Biophysics*, Springer-Verlag New York.

(45) Janovjak, H., Struckmeier, J., and Müller, D. J. (2005) Hydrodynamic effects in fast AFM single-molecule force measurements. *European biophysics journal: EBJ 34*, 91.

(46) Mai Suan, L., and Maksim, K. (2009) Dependence of protein mechanical unfolding pathways on pulling speeds. *The Journal of Chemical Physics 130*, 145102.

(47) King, W. T., Su, M., and Yang, G. (2009) Monte Carlo simulation of mechanical unfolding of proteins based on a simple two-state model. *International Journal of Biological Macromolecules 46*, 159-166.

(48) King, W. T., and Yang, G. (2009) Effects of Cantilever Stiffness on Unfolding Force in AFM Protein Unfolding. *Biophysical Journal 96*, 37a-38a.

(49) Dietz, H., and Rief, M. (2004) Exploring the energy landscape of GFP by single-molecule mechanical experiments. *Proceedings of the National Academy of Sciences of the United States of America 101*, 16192-16197.

(50) Hyeon, C., Morrison, G., Pincus, D. L., and Thirumalai, D. (2009) Refolding dynamics of stretched biopolymers upon force quench. *Proceedings of the National Academy of Sciences 106*, 20288-20293.

(51) Mickler, M., Dima, R. I., Dietz, H., Hyeon, C., Thirumalai, D., and Rief, M. (2007) Revealing the bifurcation in the unfolding pathways of GFP by using single-molecule experiments and simulations. *Proceedings of the National Academy of Sciences 104*, 20268-20273.

(52) Borgia, A., Williams, P. M., and Clarke, J. (2008) Single-Molecule Studies of Protein Folding. *Annual Review of Biochemistry Vol. 77*, 101-125.

(53) Gao, M., Lu, H., and Schulten, K. (2001) Simulated Refolding of Stretched Titin Immunoglobulin Domains. *Biophysical Journal 81*, 2268-2277.

(54) Li, M. S., Hu, C.-K., Klimov, D. K., and Thirumalai, D. (2006) Multiple stepwise refolding of immunoglobulin domain I27 upon force quench depends on initial conditions. *Proceedings of the National Academy of Sciences of the United States of America 103*, 93-98.

(55) Seckler, R., and Jaenicke, R. (1992) Protein folding and protein refolding. *FASEB J. 6*, 2545-2552.

(56) Andreas, J., Marcus, N., York, O., and Harald, F. (2000) Force Spectroscopy of Molecular Systems - Single Molecule Spectroscopy of Polymers and Biomolecules. *Angewandte Chemie 39*, 3212-3237.

(57) Kim, D. E., Fisher, C., and Baker, D. (2000) A breakdown of symmetry in the folding transition state of protein L. *Journal of Molecular Biology 298*, 971-984.

(58) Crampton, N., Al-Zahrani, K., Brockwell, D. J., and Connell, S. D. Mechanical unfolding of Protein L using a novel laser-feedback controlled cantilever reveals multiple transition barriers. *unpublished*.

(59) Taniguchi, Y., Brockwell, D. J., and Kawakami, M. (2008) The Effect of Temperature on Mechanical Resistance of the Native and Intermediate States of I27. *95*, 5296-5305.

(60) Yamashita, H., Kodera, N., Miyagi, A., Uchihashi, T., Yamamoto, D., and Ando, T. (2007) Tip-sample distance control using photothermal actuation of a small cantilever for high-speed atomic force microscopy. *Review of Scientific Instruments 78*, 083702.

(61) Arai, T., and Fujihira, M. (1994) Effect of tip shape on force-distance curves for AFM in aqueous electrolytes. *Journal of Electroanalytical Chemistry 374*, 269-273.

(62) Fukuma, T., and Jarvis, S. P. (2006) Development of liquid-environment frequency modulation atomic force microscope with

low noise deflection sensor for cantilevers of various dimensions. *Review of Scientific Instruments 77*, 043701.

(63) Ferdjallah, M., and Barr, R. E. (1990) Frequency-domain digital filtering techniques for the removal of powerline noise with application to the electrocardiogram. *Computers and Biomedical Research 23*, 473-489.

(64) Li, B. F., Yin, B. S., and Yu, D. K. (2002) Fast elimination of 50-Hz noise in PC-based application system. *Di 1 jun yi da xue xue bao= Academic journal of the first medical college of PLA 22*, 1131.

(65) Ott, H. W. (1988) *Noise reduction techniques in electronic systems*, Wiley New York.

(66) Hann, E., Kirkpatrick, N., Kleanthous, C., Smith, D. A., Radford, S. E., and Brockwell, D. J. (2007) The effect of protein complexation on the mechanical stability of Im9. *Biophysical journal 92*, L79-L81.

Chapter 7
Conclusions

The aim of the work presented in this thesis was to develop and test a new instrument (CD-AFM) for improving AFM force measurement. Force resolution can be improved using soft AFM cantilevers but such cantilevers are susceptible to mechanical instabilities that can limit their applicability. Cantilever mechanical instability can be manifested as a thermal fluctuation of cantilever position (thermodynamic noise) or as a discontinuity in the force distance curves, such as near the surface. The source of the thermal fluctuation is due to collisions of the surrounding molecules with the cantilever (Brownian motion). AFM cantilevers Brownian motion might obscure force measurement because the amplitude of Brownian motion could be comparable to the magnitude of the sample-cantilever interactions. When the force gradient in the vicinity of the surface exceeds the stiffness of the cantilever, the cantilever becomes unstable, or jumps to the surface, causing a discontinuity in the force distance curves. The discontinuity depends on the stiffness of the cantilever, the lower the cantilever stiffness the higher the tip-surface separation. During the discontinuity it is not possible to measure force and valuable information about the interaction between the cantilever tip and the sample surface may be lost. To our best knowledge, CD-AFM is the

first successful attempt to minimize mechanical instabilities associated with the use of the softest cantilevers available commercially in a liquid environment by using the optical beam deflection system, and the first time force curves of protein unfolding have been obtained using force feedback without the disadvantages associated with the use of soft cantilevers. The CD-AFM system does not require an involved set-up process allowing the user to perform the force experiments without additional preparation. Moreover, the system can be operated in the standard force spectroscopy mode by just switching off the feedback circuit. This gives the CD-AFM system an advantage over other methods used to control AFM cantilever instabilities.

The concept, design and operation of CD-AFM were introduced in chapter 3. The principle focus was on minimizing thermodynamic noise using an optical feedback system, the origin aim of this project. The CD-AFM design is based on the use of two laser diodes, 780 nm and 670nm. The 670 nm laser is used to read out the cantilever position and the higher-powered (780 nm) laser providing the force required for damping the cantilever oscillation.

Previous methods used to minimize cantilever instability were discussed. For example, the method based on magnetic force feedback has been used to overcome the cantilever instability associated with jump-to-contact and thermodynamic noise. However, such a method is technically demanding and not user-friendly because attaching magnets to the cantilever and placing the coils near the tip are a time consuming process. In addition, to our best knowledge, such a method has not been applied to detect a very small force for biological and non-biological samples as the use of very soft magnetized cantilevers are difficult. The soft cantilevers have a low mechanical quality factor in liquid, thus, attaching a magnet to them would deteriorate the quality factor further making the cantilever

response to force variations poor. Moreover, such cantilevers are prone to damage during attaching the magnet.

The performance of the CD-AFM was greatly enhanced by means of reducing the deflection system noise, such as shot and hop noise. It was shown that the level of damping is proportional to the level of the deflection system noise. The laser employed to suppress the cantilever deflection relies on the output of the optical detection system. Therefore, if the deflection signal is contaminated with noise the achievable damping level will be limited. The feedback system is therefore working to reduce noise that is not present mechanically, thereby inducing actual deflection oscillations across the frequency spectrum where none previously existed. The approach to reducing the noise was to first gain a full theoretical understanding for the origin of the noise, and the parameters that govern the signal to noise ratio in AFM optical lever detection system.

Moreover, the effect of proportional and integral gain (PI) values on the system performance was discussed. To maintain the setpoint constant PI values should be tuned carefully.

The thermodynamic noise of three soft cantilevers was decreased using CD-AFM. For example, the thermodynamic noise in the position of a microcantilever C (Veeco-spring constant=10pN/nm) was considerably reduced from ~3 nm to ~0.4 nm. This substantial reduction in cantilever thermal noise leads to improvement in the force resolution from ~30 pN to ~3 pN, which is equivalent to cooling the cantilever ~3 K. However, further decrease in the deflection system noise would result in a higher force resolution.

In chapter 4, a method to calibrate laser power to force was introduced. Forces cannot be acquired by the deflection signal as those forces were

balanced by optomechanical forces leaving the cantilever deflection constant. Thus, changes in the laser, employed to suppress the mechanical noise of the lever, was used instead of the deflection signal. The calibration was achieved by driving the cantilever harmonically using intensity-modulated laser. The cantilever response was treated as a forced harmonic system that allows the computation of the driving force using the forced harmonic oscillator equation. The calibration method is based on relating the force sensitivity (converting the driving voltage of laser intensity into force) to the frequency at which the cantilever is driven. Therefore, the force sensitivity can be used as a conversion factor.

We found that the force applied on an AFM cantilever is frequency dependent. The excitation force acting on a cantilever modulated using a periodic heat source (in this case, a laser beam) is not constant. Two forces are generated; photon and photothermal forces. The photothermal force becomes more distinct at lower modulation frequency resulting in an increase of the oscillation amplitude of the microlever. In the low frequency regime, <300 Hz, the force sensitivity increases exponentially with decreasing driving frequency. Three microcantilever were calibrated and all show the same general behavior, but with different responses and frequency ranges depending upon each cantilevers geometry and thermal properties.

Photon force is dominant at higher frequencies. For all cantilevers at higher frequencies the force sensitivity is constant at ~0.2 pN/nm, and that indicates the force at this regime does not depend on the cantilevers thermal properties, and by comparing this value to the one calculated for force radiation a good agreement found. To prove that the photothermal force, in the low frequency regime is prevailing, the force sensitivity was computed as a function of frequency utilizing the concept of temperature propagation inside the cantilever having wave-like behavior. The results

show an agreement with the experimental results indicating the predominant force in this regime is photothermal force.

The use of CD-AFM to obtain force distance curves was the major subject of chapter 5. In this chapter, the procedures followed to acquire a force distance curve using a locked cantilever were introduced. The force distance curves recorded using CD-AFM were shown to be a close replica to those obtained using conventional AFM.

A method to scale curves recorded using CD-AFM in force was introduced. The force sensitivity (pN/mV) found in chapter 4 is not straightforward to apply to a force curve because the rate of change of deflection is not constant. To overcome this drawback we proposed a relation between the force sensitivity and the rate change of laser power, instead of the driving frequency. The laser curve was divided into different segments of constant rate of change, and after converting to force, each region was added to each other to compute the resulting force.

The CD-AFM system can provide similar force and spatial resolution to those obtained by conventional AFM but without cantilever instabilities. To prove this, and test the laser power calibration method, two experiments were conducted. The first experiment was to study the electrostatic force generated between an AFM tip and mica surface acquired at different salt concentrations. The curves either obtained by conventional AFM or CD-AFM show the same behavior in which the maximum repulsive force measured prior to jump-to-contact decreases with increasing the salt concentrations and decays exponentially with increasing tip-surface separation with a decay length as a function of the salt concentration. Both conventional AFM and CD-AFM showed that the decay length at 10^{-5} M NaCl is ~20 nm decreasing to ~7 nm at 0.01 M. The repulsive force maximum measured by either conventional AFM or CD-AFM at each

concentration shows a good agreement indicating that the calibration method introduced in chapter 4 and 5 is valid. For instance, at 0.01 M NaCl the maximum repulsive force recorded using conventional AFM and CD-AFM was ~ 184 pN and ~178 pN respectively. One of the significant achievements in this chapter is that the cantilever deflection was kept constant at approximately 0.3 nm after jump-to-contact. This means CD-AFM is capable of recording surface forces using a softer cantilever in proximity of the surface that has never been explored before. The measurements show that the discontinuity in the force distance curve due to jump- to- contact using conventional AFM is ~7nm. This value approaches zero using CD-AFM.

The second experiment was devoted to study the behavior of CD-AFM on a soft surface. Young's modulus and the lipid bilayer thickness measured by either conventional AFM or CD-AFM showed no difference.

However, beyond the jump-to-contact point, the laser signal shows a linear increase whereas the cantilever deflection remains locked and the piezos-canner keeps moving. The cantilever deflection, the piezo displacement and the laser signal were recorded simultaneously. The source of the linear increase in laser signal upon contact is one of the drawbacks related to force-distance curves acquired using CD-AFM. We proposed the CD-AFM system keeps the cantilever locked on the surface and that linear increase is due to the friction effect. The cantilever bows forwards resulting in deformation of the cantilever that is suppressed by increasing the laser power. However, such a scenario needs more investigation.

In chapter 6, unfolding force-extension curves of proteins were obtained using the CD-AFM system. $(I27)_5$ construct was used as a proof of principle. Both curves recorded using CD-AFM or conventional AFM show the same unfolding curve of I27. The WLC model was used successfully to

fit unfolding force peaks of I27. The full unfolded length was found to be ~27 nm which in a good agreement with the value measured using conventional AFM. However, the unfolding forces measured by CD-AFM are always higher than those measured using conventional AFM. This may be due to an increase in the loading rate. Increasing the loading rate minimizes the thermal contribution in the unfolding process resulting in an accurate measurement of the force. Bell's model predicts that unfolding force is affected by the system stiffness and hence the loading rate. Thus, the higher the effective stiffness the higher the unfolding forces. In a CD-AFM experiment, the compliance of the cantilever is approximately zero, which increases the system effective stiffness, and hence loading rate. Consequently, CD-AFM can widen the accessible dynamic range with high force resolution. Usually, high loading rate is achieved either by increasing the cantilever spring constant or by retracting the cantilever attached to the protein at high pulling speed. However, the accessible loading rate in conventional AFM is limited because of the use of stiffer cantilever would decrease the force resolution and higher pulling speed is affected by an increasing hydrodynamic effect.

One of the most distinct results attained is the removal of cantilever recoil which prevents the formation of refolding peaks after unfolding because further tension may be loaded on the protein. The use of conventional AFM would obscure such peaks. For example, the unfolding force distance curve of protein L, which has observable refolding peaks, shows no sign of refolding peaks. However, such peaks can be readily observed on the force distance curve obtained by CD-AFM.

Is the cantilever cooled or stiffened?

In chapter 3, we described the reduction in the cantilever deflection induced by its Brownian motion (known as thermal noise) as cooling. However, in chapter 6 the reduction in the deflection resulting from

applying a load to the cantilever is described as stiffening. What appears as an inconsistency or discrepancy between the two descriptions can be explained as follows.

The working principle of laser cooling illustrated in chapter 1(section 1.12) is based on minimizing the atoms or oscillators velocities via a velocity dependent force. An increase in velocity increases the systems mean energy and hence the effective temperature (as described by the equipartition theorem).

Furthermore, it follows from the equipartition theorem the area beneath the thermal resonance peak of a mechanical oscillator can be used as a measure of its effective temperature (chapter 3, section 3.1). In principle, when damping thermal oscillations, the cantilever velocity and hence its mean energy reduces leading to freezing at the cantilever motion. Therefore, a reduction in the area beneath the thermal resonance peak can be considered as cooling if the optical force applied to reduce the thermal noise is velocity dependent. In chapter 4, we established that indeed the optical feedback force ‘is’ velocity dependent.

Alternatively, in chapter 6, the deflection is induced by applying a load on the cantilever at constant speed, so the feedback force works to resist this loading by applying a balancing force, leading to a constant deflection. Since the pulling speed is constant, the applied force is position dependent not velocity dependent. The optical feedback force increases or decreases according to the relative position of the cantilever from its equilibrium. Therefore, in summary, damping of the thermal resonance peak may be considered as ‘cooling’, and the locking of the cantilevers static position in protein unfolding experiments (CD-AFM) may be considered as ‘stiffening’.

We may understand the principle of CD-AFM in protein unfolding experiments as follows. If a load is applied onto two springs connected in series, the softer one extends more. A similar principle can be applied to the pulling experiment. The protein and the cantilever are connected as two springs in series. If the cantilever stiffness is smaller than the protein, the cantilever bends first allowing the thermal force to dominate the unfolding force. On the contrary, applying a balancing force minimizes the cantilever compliance and hence increases its effective stiffness. The load is transmitted entirely to the protein reducing the thermal force contribution by shortening the unfolding time and hence increasing the measured unfolding force. Therefore, the role of the balancing force is equivalent to stiffening the cantilever.

In summary, the CD-AFM system capability has been successfully proved and tested. Currently, thermodynamic noise which presents a fundamental limit to high force resolution experiments has been reduced to 3 pN. Moreover, the balancing force introduced using optical feedback force eliminates the effect of soft cantilever instabilities close to the surface allowing us to detect surface forces without a discountinity in the force separation curves associated with the use of conventional AFMs. Furthermore, loading rate in conventional AFM that is limited by the cantilever stiffness and pulling speed, can be increased using CD-AFM but without degenerating the force resolution. Using CD-AFM the cantilever recoil was removed and the refolding events of proteins, if exist, become observable. However, the electronic noise associated with the laser signal presents another limit to the force resolution, ~30 pN, that can be eliminated or reduced with some modifications in the system.

CD-AFM system can open the door for ultrahigh force resolution, and can be the source of detailed information about very short range tip-surface interactions. However, future work should be focused on increasing the

signal to noise ratio as electronic noise associated either with the deflection or laser signal can set a limit for high force resolution.

7.1 Future work

In this thesis we introduce a new method to lock cantilever deflection. However, potential possibilities of further work are still open, some of which will be described here.

In the mechanical unfolding of protein experiments, the CD-AFM system helps to extend the dynamic range of these experiments which is limited in conventional AFM experiments by the cantilever stiffness and the pulling velocity, and minimize the effect of cantilever's recoil that prevents refolding events. However, the force resolution is still limited to ~3 pN theoretically due to remaining thermodynamic noise r and ~30 pN practically because of electronic noise. This problem can be considered as a part of future work. Here we suggest a few steps that can help to achieve this goal.

1- Use of an isolation transformer

   Noise generated from variations in the ground potential of power outlets, when two or more pieces of electronic equipment are plugged in different power supplies, then linked together, could be few to tens millivolts added to the real signal. The use of a filter to remove this noise is not suitable as fast events may also be removed. The isolation transformer can help to improve the signal to noise ratio by means of eliminating the ground potential variation without affecting the real signal.

2- Use of a sensitive photodetector

The photodetector used in the CD-AFM head has low photo sensitivity and wide gaps between its segments which may increase the detection system noise, such as shot noise, that affects the performance of the feedback system. We suggest the use of four-segment Si *PIN (*photodiode -Hamamatsu Photonics: S6695-01) which has higher photo sensitivity and lower gap between its segments. Although this will reduce the ability of the AFM head to be used for conventional force spectroscopy, the gain in sensitivity should compensate for a reduction in versatility.

3- Use of a more powerful laser

The laser used to suppress cantilever deflection is LD2 (HL7851G, 50 mW, 780 nm, Hitachi). In order to increase the dynamic range of laser curves recorded via laser signal and to improve signal to noise ratio, we propose to replace LD2 with a powerful laser.

One area of research not explored in this thesis is the possibility to use the CD-AFM system for visualizing surface's topographies. In section 3.5 we showed that if the CD-AFM system is driven at frequencies higher than 30 KHz the system will amplify the cantilever motion (positive feedback) rather than suppressing the motion. The use of low stiffness cantilevers to image surfaces is not adequate as these levers have low mechanical quality factor (1-3) and low resonance frequency (<3 kHz) that would deteriorate the quality of imaging. However, such cantilevers have low applied force onto surfaces, in particular soft surfaces. The use of stiff cantilevers to image a soft surface, such as DNA, could change some aspect of the sample such as affecting the height of the sample, which can be compressed under the high force.

In order to prove that imaging by the CD-AFM system is possible, we imaged a reference grid (TGT01,Mikro-Masch, 3 µm pitch, 26 nm step-

height) using our system and compared it to standard taping mode image. In this setup the system was operated in tapping mode at driving frequency of 38 kHz and driving amplitude of 100 mV using microcantilever C (10 pN/nm) (image below). The system's feedback works on maintaining the setpoint constant, but due to high driving frequency the system actuates the cantilever instead of locking its motion.